

Mauren Abreu de Souza  
Humberto Remigio Gamba  
Helio Pedrini *Editors*

# Multi- Modality Imaging

Applications and Computational  
Techniques

 Springer

# Multi-Modality Imaging

Mauren Abreu de Souza  
Humberto Remigio Gamba • Helio Pedrini  
Editors

# Multi-Modality Imaging

Applications and Computational Techniques

 Springer

*Editors*

Mauren Abreu de Souza  
Graduate Program on Health  
Technology (PPGTS)  
Pontifical Catholic University of  
Paraná – PUCPR  
Curitiba, Paraná, Brazil

Humberto Remigio Gamba  
Federal University of Technology – Paraná  
(UTFPR)  
Curitiba, Paraná, Brazil

Helio Pedrini  
Institute of Computing  
University of Campinas  
Campinas, SP, Brazil

ISBN 978-3-319-98973-0      ISBN 978-3-319-98974-7 (eBook)  
<https://doi.org/10.1007/978-3-319-98974-7>

Library of Congress Control Number: 2018960266

© Springer Nature Switzerland AG 2018

This work is subject to copyright. All rights are reserved by the Publisher, whether the whole or part of the material is concerned, specifically the rights of translation, reprinting, reuse of illustrations, recitation, broadcasting, reproduction on microfilms or in any other physical way, and transmission or information storage and retrieval, electronic adaptation, computer software, or by similar or dissimilar methodology now known or hereafter developed.

The use of general descriptive names, registered names, trademarks, service marks, etc. in this publication does not imply, even in the absence of a specific statement, that such names are exempt from the relevant protective laws and regulations and therefore free for general use.

The publisher, the authors and the editors are safe to assume that the advice and information in this book are believed to be true and accurate at the date of publication. Neither the publisher nor the authors or the editors give a warranty, express or implied, with respect to the material contained herein or for any errors or omissions that may have been made. The publisher remains neutral with regard to jurisdictional claims in published maps and institutional affiliations.

This Springer imprint is published by the registered company Springer Nature Switzerland AG  
The registered company address is: Gewerbestrasse 11, 6330 Cham, Switzerland



# Preface

This book presents different approaches on multimodality imaging with a focus on biomedical applications. In terms of medical imaging, it is possible to divide into two categories: functional (related to physiological body measurements) and anatomical (structural) imaging modalities.

It is worth mentioning that this book covers some imaging combination coming from the usual popular modalities (such as the anatomical modalities, e.g. X-ray, CT and MRI); but it also includes some promising and new imaging modalities that are still being developed and improved (such as infrared thermography (IRT) and photoplethysmography imaging (PPGI)), implying in potential approaches for innovative biomedical applications.

Moreover, it includes a variety of tools on computer vision, imaging processing and computer graphics, which led to the generation and visualization of 3D models, allowing the most recent advances in this area possible. This is an ideal book for students and biomedical engineering researchers covering the biomedical imaging field.

The book covers a wide range of topics employing different multimodality imaging techniques for biomedical applications. The book is distributed in nine chapters, as follows:

## **Chapter 1—Infrared Thermography**

Regarding non-invasive and non-contact imaging modalities, **infrared thermography (IRT)** is presented in the first chapter. Such modality is also called infrared (IR) imaging or thermal imaging. The main approach here is related to the diagnosis of several diseases, including breast cancer, rheumatic diseases, vascular diseases, etc. Apart from the diagnostic approach, the constant monitoring is also increasing its relevance in a wide range of different medical fields (i.e. the acquisition of vital signs, including temperature, respiratory rate, heart rate and blood perfusion). A recent approach still to be further explored involves the expansion towards 3D infrared imaging applications.

## **Chapter 2—Photoplethysmography Imaging and Common Optical Hybrid Imaging Modalities**

Still presenting non-invasive and contactless approaches, the second chapter allows obtaining skin perfusion studies. In such modality, the active photoplethysmography imaging (PPGI) provides the mapping of dermal blood perfusion dynamics. The definition of PPGI consists in a classical photoplethysmography and pulse oximetry ( $\text{SpO}_2$ ), which actually involves the remote opto-electronical measurement of arterial and/or venous blood volume changes. Although the results presented are very promising, they are still preliminary, since they still need to be standardized as a clinical application, especially for removing movement artefacts.

## **Chapter 3—Multimodal Image Fusion for Cardiac Resynchronization Therapy Planning**

Cardiac resynchronization therapy (CRT) is due to treat patients with left-sided heart failure. This chapter presents optimizations of preoperative CRT plan, in order to produce increasing rates of such therapies. They had used a variety of imaging modalities, describing the anatomy, mechanical activation and tissue characteristics of the left ventricular (LV) under study. The authors developed a full workflow to process, register and fuse computer tomography (CT) images, ultrasound (US) images and magnetic resonance imaging (MRI). The results are represented as 3D patient-specific models, describing the anatomy of the involved heart regions (such as the LV, the coronary veins), even the electromechanical delays and the presence of fibrosis. The results obtained with such 3D patient-specific models are helping physicians to select the best surgical procedures, involving the most adequate LV pacing sites.

## **Chapter 4—CFD-Based Postprocessing of CT-MRI Data to Determine the Mechanics of Rupture in Abdominal Aortic Aneurysms**

An approach employing a combination of two different imaging modalities (CT and MRI) for an application involving computational fluid dynamics (CFD) is presented in this chapter. The application involves a case study of diagnosis and surgical intervention's decision on abdominal aortic aneurysms (AAA). In the presented study, since the clinical metric is not enough for the prognoses rupture, a mechanics-based approach and computational fluid dynamics (CFD) are also undertaken. This is important since a patient-specific geometry and boundary conditions are employed for the analysis. In addition, a fluid structure interaction (FSI)-based analysis of the abnormal aorta is employed. An important conclusion is outlined in this study that the maximum transverse diameter is not the only parameter of AAA rupture's risk. Additionally, the mechanics approach based on multimodality image methodology produced a better diagnosis.

## **Chapter 5—Human Head Modelling Simulation Applied to Electroconvulsive Therapy**

Regarding the generation of 3D realistic human head models, this chapter reconstructed such models based on magnetic resonance images. The problematic here is because it is aimed for electroconvulsive therapy (ECT) applications for treating

neurological conditions, once ECT uses low frequency and high amplitude of current, during a short period of time. Then, such electrical stimulation may generate heat due to the Joule effect. So, bio-heat transfer equation and Laplace equation were implemented for computational investigation. The results were analysed based on two points of view: thermal conductivity (which proved to be brain's safe) and electrical conductivity (which is an important factor to be taken into account).

### **Chapter 6—Use of Photon Scattering Interactions in Diagnosis and Treatment of Diseases**

Regarding the use of invasive imaging modalities, such as photon scattering applications in medicine, it presented two types of scattering events: incoherent (Compton) and coherent (Rayleigh). Therefore, first this chapter presents an overview of Compton cameras for gamma imaging, in the context of proton beam therapy. Potential methods for in vivo proton range verification are also presented. Additionally, the principle of operation of the Compton cameras and imaging reconstruction techniques is included (i.e. back-projection and stochastic approaches). Later, the chapter presents tissue diffraction, which is based on coherent scattering as a diagnostic tool. X-ray diffraction (XRD) is presented in order to help in the differentiation of both health and cancerous tissue, based on the ability to discriminate tissue types. Further, some results including the generation of surface-rendered 3D volumes are presented, in order to allow the 3D differentiation of the tissues investigated (between tumour and normal tissue).

### **Chapter 7—Digital Breast Tomosynthesis: Systems, Characterization and Simulation**

This chapter also focuses on invasive imaging modalities. Digital breast tomosynthesis (DBT) is an imaging application for breast cancer detection, which allows the generation of quasi-3D reconstruction images. First, this chapter presents an introduction and extensive review about digital X-ray tomosynthesis, including details about geometries, performance of the detectors, automatic exposure control performance, response function noise analysis, modulation transfer function (MTF), etc. Then, the image quality measurements are presented, since these issues are important for clinical tasks, such as the detection of microcalcifications. The last part of this chapter covers image simulation methods for DBT optimization. Several aspects are considered (e.g. image acquisition parameters, detector response, system geometry, radiation dose and image processing and reconstruction algorithms) considering acceptable breast doses as well. Regarding the clinical trials, there are two approaches, either involving a huge group of volunteers (asymptomatic women) or based on image simulation methods (virtual trials). The last option consists in fast, radiation-free and cost-effective option.

### **Chapter 8—Out-of-Core Rendering of Large Volumetric Data Sets at Multiple Levels of Detail**

Regarding the massive high-resolution volume data (especially obtained from the anatomical imaging modalities, such as X-ray, microtomography, ultrasonography and magnetic resonance imaging), there is a constant need for being able to

computationally deal with all these data. Then, the traditional in-core volume rendering is quite limited. So, this chapter presents an architecture for out-of-core volume rendering, keeping the levels of detail. Therefore, several experiments were conducted in order to show the improvements of such approach, especially in terms of memory storage, computational required time during the rendering process and even frame rate.

### **Chapter 9—Geometric and Topological Modelling of Organs and Vascular Structures from CT Data**

Still related to the generation and visualization of 3D models, the automatic segmentation of computer tomography (CT) images is a topic of interest. So, this chapter deals with the several modelling problems, mainly for surgery planning and training applications. For example, some of the issues presented are transformation and extraction of DICOM data, organs with branching or complex structures, polygon triangulation and file formats, among other issues. In general, the proposed solutions are related to allow the algorithms to be used together in order to provide surface-based reconstructions not only of organs but also at vascular structures, which can even be visualized with transparency.

The common approach among all these chapters is that either they employ the combination of functional and/or anatomical imaging, leading to multimodality imaging, or they apply different imaging modalities in order to generate 3D imaging data. The promising biomedical applications presented here are (1) the acquisition of vital signs from infrared thermography images (including temperature, respiratory rate, heart rate and blood perfusion), (2) dermal blood perfusion dynamics (involving photoplethysmography and optical hybrid imaging modalities), (3) 3D generation of abdominal aortic aneurysms (AAA) (including computational fluid dynamics (CFD), fluid structure interaction (FSI) and mechanical approaches), (4) cardiac resynchronization therapy (CRT) involving the 3D generation of not only the heart but also specific regions of it (e.g. left ventricular (LV) and coronary veins) and (5) the generation of 3D realistic human head models (from MRI data) for electroconvulsive therapy applications; regarding the use of invasive radiation, such as (6) X-ray diffraction (XRD) for 3D differentiation between tumour and normal tissues and (7) digital breast tomosynthesis (DBT) for the generation of quasi-3D reconstruction of the breast, for cancer detection; and finally, some of the computational techniques that are allowing all these lately improvements, for example, (8) dealing with the out-of-core volume rendering of all the massive high resolution volume data involving medical imaging and (9) the generation and visualization of 3D models mainly for surgery planning and training applications.

Curitiba, Paraná, Brazil  
Curitiba, Paraná, Brazil  
Campinas, SP, Brazil

Mauren Abreu de Souza  
Humberto Remigio Gamba  
Helio Pedrini

# Contents

<b>1 Infrared Thermography</b> .....	1
Carina Barbosa Pereira, Xinchu Yu, Stephan Dahlmanns, Vladimir Blazek, Steffen Leonhardt, and Daniel Teichmann	
<b>2 Photoplethysmography Imaging and Common Optical Hybrid Imaging Modalities</b> .....	31
Vladimir Blazek, Stephan Dahlmanns, Carina Barbosa Pereira, Xinchu Yu, Nikolai Blanik, Steffen Leonhardt, and Claudia Rosa Blazek	
<b>3 Multimodal Image Fusion for Cardiac Resynchronization Therapy Planning</b> .....	67
Sophie Bruge, Antoine Simon, Nicolas Courtial, Julian Betancur, Alfredo Hernandez, François Tavad, Erwan Donal, Mathieu Lederlin, Christophe Leclercq, and Mireille Garreau	
<b>4 CFD-Based Postprocessing of CT-MRI Data to Determine the Mechanics of Rupture in Abdominal Aortic Aneurysms</b> .....	83
Tejas Canchi, Eddie Y. K. Ng, Ashish Saxena, and Sriram Narayanan	
<b>5 Human Head Modelling Simulation Applied to Electroconvulsive Therapy</b> .....	103
Marília Menezes de Oliveira, Bo Song, Tony Ahfock, Yan Li, and Paul Wen	
<b>6 Use of Photon Scattering Interactions in Diagnosis and Treatment of Disease</b> .....	135
Robert Moss, Andrea Gutierrez, Amany Amin, Chiaki Crews, Robert Speller, Francesco Iacoviello, Paul Shearing, Sarah Vinnicombe, and Selina Kolokytha	
<b>7 Digital Breast Tomosynthesis: Systems, Characterization and Simulation</b> .....	159
Anastasio Konstantinidis, Selina Kolokytha, and Andria Hadjipanteli	

<b>8 Out-of-Core Rendering of Large Volumetric Data Sets at Multiple Levels of Detail</b> .....	191
Paulo Henrique Junqueira Amorim, Thiago Franco de Moraes, Jorge Vicente Lopes da Silva, and Helio Pedrini	
<b>9 Geometric and Topological Modelling of Organs and Vascular Structures from CT Data</b> .....	217
João Fradinho Oliveira, José Blas Pagador, José Luis Moyano-Cuevas, Francisco Miguel Sánchez-Margallo, and Hugo Capote	
<b>Index</b> .....	249

# Contributors

**Tony Ahfock** University of Southern Queensland, Darling Heights, QLD, Australia

**Amany Amin** John Radcliffe Hospital, Oxford, UK  
St Bartholomew's Hospital, London, UK

**Paulo Henrique Junqueira Amorim** Division of 3D Technologies, Center for Information Technology Renato Archer, Campinas, SP, Brazil

**Carina Barbosa Pereira** Chair for Medical Information Technology, Helmholtz-Institute for Biomedical Engineering, RWTH Aachen University, Aachen, Germany

**Julian Betancur** Univ Rennes, CHU Rennes, Inserm, LTSI – UMR 1099, Rennes, France

Université de Rennes 1, LTSI, Rennes, France

**Nikolai Blanik** Chair for Medical Information Technology, Helmholtz-Institute for Biomedical Engineering, RWTH Aachen University, Aachen, Germany

**Claudia Rosa Blazek** The Private Clinic of Dermatology, Haut im Zentrum, Zurich, Switzerland

**Vladimir Blazek** Chair for Medical Information Technology, Helmholtz-Institute for Biomedical Engineering, RWTH Aachen University, Aachen, Germany

Czech Institute of Informatics, Robotics and Cybernetics (CIIRC), Czech Technical University in Prague, Prague, Czech Republic

**Sophie Bruge** Univ Rennes, CHU Rennes, Inserm, LTSI – UMR 1099, Rennes, France

Université de Rennes 1, LTSI, Rennes, France

**Tejas Canchi** School of Mechanical and Aerospace Engineering, Nanyang Technological University, Singapore, Singapore

**Hugo Capote** Hospital Dr. José Maria Grande, Portalegre, Portugal

**Nicolas Courtial** Univ Rennes, CHU Rennes, Inserm, LTSI – UMR 1099, Rennes, France

Université de Rennes 1, LTSI, Rennes, France

**Chiaki Crews** Department of Medical Physics & Biomedical Engineering, University College London, London, UK

**Stephan Dahlmanns** Chair for Medical Information Technology, Helmholtz-Institute for Biomedical Engineering, RWTH Aachen University, Aachen, Germany

**Erwan Donal** Univ Rennes, CHU Rennes, Inserm, LTSI – UMR 1099, Rennes, France

Université de Rennes 1, LTSI, Rennes, France

**Mireille Garreau** Univ Rennes, CHU Rennes, Inserm, LTSI – UMR 1099, Rennes, France

Université de Rennes 1, LTSI, Rennes, France

**Andrea Gutierrez** Department of Medical Physics & Biomedical Engineering, University College London, London, UK

**Andria Hadjipanteli** Medical School, University of Cyprus, Nicosia, Cyprus

**Alfredo Hernandez** Univ Rennes, CHU Rennes, Inserm, LTSI – UMR 1099, Rennes, France

Université de Rennes 1, LTSI, Rennes, France

**Francesco Iacoviello** Electrochemical Innovation Lab, Department of Chemical Engineering, University College London, London, UK

**Selina Kolokytha** Empa, Centre for X-Ray Analytics, Swiss Federal Laboratories for Materials Science and Technology, Dübendorf, Switzerland

**Anastasios Konstantinidis** Diagnostic Radiology and Radiation Protection Service, Christie Medical Physics and Engineering, The Christie NHS Foundation Trust, Manchester, UK

**Christophe Leclercq** Univ Rennes, CHU Rennes, Inserm, LTSI – UMR 1099, Rennes, France

Université de Rennes 1, LTSI, Rennes, France

**Mathieu Lederlin** Univ Rennes, CHU Rennes, Inserm, LTSI – UMR 1099, Rennes, France

Université de Rennes 1, LTSI, Rennes, France



**Steffen Leonhardt** Chair for Medical Information Technology, Helmholtz-Institute for Biomedical Engineering, RWTH Aachen University, Aachen, Germany

**Yan Li** University of Southern Queensland, Darling Heights, QLD, Australia

**Marília Menezes de Oliveira** The University of Sydney, Sydney, NSW, Australia  
University of Southern Queensland, Darling Heights, QLD, Australia

**Thiago Franco de Moraes** Division of 3D Technologies, Center for Information Technology Renato Archer, Campinas, SP, Brazil

**Robert Moss** Department of Medical Physics & Biomedical Engineering, University College London, London, UK

**José Luis Moyano-Cuevas** Bioengineering and Health Technology Unit, Jesús Usón Minimally Invasive Surgery Center, Cáceres, Spain

**Sriram Narayanan** Department of General Surgery, Tan Tock Seng Hospital, Singapore, Singapore

**Eddie Y. K. Ng** School of Mechanical and Aerospace Engineering, Nanyang Technological University, Singapore, Singapore

**João Fradinho Oliveira** C3i + CIAUD, Instituto Politécnico de Portalegre + Universidade de Lisboa, Lisboa, Portugal

**José Blas Pagador** Bioengineering and Health Technology Unit, Jesús Usón Minimally Invasive Surgery Center, Cáceres, Spain

**Helio Pedrini** Institute of Computing, University of Campinas, Campinas, SP, Brazil

**Francisco Miguel Sánchez-Margallo** Jesús Usón Minimally Invasive Surgery Center, Cáceres, Spain

**Ashish Saxena** School of Mechanical and Aerospace Engineering, Nanyang Technological University, Singapore, Singapore

**Paul Shearing** Electrochemical Innovation Lab, Department of Chemical Engineering, University College London, London, UK

**Jorge Vicente Lopes da Silva** Division of 3D Technologies, Center for Information Technology Renato Archer, Campinas, SP, Brazil

**Antoine Simon** Univ Rennes, CHU Rennes, Inserm, LTSI - UMR 1099, Rennes, France

Université de Rennes 1, LTSI, Rennes, France

**Bo Song** University of Southern Queensland, Darling Heights, QLD, Australia

**Robert Speller** Department of Medical Physics & Biomedical Engineering, University College London, London, UK

**François Tavard** Univ Rennes, CHU Rennes, Inserm, LTSI - UMR 1099, Rennes, France

Université de Rennes 1, LTSI, Rennes, France

**Daniel Teichmann** Chair for Medical Information Technology, Helmholtz-Institute for Biomedical Engineering, RWTH Aachen University, Aachen, Germany

**Sarah Vinnicombe** The Breast Unit, Cheltenham, Gloucestershire Hospitals NHS Foundation Trust, Gloucester, UK

The University of Dundee, Dundee, UK

**Paul Wen** University of Southern Queensland, Darling Heights, QLD, Australia

**Xinchi Yu** Chair for Medical Information Technology, Helmholtz-Institute for Biomedical Engineering, RWTH Aachen University, Aachen, Germany

# Chapter 1

## Infrared Thermography



**Carina Barbosa Pereira, Xinchu Yu, Stephan Dahlmanns, Vladimir Blazek, Steffen Leonhardt, and Daniel Teichmann**

**Abstract** Infrared thermography (also infrared imaging or thermal imaging) is a new remote, non-contact and non-invasive diagnostic and monitoring technique with increasing relevance in a wide range of medical fields. This is mainly due to the several advantages of this technology. Thermal imaging is a passive technique which detects the radiation naturally emitted from an object, in this case the human skin, and does not use any harmful radiation. Thus, infrared thermography (IRT) is suitable for prolonged and repeated use. In the last decades, new medical applications for thermal imaging have arisen. These techniques have been successfully used in the diagnosis of several pathologies, including breast cancer, rheumatic diseases, dry eye syndrome, vascular diseases, etc. Infrared thermography has also demonstrated its potential in the monitoring of several vital signs, including temperature, respiratory rate, heart rate, and blood perfusion. Recently, there has been new advance in 3D infrared imaging. A three-dimensional thermal signature may provide several advantages in the detection and monitoring of the course of several pathologies including arthritis, thyroid dysfunctions, breast cancer, sports lesions, and diabetic foot. The current chapter focuses on advances in the area of medical IRT. First, it reviews the basics of IRT and essential theoretical background. Second, some medical applications and corresponding methods are

---

Carina Barbosa Pereira, Xinchu Yu, and Stephan Dahlmanns contributed equally to this work.

C. Barbosa Pereira (✉) · X. Yu · S. Dahlmanns · S. Leonhardt · D. Teichmann  
Chair for Medical Information Technology, Helmholtz-Institute for Biomedical Engineering,  
RWTH Aachen University, Aachen, Germany  
e-mail: [pereira@hia.rwth-aachen.de](mailto:pereira@hia.rwth-aachen.de)

V. Blazek  
Chair for Medical Information Technology, Helmholtz-Institute for Biomedical Engineering,  
RWTH Aachen University, Aachen, Germany  
Czech Institute of Informatics, Robotics and Cybernetics (CIIRC), Czech Technical University  
in Prague, Prague, Czech Republic

described in detail. Third, it gives an overview on the recent advances on “3D Infrared Thermography”.

**Keywords** Infrared thermography · Medical applications · Diagnostic · Monitoring · 3D infrared thermography

## 1.1 Introduction

Infrared thermography (IRT), also known as thermal imaging, is an imaging modality, which senses infrared radiation (heat) emitted by objects. In contrast to other imaging techniques in medicine, such as X-Ray, computed tomography (CT), and magnetic resonance imaging (MRI), IRT is a completely passive—i.e., non-invasive and non-radiating—measurement technique. The first infrared thermogram of a human was recorded in 1928 by Prof. Czerny in Frankfurt, Germany [1]. Initially, only single infrared detectors have been used. Later on, during World War II, infrared detectors have been developed and used for military applications [2]. Besides the issues regarding availability (military restrictions) and price, that technology was unsuitable for medical applications: both thermal resolution (approx. 0.5 K) and spatial resolution (approx. 5 mm at a target size of 50 cm<sup>2</sup>) were too low in order to detect small temperature differences and anatomic structures on the human body. Moreover, the infrared detectors were big and needed cooling by, e.g., nitrogen, argon gas, or a sterling cooler [3]. It was only in the 1990s and early 2000s when the development and availability of uncooled microbolometer focal plane arrays (FPA) pioneered the usage of IRT in medicine. In contrast to the old devices with single detectors, the new cameras with FPAs provided a high spatial and thermal resolution. Also temporal resolution (sample rate or scanning speed) increased, enabling real-time and high-speed recordings. Another factor was the availability of computers and more user-friendly image processing software [3, 4].

A widely known medical application of modern IRT is mass fever screening during worldwide pandemics, for example, at airports. With the general trend in medicine away from a reactive, curative approach (diagnosis and treatment) towards a proactive and preventive approach (identification of risks and elimination of those), IRT is playing an important role. Since it can easily detect anomalies of body surface temperature, i.e., hyperthermia due to inflammation or hypothermia induced by poor perfusion, there are multiple medical applications [4]. In this chapter, we will introduce some of them—detection of breast cancer, diagnosis of rheumatic diseases, dry eye syndrome, wounds, monitoring of vital signs (respiratory rate, cardiac pulse, and perfusion) as well as the capabilities of 3D thermal imaging.

## 1.2 Physical Principles of Infrared Thermography

Thermographic cameras are unable to sense the surface temperature of an object directly. Rather, the power of electromagnetic rays that hit the sensors of the cameras is measured. In this section the physical principles for the calculation of the surface temperature from its radiation are introduced. Additionally, the effects of non-ideal objects as well as effects of the transport medium in medical applications of thermographic measurements will be considered.

### 1.2.1 Thermal Radiation

All objects with a surface temperature above absolute zero (0 K or  $-273.15^\circ\text{C}$ , respectively) emit electromagnetic radiation with a particular wavelength ( $\lambda$ ). This phenomenon is different from heat transfer due to the collusion of particles, called conduction, where the energy transport depends on the temperature gradient inside the transport medium. Radiation, on the other hand, describes the energy transfer by electromagnetic waves, which is solely dependent on the temperature of the radiation source. For example, the electromagnetic radiation of the sun reaches Earth even though the temperature of outer space is constant.

The theory of radiant heat was first described by Max Planck in 1913 and is the fundamental basis of the calculation of surface temperatures based on the spectral analysis of its radiation [5].

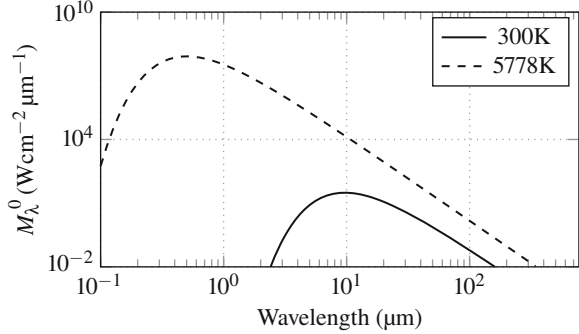
### 1.2.2 Blackbody Radiation

A practical way to describe the energy flux of radiation is via an idealized physical body called “blackbody”. A blackbody absorbs all incident radiant energy without reflection and is homogeneous as well as isotropic. Hence, its radiation is emitted uniformly in all directions of space. In addition, it is postulated that all radiation of a blackbody is entirely dependent on the body’s absolute temperature, therefore the phenomena of luminescence are excluded from calculations. In order to describe thermal radiation, the permanent state will be investigated, which means that the energy and thus the temperature of the blackbody are distributed equally inside its volume.

Based on these assumptions, it is possible to calculate the spectral distribution of thermal radiation emitted by a blackbody. This function was first described by Max Planck as the Planck spectrum  $M_\lambda^0$  and follows the equation:

$$M_\lambda^0(\lambda, T) = \frac{2\pi hc^2}{\lambda^5 \cdot (e^{\frac{hc}{\lambda kT}} - 1)}. \quad (1.1)$$

**Fig. 1.1** Spectral radiant exitance of a body ( $M_\lambda^0$ ) at two different temperatures: 300 and 5778 K (surface temperature of the sun)



Here,  $M_\lambda^0$  represents the spectral radiant exitance of the blackbody in ( $\text{W m}^{-2} \mu\text{m}^{-1}$ ),  $\lambda$  is the wavelength ( $\mu\text{m}$ ),  $T$  stands for the surface temperature (K),  $h$  denotes the Planck constant ( $h = 6.626 \times 10^{-34}$  J s),  $k = 1.3807 \times 10^{-23}$  J K $^{-1}$  corresponds to the Boltzmann constant, and  $c = 2.998 \times 10^8$  m s $^{-1}$  is the speed of light in vacuum.  $M_\lambda^0$  is a function of  $\lambda$ , which means that the total energy content is distributed over a range of wavelengths. This resulting energy distribution is dependent on the temperature  $T$  of the blackbody as displayed in Fig. 1.1.

The shape of the Planck spectrum is similar for all temperatures, but its amount of power as well as the wavelength of maximum power ( $\lambda_{\text{max}}$ ) is shifted based on the surface temperature. For example, the surface temperature of the sun equals 5778 K; this creates a spectrum with a wavelength of maximum power at around  $\lambda_{\text{max}} \approx 500$  nm (the wavelength where human eyes evolved to be most sensitive ranges between about 390 and 700 nm). Bodies with surface temperatures around 300 K (26.85 °C) generate a Planck spectrum between 2.5 and 150  $\mu\text{m}$ . As temperature decreases, the radiation emitted is more in the range of longer wavelengths. This effect is explained by Wien's displacement law. Wavelengths created by surface temperatures of around 300 K are invisible for the human eye, but sensors that are sensitive around 10  $\mu\text{m}$  are able to detect this radiation, just like human eyes can detect the radiation emitted by the sun [6].

Surface temperatures can be calculated based on the total radiant power per surface area  $M$  ( $\text{W m}^{-2}$ ). Hence, it is not necessary for thermal detectors to distinguish between different wavelengths. In general,  $M$  describes the area underneath the curves given in Fig. 1.1; it can be calculated by integrating  $M_\lambda^0$  over the range of all significant wavelengths as given by

$$M = \int_{\lambda^0=0}^{\infty} M_\lambda^0 d\lambda. \quad (1.2)$$

The solution of the integral can be estimated by applying the Stefan-Boltzmann law:

$$M = \sigma \cdot T^4, \quad (1.3)$$

where  $\sigma = 5.67 \times 10^{-8}$  W m $^{-2}$  K $^{-4}$  is the Stefan-Boltzmann constant. With this equation the surface temperature of an object can be easily calculated based on the

measurement of the radiated power per surface area. This is the general working principle of sensors integrated in thermographic cameras.

### 1.2.3 Greybody Radiation

Both Planck's and Stefan-Boltzmann's law describe the radiation of a blackbody under ideal conditions. Nevertheless, real bodies often do not absorb all radiant energy. In general, objects interact in three different ways with radiation: by absorption ( $\alpha$ ), reflection ( $\beta$ ), and transmission ( $\gamma$ ). Considering the law of conservation of energy,  $\alpha + \beta + \gamma = 1$  applies. For black bodies, the absorption value  $\alpha$  equals 1 and reflection and transmission are zero. If the absorption value is less than 1, the considered object is called a "greybody". Solid bodies are generally opaque (transmission  $\gamma = 0$ ), and consequently  $\alpha + \beta = 1$ .

According to Kirchhoff's law, at a given temperature the ratio of radiant absorbance to emittance is constant for greybodies ( $\alpha = \epsilon$ ), therefore the emissivity for each wavelength is described by

$$\epsilon = 1 - \beta_{\lambda}. \quad (1.4)$$

For greybodies the Stefan-Boltzmann law takes the form

$$M = \epsilon \cdot \sigma \cdot T^4, \quad (1.5)$$

where  $\epsilon$  is constant for all wavelengths. Since  $\epsilon$  is smaller than 1 for greybodies, their temperature has to be larger to create the same total radiant power of blackbodies.

### 1.2.4 Temperature Measurement

As mentioned previously, thermal cameras measure and convert the radiation energy emitted by a body into a temperature value. However, not all radiation detected by the camera sensors corresponds to the target object. The measured energy ( $W_{\text{tot}}$ ) rather consists of the emission of the object ( $E_{\text{obj}}$ ) plus reflected emission from ambient sources ( $E_{\text{amb}}$ ) and emission from the atmosphere ( $E_{\text{atm}}$ ).

The atmosphere describes the transport medium of heat radiation. In this medium, there are molecules that interact with the heat rays: some of its energy gets absorbed or scattered and the atmospheric transmittance  $\gamma_{\text{atm}}$  must be considered. Therefore, the Stefan-Boltzmann law for black bodies in vacuum,

$$M_{\text{measured}} = \sigma \cdot T_{\text{obj}}^4, \quad (1.6)$$

**Table 1.1** Parameters used to calculate the temperature of the target object  $T_{\text{obj}}$ 

Parameter	Symbol	Value
Total radiant power	$M_{\text{measured}}$	Measured by the camera
Emittance of object	$\epsilon_{\text{obj}}$	Unknown/estimated
Transmittance of atmosphere	$\gamma_{\text{atm}}$	Approximated: $\gamma_{\text{atm}} \cong 1$
Stefan-Boltzmann constant	$\sigma$	$5.67 \times 10^{-8} \text{ W m}^{-2} \text{ K}^{-4}$
Temperature of ambient objects	$T_{\text{amb}}$	Unknown
Temperature of the atmosphere	$T_{\text{atm}}$	Unknown

must be adapted for greybodies in the atmosphere:

$$M_{\text{measured}} = \epsilon_{\text{obj}} \cdot \gamma_{\text{atm}} \cdot \sigma \cdot T_{\text{obj}}^4 + (1 - \epsilon_{\text{obj}}) \cdot \gamma_{\text{atm}} \cdot \sigma \cdot T_{\text{amb}}^4 + (1 - \gamma_{\text{atm}}) \cdot \sigma \cdot T_{\text{atm}}^4. \quad (1.7)$$

The parameters necessary to compute the temperature of the target object  $T_{\text{obj}}$  are displayed in Table 1.1. Next to the Stefan-Boltzmann constant  $\sigma$  and the measured radiation  $M_{\text{measured}}$ , additional information about the object itself (namely, object's emittance  $\epsilon_{\text{obj}}$ ) and its environment (such as temperature of the atmosphere  $T_{\text{atm}}$ , temperature of ambient objects  $T_{\text{amb}}$ , and transmittance of the atmosphere  $\gamma_{\text{atm}}$ ) need to be known.

The transmittance of a medium can vary very strongly for different wavelengths. For example, visible light propagates through water with few losses (you can see very far in clear water) in contrast to infrared light that is completely absorbed by the water molecules. The transmittance for wavelengths above 1500 nm approximates zero. This makes impossible the use of IRT under water. The transmittance of air  $\gamma_{\text{atm}}$  is dependent on the wavelength as well. As opposed to water, there exists a transmittance window that makes thermography possible. For a significant range of wavelengths,  $\gamma_{\text{atm}}$  is approximately 1. Thus, when air is the transport medium, Eq. (1.7) can be further simplified

$$M_{\text{measured}} \cong \epsilon_{\text{obj}} \cdot \sigma \cdot T_{\text{obj}}^4 + (1 - \epsilon_{\text{obj}}) \cdot \sigma \cdot T_{\text{amb}}^4. \quad (1.8)$$

Now, the relation between measured power and the object's temperature is independent from air temperature.

There are many sources of thermal radiation that could increase the thermal radiation without increasing the object's temperature, for example, the sun, heating or light bulbs, especially when the emissivity of the greybody is noticeably below 1. In practice, the operator of a thermal camera should make sure that there are no ambient heat radiation sources close to the object of interest. In this case the equation further simplifies to

$$M_{\text{measured}} \cong \epsilon_{\text{obj}} \cdot \sigma \cdot T_{\text{obj}}^4. \quad (1.9)$$



Finally, in order to correctly calculate a surface temperature based on the radiation, the emissivity  $\epsilon_{\text{obj}}$  of the object needs to be known. Many thermal cameras give the option to input the emissivity value of the object that is currently measured. However, this value is often unknown or multiple objects with different emissivity values are measured at the same time. The consequences are systematic measurement errors that distort the results, i.e., the output of the camera.

In medical applications, the surface area of interest often consists of human skin. Its emissivity  $\epsilon_{\text{skin}}$  is well known, approximately 0.97–0.99 for temperatures around 300 K. Therefore, blackbody theory can be applied for the measurement of skin surface temperatures. In contrast, the emissivity of inner organs like the heart is noticeably below 1. This has to be considered for surgical applications of thermal imaging [7, 8].

### 1.2.5 Thermal Cameras

There are multiple types of thermal detectors capable of converting infrared radiation into electrical signals. For medical applications, these systems need to be saved, easy to use, and inexpensive. Traditionally, thermographic cameras have been used for maintenance and research especially in industrial processes, like engine diagnostics or power electronics. These cameras are capable of covering a thermal range from values below 0 °C up to temperatures far above 1000 °C and use detectors that often require active cooling. Additionally, the lenses of most thermal cameras cannot to be made of glass whose transmissivity approaches zero for wavelengths above 4500 nm. Hence, rare materials such as Germanium or sapphire crystals need to be incorporated.

Cameras for standard clinical applications use sensors that cover the wavelength spectrum from 3 to 5  $\mu\text{m}$  (mid-wave infrared) and from 7 to 14  $\mu\text{m}$  (long wave infrared), and therefore the bulk of the Planck spectrum of human skin temperatures (around 300 K). They reach temporal resolutions of 30 frames per second (fps) and make the analysis of dynamic temperature changes possible.

Thermographic cameras do not reach the spatial resolution of modern cameras in the visible spectrum, primarily because the sensor technology, active cooling, and materials for lenses are very expensive. High sensitivity hand-held infrared cameras reach resolutions of 2048  $\times$  1536 pixels. Today, there are standard thermographic cameras on the market that do not require cooling and reach resolutions of 1024  $\times$  768 pixels. Those camera types are often used for medical applications that will be further described in Sect. 1.3. Cameras for standard clinical applications use modern sensor technologies like microbolometer disposed on FPAs. These technologies reach thermal sensitivities below 0.1 °C, and their accuracy lies around 1 °C. They enable the analysis of small temperature changes on the surface of an object, like the temperature distribution on the human skin [9]. Nevertheless, the thermal accuracy of infrared cameras does not allow for sophisticated diagnostics of absolute temperatures, especially when the effects of unknown emissivities (as described above) are taken into account [10, 11].

## 1.3 Medical Applications

In the last decades several medical applications for thermal imaging cameras started to emerge. The next sections present some of the current applications of IRT for both medical fields, diagnosis and monitoring.

### 1.3.1 *Diagnosis*

A healthy human body presents a symmetric temperature distribution around the sagittal plane [12]. However, there are several biological factors that might influence the human body temperature, locally or systemically. Therefore, any deviation from normal can be an indicator of pathophysiologic anomalies, such as inflammation, carcinogenesis, or neuropathology [13]. The first use of temperature for health assessment dates back to 400 BC in the writings of Hippocrates. Hippocrates routinely slathered wet mud and clay over the patients' bodies speculating that the areas where the mud dried first had a disease [14]. Abnormal thermal patterns can be easily recognized in thermal imaging. Therefore, an early diagnosis of certain diseases is possible through the analysis of thermograms. In the last couple of years, IRT has found a wide acceptance among the medical community due to its advantages. Thermal imaging is a remote, non-contact, non-invasive, and passive technique. It only records the natural radiation emanated from the skin surfaces and does not use any harmful radiation [2, 15]. Lastly, IRT is a real-time technology, enabling monitoring of dynamic variations of body temperature. Due to all these advantages, thermal imaging has been considered an effective alternative diagnosis tool [2]. It has been being used in a variety of medical applications, including fields such as neurology, oncology, orthopedics, and dermatology [16]. Table 1.2 describes some medical applications, relevant research studies, and the hardware used. In the following sections only four applications will be presented in detail.

#### 1.3.1.1 **Detection of Breast Abnormalities**

According to the World Health Organization, 1.7 million breast cancer cases occurred in 2012 worldwide. It is the most frequent cancer in women in 150 countries (approximately 25% of all cancer cases) as well as the most common cause of cancer-related death. It was estimated that 522,000 women died from this cancer in 2012 worldwide [38]. Studies demonstrated that an early detection can lead to 85% survival chance while a late detection of breast cancer leads to only 10%. Therefore, it is very important for physicians to identify in due course potentially threatening malignant tumors for a successful treatment [2]. Mammography is the current gold standard to examine the human breast. However, this technique exhibits low sensitivity in young women and in women with a

**Table 1.2** Medical applications of IRT (Ref.—references)

Application	Year	Authors [Ref.]	IRT system
Breast cancer	2011	Kontos et al. [17]	Meditherm Med2000™ Pro (Meditherm, Medical Monitoring Systems Pty Ltd., Beaufort, NC, USA)
	2011	Umadevi et al. [18]	Fluke Ti40FT (M/s Fluke Corp., Everett, Washington, USA) and Varioscan 3021 ST (InfraTec GmbH, Dresden, Germany)
Complex regional pain syndrome	2006	Niehof et al. [19]	ThermaCam SC2000 (FLIR, Danderyd, Sweden)
	2008	Gardiner et al. [20]	FLIR A40M (FLIR Systems Boston, MA, USA)
	2016	Cho et al. [21]	IRIS-5000 (Medicore Co., Seoul, Korea)
Diabetic neuropathic foot	2006	Bharara et al. [22]	Unknown
Dry eye syndrome	2010	Tan et al. [23]	VarioCAM, JENOPTIK Laser (Germany)
	2017	Matteoli et al. [24]	FLIR 320A (FLIR Systems, Oregon, USA)
Knee injuries	2010	Hildebrandt et al. [4]	TVS-500EX (NEC Avio Infrared Technologies, Tokyo, Japan)
Low back pain	2006	Zaproudina et al. [25]	IRTIS-2000 C (IRTIS Ltd, Moscow, Russia)
Osteoarthritis	1981	Ring et al. [26]	Unknown
	2004	Varju et al. [27]	Compix PC2000e (Compix, Lake Oswego, OR, USA)
	2010	Denoble et al. [28]	Meditherm Med2000™ Pro (Meditherm, Medical Monitoring Systems Pty Ltd., Beaufort, NC, USA)
Peripheral arterial disease	2009	Bagavathiappan et al. [29]	AGEMA Thermovision 550 system (Danderyd, Sweden)
	2011	Huang et al. [30]	Spectrum 9000-MB Series (United Integrated Service Co. Ltd, Taipei Hsien, Taiwan)
	2016	Staffa et al. [31]	FLIR B200 (Flir Systems, Danderyd, Sweden)
Raynaud's phenomena	2014	Lim et al. [32]	IRIS-XP® (Medicore, Seoul)
Rheumatoid arthritis	2015	Lasanen et al. [33]	FLIR A325 (FLIR Systems Inc., USA)
	2017	Lerkvaleekul et al. [34]	FLIR E60 (FLIR System Inc., USA)
Shoulder impingement syndrome	2007	Park et al. [35]	IRIS 5000 (Medicore, Seoul, Korea)
Wound assessment	2015	Dini et al. [36]	FLIR T620 Thermal Imager (FLIR Systems Boston, MA, USA)
	2017	Keenan et al. [37]	FLIR A325 (FLIR Systems Boston, MA, USA)

greater breast density. In addition, this technique requires breast compression during screening and exposes the patient to harmful radiation (X-rays usually around 30 kVp). Several studies have demonstrated that thermal imaging may be a potential adjunctive tool for detecting this kind of cancer [38]. Breast thermography was firstly introduced by Lawson in 1956 [39]. According to this author, one of the biological characteristics of malignant tumors is the increased rate of growth in comparison to that of the surrounding tissues. This leads to an accelerated local metabolism, which is supported by increased blood and lymphatic vascularity, and consequently to localized hot spots [2, 39]. Amalric et al. screened over a period of 10 years 61,000 women using thermography [40]. Their outstanding study showed that thermal imaging was the earliest marker of breast cancer in approximately 60% of the cases [40]. In addition to passive breast imaging, there are other procedures to enhance thermographic contrast of tumors. The first is based on cold stimulation. The blood vessels which supply the tumors are simply endothelial tubes devoid of a muscular layer. Thus, during cold stress (sympathetic stimulus) they fail to vasoconstrict and show instead a hyperthermic pattern due to vasodilation [2]. The second procedure is based on induced evaporation. Deng and Liu [41] demonstrated that this technique enhances the temperature contrast in case of tumors underneath the skin. In short, the authors sprayed water and 75% of ethanol solution (evaporant) before imaging acquisition. They conclude that this method permitted to improve diagnostic accuracy, particularly in the early stage of deeply embedded tumors [41].

In 2012, Boquete et al. proposed a novel approach capable of detecting high tumor risk areas [42]. It was based on independent component analysis. For validation purposes, they used the database of the *Ann Arbor thermography center* comprising eight case studies, where two out of eight were control cases. The thermograms had YCbCr 480 × 380 pixels format and followed a color code: lower temperatures were shown in blue and higher temperatures in yellow-red tones; the highest temperatures were displayed in white. While Fig. 1.2a shows a control case, Fig. 1.2b, c denotes two cases of ductal carcinoma. The proposed method corroborated that the hot spots in the thermogram of the breast indicate a potentially cancerous zone. It presented a sensitivity of 100% and specificity of 94.7%. The positive and negative predictive values were 83% and 100%, respectively [42].

### 1.3.1.2 Rheumatic Diseases

Rheumatic diseases are a group of over 150 systemic autoimmune diseases (e.g., rheumatic arthritis, osteoarthritis and autoimmune diseases, such as systemic lupus erythematosus, scleroderma, osteoporosis, back pain, gout, fibromyalgia, and tendonitis) which are characterized by inflammation affecting the connecting or supporting structures of the body, mostly joints, but also tendons, ligaments, bones, and muscles. Common symptoms of these diseases include swelling, pain, stiffness, and decreased range of motion. Rheumatic diseases are one of the leading causes of disability in the USA affecting more than 50 million people of all ages, genders, and races. By 2040, the number of adults in the USA is expected to increase to 78.4 million.

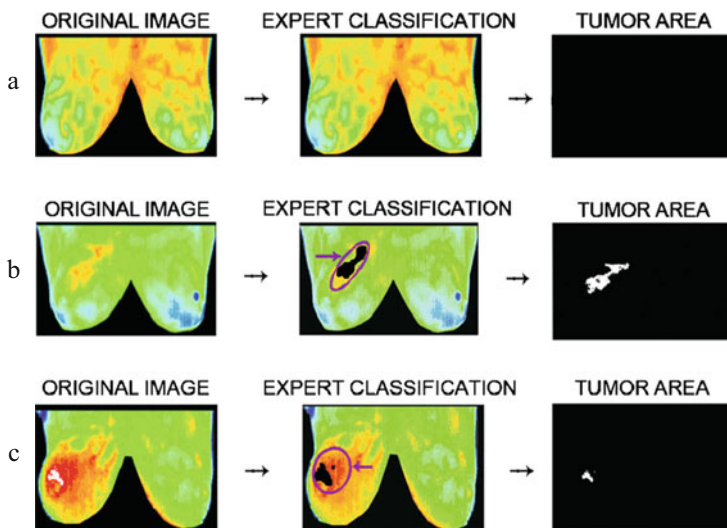


**Fig. 1.2** (a) Control case. (b, c) Ductal carcinoma. Modified from Boquete et al. [42]

Currently, there are few tools for early diagnosis of rheumatic diseases and for assessing the effectiveness of therapies: bone scintigraphy, ultrasound, contrast enhanced ultrasound, magnetic resonance (MR), and contrast enhanced MR. However, these techniques are not readily available for the masses and waiting lists in many countries are very long. Therefore, less expensive technologies for diagnosis and therapy monitoring would be beneficial in this medical field.

IRT has been used in the diagnosis and assessment of recovery of some rheumatic diseases, including Raynaud's phenomena, gout, and arthritis [2]. In an outstanding publication, Ring [43] demonstrated that patients suffering from juvenile arthritis,<sup>1</sup> osteoarthritis,<sup>2</sup> rheumatoid arthritis,<sup>3</sup> gout,<sup>4</sup> among others show abnormal temperature distributions over joints. To quantify joint inflammation, Collins et al. [44] developed in 1974 a "thermographic index":

<sup>1</sup>Juvenile arthritis, also known as pediatric rheumatic disease, is an umbrella term that describes autoimmune and inflammatory conditions or pediatric rheumatic diseases developed in children under the age of 16.

<sup>2</sup>Osteoarthritis is the most frequent chronic condition of the joints, affecting more than 30 million Americans. It can affect any joint, but it occurs most commonly in knees, hips, lower back and neck, small joints of the fingers, among others.

<sup>3</sup>Rheumatoid arthritis is an autoimmune disease in which the body's immune system mistakenly attacks the joints.

<sup>4</sup>Gout is a form of inflammatory arthritis that affects people who have high levels of uric acid in the blood. Uric acid can form needle-like crystals in the joints. The most common symptoms are sudden and severe episodes of pain, tenderness, redness, warmth, and swelling.

$$\frac{\sum(\Delta t \times a)}{A}, \quad (1.10)$$

where  $\Delta t$  stands for the difference between the measured isothermal temperature and a constant (26 °C);  $a$  is the area occupied by isotherm (region of the thermogram with the same temperature); and  $A$  corresponds to the total area of the thermogram. In other study, Ring et al. [45] studied the ability of thermal imaging to detect and quantify the effects of non-steroidal anti-inflammatory drugs (such as aspirin, indomethacin, and benorylate) in patients with gout and rheumatoid arthritis [45]. The results indicated that IRT is a suitable tool for assessment of the response to the anti-inflammatory treatment; the administration of a local anti-inflammatory caused a fall in the thermographic index of the inflamed joint. Frize et al. used, in turn, IRT for diagnosis of rheumatoid arthritis [46]. The authors reported that metacarpophalangeal joints of the index, middle fingers, and knee are the best indicators of the presence and absence of this disease [46]. Lerkvaleekul et al. studied the capability of IRT to detect wrist arthritis in juvenile idiopathic arthritis patients [34]. Using the mean temperature and maximum temperature at the skin surface in the region of interest, moderate wrist joint arthritis could be differentiated from severe and inactive arthritis. In 2009, Wu et al. published a work where they claimed that local skin temperature near the coccyx region decreases significantly after therapy in patients suffering from coccygodynia (pain in the coccyx or tailbone area) [47]. In this case, thermal imaging has demonstrated to be an effective tool for the assessment of coccygeal pain intensity after treatment. In contrast, Park et al. used IRT for the assessment of shoulder impingement syndrome [35]. They prospectively evaluated 100 patients with unilateral impingement syndrome, and a control group of 30 subjects. In IRT findings, 73% of the patients presented abnormal thermal changes, 51% displayed hypothermia, and 22% had hyperthermia. The results confirmed that in the hypothermic group limitation of shoulder motion was significantly more prominent than in the other groups: hyperthermic and normal groups. Commonly, shoulder immobility induces a localized muscle atrophy, which in turn causes apoptosis of the muscle's cells. This phenomenon may lead to a decreased blood flow in this region, resulting in hypothermic patterns in the skin of the shoulder [35]. Vecchio and associates [48] corroborated in their papers the findings of Park et al. [35]. They stated that the most part of the subjects with unilateral frozen shoulder had anomalous skin temperature distribution [48].

### 1.3.1.3 Dry Eye Syndrome and Ocular Disease

Dry eye syndrome is a disturbance of the tear film caused by a lack of adequate tears. Tears can be described as a complex mixture of water, mucus, and fatty oils, which make the surface of the eyes smoother and clear and protect them from infection. Therefore, dry eye syndrome may lead to eye inflammation, vision problems, as well as scarring on the surface of the corneas.

Nowadays, there are some methods for diagnosis of dry eye. Film breakup time and tear osmolarity give information about tear functionality but do not specify the causes of possible damage. The objective clinical examination of corneal fluorescein staining may help in the diagnosis but is very fastidious.

In recent decades, the diagnostic of dry eye syndrome and ocular diseases using infrared thermography has been analyzed. Studies have demonstrated that patients with dry eye disease have cooler ocular surfaces than those of asymptomatic normal subjects [24, 49]. In 2009, Tan and associates [23] published a review paper describing different methodologies for manual, semi-manual, and automatic measure of ocular surface temperature in IRT.

Additionally, thermal imaging can be used for diagnosis and assessment of the inflammatory state in patients with Graves' ophthalmopathy as described by Chang et al. [50]. Note that Graves' orbitopathy is an autoimmune inflammatory disorder of the orbit and periorbital tissues. It is characterized by lid lag, upper eyelid retraction, conjunctivitis, redness, among others. In their study, the authors measured the temperature at different regions, including lateral orbit (reference point), cornea, medial and lateral conjunctiva, upper and lower eyelids, and caruncle. They observed significantly higher temperature differences between reference point and other eye regions for the patients suffering from this inflammatory disorder [50].

#### 1.3.1.4 Wound Assessment

A chronic wound is commonly defined as a wound whose healing process is hampered. Commonly, wounds are classified as chronic if they need more than 3 months to heal, i.e., to recover anatomic and functional integrity. Indeed, they may require several years to heal, and in some cases remain unhealed for decades. Patients with this problem can experience pain, reduced mobility, physical and emotional distress as well as social isolation. The Wound Healing Society classifies chronic wounds into four categories: diabetic ulcers, pressure ulcers, venous ulcers, and arterial insufficiency ulcers [51].

In the USA, chronic wounds affect approximately 6.5 million patients (~2% of the US population) leading to annual costs of about 25 billion US dollars. In the Scandinavian countries, the associated medical costs correspond to 2–4% of the total health care expenses. However, the medical expenditures are increasing rapidly due to aged population and a sharp grow in the incidence of diabetes and obesity worldwide [51].

Thermal imaging can be used for non-invasive assessment of wound severity. The potential of IRT to aid in the assessment of wounds was identified by Lawson in the early 1960s [52]. He used this technology to predict burn depth. Histological analysis confirmed an accuracy of 90%. The author stated that whereas superficial burns are warmer than uninjured skin due to increased inflammatory processes, deeper burns are cooler than uninjured skin owing to structural damage of the vasculature [52]. In 1996, Hansen et al. [53] published a very interesting work where they studied the capability of IRT to assess wound severity of newly formed

temperature-modulated pressure injuries in a porcine model. They observed that relative surface temperature of the wounds strongly correlated with the presence or absence of deep tissue injury. In addition, infrared imaging permitted to assess wound depth and, thus, predict the severity of the injuries.

The measurement of skin and wound bed temperature in chronic wounds may play an important role in the assessment and diagnosis of chronic wound infection. Dini et al. [36] carried out a study whose aim was to correlate the wound bed score,<sup>5</sup> validated by Falanga [54] in 2006, to wound bed and perilesional skin temperature. It included 18 patients suffering from venous insufficiency and lower leg ulcers. In total, 24 chronic wound bed and perilesional skin ulcers were assessed using an infrared thermographic camera (FLIR T620 Thermal Imager, FLIR Systems, Boston, Massachusetts, USA). The authors conclude that wound bed temperature plays a major role in wound healing. According to them, if the temperature of the wound bed falls below the core body temperature, healing can be delayed due to lack of collagen deposition and reduced amount of late-phase inflammatory cells as well as fibroblasts [36]. Fierheller and Sibbald [55], in turn, studied the importance of periwound skin temperature. They demonstrated a statistically significant relationship between infection and increased periwound skin temperature [55].

## ***1.3.2 Monitoring***

In the last decade, thermal imaging has been used for monitoring of vital signs, such as respiratory rate (RR) and heart rate (HR), and perfusion dynamics. Possible applications are monitoring of preterm infants in neonatal intensive care units as well as critical care patients in intensive care units. Additionally, this monitoring technology can be used in the automotive branch as well for continuous monitoring of drivers. The following sections discuss the capability of IRT as a monitoring technique.

### **1.3.2.1 Respiratory Rate**

Respiratory rate (RR) is an important vital sign and is measured in breaths per minute or  $\text{min}^{-1}$ . Each breath or breathing cycle consists of two phases: inspiration and expiration. During inspiration, the diaphragm contracts and moves towards the caudal (downward) direction; due to under pressure in the pleural cavity the lungs are also pulled towards the caudal direction and air is sucked into the

---

<sup>5</sup>The wound bed score is based on healing edges (wound edge effect), presence of eschar, greatest wound depth/granulation tissue, amount of exudate amount, edema, periwound dermatitis, periwound callus and or fibrosis, and a pink/red wound bed.



lungs. Simultaneously, the rib cage moves towards the cranial and ventral (up and forward) direction in order to accommodate the increased volume of the lungs. This movement is also translated to the shoulders. During expiration, the diaphragm relaxes; the lungs and ribcage also move back into the relaxed end-expiratory position and warm air is exhaled.

Usually the RR of an average adult under resting conditions ranges from 12 to 20 breaths per minute ( $\text{min}^{-1}$ ). An abnormal RR, such as bradypnea (low RR,  $<12 \text{ min}^{-1}$ ) or tachypnea (increased RR,  $>20 \text{ min}^{-1}$ ), can be the first indication for various medical conditions including heart and lung diseases. Furthermore, analysis of the respiration pattern can provide even more information. Kussmaul's respiration, for example, which is characterized by deep breaths at normal or low RRs, can point towards a diabetic coma or kidney failure. Another example is Cheyne–Stokes respiration, which is characterized by alternating phases of hyperpnea and apnea. Additionally, the depth of the breaths increases at the beginning of the hyperpnea phase and decreases again towards the end. Underlying reasons for Cheyne–Stokes respiration can include cardiac insufficiency and cerebral damage. Despite all the information carried in the RR and respiratory pattern, it is still an often neglected parameter [56]. A study of Philip and associates [57] showed that both spot and formal assessment of RR performed by physician is sometimes highly inaccurate and that they were not able to detect abnormal RRs. The findings of this study emphasize the importance of techniques in order to reliably and easily detect RR [57].

Technical state-of-the-art for respiration monitoring includes impedance pneumography (measurement of respiration-modulated thoracic impedance), spirometry (flow measurement), capnography (measurement of exhaled carbon dioxide), piezoplethysmography (measurement of thoracic and/or abdominal effort), and thermistors (measurement of respiration-modulated temperature differences around the nostrils). All these methods rely on sensors, which need to be directly attached to the patient and usually have cables to, e.g., a patient monitor. These factors limit both patient comfort and ease of use, which is why there have been many efforts to develop non-contact methods for RR monitoring in the recent years. Among other techniques, the application of IRT for non-contact respiration monitoring has been investigated intensively.

In 2004, Murthy, Pavlidis, and Tsiamyrtzis first proposed IRT for touchless monitoring of breathing function [58]. In a dimly lit room, the faces of ten subjects were recorded in a profile view using a mid-wave infrared camera with a spectral range of 3.0–5.0  $\mu\text{m}$ , a spatial resolution of  $640 \times 512$  pixels, and a temperature sensitivity of 25 mK. Temperature changes caused by inhalation and exhalation were measured in a region of interest (ROI) a certain distance away from the nose tip. In order to determine the RR, those temperature modulations were first classified as either part of the inspiration or part of the expiration phase using statistical distributions. Afterwards, the RR could be derived from the length of the respiration cycles. This work was later extended by Fei and Pavlidis in 2007 [59] and 2010 [60]. Table 1.3 lists other works on the field of respiration monitoring using IRT.

**Table 1.3** Works on the field of respiration monitoring using IRT

Year	Authors	Summary	Reference
2005	Chekmenev et al.	Measurement of RR on 4 healthy subjects by analysis of temperature variations around the nose and wavelets for signal processing and analysis	[61]
2008	Yang et al.	Estimation of RR on 20 healthy subjects using temperature modulations measured around the nose and fast Fourier transform for signal processing and analysis	[62]
2009	Murthy et al.	Airflow monitoring on 14 healthy adult subjects and 13 adult sleep apnea patients using temperature modulations around the nose and wavelets for signal processing and analysis	[63]
2011	Abbas et al.	Monitoring of RR on seven premature infants in a hospital using temperature variations around the nostrils and wavelets for signal processing and analysis	[64]
2011	Al-Khalidi et al.	Peak detection on temperature changes around the nose for RR monitoring on 16 children	[65]
2011	Lewis et al.	Extraction of RR and relative tidal volume on 25 healthy subjects based on temperature modulations around the nose and fast Fourier transform for signal processing and analysis	[66]
2015	Pereira et al.	Monitoring of respiration dynamics on 11 healthy subjects by analysis of temperature changes around the nose and a robust interval estimator	[67]

Although the algorithms and experimental settings of the works listed in Table 1.3 differ from each other, a general structure is clearly visible: after acquisition of thermal video sequences, the image frames undergo *image preprocessing* and *image enhancement*, before *selection of a ROI*. To compensate motion, a *tracking algorithm* is applied to the ROI. Then, *extraction of the respiration waveform* from the ROI is performed and, finally, the *RR is calculated*. The following pages will focus on image processing, image enhancement, selection of ROI, extraction of respiration waveform, and calculation of RR. Tracking algorithms are not covered in this section, thus the reader is kindly referred to the original research articles.

### Selection of ROI

Research listed in Table 1.3 uses the area around the nose as the ROI. There, the temperature variation between inspiration and expiration, which lies around 0.3–0.6 K for adults, is measured (see Fig. 1.3). In the work of Murthy et al., subjects were recorded in a profile view [58]. Their approach consisted in: (1) removing the background with the Otsu’s method; (2) detecting the nose tip (regarded as the right most point); and defining a ROI (region direct below the nose tip). After experimental evaluation, considering the distance between subject and camera as

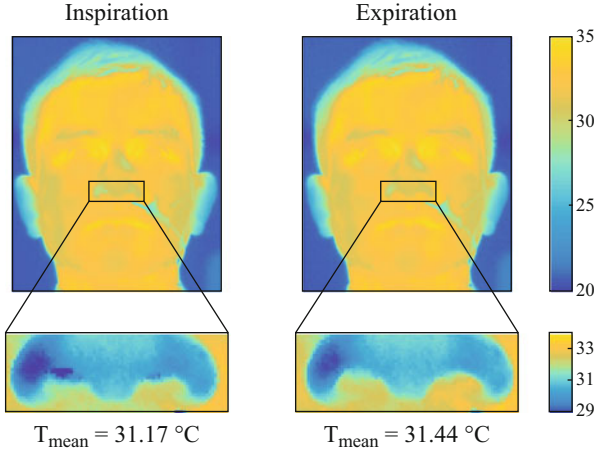


**Fig. 1.3** Temperature differences around the nostrils between inspiration and expiration

well as the lens' focal length, the size of the ROI was set to  $21 \times 9$  pixels. In a later version of their work, Fei and Pavlidis [60] recorded the subjects in a frontal view and used a semi-automatic approach in order to detect the nose. Initially, the area around the nose is manually selected in the first frame of the video and then tracked throughout the whole video sequence by a tracker. Within this tracked ROI (TROI), the exact position of the nostrils is automatically detected. This is accomplished by application of both the horizontal and vertical Sobel Operator to the TROI, which detects the spatial features of the nostril area. By calculation of the horizontal as well as vertical projection of the edge image, the boundaries of the nostrils are clearly visible and can be obtained.

Another approach was proposed by Al-Khalidi et al., which first segments the face of the subject recorded from a frontal perspective and detects the two warmest points in the face [65]. Due to the facial temperature distribution, those points coincide with the periorbital regions. From there downwards, the coldest point is the tip of the nose.

However, although commonly used, the nose is not the only suitable region in order to extract a respiration waveform. Another suitable ROI is the mouth. Al Khalidi et al., for example, had to exclude four subjects from analysis, since they were breathing through the mouth [65]. In 2016, Pereira et al. presented a robust algorithm for estimation of RR [68]. In addition to the nose, the mouth and both shoulders were added as ROIs. While the respiration waveform around the nose and mouth was caused by temperature changes during inspiration and expiration, the respiration waveform around the shoulders was induced by respiration-related movement of the shoulders. Respiratory rate was estimated independently for each ROI and fused afterwards; different fusion algorithms (Bayesian fusion, median, and a signal quality-based algorithm) were investigated.

## Extraction of Respiration Waveform and Calculation of Respiratory Rate

The respiration waveform is usually obtained from the 2D average temperature over time according to Eq. (1.11)

$$s(t) = \frac{1}{XY} \sum_{x=1}^X \sum_{y=1}^Y I(x, y, t), \quad (1.11)$$

with  $s(t)$  being the respiration waveform at time  $t$  and  $I(x, y, t)$  the value at position  $(x, y)$  of the infrared video frame at time  $t$ . Based on this respiration waveform, the RR can be determined by many forms of signal processing and signal analysis. One frequently used method is continuous wavelet transform (CWT) according to Eq. (1.12)

$$W_{\psi,s}(a, \tau) = \frac{1}{\sqrt{|a|}} \int \psi \left( \frac{t - \tau}{a} \right) s(t) dt, \quad (1.12)$$

where  $a$  is the scaling parameter,  $\tau$  represents the translation parameter,  $\psi$  denotes the mother wavelet, and  $s$  is the signal to be analyzed. Fei and Pavlidis [60], for example, used the Mexican hat wavelet as mother wavelet and assume that the RR is represented by the scale  $a_{\max}$  with maximum energy. Finally, the RR is calculated according to

$$\text{RR} = \frac{F_c \cdot fs}{a_{\max}}, \quad (1.13)$$

where  $F_c$  is the center frequency of the mother wavelet and  $fs$  is the sampling rate of the respiration waveform. Abbas et al. use the Daubechies wavelet as the mother wavelet instead of the Mexican hat [64].

Another method for calculation of the RR is the short time Fourier transform (STFT), given by

$$S(\omega, \tau) = \int s(t) \cdot w(t - \tau) \cdot e^{-j\omega t} dt. \quad (1.14)$$

Here  $s$  is the signal to be transformed and  $w$  is a windowing function (e.g., Hamming, Hann, Gaussian window). The window size must be chosen carefully with regard to temporal and spectral resolution. Zero padding can be applied in order to increase the number of frequency points in the spectrum and therefore increase the precision of peaks within the spectrum. However, it should be noted that zero padding does not increase the spectral resolution. Afterwards, the RR can be obtained from the spectrum by selecting the frequency with maximum spectral energy. This method was used by Lewis et al. [66] and Pereira et al. [68].

There are other techniques to determine RR from the respiration waveform, for instance, (1) bandpass-filtering of the respiratory waveform and calculation of the time peak-to-peak [65] or (2) using a robust breath-to-breath interval estimator [67].

In the publication of Murthy et al., the average RR obtained with IRT was compared with the RR measured by a piezo belt (reference). On average, an accuracy of 92% (over ten healthy subjects) was obtained [58]. In the work of Yang et al. the absolute deviations ranged from 0.8 to 2.2 breaths/min between average IRT respiratory rate and average ground truth [62]. In 2011, Abbas et al. first measured RR with IRT on five premature neonates in a neonatal intensive care unit [64]. The average deviation between average IRT respiratory rate and reference respiratory rate was approximately 1 breaths/min and the largest average deviation was 2.25 breaths/min. In 2016, Pereira et al. used fusion of multiple ROIs for RR estimation [68]. Among others, they investigated the effects of different breathing patterns on the algorithm's performance. To validate the approach, an experiment on 12 healthy subjects was conducted. For normal breathing, the root mean squared error (RMSE) was 0.28 breaths/min and correlation between IRT respiratory rate and ground truth was 0.98 (averaged over all 12 subjects). For the simulated respiration patterns, RMSE averaged 3.36 breaths/min and the correlation was 0.95. The increased RMSE could be explained by an imperfect time synchronization between IRT and ground truth in combination with rapid changes of RRs. In total, both lab experiments and clinical studies indicate that IRT is a very promising method for RR monitoring.

### 1.3.2.2 Cardiac Pulse

In addition to RR, some research groups studied the capability of IRT to monitor the cardiac pulse [69, 70]. In 2007, Garbey et al. proposed a novel method to monitor HR at a distance [70]. Their aim was to develop a non-invasive and contactless method capable of assessing the human anatomic nervous system activity and psychophysiology state. According to them, in psychophysiological experiments, the physiological responses of a subject should be measured without any interfere, otherwise an extra variable must be introduced to his psychological state. In these cases, a contact-free measurement modality for monitoring of vital signs (e.g., RR and cardiac pulse) is very appealing [70]. Such measurement methodology can also be beneficial in critical care medicine, especially in the monitoring of burned and traumatized patients as well as premature infants [68].

As well known, during ventricular systole the heart contracts generating blood pressure and flow fluctuations that propagate as waves through the arterial tree [71]. The approach proposed by Garbey and associates [70] is based on the hypothesis that pulsative blood flow modulates temperature of surrounding tissues (e.g., skin) as a result of heat exchange by convection and conduction (between vessels and surrounding tissue). Certainly, this modulation is more pronounced in the vicinity of greater blood vessels. To verify the hypothesis, the authors implemented a mathematical model to simulate the heat transfer processes on the skin, including the influence of core tissue and major superficial blood vessels. The simulations showed that the skin temperature waveform is similar to the pulse waveform; the amplitude of the temperature variation ranged between 0.02 and 0.03 °C [70].

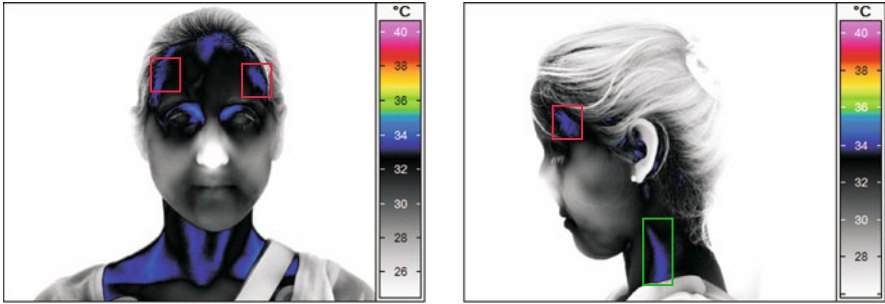


**Fig. 1.4** Regions where the cardiac pulse can be extracted using thermal imagery: superficial temporal vessel complex (red boxes) and carotid vessel complex (green box)

Due to tissue thermal diffusion, variation of skin temperature is strongest along the superficial blood vessels, as demonstrated in [30]. Based on that assumption, Garbey et al. focus their research on three different body regions: neck (external carotid complex), temporal area (superficial temporal artero-venous complex), and wrist (radial artero-venous complex) [70]. Figure 1.4 shows two of these regions: red boxes enclose the temporal vessel complex and the green box encloses the carotid vessel complex. As displayed the blood vessels are hot spots in the thermogram. In short, the approach of this research group consisted in manually selecting a “line-based region” (ROI) along visible vessels in the first frame of thermal video. To compensate involuntary movements of the subjects, a motion tracking algorithm was integrated; the authors chose the conditional density propagation tracker with thresholding as its feedback mechanism. Then, they applied the fast Fourier transform (FFT) to the individual pixels along the line of interest to capitalize upon the pulse propagation phenomenon. As a blood vessel is a long and narrow structure, the pulse’s thermal propagation effect induces a slight phase shift on the temperature profile along it. Within this context, each single pixel along the line of interest has a unique periodic temperature profile, which was considered to be shifted with regard to the others. Thus, the temperature profiles of the pixels are shifted in the time domain but not in the frequency domain. Lastly, an adaptive estimation function was applied on the average FFT outcome to extract the dominant pulse frequency [70].

To validate their approach, the authors carried out experiments on 34 healthy human subjects using a high sensitive mid-wave infrared camera from FLIR (FLIR Inc., Santa Barbara, CA). It presents a temperature resolution of <25 mK and a full spatial resolution of  $640 \times 480$  pixels. Thermal videos (5 min) were acquired with a frame rate of 30 fps. The HR obtained with thermal imaging was compared to a standard ground-truth (GT), a piezoelectric transducer [70]. On average, the performance of the method, given by complement of the absolute normalized difference (CAND),<sup>6</sup> was 88.52%.

<sup>6</sup>CAND =  $1 - \frac{|GT - IRT|}{GT}$ , where GT corresponds to the HR obtained with the ground truth and IRT stands for the HR estimated with infrared thermography.

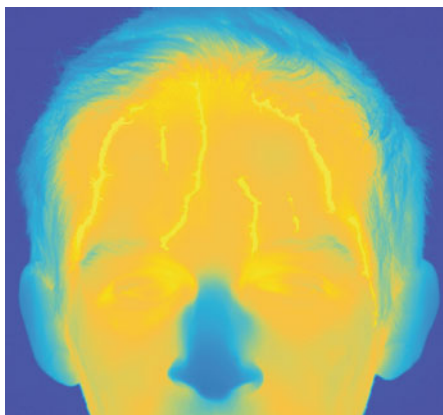
A research group of the University of Louisville (Louisville, Kentucky, USA) proposed a similar approach to that of Garbey et al. [70]. In 2007, Chekmenev et al. developed a multi-resolution method for non-contact measurement of the arterial pulse [69]. In general, the algorithm detects in the ROI the skin area where the arterial periodic heat pattern is more prominent. Then, multiscale decomposition models are applied to each frame in order to extract the scales containing most of the arterial pulse information. As a result, the influence of irrelevant noise is minimized and a better accuracy can be achieved. The next step consists in selecting the coarse scales to track the ROI. Afterwards, the ROI is divided into  $K$ -cells and the mean temperature value is calculated; this results in  $K$  one-dimensional waveforms. For each waveform, continuous waveform analysis is applied to detect systolic peaks/maxima for each single waveform; this method permits to remove high frequency noise and to extract arterial pulse structures. Finally, the waveform with higher periodicity is used to calculate the cardiac pulse; the cell corresponding to this waveform is defined as region of measurement [69].

To validate the approach, measurements on five healthy subjects were carried out. The research group used a long-wave Phoenix infrared camera from FLIR (FLIR Inc., Santa Barbara, California, USA) with the following characteristics: thermal sensitivity of 25 mK; 14-bit dynamic range; spatial resolution of  $320 \times 256$  pixels. In this experiment the acquisition time ranged between 20 and 50 s and the frame rate was 30 fps. The HR obtained with IRT was compared to a standard ground truth (GT), a portable HR monitor from Polar USA. According to the authors, a 100% accuracy on the carotid artery area was obtained [69].

In 2013, the same research group presented a full-automatic approach to estimate the pulse signal. In contrast to the previous works, the new algorithm identifies the forehead in the thermogram and extracts the vascular maps (Fig. 1.5). Every vessel segmented in the forehead is then used to calculate the HR [72].

In this work an experiment with 32 subjects was carried out. Here, three different scenarios were tested. In the first scenario (phase A—normal condition), the thermal videos were recorded during normal conditions. During phase B (second scenario—

**Fig. 1.5** Thermal facial region and vascular maps of the forehead





mild pain), the healthy subjects submerged their right hand in an ice bath to induce pain. In the last phase (phase C—mild exercise), subjects held 20–40 lbs of weight in order to increase HR [72].

The results showed an overall accuracy of almost 90% (median). Under normal conditions, the best outcome was achieved, the median averaged 92.5%. In phase B (pain) and phase C (mild exercise) the median was approximately 91% and 82%, respectively [72].

### 1.3.2.3 Perfusion

Acute circulatory disorders are still one of the main causes of death worldwide. In critical care medicine, this complication is frequently triggered by sepsis or SIRS (systemic inflammatory response syndrome). Sepsis is considered a severe disease consisting of both infection and SIRS. It may evolve into severe sepsis or septic shock. Whereas the first is an aggravated sepsis by acute organ dysfunction, the second corresponds to a severe sepsis plus hypotension, which cannot be settled with fluid resuscitation [73, 74].

According to the World Health Organization (WHO), severe sepsis and septic shock are the main factors of morbidity and mortality in intensive care units [75] and neonatal intensive care units [76]. In the USA, approximately 751,000 cases of severe sepsis occur annually with a mortality rate of 28.6%. This estimation was presented by Angus et al. in 2001 [77]. In 2003, Martin and associates observed an increase in septicemia incidence and septicemia-related deaths over the past 20 years in the USA [78]. This trend is expected to continue due to several reasons including aging of the population, increasing number of immunosuppressive therapies, transplantations, chemotherapies, and invasive procedures [79]. Furthermore, a study carried out by Lawn et al. [80] evidenced that severe infections such as sepsis/pneumonia, tetanus, and diarrhea are the second major cause of death in neonates at the age of 0–27 days. According to the publication, of 3.072 million deaths in 2010, approximately 27% were due to severe infections [80].

During sepsis cardiovascular changes are patent. Commonly, they lead to tissue hypoperfusion, which can further result in the development of multiple organ dysfunction. Thus, to improve the outcome of the patients through appropriate clinical interventions (e.g., antibiotic therapy and organ support) the diagnosis must be performed in due course [73, 81]. The remarkable work of Kumar et al. evidenced an increase of circa 7.6% in mortality rate for every single hour by which antimicrobial was tardily administered [82]. However, a prompt identification of sepsis is still a major challenge for clinicians as its signs and symptoms are nonspecific [82].

Body temperature, and consequently skin temperature, is dependent on several factors such as heat-exchange processes between skin, inner tissues, and vasculature as well as on metabolic activity and sympathetic and parasympathetic activity. As a result, its distribution may provide evidence of the centralization's progress due to peripheral hypoperfusion (restriction of blood flow to vital organs at the expense of peripheral organs) [15].



In 2014, Pereira et al. analyzed the capability of IRT (a) to detect acute impairments of body circulation and perfusion as well as (b) to monitor the progress of temperature centralization in a porcine animal model of acute lung injury (ALI) [15]. For that, two new indices (standard deviation and  $\Delta T/\Delta x$ ) were developed. They aimed to quantify peripheral temperature gradients and, thus, peripheral perfusion [15].

In this study, ALI, one of the major causes leading to SIRS and sepsis, was experimentally induced in six female piglets. To evaluate the progress of skin temperature distribution, 15 measurements were performed with a long wave infrared camera at different points of time (approximately at two-hourly intervals). The thermograms were acquired with a VARIOCAM<sup>®</sup> hr head (InfraTec GmbH, Dresden, Germany), which presented a thermal sensitivity of 0.03 °C at 30 °C and a spatial resolution of 384 × 288 pixels [15].

As referred previously, two indices were proposed, standard deviation (SD) and  $\Delta T/\Delta x$ . The former corresponds to the standard deviation of the skin temperature distribution. The latter can be considered as a measure of the spatial temperature profile, i.e., it describes the change in temperature  $\Delta T$  with the distance  $\Delta x$  between the body center (hottest point next to the coolish sternal region) and the most peripheral point visible in the thermogram (animal's paw). To evaluate the capability of IRT to detect acute impairments of body circulation and to monitor the progress of temperature centralization, both SD and  $\Delta T/\Delta x$  were compared with clinical parameters such as shock index (SI),<sup>7</sup> mean arterial pressure (MAP), PaO<sub>2</sub> (partial pressure of oxygen), and Carrico index,<sup>8</sup> which are markers of circulatory impairments and oxygenation [15].

The results demonstrated that at the baseline measurement the body temperature of the piglets was uniformly distributed. However, with the progress of the disease's severity, the temperature gradient between center and periphery increased (temperature centralization) as a result of peripheral hypoperfusion. Figure 1.6 displays the development of the skin temperature distribution. Figure 1.6a and c represents the thermograms at two different time measurements, baseline and ALI 25 (last measurement). They show an increase of temperature profile due to hypoperfusion. Figure 1.6b, d shows the corresponding histograms. In general, differences of shape of the probability distributions between baseline and ALI were observed. At the baseline, the histograms presented a higher negative asymmetry and a higher kurtosis distribution, characterized by a sharper and longer peak. The latter means that the distribution is more clustered around the mean, which results in relatively smaller SDs, i.e., a more homogeneously distributed body temperature (Fig. 1.6a, b). During ALI the histograms presented smaller negative asymmetries and lower

---

<sup>7</sup>SI, a marker of shock, is the ratio of HR to systolic blood pressure. It is an effective marker for the initial assessment of sepsis.

<sup>8</sup>Carrico index, also denominated PaO<sub>2</sub>/F<sub>i</sub>O<sub>2</sub>, is the ratio of arterial oxygen concentration to the fraction of inspired oxygen. In critical care medicine, this parameter describes the severity of pulmonary dysfunction.

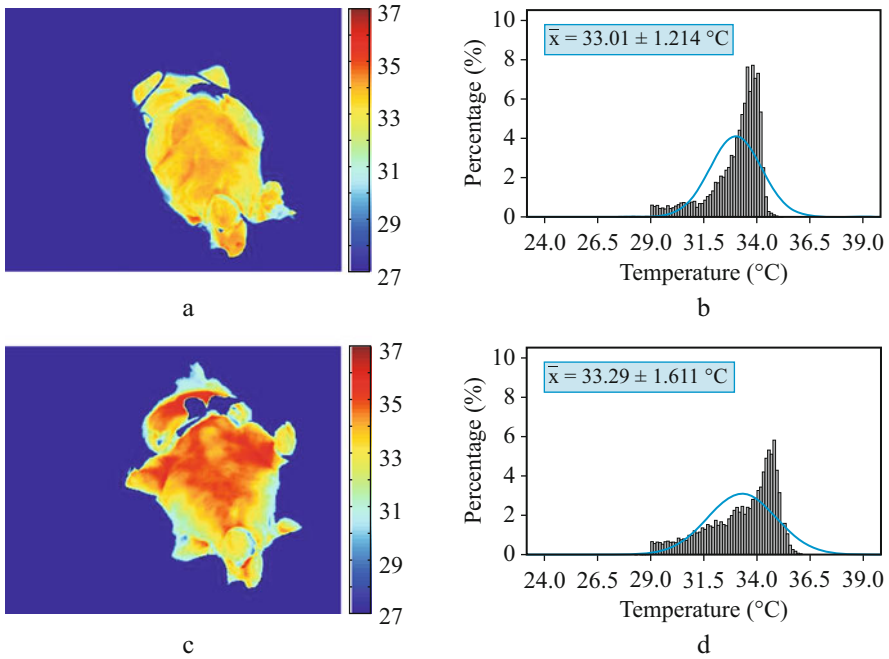


**Fig. 1.6** Original thermograms at two different points of time: (a) Baseline and (c) ALI 25 (last measurement). Histograms representing the relative skin temperature distribution of the ROI (head, superior limbs and trunk) at these two time points: (b) Baseline and (d) ALI 25 (last measurement)

kurtosis distributions. A lower peak in the histogram denotes, on the contrary, that the distribution is less clustered around the mean. This can be translated into higher standard deviations and, consecutively, a heterogeneously distributed body temperature (temperature centralization) [15].

In addition, possible correlations between the two new indices and both SI and MAP were analyzed, as denoted in Table 1.4. Note that they are markers of circulatory impairments. The Pearson product-moment correlation evidenced a strong correlation between SD and SI as well as between  $\Delta T/\Delta x$  and SI. Moreover, the same method demonstrated a strong negative correlation between both parameters, SD and MAP, and  $\Delta T/\Delta x$  and MAP. The authors observed that the progress of the disease severity is accompanied by an increase in SD,  $\Delta T/\Delta x$ , and SI and a decrease in MAP. Commonly, sepsis and shock include hypotension and are characterized by an impaired blood flow to peripheral body tissues (hypoperfusion), which leads to temperature centralization (increased  $\Delta T/\Delta x$  and SD). The Pearson product-moment correlation pointed out a moderate negative correlation between SD,  $\Delta T/\Delta x$ , SI and both PaO<sub>2</sub> and PF as well. Hypoperfusion is frequently accompanied by tissue hypoxia as there is an inability to meet the oxygen demands of the tissues [15].

**Table 1.4** Pearson product-moment correlation between SD,  $\Delta T/\Delta x$ , SI and SI, MAP, PaO<sub>2</sub> and Carrico index [15]

		Standard deviation	$\Delta T/\Delta x$	SI
SI	Pearson correlation	0.593 <sup>a,b</sup>	0.561 <sup>a,b</sup>	—
	<i>p</i> -Value	<0.0005	<0.0005	—
MAP	Pearson correlation	-0.587 <sup>a,b</sup>	-0.534 <sup>a,b</sup>	-0.519 <sup>a,b</sup>
	<i>p</i> -Value	<0.0005	<0.0005	<0.0005
PaO <sub>2</sub>	Pearson correlation	-0.344 <sup>a,c</sup>	-0.334 <sup>a,c</sup>	-0.326 <sup>a,c</sup>
	<i>p</i> -Value	0.004	0.005	0.007
PF ratio	Pearson correlation	-0.315 <sup>a,c</sup>	-0.319 <sup>a,c</sup>	-0.326 <sup>a,c</sup>
	<i>p</i> -Value	0.009	0.008	0.007

<sup>a</sup> Correlation is significant at the 0.01 level (two-tailed)

<sup>b</sup> Strong correlation [ $0.40 < |r| < 0.70$ ]—according to Weinberg et al. [83]

<sup>c</sup> Moderate correlation [ $0.30 < |r| < 0.39$ ]—according to Weinberg et al. [83]

In sum, the study demonstrated the ability of thermal imaging to monitor circulation and perfusion in a porcine animal model. The two new indices were capable of quantifying the course and severity of the disease.

## 1.4 Recent Advances in 3D Infrared Thermography

Infrared thermography is a powerful tool to gather information about temperature distribution on the surface of objects. A major disadvantage of thermographic cameras is that 3D bodies are represented by 2D images, which leads to the loss and distortion of information [84]. Especially for medical applications it can be very useful to visualize 3D representations of the temperature distribution of an object. This enables a more intuitive and precise analysis of the thermography data for the physician. Furthermore, the fusion of different image modalities becomes possible, for example, the fusion of thermal information with those of 3D models created by MRI scans [84, 85].

In order to create a 3D representation of the temperature distribution of a body surface, it is necessary to create a multitude of different 2D images that then are combined to obtain information about the depth of an object. A possible apparatus to create more than one image are stereo cameras. These consist of two cameras that create images of the same object from two different vantage points (like human binocular vision). Based on the relative positions of the object on these two different images, it is then possible to extract 3D information about the object, for example, the depth of a wound bed. Thermographic stereo cameras have been introduced in studies for breast cancer detection [86] and diabetic foot disease [87]. These devices generate information about the depth of surface structures, nevertheless it is not possible to produce a whole 3D surface model. A more sophisticated approach poses the recording of images from different angles. A major advantage of this technique

is that regular infrared cameras can be used by taking images from the same object from different locations. For example, it is possible to generate a temperature map of the human head by taking four pictures with the same camera (one frontal image, one image of the left side, one image of the back, one image of the right side). These four 2D projections then have to be combined with an existing 3D model from another imaging modality. This could be a 3D scanning system that generates spatial models as well as the 3D models that are obtained by MRI or CT scans. The infrared images then are registered onto the 3D model. This registration process includes multiple image processing calculations that will not be discussed here. The resulting model then carries the combined 3D information of both imaging modalities [88].

MRI or CT scans are used to create 3D models of a variety of body parts like the brain, bone structures, or the heart in everyday clinical practice. These models contain anatomical information for medical diagnostics, for example, information about the integrity of bones and vessel walls as well as the location and size of tumors. Infrared images on the other hand are used to provide physiological information and therefore complement the anatomical information of MRI and CT scans. Possible medical applications lie in sports medicine as well as in tumor diagnostics as well as in breast cancer diagnostics, where a 3D model of the breast can be very useful to precisely detect regions of possible tumor development. The regions of inflammation detected by IRT can be mapped on the 3D model of a fracture and increased hemodynamics could provide crucial information about the development of a tumor that has been scanned with MRI.

## 1.5 Summary

The use and the fields of applications of thermal imaging have been growing throughout the last decades. Consecutive innovations in the production of infrared detectors made IRT an accurate and sensitive technology. The spatial resolution allied to the high sensitivity of infrared cameras contributed to their increasing use in medicine. Studies indicate the potential of thermal imaging in the diagnosis of breast cancer, rheumatic disease, chronic wounds, among others. In addition, IRT has demonstrated its potential as a monitoring technique (HR, RR, and perfusion), not only because of its sensitivity but also because is a passive and non-invasive method, which does not need a light source. In the last years, some advances in 3D thermal imaging were patent. Three-dimensional representations enable a more intuitive and precise visualization of body temperature distribution. In addition, more information can be achieved by combining 3D thermal imaging with other 3D models, for instance, from CT or MRI.

## References

1. R. Berz et al., *Thermografie Kolloquium 2007* (2007)
2. B.B. Lahiri, S. Bagavathiappan, T. Jayakumar, J. Philip, *Infrared Phys. Technol.* **55**(4), 221 (2012)
3. E. Ring, K. Ammer, *Physiol. Meas.* **33**(3), R33 (2012)
4. C. Hildebrandt, C. Raschner, K. Ammer, *Sensors (Basel)* **10**(5), 4700 (2010)
5. M. Planck, *The Theory of Heat Radiation* (P. Blakiston's Son & Co., Philadelphia, 1914)
6. M. Planck, *Ann. Phys.* **4**, 553 (1901)
7. B.F. Jones, *IEEE Trans. Med. Imaging* **17**(6), 1019 (1998)
8. J. Steketee, *Phys. Med. Biol.* **18**(5), 686 (1973)
9. J.J. van Netten, J.G. van Baal, C. Liu, F. van der Heijden, S.A. Bus, *J. Diabetes Sci. Technol.* **7**(5), 1122 (2013)
10. S. Bagavathiappan, B.B. Lahiri, T. Saravanan, J. Philip, T. Jayakumar, *Infrared Phys. Technol.* **60**, 35 (2013)
11. B.F. Jones, P. Plassmann, *IEEE Eng. Med. Biol. Mag.* **21**(6), 41 (2002)
12. R. Resmini, A. Conci, L.F. da Silva, G.O. Sequeiros, F. Araújo, C. de Araújo, A.d.S. Araújo, R. Rodríguez-Ramos, F. Lebon, in *Application of Infrared to Biomedical Sciences*, 1st edn., ed. by E.Y. Ng, M. Etehadtavakol (Springer, Berlin, 2017)
13. Y. Chen, B. Kateb, *Neurophotonic and Brain Mapping* (CRC Press, Boca Raton, 2017)
14. F.S. Nahm, *Korean J. Pain* **26**(3), 219 (2013)
15. C.B. Pereira, M. Czaplík, N. Blaník, R. Rossaint, V. Blazek, S. Leonhardt, *Biomed. Opt. Express* **5**(4), 1075 (2014)
16. C. Hildebrandt, K. Zeilberger, E.F.J. Ring, C. Raschner, The application of medical infrared thermography in sports medicine, in *An International Perspective on Topics in Sports Medicine and Sports Injury (InTech, 2012)*
17. M. Kontos, R. Wilson, I. Fentiman, *Clin. Radiol.* **66**(6), 536 (2011)
18. V. Umadevi, S.V. Raghavan, S. Jaipurkar, *Indian J. Med. Res.* **134**(5), 725 (2011)
19. S.P. Niehof, F.J. Huygen, R.W. van der Weerd, M. Westra, F.J. Zijlstra, *Biomed. Eng. Online* **5**, 30 (2006)
20. A. Gardiner, R. Florin, C. Haber, in *Proceedings of Light-Activated Tissue Regeneration and Therapy Conference*, vol. 12, ed. by R. Waynant, D. Tata. Lecture Notes in Electrical Engineering (Springer, Boston, 2008), pp. 283–292
21. C.W. Cho, F.S. Nahm, E. Choi, P.B. Lee, I.K. Jang, C.J. Lee, Y.C. Kim, S.C. Lee, *Medicine (Baltimore)* **95**(52), e5548 (2016). <https://doi.org/10.1097/MD.0000000000005548>
22. M. Bharara, J.E. Cobb, D.J. Claremont, *Int. J. Low. Extrem. Wounds* **5**(4), 250 (2006)
23. J.H. Tan, E.Y.K. Ng, U. Rajendra Acharya, C. Chee, *Infrared Phys. Technol.* **53**(2), 120 (2010)
24. S. Matteoli, E. Favuzza, L. Mazzantini, P. Aragona, S. Cappelli, A. Corvi, R. Mencucci, *Physiol. Meas.* **38**(8), 1503 (2017). <https://doi.org/10.1088/1361-6579/aa78bd>
25. N. Zaproudina, Z. Ming, O.O.P. Hänninen, J. Manip. *Physiol. Ther.* **29**(3), 219 (2006)
26. E.F. Ring, P.A. Dieppe, P.A. Bacon, *Br. J. Clin. Pract.* **35**(7–8), 263 (1981)
27. G. Varjú, C.F. Pieper, J.B. Renner, V.B. Kraus, *Rheumatology (Oxford)* **43**(7), 915 (2004)
28. A.E. Denoble, N. Hall, C.F. Pieper, V.B. Kraus, *Clin. Med. Insights Arthritis Musculoskelet. Disord.* **3**, 69 (2010)
29. S. Bagavathiappan, T. Saravanan, J. Philip, T. Jayakumar, B. Raj, R. Karunanithi, T.M.R. Panicker, M.P. Korath, K. Jagadeesan, *J. Med. Phys.* **34**(1), 43 (2009). <https://doi.org/10.4103/0971-6203.48720>
30. C.L. Huang, Y.W. Wu, C.L. Hwang, Y.S. Jong, C.L. Chao, W.J. Chen, Y.T. Wu, W.S. Yang, *J. Vasc. Surg.* **54**(4), 1074 (2011). <https://doi.org/10.1016/j.jvs.2011.03.287>

31. E. Staffa, V. Bernard, L. Kubicek, R. Vlachovsky, D. Vlk, V. Mornstein, A. Bourek, R. Staffa, *Vascular* **25**(1), 42 (2017). <https://doi.org/10.1177/1708538116640444>
32. M.J. Lim, S.R. Kwon, K.H. Jung, K. Joo, S.G. Park, W. Park, *J. Korean Med. Sci.* **29**(4), 502 (2014). <https://doi.org/10.3346/jkms.2014.29.4.502>
33. R. Lasanen, E. Piippo-Savolainen, T. Remes-Pakarinen, L. Kröger, A. Heikkilä, P. Julkunen, J. Karhu, J. Töyräs, *Physiol. Meas.* **36**(2), 273 (2015). <https://doi.org/10.1088/0967-3334/36/2/273>
34. B. Lerkvaleekul, S. Jaovisidha, W. Sungkarat, N. Chitrapazt, P. Fuangfa, T. Ruangchaijatuporn, S. Vilaiyuk, *Physiol. Meas.* **38**(5), 691 (2017). <https://doi.org/10.1088/1361-6579/aa63d8>
35. J.Y. Park, J.K. Hyun, J.B. Seo, *J. Shoulder Elbow Surg.* **16**(5), 548 (2007)
36. V. Dini, P. Salvo, A. Janowska, F. Di Francesco, A. Barbini, M. Romanelli, *Wounds* **27**(10), 274 (2015)
37. E. Keenan, G. Gethin, L. Flynn, D. Watterson, G.M. O'Connor, *Physiol. Meas.* **38**(6), 1104 (2017)
38. A.A. Wahab, M.I.M. Salim, M.N.C. Aziz, in *Application of Infrared to Biomedical Sciences*, ed. by E.Y. Ng, M. Etehadtavakol. Series in BioEngineering (Springer, Singapore, 2017), pp. 109–131
39. R. Lawson, *Can. Med. Assoc. J.* **75**(4), 309 (1956)
40. R. Amalric, D. Giraud, C. Altschuler, F. Amalric, J.M. Spitalier, H. Brandone, Y. Ayme, A.A. Gardiol, *Prog. Clin. Biol. Res.* **107**, 269 (1982)
41. Z.S. Deng, J. Liu, *2005 IEEE Engineering in Medicine and Biology 27th Annual Conference* (2005), pp. 7525–7528
42. L. Boquete, S. Ortega, J.M. Miguel-Jiménez, J.M. Rodríguez-Ascariz, R. Blanco, *J. Med. Syst.* **36**(1), 103 (2012)
43. E.F. Ring, *Bibl. Radiol.* **1**(6), 97 (1975)
44. A.J. Collins, E.F. Ring, J.A. Cosh, P.A. Bacon, *Ann. Rheum. Dis.* **33**(2), 113 (1974)
45. E.F. Ring, A.J. Collins, P.A. Bacon, J.A. Cosh, *Ann. Rheum. Dis.* **33**(4), 353 (1974)
46. M. Frize, C. Adéa, P. Payeur, G. Di Primio, J. Karsh, A. Ogungbemile, *Proceedings of SPIE*, vol. 7962 (2011), pp. 79620M–79620M-11
47. C.L. Wu, K.L. Yu, H.Y. Chuang, M.H. Huang, T.W. Chen, C.H. Chen, *J. Manip. Physiol. Ther.* **32**(4), 287 (2009)
48. P.C. Vecchio, A.O. Adebajo, M.D. Chard, P.P. Thomas, B.L. Hazleman, *Clin. Rheumatol.* **11**(3), 382 (1992)
49. P.B. Morgan, A.B. Tullo, N. Efron, *Eye (London)* **9**(Pt 5), 615 (1995)
50. T.C. Chang, Y.L. Hsiao, S.L. Liao, *Graefes Arch. Clin. Exp. Ophthalmol.* **246**(1), 45 (2008)
51. C.K. Sen, G.M. Gordillo, S. Roy, R. Kirsner, L. Lambert, T.K. Hunt, F. Gottrup, G.C. Gurtner, M.T. Longaker, *Wound Repair Regen.* **17**(6), 763 (2009). <https://doi.org/10.1111/j.1524-475X.2009.00543.x>
52. R.N. Lawson, J.P. Gaston, *Ann. N. Y. Acad. Sci.* **121**(1), 90 (1964)
53. G.L. Hansen, E.M. Sparrow, N. Komamuri, P.A. Iazzo, *Wound Repair Regen.* **4**(3), 386 (1996)
54. V. Falanga, L.J. Saap, A. Ozonoff, *Dermatol. Ther.* **19**(6), 383 (2006)
55. M. Fierheller, R.G. Sibbald, *Adv. Skin Wound Care* **23**(8), 369 (2010)
56. M.A. Cretikos, R. Bellomo, K. Hillman, J. Chen, S. Finfer, A. Flabouris, *Med. J. Aust.* **188**(11), 657 (2008)
57. K.E. Philip, E. Pack, V. Cambiano, H. Rollmann, S. Weil, J. O'Beirne, *J. Clin. Monit. Comput.* **29**(4), 455 (2015)
58. R. Murthy, I. Pavlidis, P. Tsiamyrtzis, *Engineering in Medicine and Biology Society, 2004. IEMBS'04. 26th Annual International Conference of the IEEE*, vol. 1 (IEEE, Piscataway, 2004), pp. 1196–1199

59. J. Fei, I. Pavlidis, *Engineering in Medicine and Biology Society, 2007. EMBS 2007. 29th Annual International Conference of the IEEE* (IEEE, Piscataway, 2007), pp. 250–253
60. J. Fei, I. Pavlidis, *IEEE Trans. Biomed. Eng.* **57**(4), 988 (2010)
61. S.Y. Chekmenev, H. Rara, A.A. Farag, *The First International Conference on Graphics, Vision, and Image Processing (GVIP)*, Cairo (2005), pp. 107–112
62. M. Yang, Q. Liu, T. Turner, Y. Wu, *IEEE Conference on Computer Vision and Pattern Recognition, 2008. CVPR 2008* (IEEE, Piscataway, 2008), pp. 1–8
63. J.N. Murthy, J. van Jaarsveld, J. Fei, I. Pavlidis, R.I. Harrykissoon, J.F. Lucke, S. Faiz, R.J. Castriotta, *Sleep* **32**(11), 1521 (2009)
64. A.K. Abbas, K. Heimann, K. Jergus, T. Orlikowsky, S. Leonhardt, *Biomed. Eng. Online* **10**(1), 93 (2011)
65. F. Al-Khalidi, R. Saatchi, H. Elphick, D. Burke, *Am. J. Eng. Appl. Sci.* **4**(4), 586 (2011)
66. G.F. Lewis, R.G. Gatto, S.W. Porges, *Psychophysiology* **48**(7), 877 (2011)
67. C.B. Pereira, X. Yu, M. Czaplik, R. Rossaint, V. Blazek, S. Leonhardt, *Biomed. Opt. Express* **6**(11), 4378 (2015)
68. C.B. Pereira, X. Yu, M. Czaplik, V. Blazek, B. Venema, S. Leonhardt, *J. Clin. Monit. Comput.* **31**(6), 1241–1254 (2017)
69. S.Y. Chekmenev, A.A. Farag, E.A. Essock, *2007 IEEE Conference on Computer Vision and Pattern Recognition* (2007), pp. 1–6
70. M. Garbey, N. Sun, A. Merla, I. Pavlidis, *IEEE Trans. Biomed. Eng.* **54**(8), 1418 (2007)
71. F.N.v.d. Vosse, N. Stergiopoulos, *Annu. Rev. Fluid Mech.* **43**(1), 467 (2011)
72. T.R. Gault, A.A. Farag, *2013 IEEE Conference on Computer Vision and Pattern Recognition Workshops (CVPRW)* (2013), pp. 336–341
73. R.P. Dellinger, M.M. Levy, J.M. Carlet, J. Bion, M.M. Parker, R. Jaeschke, K. Reinhart, D.C. Angus, C. Brun-Buisson, R. Beale, T. Calandra, J.F. Dhainaut, H. Gerlach, M. Harvey, J.J. Marini, J. Marshall, M. Ranieri, G. Ramsay, J. Sevransky, B.T. Thompson, S. Townsend, J.S. Vender, J.L. Zimmerman, J.L. Vincent, International Surviving Sepsis Campaign Guidelines Committee, American Association of Critical-Care Nurses, American College of Chest Physicians, American College of Emergency Physicians, Canadian Critical Care Society, European Society of Clinical Microbiology and Infectious Diseases, European Society of Intensive Care Medicine, European Respiratory Society, International Sepsis Forum, Japanese Association for Acute Medicine, Japanese Society of Intensive Care Medicine, Society of Critical Care Medicine, Society of Hospital Medicine, Surgical Infection Society, World Federation of Societies of Intensive and Critical Care Medicine, *Crit. Care Med.* **36**(1), 296 (2008)
74. M. Odeh, *Postgrad. Med. J.* **72**(844), 66 (1996)
75. S.C.P.L. Shiramizo, A.R. Marra, M.S. Durão, Á.T. Paes, M.B. Edmond, O.F. Pavão dos Santos, *PLoS ONE* **6**(11), e26790 (2011)
76. J.H. Wu, C.Y. Chen, P.N. Tsao, W.S. Hsieh, H.C. Chou, *Pediatr. Neonatol.* **50**(3), 88 (2009)
77. D.C. Angus, W.T. Linde-Zwirble, J. Lidicker, G. Clermont, J. Carcillo, M.R. Pinsky, *Crit. Care Med.* **29**(7), 1303 (2001)
78. G.S. Martin, D.M. Mannino, S. Eaton, M. Moss, *N. Engl. J. Med.* **348**(16), 1546 (2003)
79. F.B. Mayr, S. Yende, D.C. Angus, *Virulence* **5**(1), 4 (2014)
80. J.E. Lawn, S. Cousens, J. Zupan, Lancet Neonatal Survival Steering Team, *Lancet* **365**(9462), 891 (2005)
81. T. Koch, S. Geiger, M.J. Ragaller, *J. Am. Soc. Nephrol.* **12**(Suppl. 17), S53 (2001)
82. A. Kumar, D. Roberts, K.E. Wood, B. Light, J.E. Parrillo, S. Sharma, R. Suppes, D. Feinstein, S. Zanotti, L. Taiberg, D. Gurka, A. Kumar, M. Cheang, *Crit. Care Med.* **34**(6), 1589 (2006)
83. S.L. Weinberg, S.K. Abramowitz, *Statistics Using SPSS: An Integrative Approach* (Cambridge University Press, Cambridge, 2008)

84. M. Unger, A. Franke, C. Chalopin, *Curr. Dir. Biomed. Eng.* **2**(1), 369 (2016)
85. M.A. de Souza, I.J. Sanches, H.R. Gamba, P. Nohama, *Conf. Proc. IEEE Eng. Med. Biol. Soc.* **2013**, 3371 (2013)
86. I. Grubisic, L. Gjenero, T. Lipic, I. Sovic, T. Skala, *Proceedings of the 34th International Convention MIPRO* (2011), pp. 269–273
87. S. Barone, A. Paoli, A.V. Razionale, *XVIII Congreso Internaccional de Ingenieria Grafica*, Sitges (2006)
88. M.A. de Souza, A.G. Krefer, G.B. Borba, T.M. Centeno, H.R. Gamba, *Conf. Proc. IEEE Eng. Med. Biol. Soc.* **2015**, 2395 (2015)



# Chapter 2

## Photoplethysmography Imaging and Common Optical Hybrid Imaging Modalities



Vladimir Blazek, Stephan Dahlmanns, Carina Barbosa Pereira, Xinchu Yu, Nikolai Blanik, Steffen Leonhardt, and Claudia Rosa Blazek

**Abstract** Due to their obvious advantages, active and passive optoelectronic sensor concepts for monitoring cardiorespiratory vital signs and detection of rhythmical phenomena in dermal blood perfusion are being investigated by various biomedical groups, particularly their camera-based variants. Such methods are noninvasive and contactless, and allow spatially resolved skin perfusion studies.

This chapter presents one of these medical imaging modalities (developed by and clinically tested at RWTH Aachen University), i.e., active photoplethysmography imaging (PPGI) for the mapping of dermal blood perfusion dynamics. PPGI is an enhancement of the classical photoplethysmography and pulse oximetry (SpO<sub>2</sub>) and describes the remote “opto-electronical measurement of arterial and/or venous blood volume changes”. Approved algorithms from these established methods, e.g., algorithms that extract the heart rate, heart rate variability, respiratory rate, and/or pulse wave form-related stress/pain signals, can easily be adapted to PPGI. This remote monitoring technique allows measurement of body signals without contact (unobtrusive) and with spatial resolution; moreover, it can be adapted to specific measurement scenarios, such as the monitoring of neonates and acquiring vital information from within the area of a wound.

Selected medical applications have been validated by our group using the PPGI technology in a stand-alone or hybrid camera configuration. Although these

---

V. Blazek (✉)

Chair for Medical Information Technology, Helmholtz-Institute for Biomedical Engineering, RWTH Aachen University, Aachen, Germany

Czech Institute of Informatics, Robotics and Cybernetics (CIIRC), Czech Technical University in Prague, Prague, Czech Republic  
e-mail: [blazek@hia.rwth-aachen.de](mailto:blazek@hia.rwth-aachen.de)

S. Dahlmanns · C. Barbosa Pereira · X. Yu · N. Blanik · S. Leonhardt  
Chair for Medical Information Technology, Helmholtz-Institute for Biomedical Engineering, RWTH Aachen University, Aachen, Germany

C. R. Blazek

The Private Clinic of Dermatology, Haut im Zentrum, Zurich, Switzerland

© Springer Nature Switzerland AG 2018

M. Abreu de Souza et al. (eds.), *Multi-Modality Imaging*,  
[https://doi.org/10.1007/978-3-319-98974-7\\_2](https://doi.org/10.1007/978-3-319-98974-7_2)

preliminary results are promising, additional research and development is necessary (especially for the detection and elimination of movement artifacts) before this novel technology can be transferred into a standardized clinical application.

**Keywords** Remote PPGI · Signal analysis · Medical applications · Functional imaging · Space-resolved mapping · Skin perfusion · Vital parameters · Optical Hybrid Imaging

## 2.1 Principle of Remote PPGI Measurement and Signal Composition

For many years, classical photoplethysmography (PPG) has been one of the most popular noninvasive (skin-attached) methods for functional monitoring of peripheral vascular status. In 1937, after the pioneering work of Cartwright [1], Haxthausen [2], Mathes [3], and Molitor [4], the physiologist Alrick B. Hertzman (St. Louis University School of Medicine, USA) [5, 6] discovered the relationship between the intensity of backscattered (or transmitted polychromatic light) and blood volume inside the skin. A diagram of the sensor he invented is shown in Fig. 2.1a. The measurement principle of the PPG is based on the fact that hemoglobin in human blood has a higher absorption coefficient for infrared (IR) light than the surrounding skin tissue. Therefore, blood volume changes can be measured based on the amount of IR light that reaches the photocell after it has travelled through the skin. The more the light detected by the photocell, the less the blood contained in that tissue. With this technique, blood volume changes in the cutaneous and (partially) in the subcutaneous vessel plexus can be detected. The signal itself is composed of: (1) a large constant part which is independent from the perfusion (light scattering in tissue), (2) a smaller quasi-static signal reflecting the blood volume stored inside the veins, and (3) a very small, periodically modulated arterial signal.

The first modern PPG imaging (PPGI) system was developed at RWTH Aachen University (Germany) in the late 1990s [7–9]. Since then, PPGI has been adapted by many research groups and tested in different medical applications. The PPG imaging technology consists of an active, camera-based sensor strategy (Fig. 2.1b) that allows contactless recording and processing of sequences of selected skin areas. Among other possibilities, it visualizes skin vessels biometrically and analyzes dermal perfusion in each camera pixel. The body area to be assessed is illuminated by polychromatic (Fig. 2.1c) or monochromatic light (generally, multiple LED panels, Fig. 2.1d). Unfortunately, this adaptation leads to a variety of names referring to PPGI that now exist in the literature, like “remote PPG (rPPG)”, “camera-based PPG (cbPPG)”, “noncontact PPG (ncPPG)”, “imaging PPG (iPPG)”, and “DistancePPG” [10–17]. The measurement technology that is presented in this book chapter can be described by either of these terms. For consistency reasons, we will refer to the original term “PPG imaging (PPGI)” without limitation of generality.

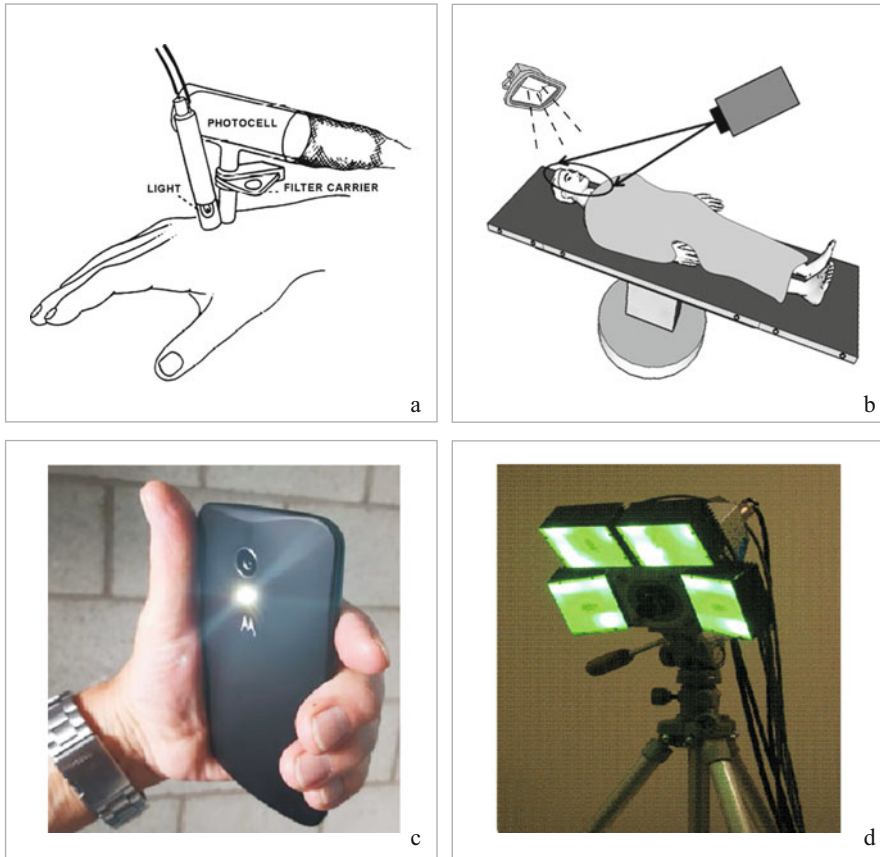


**Fig. 2.1** From the first Herzman's photoplethysmographic device (1938) to the current remote photoplethysmography imaging (PPGI)

The size of the observed skin/body region and the spatial resolution can be arbitrarily chosen, depending on the camera lens used and the distance between the camera and the measured object. The camera (which has a high dynamic range to measure optical damping of the skin) is connected to a computer which controls its settings, records the PPGI sequences, stores the video data, and performs automated analyzing routines.

In contrast to PPGI, infrared thermography imaging (IRT) [18, 19] is not based on randomly scattered light injected into the organism, but on (black) body radiation as a function of local temperature and skin emissivity. IRT is considered a highly advantageous monitoring method since it is fully unobtrusive and provides important functional insight into human physiology (see Chap. 1). IRT differs from PPGI in that it is passive (no active illumination is required) and can be applied in total darkness. However, because skin perfusion is the method by which the

body transfers heat energy from the core to periphery, it can be assumed that local temperature is correlated with local perfusion. With this assumption in mind, the combination of IRT and PPGI offers a comprehensive tool for visualization of the complex processes inside the human body. Our group was the first to propose fusion of these camera-based modalities to enable a hybrid hyperspectral imaging strategy [20–22].

### 2.1.1 Genesis of the PPG/PPGI Signal Waveform

In evidence-based medical diagnostics, all the required functional information is contained in the waveform of the received signal. Information on venous and/or arterial hemodynamics, venous reflux or outflow obstructions, arterial stiffness behavior, left ventricle and respiration activity, and dynamics of the autonomic nervous system can be extracted from the composition of the time-dependent PPG/PPGI signal. The received light intensity is derived from different sources, including physical blood circulation properties and optical tissue parameters. Figure 2.2a shows the superficial composition of the received light. Bloodless tissue-scattering parameters cause a large constant part of the signal; this contributes to approximately 90% of the total signal. Venous blood volume causes the small quasi-static part (in humans at rest), which constitutes about 10% of the measured signal [23]. Blood volume in the dermal venous plexus also varies due to vasomotor activity, thermoregulation, and respiration; however, because this variation is very slow and almost constant, it is called “quasi-static”. Rapid blood volume changes can be observed in macro- and micro-arterial vessels and contribute to the periodic changes in the PPG/PPGI signal (the AC signal component). Unfortunately, those changes occupy only about 0.1% of a total measured signal. Figure 2.2b shows a typical PPG signal, measured in the 900-nm band in the ear channel [24].

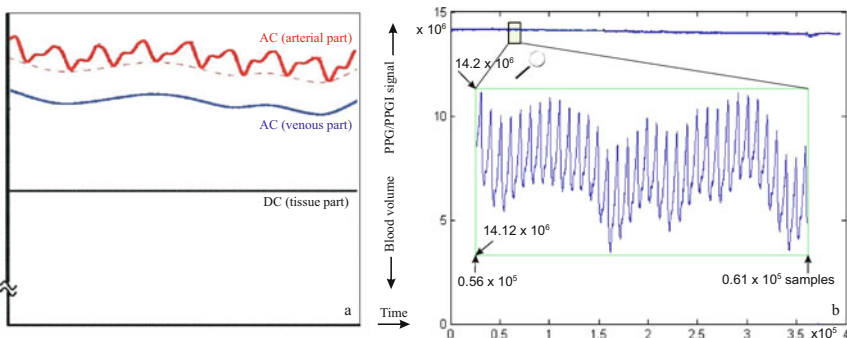


**Fig. 2.2** Schematic presentation of the PPG/PPGI signal composition (a), and typical blood volume dynamics detected in the ear channel of a volunteer at rest (b). In this case, the DC-signal amplitude is approximately  $14.15 \times 10^6$ , the AC-signal  $0.5 \times 10^4$

As mentioned, an advantage of PPGI compared with classic PPG is that, in the former, any pixel of the camera sensor can be assumed to be equivalent to one single PPG sensor. The curve of the recorded light intensity of that pixel  $I_{x,y}(t)$  corresponds to the PPG signal  $I_{\text{PPG}}(t)$ . In order to produce more stable signals that are less affected by noise, several pixels are grouped together into regions of interest (ROIs). The mean intensity value of all pixels inside the ROI can then be assigned to the PPG time signal:

$$I_{\text{PPG}}(t) = \frac{\sum_{\text{ROI}} I_{x,y}(t)}{|\text{ROI}|}. \quad (2.1)$$

This PPG time signal can be further processed by employing classic PPG analyzing routines. The monitoring and analysis of vital parameters (e.g., heartbeat, or breathing rhythms) requires the assessment of the composition of the recorded light intensity  $I_{x,y}$  at each pixel. Hence, the variable blood volume inside the vessels extinguishes ( $E(t)$ ) parts of the detected light  $I_{\text{PPG}}(t)$ . Therefore,  $I_{\text{PPG}}(t)$  depends on the intensity of the injected light  $I_0$ , the time variant extinction, and the modulation through the tissue:

$$I_{\text{PPG}}(t) = \tilde{I}_0 \cdot E(t) + I_{\text{err}}, \quad \text{with} \quad \tilde{I}_0 = \xi_{\text{T-PPG}} \cdot I_0, \quad \xi_{\text{T-PPG}} \in [0, 1]. \quad (2.2)$$

$\tilde{I}_0$  corresponds to the part of the injected light intensity ( $\xi_{\text{T-PPG}}$ ) which propagates towards the direction of the detector if the attenuation is zero.  $I_{\text{err}}$  includes all the sources of error that occur, e.g., sensor/quantization noise, or image artifacts due to movement of the measured object. Since  $I_0$  is given, and  $\xi_{\text{T-PPG}}$  is constant, the only unknown modulation of  $I_{\text{T-PPG}}$  is caused by the changes of  $E(t)$ .

Even though the Beer–Lambert Law requires isotropy, it allows an approximation of tissue behavior:

$$E(t) = e^{-\varepsilon(\lambda)c(t)d}. \quad (2.3)$$

In the Beer–Lambert equation,  $\varepsilon$  describes the mean extinction coefficient of the tissue dependent on the wavelength of light  $\lambda$ ;  $c$  is the time-dependent concentration of tissue (among others, blood volume), and  $d$  is the mean path of the photons. If sensor and detector are placed in a so-called reflection mode PPG/PPGI measuring setup (the most common sensor configuration is: light source/light detector located at the same side of the tissue; Fig. 2.1), the light paths directed towards the sensor via bloodless epidermal layers have also to be considered. The reason for this is that, since these regions are not affected by blood volume changes, they reduce the percentage of the detected signal which contains vital rhythms:

$$I_{\text{R-PPG}}(t) = \xi_{\text{R-PPG}} \cdot I_0 \cdot E(t) + \xi_{\text{epidermis}} \cdot E_{\text{const}} + I_{\text{err}}. \quad (2.4)$$

As a result, the most common reflective mode that PPG sensors utilize is a single point illumination: distinct light paths which originate at the illumination point and

head towards the area being measured become relevant for the PPG signal. Direct cross talk by reflection at the skin surface is prevented by an optical barrier.

In the reflective PPGI, the detected light intensity of a single pixel complies with the light intensity of the corresponding skin area, emitted towards the camera. The signal is composed as follows:

$$I_{\text{PPGI}}(t) = I_0 \cdot R + \sum_{x,y} (I_{\text{R-PPG}}(t, x, y)) + I_{\text{err}}. \quad (2.5)$$

Large portions of the detected light result from direct skin surface reflections and do not contribute information about vital parameters. Only minor quantities of the light actually get backscattered from deeper tissue layers. In contrast to the reflective mode, the PPGI signal parts receive information from all possible paths in the illuminated surroundings of the field being measured, and are not restricted to a single LED position  $(x, y)$ . Again,  $I_{\text{err}}$  summarizes all sources of error.

The ability to register small AC signal parts is an important requirement for the PPGI setup, as is the frame rate of the camera and cost-effectiveness. The most important prerequisites are:

- Dynamic range of the camera
- Spatial resolution
- Intrinsic sensor noise (dark current)
- Illumination wavelength and intensity
- Obtainable frame rate
- Price of the system

### ***2.1.2 First- and Second-Generation PPGI***

The first PPGI system was introduced in 1997 by the optical research laboratory of the RWTH Aachen University (Germany) with the support of the Deutsche Forschungsgemeinschaft (DFG). The system is based on the Life Science Resources UltraPix FE 250 CCD camera (EEV 37–10 imaging sensor) and characterized by its high dynamic range of up to 84 dB. This value can be obtained by cooling the sensor chip down to a temperature of  $-40^\circ\text{C}$  with a Peltier element, which effectively reduces temperature noise. Furthermore, the camera offers a spatial resolution of  $512 \times 512$  pixels and a maximum frame rate of 12 fps at full frame resolution. Like most CCD cameras, this value can be increased by reducing the spatial resolution. The spectral range of the UltraPix Fe 250 includes most of the visible wavelengths plus the near IR spectrum (total spectral range is 400–1100 nm). The camera also has a quantum efficiency of 40% at 800 nm [25]. During measurement, the object of interest can be illuminated either by polychromatic environmental light or by monochromatic LED panels at distinct wavelengths, generally in green color (Fig. 2.3).

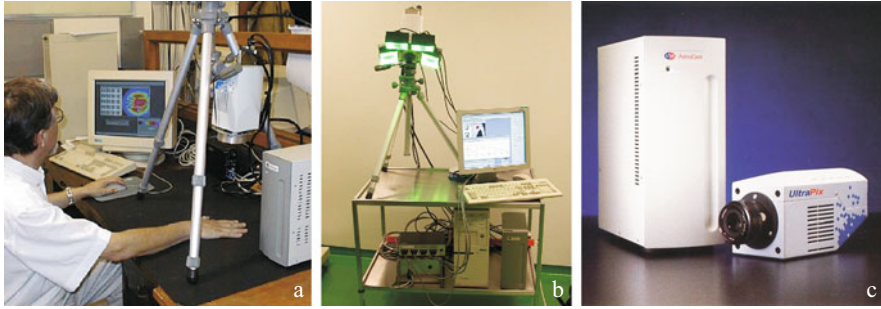


**Fig. 2.3** First generation of experimental PPGI setup during measurement with environmental light (a), first clinically used PPGI setup (b), and our cooled CCD camera UltraPix FE (c)

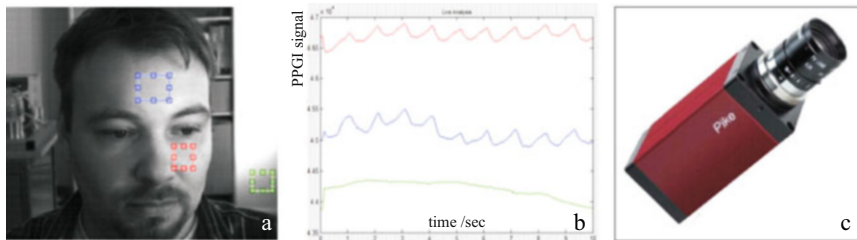


**Fig. 2.4** Second generation of our experimental PPGI setup. First frame of PPGI recordings with marked ROIs (a); PPG time series of respective ROIs (b). One of the three ROIs was used to detect the course of time of the ambient light by placing the ROI on a homogeneous surface of the background; AVT Pike F 210 B camera used (c); modified from [26]

The second-generation PPGI system was setup in 2008; this system used the Pike F 210 B CCD camera from Allied Vision Technologies (AVT), Stadroda, Germany (Fig. 2.4). Compared to the first-generation system, its sensor chip (the TrueSense KAI-2093) has a higher spatial resolution of  $1920 \times 1080$  pixels (full HD resolution), and a faster readout speed of 31 frames at full frame resolution [26]. Again, this value can be increased by reducing the spatial resolution. The sensitive spectrum ranges from 300 to 1000 nm, with a maximum quantum efficiency of approximately 40% at 500 nm.

### 2.1.3 Low-Cost Cameras (Webcams and Smartphone Cameras)

Cameras are currently involved in all aspects of daily life, e.g., digital cameras can record video sequences, webcams are present in nearly every laptop, and smartphones invariably have cameras. Although most of them are not high-end specialized PPGI cameras, they can perform remote sensing with intelligent algorithms that compute appropriate ROIs (Fig. 2.5).



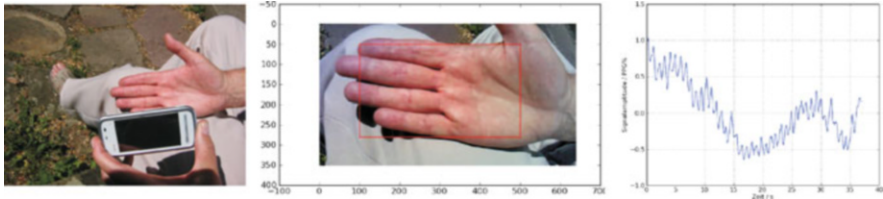


**Fig. 2.5** “Selfie” examination of blood perfusion behavior on the palmar side of the right hand in sitting position, illumination with daylight. Choosing only one ROI, the PPGI signal can be “grabbed” from the noise and visualized online. Heart rate and heart rate variability can be monitored by this setup, but not the exact waveform of the peripheral arterial blood volume pulse

Although spatial information tends to get lost when increasing the size of the ROI, the dynamic sensitivity of the sensor chips also increases. This enables to record the heartbeat-correlated AC part of the signal, even with 8-bit sensor arrays. Again, opportunities arise to extract PPG information from the different color channels of the chip, thereby increasing the quality of the extractable vital parameters.

In combination with the primary functions of the device (e.g., the telecommunication task of a smartphone), new fields of applications open up for PPGI technology. For example, the smartphone can become part of a fitness tracker, ambient-assisted living, or even a medical monitor for emergency tele-aid.

## 2.2 PPGI Signal Analysis

### 2.2.1 Basic Analysis

The processing of PPGI video sequences is generally conducted in a way similar to that of classic PPG methods, based on the analysis of time series extracted from the video sequences. An ROI is marked inside the recorded frame and the related time signal is extracted by applying Eq. (2.5). Subsequently, a one-dimensional PPG plethysmogram is received. This allows the utilization of existing algorithms from skin-contact PPG for the PPGI time series. In this way, parameters such as heart rate (HR), heart rate variability (HRV), RR (respiratory rate), RRV (respiratory rate variability), perfusion index, and  $SpO_2$  can be evaluated. Depending on the application, the signals can be presented and analyzed in one of the following domains:

- the time domain,
- the frequency domain, or
- a mixed time–frequency domain.



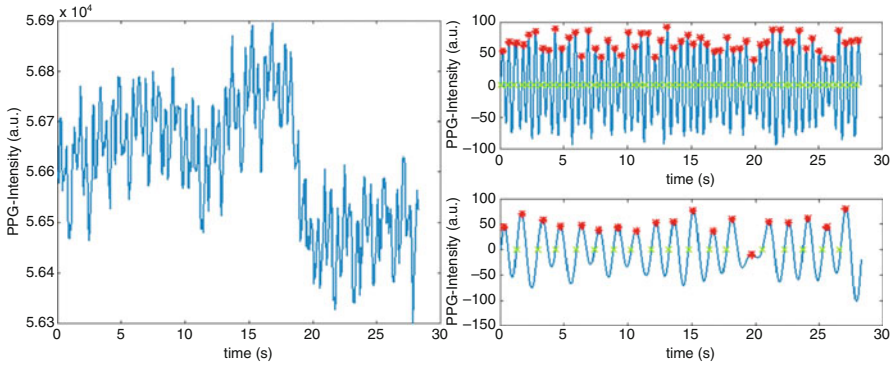


**Fig. 2.6** Raw plethysmogram extracted from PPGI sequence (left); the same signal after bandpass filtering: heartbeat frequency band (top right), respiration band (bottom right) [26]

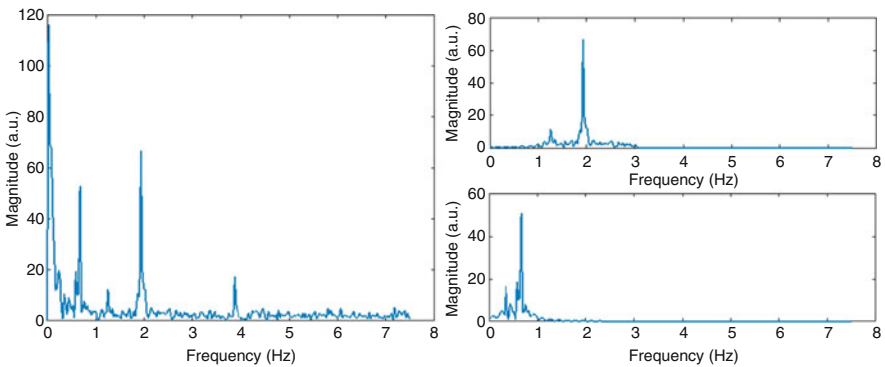


**Fig. 2.7** Transfer of the PPGI time series in the frequency domain (offset removed) (left); corresponding bandpass filtered signal (right) [26]

Visual analysis of a raw PPGI plethysmogram enables recognition of the basic waveform of a PPG heartbeat signal (Fig. 2.6, left). Digital filters can be applied to improve the detectability (also for automated recognition). In Fig. 2.6 (top right), a Butterworth bandpass filter with cutoff frequencies at 0.8 and 3.5 Hz is applied to the raw signal. Zero-crossings (from negative to positive, green) are marked, as well as local maxima (red), both of which correspond to single heartbeats: continuous fluctuations of the distances between neighboring peaks are generally caused by heartbeat variability. The same can be achieved for the respiration rhythm, by adapting the cutoff frequencies of the bandpass filter (Fig. 2.6, bottom right).

Alternatively, the signal can be analyzed in the frequency domain. In Fig. 2.7, the same signal from Fig. 2.6 is transformed into the frequency domain using the fast Fourier transform. Due to the heartbeat variability, the HR is not always visible as

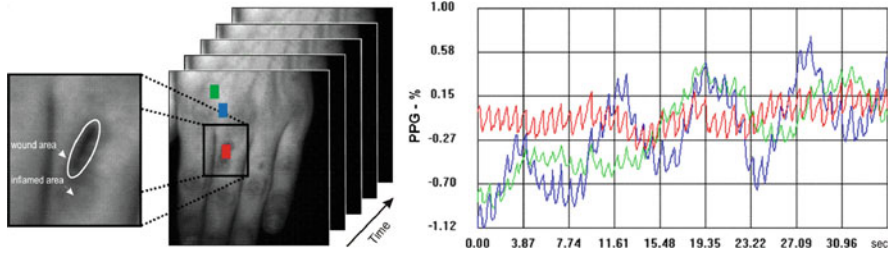


**Fig. 2.8** PPGI recording of a hand with a wound on the middle finger with calculated perfusion signals for selected ROIs, modified from [27]

a single sharp peak but is represented as a widened rise around the intermediate heart beat frequency. The temporal assignment of a current HR is not possible, especially for changing heartbeats. The peak around the heartbeat frequency is not the only one visible in the frequency domain: more peaks are visible just below the heartbeat. These correspond to other central and local oscillators in the human body, in this case the respiration and vasomotor oscillations. Further analysis of the perfusion patterns with the classical Fourier transform does not reveal much new information. Although it may be possible to recognize differences at low frequencies, the resolution is limited because the fast Fourier transform is not well suited for analysis of transient signals. Instead, additional and new insight into the spatiotemporal distribution of perfusion patterns is obtained by applying the wavelet transform.

To illustrate this point, an additional example is given in Fig. 2.8; this presents the recording of a hand with a small wound proximal to the middle finger. Three ROIs are defined and the associated PPG plethysmograms are plotted. Two of the ROIs are positioned on healthy skin, while the third is placed within the wounded area. It can be seen that the perfusion patterns from within the wounded area markedly differ from the healthy ones. Examination of only the perfusion amplitude of the heartbeat from inside the wound reveals that it is slightly increased, despite that the analysis is not restricted solely to heartbeat-correlated patterns.

Adjustment of the cutoff frequencies of the applied bandpass filter enables to assess other frequency components, such as vasomotor rhythm (which is around 0.1 Hz). When so doing, it becomes evident that these lower-frequency components (associated with the 0.1-Hz rhythm) differ considerably for different ROIs: inside the wound, they are almost nonapparent. Distinct differences are visible, even in the ROIs of healthy tissues that are close to each other, indicating the presence of a strong local variability of the 0.1 Hz rhythm. This becomes even more obvious when the signals are transformed into a time–frequency domain by wavelet transformation (Fig. 2.9).

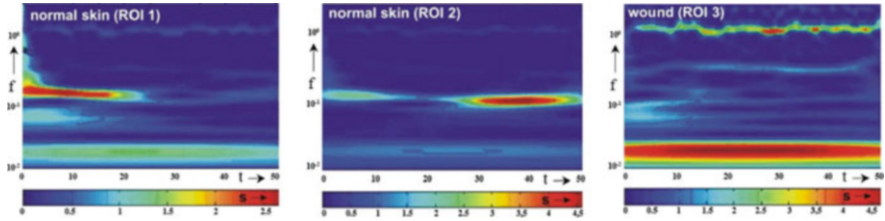


**Fig. 2.9** Typical example of the advanced analysis of transient perfusion signals: Wavelet transformation of selected signals from Fig. 2.7. The frequency components at 0.1 Hz are best visible in measurements on normal skin, although their characteristics are time dependent. Inside of wounds heartbeat frequency (approx. 75 bpm; slightly above 1 Hz) becomes the dominant oscillation, modified from [27]

### 2.2.2 Advanced Signal Analysis, Space-Resolved Mapping, and Visualization of Skin Perfusion

During analysis of single and handpicked ROIs, it is often assumed either that the extracted vital parameters are valid for the recorded PPGI sequences in totality or that a measurement with spatial resolution is unnecessary and therefore not worth calculating. This might be true for vital parameters, like HR, where (due to the role of the heart as central oscillator) the detected HR is not dependent on the measurement spot, as long as every pixel of the chosen ROI shows parts of the same subject. However, in contrast to the heart beat, other vital parameters (e.g., blood perfusion or local thermoregulation) exhibit the property of spatial distribution and, therefore, a single ROI is continuously moved along the image and, for every position, the appropriate PPG signal (associated with the respective vital parameter) is extracted and analyzed. These parameters are subsequently assigned to the position of the ROI, thus creating a functional mapping. This two-dimensional map represents the image plane of the PPGI frame, with the option to include the time dimension if the analyzed parameters change over time. Although additional dimensions are also possible, for single snapshots of vital parameters (e.g., skin perfusion) the resulting maps are usually three-dimensional ( $x$ ,  $y$ , and time  $t$ ).

An example of functional mapping is shown in Fig. 2.10. First, the PPG time signal  $s(t)$  is (pixel per pixel) filtered by a 4th-order elliptic bandpass with cutoff perfusion rhythms of 0.6 and 2.5 Hz. From the resulting filtered signal, the mean perfusion amplitude is calculated as the total variation, and defined as:

$$v = \sum |I(t) - I(t - 1)|. \quad (2.6)$$

The resulting parameter  $v$  (with arbitrary units) is directly proportional to the time amplitude of the arterial blood volume pulse at the given pixel. An algorithm implemented in PPGI software can now place an ROI of specified size on one edge of the image sequence and then scan the whole region. For each position,

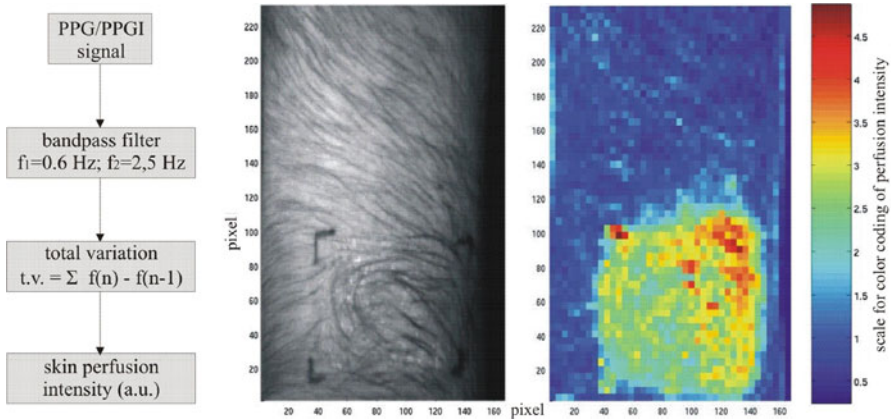


**Fig. 2.10** Demonstration of our advanced PPGI algorithm for automatic multidimensional signal post-processing to visualize the distributed dermal perfusion status functionally. Shown is one image from the PPGI video sequence (middle, the marked skin region was treated with Finalgon® Crème, a vasoactive liniment) and final PPGI perfusion map (right). Spatial resolution (analyzed pixel size) in this case is  $0.35 \times 0.35$  mm

the mean value of the PPGI perfusion signal is obtained, the functional parameter is calculated, and the pixel/pixels belonging to the actual ROI are then colored based on a specified multidimensional color map (Fig. 2.10, PPGI perfusion map). In the study shown in Fig. 2.10, the perfusion effect of treatment of the lower arm with vasoactive liniment was monitored. The resulting functional image no longer depends on morphological information, but solely on the distributed perfusion status in the selected skin area.

### 2.2.2.1 Additional Analysis of Morphologic Features

In addition to analysis of the temporal development of pixels or ROI intensities, the spatial picture content can be analyzed directly. For this, morphologic features can be extracted from a single frame or sequence of PPGI frames, thereby providing additional information about the recorded sequence or the monitored subject, which can be used for the following:

- segmentation of image content (e.g., distinguishing between background and foreground, or recognition of body parts),
- recognition of body posture,
- detection of gestures, or
- detection of facial expressions.

Depending on the specific application, several methods of digital image processing are available [28–31]. (Note: the individual algorithms are not discussed in detail here).

## 2.3 Detection and Compensation of Movement Artifacts in the PPGI Plethysmogram

Successful detection of human vital parameters is only possible if the algorithms can detect and correct arbitrary movements between the measured area and the camera sensors. Due to the remote sensing concept of the PPGI, movements cannot be completely avoided; this is in contrast to (adhesive) skin-contact sensors which always receive body signals from the tissue directly below them. In the PPGI camera setup, the pixel sensors can be assigned to different skin regions if the measured object is moving relative to the camera. As a result, changes of detected brightness are not only caused by tissue properties but also by varying levels of brightness of different skin surfaces which are recorded at the same pixel over time. Depending on the measurement site and the type and amplitude of motion, such movement artifacts can sometimes completely mask the vital signals in the recorded data.

Consequently, the optimum approach for PPGI recordings is to prevent movement artifacts at the very start. This particularly applies for recordings under laboratory conditions, in which case the object under study should be fixed, or at least positioned appropriately. Since the use of fixation imposes considerable constraints on possible applications, movement maneuvers should be detected and overcome by means of digital imaging and/or video processing.

If the aim is to extract vital parameters from a short sequence, it is advisable to record for a period longer than the minimum required duration, and then select and analyze the sections containing the least/smallest artifacts. A quick method for the assessment of artifacts is described below. The underlying principle is to conduct continuous monitoring by employing movement tracking and compensation methods. Various algorithms are available for a wide range of applications; these (together with a selection of different principles) are discussed below.

### 2.3.1 Initial Assessment of Movement Events

The first step in the analysis of PPGI sequences is to determine whether movement artifacts occur and, if so, both where and when. This is the basis for identification of the spatial and temporal sections within the recordings that are best suited for further analysis.

For this purpose, the actual disturbance produced by the artifact itself can be used. Different positions assigned to the measured object, with varying levels of brightness applied to the same pixel over a specific period of time, produce strong fluctuations in pixel intensity. With this in mind, a rapid approach that is being analyzed based on a threshold method, which considers changes in consecutive images  $I_{t-1}$  and  $I_t$ , pixel by pixel:

$$I_D(x, y) = \frac{\sum_{t=1}^l |I_t(x, y) - I_{t-1}(x, y)|}{t_l - t_0}. \quad (2.7)$$

In Eq. (2.7),  $t_0$  and  $t_l$  represent the initial and final time of measurement, respectively. Entries of  $I_D$  exceeding a prescribed threshold indicate the motion artifacts. Subsequently, assessment of the temporal boundaries of motion artifacts can be made by performing a summation along the spatial axes instead of the temporal axes:

$$I_D(t) = \frac{\sum_{x,y} |I_t(x, y) - I_{t-1}(x, y)|}{m \cdot n}. \quad (2.8)$$

In the above expression,  $m$  and  $n$  correspond to the spatial resolution of the image frame. The level of the threshold is defined by the application and generally varies between different measurements. Among other factors, it is dependent on the filling ratio between the image foreground and background, the scene illumination, the background noise of the camera chip, the dynamic range of the camera, the character of the obtained vital signs, and the artifacts.

### 2.3.2 Motion Tracking and Compensation Algorithms

Various motion compensation algorithms are available that suit different applications of the PPGI system. Some of the most important and commonly utilized motion compensation algorithms are described below.

#### 2.3.2.1 Block Matching Method

The block matching method is based on continuous iterated comparison of image regions. The initial image (usually the first frame of a PPGI video sequence) is divided into smaller equal-sized square blocks so that all ROIs either correspond directly to one block or are contained in at least one block. To determine the movement of an object in consecutive frames, the displacement vector of each block is determined. In order to minimize the computing effort, the search area is limited to predefined boundaries around the initial position. A matching criterion (e.g., mean squared or absolute difference of pixel values between the new and reference position) is applied for any position within these boundaries. The maximum similarity of the reference and shifted block is determined by minimizing the error of the matching criterion; then, the respective values for an established position give the displacement vector from the origin [32, 33].

A reasonable selection of the block size, as well as the search area, is essential for the tracking of objects. To summarize: it can be stated that the block matching algorithm is particularly suited for compensation of small translated movements. The computing capacity required increases rapidly with enlargement of the search area and the matching accuracy (subdivision up to pixel or even interpolated subpixel level). A major disadvantage of the block matching method is the recovery

of scaling, and that (partly) covering or rotation/deformation of the tracked object are barely supported. The currently available variants of the algorithm aim to minimize the required number of mathematical steps, and/ or to improve matching of the results [34, 35].

### 2.3.2.2 Optical Flow Method

The optical flow method is an algorithm that is easy to implement. It detects movements of objects by analyzing the displacement of brightness information in the image plane of two consecutive frames. A vector field is calculated, representing individual displacements for each pixel. This vector field is often directly addressed as the optical flow and several approaches are available to quantify it [36, 37].

Estimation of the optical flow is achieved by the spatial and temporal derivation of the pixel intensity in the observed image region. It is assumed that the pixel intensity  $g$  is a function of only image coordinates  $x$  and  $y$  and time  $t$ :

$$g(t) = f(x(t), y(t), t). \quad (2.9)$$

For the optical flow method, it is required that the local brightness of an object does not alter during movements. To fulfill this requirement, the scene of the measurement scenario must be illuminated homogeneously, so that tracked objects do not possess location-dependent brightness values. Assuming only translational movements of the monitored object within the image plane, the temporal change of a tracked picture element equals zero:

$$\frac{dg(t)}{dt} = 0. \quad (2.10)$$

Together with Eq. (2.9), it follows that:

$$\frac{df}{dx} \frac{dx}{dt} + \frac{df}{dy} \frac{dy}{dt} + \frac{df}{dt} = (\nabla f)^T \cdot \vec{v} + \frac{df}{dt} = 0, \quad (2.11)$$

in which  $\vec{v}$  corresponds to the displacement vector of the optical flow. In general,  $\vec{v}$  can be estimated directly from Eq. (2.11) but, as in the block matching method, aperture problems can occur which can lead to ambiguities and inaccuracies in the calculated vector field.

Ambiguities of Eq. (2.11) can be mitigated by introducing global and local methods: the former assumes a dependency of displacement vectors of any pixel and aims to obtain optimum smoothness of distribution in the resulting vector field [38]. It follows that the deduced minimization problem must be solved:

$$\iint \left( (\nabla f)^T \cdot \vec{v} + \frac{df}{dt} \right)^2 + \tau^2 \left( \left\| \nabla \frac{dx}{dt} \right\|^2 + \left\| \nabla \frac{dy}{dt} \right\|^2 \right) dx dy \rightarrow \min. \quad (2.12)$$

The second summand (weighted by  $\tau$ ) in Eq. (2.12) satisfies the requirement for smoothness of distribution. However, because solving this equation can be time consuming, an alternative local approach can be adopted. By ascertaining the surface integral in a small neighborhood around the considered pixel, a speedup can be achieved. Furthermore, the density of entries in the displacement vector field is reduced according to the size of the chosen neighborhood.

This restriction is an accepted norm for PPGI motion tracking. During most of the measurement, specific, connecting body regions are monitored. Further, it can be assumed that neighboring positions on the skin exhibit almost identical motion vectors which can be fused to one displacement vector of the local optical flow algorithm.

Summarizing, the optical flow method is suitable for the detection and tracking of translational movements and rotations along the camera axis. Nevertheless, the ability to detect scaling, temporal (partial) covering, rotations around the axis in the image plane as well as deformations of the observed object is limited. Since local displacement vectors can be directly read from the calculated vector field, the optical flow method is particularly appropriate when aiming to track multiple ROIs. Individual motion tracking of each separate ROI is not necessary.

### 2.3.2.3 Kanade–Lucas–Tomasi Feature Tracker

The Kanade–Lucas–Tomasi (KLT) feature tracker (named after its inventors) is an algorithm to detect and track suitable features inside video sequences. It is based on the fact that only the best-suited feature correspondences are tracked by the algorithm [39, 40].

The KLT tracker aims to minimize the squared error  $e$  of the differences between two images  $I_t$  and  $I_{t+1}$  in the neighborhood  $N$  of a pixel  $\mathbf{x}_0 = (x_0, y_0)$ :

$$e = \iint_N (I_t(\mathbf{x} + v) - I_{t+1}(\mathbf{x}))^2 \omega(x) \, d\mathbf{x}. \quad (2.13)$$

$v$  corresponds to the displacement vector between two images. This quantity is assumed to be constant in  $N$ . Optionally, single pixels in  $N$  can be weighted by their position with  $\omega(x)$ . The linear part of the Taylor Series offers a solution for this minimizing problem:

$$\frac{\partial e}{\partial v} = 2 \iint_N \left( I_t(\mathbf{x}) - I_{t+1}(\mathbf{x}) + g(\mathbf{x})^T v \right) g(\mathbf{x}) w(\mathbf{x}) \, d\mathbf{x} = 0, \quad (2.14)$$

with  $g = \left[ \frac{\partial}{\partial x} I_t, \frac{\partial}{\partial y} I_t \right]^T$ .

This can be transformed into the two-dimensional linear system:

$$Gv = \mathbf{e}, \quad (2.15)$$

with  $G = \iint_N g g^T w(\mathbf{x}) \, d\mathbf{x}$  and  $\mathbf{e} = \iint_N (I_t - I_{t+1}) g w(\mathbf{x}) \, d\mathbf{x}$ .



The tracking of features necessitates the solving of Eq.(2.15). This can be achieved by the inverted matrix  $G^{-1}$ . In this process, the required features can be recognized as they produce large eigenvectors of  $G^{-1}$ . A common approach to find such satisfactory feature points is to utilize the Viola Jones algorithm based on a cascaded classifier, Adaboost Training Algorithm of a Haar feature selection [41].

In addition to the KLT tracker, the Scale-Invariant Feature Transform (SIFT) and the Speeded-Up Robust Features (SURF) algorithms are other examples of feature-based tracking algorithms (but are not described here).

#### 2.3.2.4 Additional Tracking Algorithms

Besides the tracking algorithms mentioned above, a wide range of other approaches can be applied to eliminate movement from video sequences, while tracking objects along their trajectory through the image plane. Although they are not (yet) implemented for specific PPGI applications, the individual approaches are promising to improve the technique of tracking objects [42–48].

## 2.4 Selected PPGI Results and Applications

### 2.4.1 Proof of Concept Studies

#### 2.4.1.1 Skin Perfusion Changes After Mechanical Irritation

A first clinically relevant application of the PPGI technology is the mapping of microcirculation. In contrast to the classical dermographometric examination [49], quantitative diagnostics become possible with PPGI. Figure 2.11 shows the PPGI perfusion map of a part of the forearm taken about 2 min after mechanical irritation along the arm axis. After this heavy force irritation (made with the nail-side of the right-hand thumb), the heartbeat (HB) synchronous perfusion in the stressed skin area increased (physiological reaction) for a limited period of time. In this case, the mean increasing factor amounts to 2.2 when comparing the color-coded intensity value in ROI No. 2 with that in the control area (ROI No. 1, normal skin perfusion).

#### 2.4.1.2 Highly Distributed Skin Perfusion in Melanoma

Figure 2.12 shows a highly distributed, HB-related perfusion intensity in the area of malignant skin tumor on the heel. The microcirculation status of skin tumors in vivo can be visualized with state-of-the-art noninvasive imaging methods (dermoscopy, and capillaroscopy) and with laser Doppler fluxmetry (LDF). With laser Doppler perfusion imaging (LDPI), the distributed perfusion status can be quantified, but not in all tumor areas at the same time [51, 52]. However, this is possible when

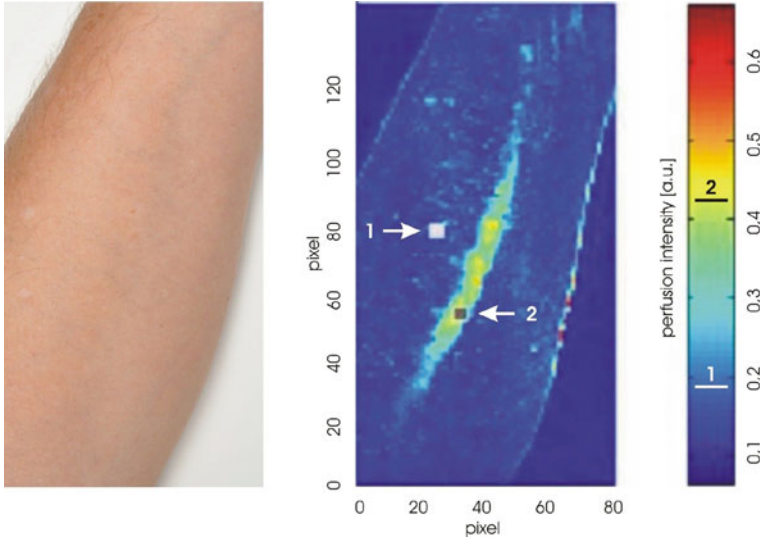


**Fig. 2.11** Quantitative dermatographic skin perfusion examination on the volar side of the lower-left arm, quantified by photoplethysmography imaging. The virtual PPGI perfusion map, calculated about 120 s after mechanical skin irritation in the long arm axis, documents the physiological skin perfusion reaction (increased perfusion) [50]



**Fig. 2.12** Blood perfusion study in the melanoma area and surrounding skin on the heel: Digital photography (a), one black–white PPG image snapshot (b), and the final PPGI perfusion map (c). The heartbeat-related, distributed hot spots in the color-coded perfusion map show significantly higher amplitudes of the local arterial blood volume pulse in some tumor areas [50]

using the novel PPGI device. In the present study, to illuminate deeper skin layers, LED near-IR light with wavelengths about 940 nm was used. As shown in the PPGI perfusion map (Fig. 2.12c), higher amplitudes of the local arterial blood volume (hot spots) can be found in the tumor perfusion. Although Jünger et al. [53] also reported on increased perfusion in tumor areas, their study investigated only the geometric center of the tumor. However, our preliminary results indicate that a spatially resolved PPGI quantification of tumor perfusions can be successfully performed in the future and might provide diagnostically relevant information.

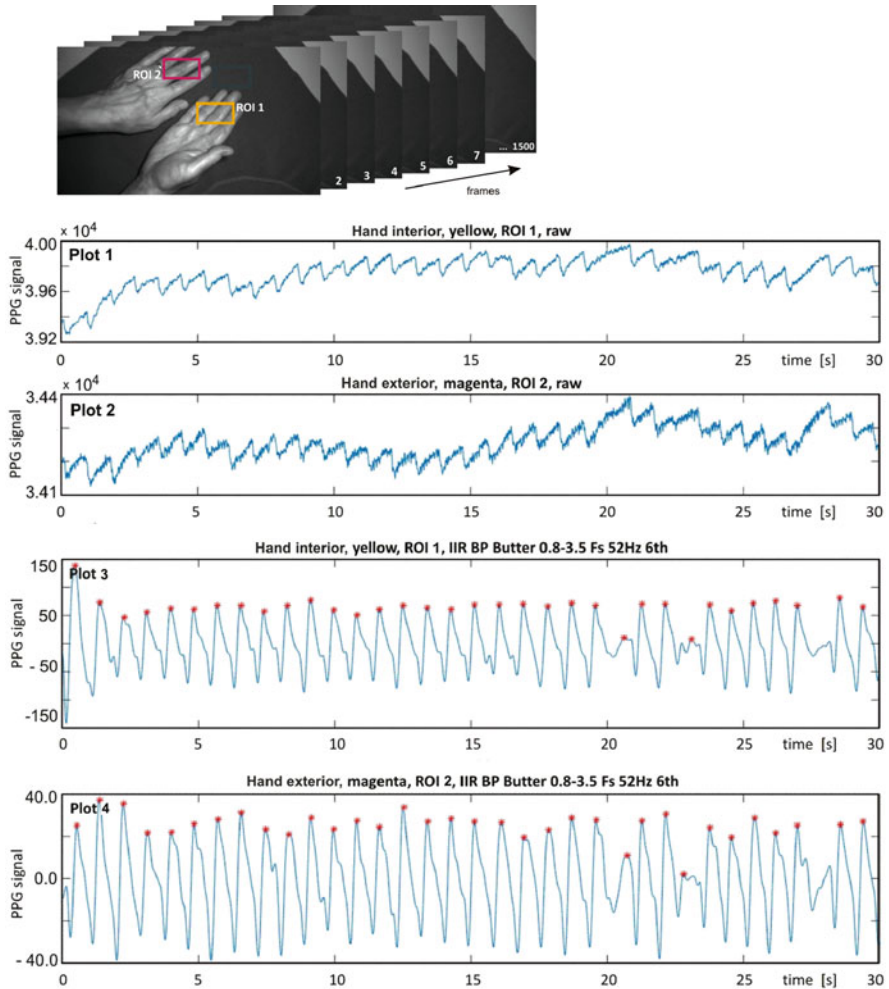


**Fig. 2.13** Bilateral skin perfusion analysis. ROI indicates the analyzed skin regions. Typical PPGI time series measured in both ROIs on the outside of the left hand and the inner side of the opposite hand in a 69-year-old patient with impaired cardiac perfusion and arrhythmia. Plots 1 and 2: raw signals. Plots 3 and 4: filtered PPGI signals that allow the robust detection of heart rate and heart rate variability, modified from [54]

### 2.4.1.3 Comparison of Bilateral Heartbeat-Related Skin Perfusion Amplitude

Figure 2.13 presents an example of bilateral PPGI registrations on the left (ROI 1) and right hand (ROI 2) of a 69-year-old patient with arrhythmia. The whole video stream had a length of 1500 images, which corresponds to a period of 30 s at 50 fps. Comparison of the HB-related pulse amplitudes (plots 4 and 5) shows that these amplitudes are more than two times higher on the right hand than on the left hand.

At this point, it should be noted that PPGI allows contactless, robust detection of HR and HRV [53]. The accuracy is comparable to ECG if the PPG frame rate is higher than 50 fps. In PPG and PPGI, the local maximum in the filtered transient signal (see \* in plots 4 and 5) is suitable for such analysis, while in the electrocardiogram the R-peak is used. On the other hand, extra systoles, arrhythmic episodes (in the presented example: 3 in 30 s), or measurement artifacts (mainly produced by position changes) can lead to misinterpretation. In our study, we compared the consecutive beat-to-beat intervals, measured with ECG as a gold standard and with reflective in-ear PPG on healthy subjects in steady state. The correlation coefficient between detected beat pairs between 48.4 and 116.4 bpm was 0.9987, the sum of the squared errors for all compared heartbeats ( $n = 16,813$ ) was 1.2 bpm [54, 55].

#### 2.4.1.4 Multiwavelength Illumination PPGI Study: Towards Remote SpO<sub>2</sub>

Using multiwavelength illumination with a PPGI setup, spatially resolved skin oxygen saturation can be monitored by applying the classical photoplethysmographic pulse oximetry method. This was first described by Takuo Aoyagi in 1972 [56].

Preliminary validation of the PPGI setup was performed under laboratory conditions with 13 healthy volunteers. For this, their hands and lower arms were positioned in an arm rest at a distance of 20–30 cm from the front of the camera. To ensure valid SpO<sub>2</sub> evaluation, the signal quality of the PPG time series extracted from the PPGI video sequence had to be adequate. In particular, the arterial blood volume pulse signal portion must be clearly separable from the remaining signal on both working wavelengths, because the downstream algorithms are based on estimation of the AC/DC values and  $R$ -values. For illumination, a combination of red (630 nm) and IR (905 nm) light was used in time-multiplex mode. For each subject, a video sequence of about 30-s duration was recorded [57–59]. In the present study, a minimum of 20 fps and at least 600 PPG images were recorded and analyzed for each sequence. For reference, oxygenation was monitored by means of a commercial finger clip pulse oximeter (Choice Medical MD300C22). For all volunteers and all measurements, oxygenation was above 95% (mean 98%). For further analysis, PPG signals were extracted from each small sliding ROI (a square with 6 pixels per side length) from the whole image frame. Based on the classical skin-attached pulse oximetry procedure, the related  $R$ -value was calculated, describing the ratio between the absorbance  $A$  of hemoglobin at two different wavelengths:

$$R = \frac{A_{\lambda_1}}{A_{\lambda_2}} = \frac{-\ln\left(\frac{I_{\text{Sys},\lambda_1}}{I_{\text{Dias},\lambda_1}}\right)}{-\ln\left(\frac{I_{\text{Sys},\lambda_2}}{I_{\text{Dias},\lambda_2}}\right)} \approx \frac{I_{\text{AC},\lambda_1}}{I_{\text{DC},\lambda_1}} \frac{I_{\text{AC},\lambda_2}}{I_{\text{DC},\lambda_2}} \quad (2.16)$$

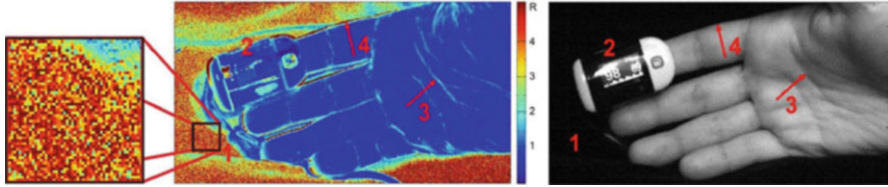


**Fig. 2.14** Left: representative color-coded functional image of calculated  $R$ -values on the inside of the right hand. Noise artifacts are visible in the background (1), reflection artifacts on the reference pulse oximeter (2), and motion artifacts at high-contrast image corners (3 & 4). Right: black and white image as reference (first frame from the PPGI sequence). Modified from [59]

$A$  can be calculated directly from the PPGI measurements and is dependent on the measured peripheral blood volume pulse amplitude (PPG signal changes during systole and diastole), measured separately with two different wavelengths. Assuming that the heartbeat-related PPG signal component ( $AC$ ) is significantly smaller than its mean intensity ( $DC$ ),  $R$  can be simplified to the ratios of  $AC$  to  $DC$  of the two wavelengths. Finally, the local  $R$ -values are composed in an arterial oxygen saturation image. Figure 2.14 is a representative example of the novel functional mapping of  $R$ -values (automatic operation mode) for red and IR illumination. As expected for healthy subjects, homogenous coloring of practically all hand skin areas is visible, representing the same level of arterial blood oxygen saturation (mean  $R$ -value was 0.54 with standard deviation 0.050; mean  $SpO_2$  was 97.85% with SD 1.14%).

#### 2.4.2 *First Clinical Trial: Allergic Skin Reactions Quantified by PPGI*

The results of a typical skin allergy test can vary depending on the experience/skill of the expert interpreting the test data. A novel method of extracting relevant test parameters through the computer-based imaging technique described here allows a result to be independent of interpretation and offers a reliable method of skin allergy testing. The method differentiates between allergy-affected skin and normal skin. A functional image is constructed using the blood perfusion signals obtained prior to application of the irritant, and signals obtained at predetermined time intervals after application of the irritant. The functional images obtained with the PPGI are time and space resolved simultaneously and, hence, superior to images obtained using the scanned laser Doppler imaging (LDI) technique. The experimental results obtained from clinical trials confirm that this method is suitable to be considered as a standard method for skin allergy testing.

**Table 2.1** Characteristics of the study population

Group: no. of subjects	Male/Female	Age (years)	Weight (kg)	Height (cm)	Body mass index ( $\text{kg}^2 \text{m}^{-1}$ )
$N_1 : n = 5$	2/3	$43.0 \pm 17.0$	$75.6 \pm 20.6$	$173.6 \pm 9.6$	$24.7 \pm 4.6$
$N_2 : n = 27$	15/13	$42.9 \pm 14.2$	$72.1 \pm 18.4$	$174.7 \pm 10.2$	$23.9 \pm 4.2$
$N_3 : n = 11$	7/5	$38.6 \pm 12.3$	$73.9 \pm 19.7$	$173.6 \pm 9.6$	$24.0 \pm 4.3$

Data are mean $\pm$ SD

Since the self-experiments by Blackley [60] in 1856, the hypersensitivity of allergic diseases has been evaluated using the skin prick test (SPT) and the intradermal test (IDT) [49, 60–63]; both tests are usually performed at the flexor side of the forearm. The reaction is read after 15–20 min. Skin tests are regarded positive when the mean wheal diameter is  $\geq 3$  mm on the SPT and  $\geq 5$  mm on the IDT.

For routine clinical diagnostic work, it is not necessary to quantify reactions to the SPT, as this is mainly used as a screening method for allergen sensitization. However, for research purposes, more precise evaluation of the results of an SPT is valuable [63]. These tests are generally considered to be the most convenient, least expensive, and most specific screening methods to detect the presence of IgE antibodies in patients with appropriate exposure histories. In these tests, histamine (an important mediator in allergic diseases) increases blood flow and microvascular permeability through cutaneous reactions, resulting in measurable wheal and flare responses. However, because assessment of the extent of local skin reaction (erythema and wheal diameters) is through semiquantitative measurements, the results of a test can vary between individual experts. Automatic assessment of the vasoactive effects of drugs in vivo through quantification of microvascular changes in skin perfusion using various measuring techniques (e.g., PPG, scanning LDI, dermal microdialysis sampling in vivo, IR thermography imaging, etc.) are associated with some underlying limitations. Although the use of scanning LDI for assessment of allergic skin reactions is clinically reliable [50, 64, 65], the major disadvantage of this method is that the image is captured point-by-point by scanning and, thus, each pixel is acquired at different points in time, resulting in an image of the skin that is not time correlated. Therefore, the scanning LDI method is not suitable for evaluating spatial and temporal variations simultaneously and is unable to assess time and space-resolved tissue perfusion simultaneously. Demographic data of the healthy volunteers (not using any medications) included in our study are presented in Table 2.1.

The study “Funktionelle Quantifizierung der Hautdurchblutung bei Testung von Soforttyp-Allergien - orts aufgelöste Erfassung der dermalen Perfusion mit Hilfe des PPGI-Verfahrens” (functional quantification of skin perfusion during immediate hypersensitivity reactions—spatially resolved assessment of dermal perfusion using

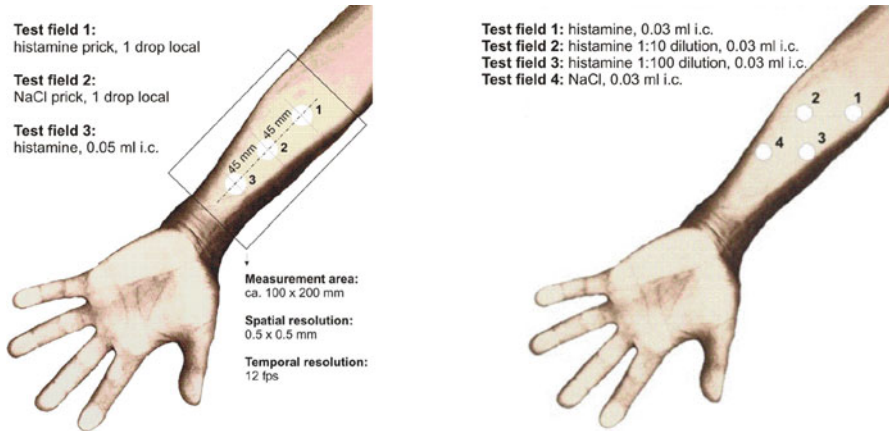


**Fig. 2.15** Left—prick and intradermal test for allergy diagnostics: schematic design of the assessed skin region. All examinations in our PPGI study were taken on the volar side of the forearm in horizontal body position. Right: schematic of the intradermal test sites (four assessed skin regions) examined in the second and third parts of the study

PPGI) was performed in the University hospital Aachen from 2007 to 2009 (EK186/06) and consisted of three parts. In the first part, PPGI examination was performed before and 5 min after skin testing (SPT and IDT) in five healthy volunteers ( $N_1$ ,  $n = 5$ ) to test the PPGI device. Figure 2.15 (left) shows a schematic design and the proposed measuring geometry of the quantitatively assessed skin region (volar side of the forearm).

Both positive (histamine) and negative (diluent) control solutions are applied to the skin in a standardized manner (SPT and IDT tests). For each experiment, four PPGI imaging streams of 2-min duration were taken: shortly before application and 5, 10, and 15 min after application. The second part of the study consisted of assessment of histamine-induced vasoactive skin reactions in three different dilutions, performed at the same skin region (Fig. 2.15, right) in 27 subjects ( $N_2$ ,  $n = 27$ ). The third part of the study aimed to show the difference in the histamine-induced skin reaction after 4 days of daily oral administration of 180 mg fexofenadine in 11 subjects ( $N_3$ ,  $n = 11$ ;  $N_3 \subseteq N_2$ ) from the  $N_2$  group.

#### 2.4.2.1 Data Acquisition and Signal Analysis

Data obtained from the PPGI camera were analyzed offline using the PPGI software. Each PPGI video lasts about 120 s, consists of nearly 1000 images (8 fps) of the same scenario, and has a mean data volume of 700 MB. After each video sequence signal, one or more arbitrary ROIs in the test fields were selected by the



examiner in the interactive operator system mode. For these marked regions, the mean backscattered light intensity was then calculated and the resulting functional PPGI images that portray perfusion sensitive parameter were displayed over time.

For the arrangement chosen (distance between the PPGI camera and the hand) for the contactless assessment of blood perfusion dynamics, the resulting resolution equaled  $0.5 \times 0.5$  mm (each pixel in the image represents an area of  $0.25 \text{ mm}^2$  of the skin). The processing algorithm grouped 144 pixels at every pixel position and computed the mean value of the PPGI perfusion signal to create a specified multidimensional color-coded perfusion map. From this map, perfusion intensity variations before and after test application as well as statistical analysis (mean  $\pm$  standard deviation,  $t$ -test and  $p$ -value) of the final parameters were performed with MATLAB.

#### 2.4.2.2 Results

Apart from establishing the proposed PPGI-based technique for skin allergy testing, the aim of the present study was to compare two well-established methods of skin allergy testing (i.e., the SPT and the IDT) to examine to what extent they differ in providing vascular response and, thereby, determine (i.e., proof of concept) the feasibility of the PPGI technique as an assessment method for allergy testing.

For all five healthy subjects tested, three test sites (TF1, TF2, and TF3) were marked with a demarcation distance of 4.5 cm on the volar side of the forearm (Fig. 2.15, left). The IDT with 0.05 ml histamine solution was administered in the site near the palm (TF1), SPT with histamine solution was applied to the site TF3, and the negative control (sodium chloride) SPT was performed in the middle site TF2.

PPGI measurements were taken just prior to application and 5 min after application. Figure 2.16 shows the results at  $t = t_0 + 5$  minutes.

The standard skin region image (color) in a 29-year-old healthy control subject is shown in Fig. 2.16a. Figure 2.16b shows a PPGI image from the gray-level image stream obtained with the monochrome PPGI camera. In both images, both erythema and wheal response can be observed. Figure 2.16c depicts the resulting perfusion map. Figure 2.16d–f shows the PPG extracted from the three selected regions (close to the application points) of interest (red indicates TF 1, green TF 2, and blue indicates TF 3). It can be seen that the time response of the measured perfusion dynamics shows significant increase in the normalized mean perfusion intensity (amplitude of the heartbeat synchronal perfusion averaged over the selected ROI and normalized to the perfusion in the same area obtained prior to application of the irritant). Also, in the histamine areas compared to the NaCl prick area taken as 100% perfusion intensity, significantly higher perfusion values were found (+70% in TF 1, +150% in TF 3;  $p < 0.001$ ).



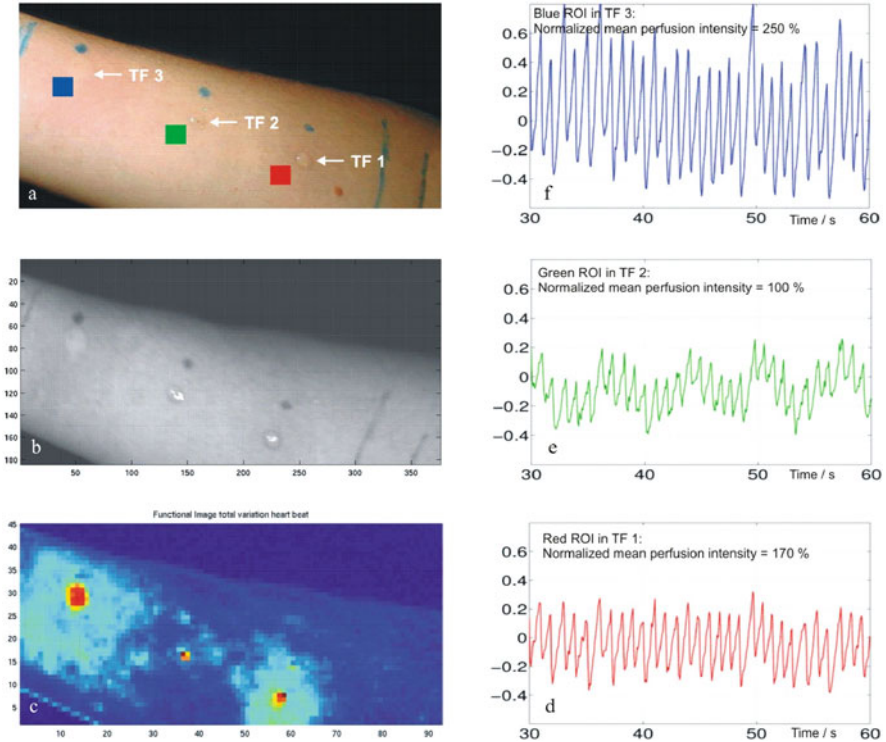


**Fig. 2.16** Results of the functional prick and intradermal test. (a) Digital photography, (b) one black–white PPG image snapshot, and (c) final PPGI perfusion map of the same measuring forearm area of healthy control subject. Calculated perfusion time series in the selected test sites: (d) TF 1, (e) TF 2, and (f) TF 3. Note: all three ROIs with the same size (12 pixels by 12 pixels, 6 mm by 6 mm)

### 2.4.2.3 Vascular Response Assessed by the PPGI Method

Based on the results of the proof-of-concept study, 27 healthy subjects were tested with intradermal histamine. Region 1 was administered with sodium chloride, whereas the other three regions were administered with 0.03 ml histamine in dilutions of 1:1, 1:10, and 1:100 (Fig. 2.15, right). A representative result from this test series is shown in Fig. 2.17, measured 10 min after applying the skin test.

As mentioned, the functional perfusion mappings allow to illustrate the dimensions of the vasoactive reactions; they are calculated from the PPGI sequences. Here, an ROI is laid over the whole area. The time signal and its other characteristics are calculated in each spot (location). The temporal development of the distributed perfusion changes is depicted in Fig. 2.18.

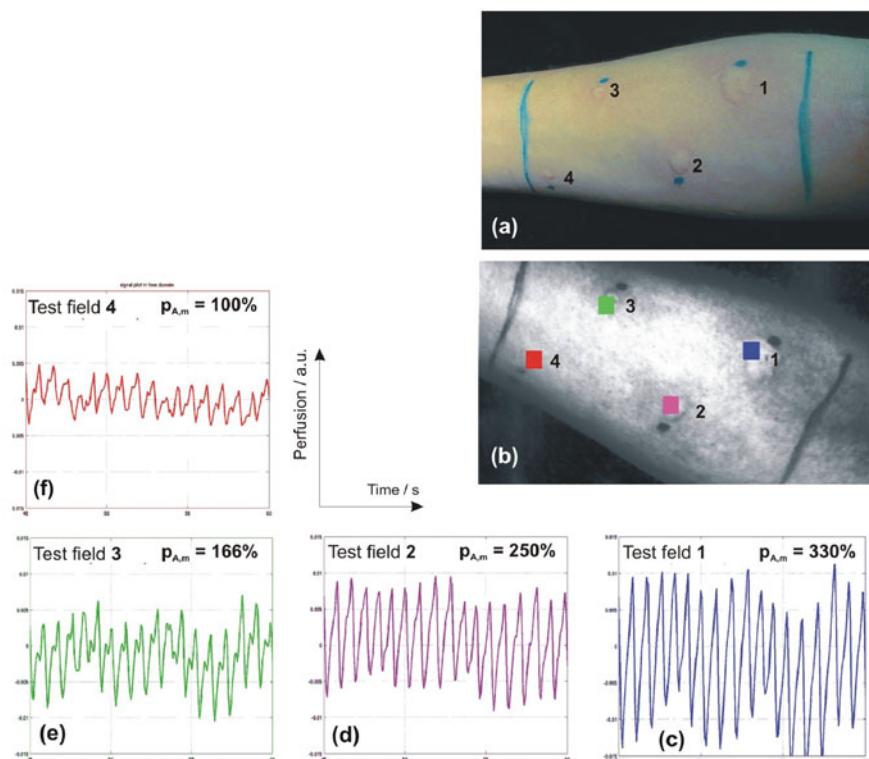


**Fig. 2.17** Microvascular response after histamine intradermal application (graded amounts of histamine). Representative results of one of the test subjects from the N<sub>2</sub> group. (a) Photograph of the tested skin area (top right), (b) an image from the PPGI sequence with the positioned ROIs (c)–(f) calculated time-dependent perfusion in the four ROIs at time  $t_0$  plus 10 min. In test region 1, for example (30  $\mu$ l, non-diluted histamine i.c.) the mean value of the perfusion attribute pulse amplitude in the ROI 1 increased significantly at 330% ( $p < 0.001$ )

Examination of the results shows that assessment of the histamine-induced skin reaction is possible. All subjects showed an increase of the pulse beat-dependent PPGI perfusion units after histamine provocation, especially within the first 5 min after application. In our study population, the time to attain the maximum value (peak) of the reaction varies; the values are presented in Table 2.2.

In some individuals, the maximum is achieved after 5 min, in others after 10 min and, in one person, after 15 min. However, the initial increase is identical in all subjects. Significant differences in skin reaction were also dependent on histamine concentration; as expected, the strongest reactions were seen with the highest concentrations. In the reference area of the sodium chloride perfusion, reactions were also detected (possibly caused by injection trauma to the skin); however, in all 27 measurements, they were weaker than the reactions due to histamine. The dose-dependent time–response curves in Fig. 2.19 show the overall average for the study participants.

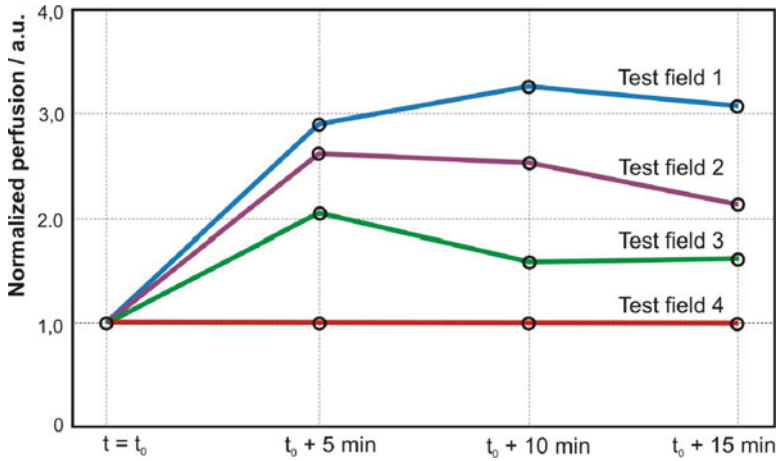


**Fig. 2.18** Calculated time–response curves for the test scenario extracted from Fig. 2.15. The time-dependent perfusion was calculated by taking the values of perfusion in the control skin region (test field 4) as reference. In this case, the maximum allergic reaction in the test field 1 was reached 10 min after the application, in the test fields 2 and 3 after 5 min

**Table 2.2** Normalized growth of the perfusion attribute: pulse amplitude

	Histamine 1:1	Histamine 1:10	Histamine 1:100	NaCl
<i>Mean</i>				
Before injection	1	1	1	1
$t_0 + 5 \text{ min}$	6.6365	5.6589	4.9065	3.0021
$t_0 + 10 \text{ min}$	6.3513	5.9870	4.0486	2.2054
$t_0 + 15 \text{ min}$	5.7549	4.5614	3.3792	1.7902
<i>SD</i>				
Before injection	0	0	0	0
$t_0 + 5 \text{ min}$	3.0611	2.2692	2.4622	1.1805
$t_0 + 10 \text{ min}$	3.5616	2.7336	2.3606	0.8583
$t_0 + 15 \text{ min}$	3.4205	2.5224	2.2132	0.7603

Results of analysis of the three subgroups in the total group  $N_2$  ( $n = 27$ )

Results of additional analysis of the 1:1 histamine measurements for the whole  $N_2$  group are presented in Fig. 2.20. Each box contains the middle 50% of the data. The length of the box corresponds to the difference between the upper and lower quartile (interquartile range, IQR) and is the degree of the scattering of the data. The length of the so-called whisker (interval between the box ends and the upper/lower extreme value) is limited to 1.5 IQR. Values between 1.5 IQR and 3 IQR are considered to be mild outliers (four values in our data set) and values above 3.0 IQR are considered to be extreme outliers (three values in our data set). Finally, the statistical significance of the histamine reaction was calculated using a  $t$ -test for paired samples. The values of the perfusion power were compared before and 5 min

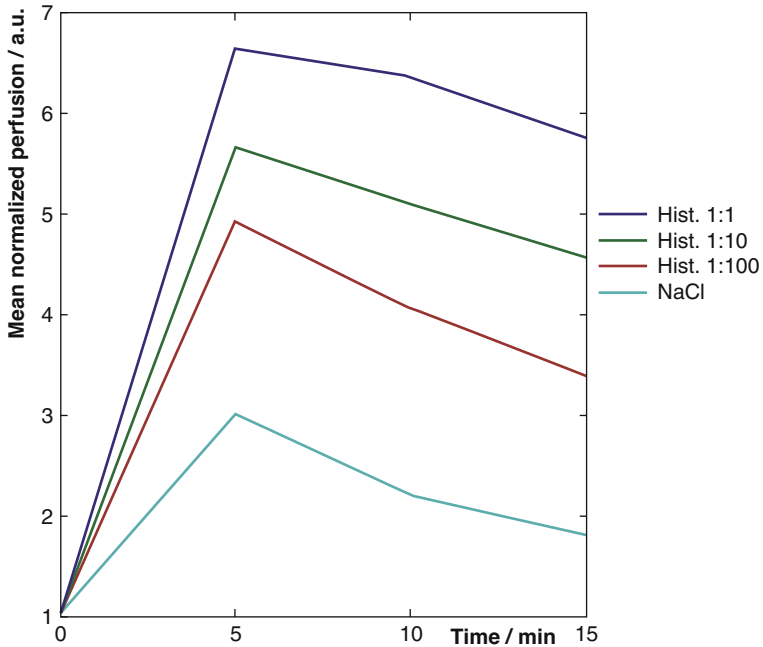


**Fig. 2.19** Calculated time–response curves for the test scenario extracted from Fig. 2.5. The time-dependent perfusion was calculated by taking the values of perfusion in the control skin region (test field 4) as reference. In this case, the maximum allergic reaction in the test field 1 was reached 10 min after the application, in the test fields 2 and 3 after 5 min

**Fig. 2.20** Time–response curves of the measured area treated with histamine 1:1. Entered here are the median boxes with limit value representation. Four mild (represented by open circle) and three extreme outliers (represented by times symbol) were identified

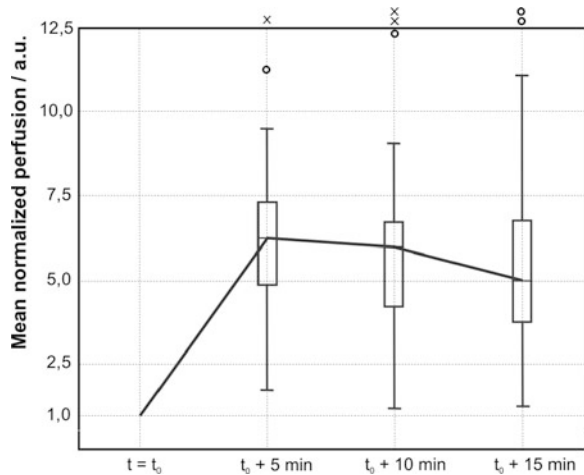
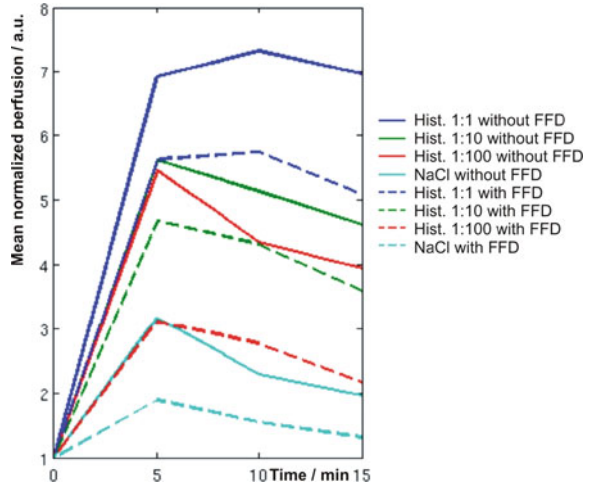


**Fig. 2.21** Time–response curves: the calculated normalized perfusion values over the subgroup  $N_3$  ( $n = 11$ ) before and after fexofenadine (FFD) medication



after application of histamine. The  $t$ -values ranged from 8.09–10.46. Thus, there was a high level of significance in all three histamine test areas compared to sodium chloride ( $p < 0.005$ ).

From the PPGI video streams taken at different times after administration of oral antihistaminic therapy, corresponding time–response curves and additional dose-dependent curves can be calculated with the PPGI software. We found a significant decrease of perfusion after a 3-day administration of fexofenadine. In 11 of the 27 subjects (subgroup  $N_3$  from the  $N_2$  group), 180 mg fexofenadine was administered daily for 3 days. Although our data are not conclusive in showing a reduction in histamine-induced vascular response, a trend in the expected direction is seen. As expected, the average reactions are on the downtrend: see the time–response curves in Fig. 2.21 and the corresponding values before/after fexofenadine medication in Tables 2.3 and 2.4. In 6 of the 11 subjects, the perfusion values were significantly lower in the second measurement (after fexofenadine administration). In three subjects, only slightly lower perfusion values were achieved and in two subjects the perfusion values were higher in the second measurement series. This random behavior can be attributed to many medical causes; for example, nonresponse on different days for different subjects. Significant  $t$ -values (on the relatively small level of  $n = 11$ ) were seen between 1.0553 and 2.9230. Therefore, a probability of between 84.0% and 99.2% can be postulated for the PPGI method to correctly detect antihistamine intake by analyzing perfusion changes.

#### 2.4.2.4 Automatic Determination of Area Affected by Allergic Reaction

Information on the extent of the area affected by allergic reaction of the skin of a patient is essential for deciding the course of optimal treatment. Using an automatic threshold technique on the PPGs extracted, the dynamic skin perfusion scene is

**Table 2.3** Normalized growth of the perfusion attribute: pulse amplitude

	Histamine 1:1	Histamine 1:10	Histamine 1:100	NaCl
<i>Mean</i>				
Before injection	1	1	1	1
$t_0 + 5$ min	7.4139	6.0519	5.5786	3.1769
$t_0 + 10$ min	7.7820	5.5354	4.4919	2.3445
$t_0 + 15$ min	7.3376	5.0172	4.0333	2.0089
<i>SD</i>				
Before injection	0	0	0	0
$t_0 + 5$ min	4.2340	2.4287	2.9509	1.4564
$t_0 + 10$ min	4.7495	2.7519	2.6500	0.9019
$t_0 + 15$ min	4.3840	2.4923	2.6591	0.8273

Results of analysis of the subgroup  $N_3$  ( $n = 11$  subjects from group  $N_2$ ) before taking fexofenadine medication

**Table 2.4** Normalized growth of the assessed perfusion attribute: pulse amplitude

	Histamine 1:1	Histamine 1:10	Histamine 1:100	NaCl
<i>Mean</i>				
Before injection	1	1	1	1
$t_0 + 5$ min	5.5200	4.7365	3.0659	1.8451
$t_0 + 10$ min	5.6021	4.4233	2.6552	1.5048
$t_0 + 15$ min	5.0063	3.6679	2.1272	1.2930
<i>SD</i>				
Before injection	0	0	0	0
$t_0 + 5$ min	2.1100	1.7077	1.3521	0.7516
$t_0 + 10$ min	2.9502	1.9141	1.3492	0.5853
$t_0 + 15$ min	2.8500	1.7562	1.2965	0.4425
<i>t Value</i>				
Before injection	0	0	0	0
$t_0 + 5$ min	1.2439 ( $p_{\min} < 0.12$ )	1.7077	1.3521	0.7516
$t_0 + 10$ min	1.7307	1.9141 ( $p_{\max} < 0.04$ )	1.3492	0.5853
$t_0 + 15$ min	1.6004	1.7562	1.2965	0.4425

Results of analysis of the subgroup  $N_3$  ( $n = 11$  subjects from group  $N_2$ ) after taking fexofenadine medication.  $p_{\min}$  and  $p_{\max}$  are significance levels, which can be accepted as a measurable reduction in allergic perfusion (improvement) occurring after medication

converted into a static binary image that clearly distinguishes the area of skin afflicted by allergic reaction from that of normal skin. The criteria for selecting the threshold to be applied to the PPG signals is obtained after careful analysis of the PPG signals extracted from areas affected by allergic skin reaction and those obtained from normal skin.

To attain the optimal value automatically, the iterative threshold selection algorithms proposed by Ridler et al. [66] and Janus [67] can be utilized. In the present study, the initial threshold value was set to 0.5 times the maximum value of the pixels of the gray-scale image shown in Fig. 2.22a. Figure 2.22b shows the

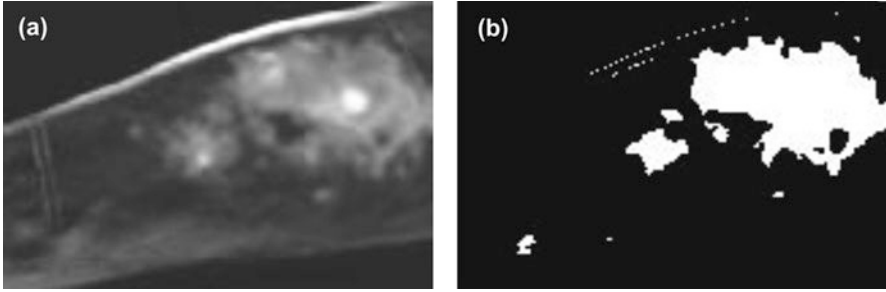


**Fig. 2.22** (a) PPGI perfusion image in gray-scale representation, (b) the binary image extracted after automatically obtaining the optimal threshold value using the proposed method. Irritated skin area in measuring field 1 (non-diluted histamine 30  $\mu$ l i.c. application) is 253.5 mm<sup>2</sup>

resulting binary image that has the same average pixel intensity as that of the gray-scale image shown in Fig. 2.22a. Here, the black portion of the image corresponds to the normal skin (normal perfusion level), and the white area indicates the area of skin with increased perfusion due to allergic skin reaction. From the binary image, it is easy to extract the area of the skin afflicted by allergic skin reaction in a functional manner, in this case 253.5 mm. Thus, using PPGI, the area of “irritated” skin can be determined objectively and fully automatically without manual intervention. It can be noted from Fig. 2.22 that the demarcation is relatively extensive and has a random shape, as expected in any of our data sets. This is a marked deviation from the areas obtained through scanning LDI, which always provides a neat circular or elliptical shape [51, 65]. We also found that setting the threshold manually (the threshold value was set by 10 different operators after visual inspection of the same scenario) results in a relatively large and unacceptable deviation in determination of the affected area ( $239.5 \pm 30.1$  mm<sup>2</sup>). Therefore, it is advised to set the threshold automatically using the near average pixel intensity condition between the perfusion image and the binary image.

The present data demonstrate that PPGI enables quantification of the dose-dependent effects of antihistamines to histamine reaction and has the potential to be used in allergologic testing to compare different therapies. In contrast to the scanning LDI method that uses a mechanical scanning system, PPGI enables simultaneous evaluation of both spatial and temporal variations, and the influence of tissue perfusion simultaneously.

## 2.5 Optical Hybrid Imaging: Combining Different Strategies

Recent advances in technology have improved both the performance and cost efficiency of cameras, thereby increasing their field of application in medical imaging. This development not only advances clinical monitoring systems for patients with cardiovascular diseases but also enables monitoring of vital signs

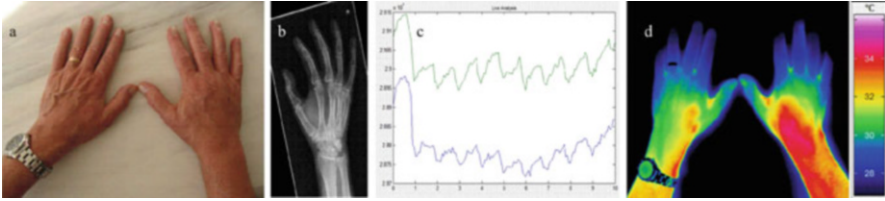


**Fig. 2.23** Example of hybrid remote imagery (photoplethysmography imaging and infrared thermography) in assessment of a local inflammatory response in the wrist and forearm of the subject's right hand after mechanical overloading

outside of hospitals, e.g., in a home-care setting, or in vehicles and airplanes. Other applications include early recognition of decubitus and monitoring of wounds during nursing as well as security applications, e.g., biometric user recognition.

This hybrid-camera approach combines the advantages of different camera sensor technologies, which can be combined for various research topics, e.g., the advantageous fusion of active PPGI and completely passive IRT (see below).

As mentioned, PPGI is the preferred choice for remote detection of heart rate, heart rate variability, and spatially distributed lower dermal blood perfusion patterns, while IRT is preferred for remote detection of respiratory rate and spatially distributed thermal signatures. Therefore, PPGI and IRT complement each other by covering different vital signs; a combination of both systems is thus advantageous and is currently under investigation. Physiological and pathological skin perfusion phenomena (e.g., sepsis, or centralization) can be analyzed, while both local temperature signature and dermal blood perfusion patterns are available.

To create such hybrid imaging, both cameras must be synchronized for data recording. In addition, their positioning and the reduction of movement artifacts is important; moreover, exactly the same ROI must be selected for both recordings. Any remaining differences in the camera's field of view must be accounted for by, e.g., image registration.

An example of the potential of our combined PPGI/IRT camera modality is shown in Fig. 2.23, which quantifies mechanical overloading in the right wrist/forearm of a 69-year-old man after a fall while gardening. The patient reported significant pain; indeed, a swollen right hand is visible (Fig. 2.23a). The radiograph (Fig. 2.23b) showed no fracture of structures and even with PPGI, no local inhomogeneity of skin perfusion is apparent in the injured area (Fig. 2.23c). However, IRT shows a marked inflammatory process inside the joint, in the center of which the temperature is increased by  $\geq 2^\circ\text{C}$  (Fig. 2.23d).

## 2.6 Conclusions

By elucidating the pathophysiology of the microvascular dermal status in a noninvasive and contactless manner, the presented PPGI technique offers new quantitative strategies for functional assessment of physiological and/or induced skin reactions.



In contrast to the classical photoplethysmography used for continuous monitoring of temporal changes in peripheral venous and/or arterial hemodynamics at a single site, the PPG imager allows to study the spatial variation of the peripheral tissue perfusion with time correlation (simultaneously). Moreover, it is not only noninvasive but is also contactless. However, it does introduce some new problems in the field of vital signs monitoring, such as movement artifacts of the subject during measurement.

In most applications, PPGI is used in reflective mode (R-mode). With this PPGI technique, the light reflected mostly from terminal blood vessels is detected. In order to obtain information about macro vessels, a significant amount of light has to transmit through the body. This is possible in acral body parts like the finger, toe, or earlobe. Therefore, PPGI is sometimes used in transmit mode (T-mode), especially in acral body regions. This is analogue to the classic PPG technology and enables the analysis of the hemodynamics in macro blood vessels even with PPGI [68].

PPGI software automatically calculates the perfusion intensity for a selected frequency range and for every part of the recorded skin surface, and visualizes the results (pixel by pixel) in a new kind of color-coded multidimensional perfusion map. Previous rhythmical patterns between normal skin and skin under histamination have been observed (data not published). The heartbeat-related blood volume pulse, respiratory synchronous rhythms, and even local vasomotor rhythms with lower frequencies are measured. Under histamine provocation, changes in HR synchronous rhythms dominate all other perfusion rhythms with lower frequencies. In all our experiments, the amplitude of the arterial blood volume pulse increased significantly and the low frequency rhythms were attenuated. Similar types of perfusion were visible in fresh, superficial wound beds (Figs. 2.8 and 2.9) as well as in skin regions treated with vasoactive liniment (Fig. 2.10). Whether these slow perfusion rhythms are dampened by inhibition of the macro- and microcirculatory vasomotion effects, or are only masked, needs to be clarified in future studies.

Additional benefits of the PPGI technique include its adaptability to special measurement scenarios, such as monitoring of the sensitive premature skin of neonates. This is possible with PPGI, as compared with classical PPG which requires contact and has possible negative side effects. For these reasons, the PPGI technique is of increasing importance as a passive and multimodal sensing technology.

## References

1. C.H. Cartwright, *J. Opt. Soc. Am.* **20**(2), 81 (1930)
2. H. Haxthausen, *Br. J. Dermatol.* **45**(12), 506 (1933)
3. K. Matthes, *Naunyn Schmiedebergs Arch. Exp. Pathol. Pharmacol.* **179**(6), 698 (1935)
4. H. Molitor, M. Kniazuk, *J. Pharmacol. Exp. Ther.* **57**(1), 6 (1936)
5. A.B. Hertzman, C.R. Spealman, *Am. J. Physiol.* **119**, 334 (1937)
6. A.B. Hertzman, *Am. J. Physiol.* **124**, 329 (1938)

7. V. Blazek, U. Schultz-Ehrenburg, in *Frontiers in Computer-Aided Visualization of Vascular Functions. Proceedings 7th Int. Symposium CNVD '97*, ed. by V. Blazek, U. Schultz-Ehrenburg, chap. 1 (VDI Verlag, Düsseldorf, 1988), pp. 1–5
8. T. Wu, V. Blazek, H.J. Schmitt, in *Proceedings of SPIE*, vol. 4163, ed. by A.V. Priezhev, P.A. Oberg (International Society for Optics and Photonics, Bellingham, 2000), p. 62
9. V. Blazek, T. Wu, D. Hoelscher, in *Proceedings of SPIE*, vol. 3923, ed. by A.V. Priezhev, T. Asakura (International Society for Optics and Photonics, Bellingham, 2000), pp. 2–9
10. M.Z. Poh, D.J. McDuff, R.W. Picard, *IEEE Trans. Biomed. Eng.* **58**(1), 7 (2011)
11. L. Tarasenko, M. Villarroel, A. Guazzi, J. Jorge, D.A. Clifton, C. Pugh, *Physiol. Meas.* **35**(5), 807 (2014)
12. M. Kumar, A. Veeraraghavan, A. Sabharwal, *Biomed. Opt. Express* **6**(5), 1565 (2015)
13. M. van Gastel, S. Stuijk, G. de Haan, *IEEE Trans. Biomed. Eng.* **62**(5), 1425 (2015)
14. D.J. McDuff, J.R. Estep, A.M. Piasecki, E.B. Blackford, in *2015 37th Annual International Conference of the IEEE Engineering in Medicine and Biology Society (EMBC)*, vol. 2015 (IEEE, Piscataway, 2015), pp. 6398–6404
15. W. Wang, S. Stuijk, G. de Haan, *IEEE Trans. Biomed. Eng.* **62**(2), 415 (2015)
16. Y. Sun, N. Thakor, *IEEE Trans. Biomed. Eng.* **63**(3), 463 (2016)
17. A. Trumpp, J. Schell, H. Malberg, S. Zauneder, *Curr. Dir. Biomed. Eng.* **2**(1), 199 (2016)
18. A.K. Abbas, K. Heimann, V. Blazek, T. Orlikowsky, S. Leonhardt, *Infrared Phys. Technol.* **55**(6), 538 (2012)
19. C.B. Pereira, M. Czaplik, N. Blanik, R. Rossaint, V. Blazek, S. Leonhardt, *Biomed. Opt. Express* **5**(4), 1075 (2014)
20. N. Blanik, K.A. Abbas, B. Venema, V. Blazek, S. Leonhardt, in *Innovations and Applications of Monitoring Perfusion, Oxygenation and Ventilation* (Yale University, New Haven, 2012)
21. N. Blanik, A.K. Abbas, B. Venema, V. Blazek, S. Leonhardt, *J. Biomed. Opt.* **19**(1), 016012 (2014)
22. N. Blanik, M. Paul, V. Blazek, S. Leonhardt, in *37th Annual International Conference of the IEEE Engineering in Medicine and Biology Society (EMBC)*, vol. 2015 (IEEE, Piscataway, 2015), pp. 2383–2386
23. V. Blazek, U. Schultz-Ehrenburg, *Quantitative Photoplethysmography: Basic Facts and Examination Tests for Evaluating Peripheral Vascular Functions* (VDI-Verlag, Düsseldorf, 1996)
24. B. Venema, N. Blanik, V. Blazek, H. Gehring, A. Opp, S. Leonhardt, *IEEE Trans. Biomed. Eng.* **59**(7), 2003 (2012)
25. M. Huelsbusch, Ein bildgestütztes, funktionelles Verfahren zur optoelektronischen Erfassung der Hautperfusion (An image-based and functional technique for the optoelectronic assessment of skin perfusion). Ph.D. thesis, RWTH Aachen University, Aachen, 2008
26. N. Blanik, in *Studies in Skin Perfusion Dynamics – Photoplethysmography and Its Applications in Medical Diagnostics*, ed. by V. Blazek, V.J. Kumar, S. Leonhardt, M.M. Rao (Springer, New Delhi, 2016)
27. V. Blazek, *Communications* **1**, 5 (2011)
28. M.H. Yang, N. Ahuja, *Face Detection and Gesture Recognition for Human-Computer Interaction* (Springer US, New York, 2001)
29. B. Jaehne, *Digital Image Processing*, 6th edn. (Springer, Berlin, 2015)
30. D. Forsyth, J. Ponce, *Computer Vision: A Modern Approach*, 2nd edn. (Prentice Hall, Upper Saddle River, 2012)
31. M. Paul, N. Blanik, V. Blazek, S. Leonhardt, in *Proc. of SPIE*, vol. 9534, ed. by F. Meriaudeau, O. Aubret (International Society for Optics and Photonics, Bellingham, 2015), pp. 95340P1–95340P7
32. F. Massanes, M. Cadennes, J.G. Brankov, *J. Electron. Imaging* **20**(3), 1 (2011)
33. A. Gyaourova, C. Kamath, S.C. Cheung, Block matching for object tracking. Tech. rep., Lawrence Livermore National Laboratory, 2003
34. C. Mayntz, J.M. Frahm, T. Aach, G. Schmitz, in *Mustererkennung 2000 (Pattern Recognition 2000)*, ed. by G. Sommer, N. Krueger, C. Perwass (Springer, Berlin, 2000), pp. 123–130

35. G.A. Jones, *Comput. Vis. Image Underst.* **65**(1), 57 (1997)
36. B. Heisele, Objektdetektion in Straßenverkehrsszenen durch Auswertung von Farbbildfolgen (Analysis of video sequences for object detection in scenes of road traffic). Ph.D. thesis, University Stuttgart, VDI-Verlag, Düsseldorf, 1998
37. S.g. Wei, L. Yang, Z. Chen, Z.f. Liu, *Procedia Eng.* **15**, 3471 (2011)
38. B.K.P. Horn, B.G. Schunck, *Artif. Intell.* **17**(1–3), 185 (1981)
39. B.D. Lucas, T. Kanade, in *Proceedings of the 7th International Joint Conference on Artificial Intelligence - Volume 2* (Morgan Kaufmann Publishers, Burlington, 1981), pp. 674–679
40. C. Tomasi, T. Kanade, Detection and tracking of point features. Tech. rep., College of Engineering, Computing and Applied Sciences, Clemson University, Technical Report CMU-CS-91–132, Clemson, 1991
41. P. Viola, M. Jones, *Int. J. Comput. Vis.* **4**, 51 (2001)
42. D.G. Lowe, Method and apparatus for identifying scale invariant features in an image and use of same for locating an object in an image (2000)
43. H. Bay, T. Tuytelaars, L. Van Gool, in *ECCV 2006: Computer Vision – ECCV 2006*, ed. by A. Leonardis, H. Bischof, A. Pinz. Lecture Notes in Computer Science (Springer, Berlin, 2006), pp. 404–417
44. G. Schwarzenberg, Objektverfolgung mit Partikel-Filter (Object tracking with a particle filter). Ph.D. thesis, University Karlsruhe, Karlsruhe, 2005
45. B. Ristic, S. Arulampalam, N. Gordon, *Beyond the Kalman Filter: Particle Filters for Tracking Applications* (Artech Print on Demand, Norwood, 2004)
46. R. Kalman, *Trans. ASME J. Basic Eng.* **82**(Series D), 35 (1960)
47. E.V. Cuevas, D. Zaldivar, R. Rojas, Kalman filter for vision tracking. Tech. rep., Technical Report B 05-12 FU Berlin, 2005
48. Y. Cheng, *IEEE Trans. Pattern Anal. Mach. Intell.* **17**(8), 790 (1995)
49. O.P. Hornstein, G. Heyer, B. Langenstein, *Acta Derm. Venereol. Suppl.* **144**, 146 (1989)
50. C. Blazek, V. Blazek, in *Studies in Skin Perfusion Dynamics – Photoplethysmography and Its Applications in Medical Diagnostics*, ed. by V. Blazek, V.J. Kumar, S. Leonhardt, M.M. Rao (Springer, New Delhi, 2016)
51. K. Wardell, A. Jakobsson, G. Nilsson, *IEEE Trans. Biomed. Eng.* **40**(4), 309 (1993)
52. K.J. Dierolf, Nichtinvasive Methoden zur Differenzierung dermalen melanozytärer Laesionen – klinische ABCD-Regel, Dermatoskopie, Laser-Doppler-Fluxmetrie (Noninvasive methods for differentiation of dermal melanocytic lesions – clinical ABCD rule, dermatoscopy, Laser Do. Ph.D. thesis, University Tuebingen, Tuebingen, 2007
53. M. Juenger, A. Steins, B. Schlagenhauff, G. Rassner, *Hautarzt* **50**(12), 848 (1999)
54. N. Blanik, K. Heimann, C. Pereira, M. Paul, V. Blazek, B. Venema, T. Orlikowsky, S. Leonhardt, *Biomed. Eng./Biomed. Tech.* **61**(6), 631 (2016)
55. V. Blazek, N. Blanik, C.R. Blazek, M. Paul, C. Pereira, M. Koeny, B. Venema, S. Leonhardt, *Anesth. Analg.* **124**(1), 104 (2017)
56. J.W. Severinghaus, *Anesth. Analg.* **105**(6), S1 (2007)
57. V. Blazek, M. Hülsbusch, M. Herzog, *Biomed. Tech.* **52**(B), 1 (2007)
58. N. Blanik, Konzept und Realisierung eines kontaktlosen Messsystems für die orts aufgelöste Erfassung der Sauerstoffsättigung der Haut (Concept development and implementation of a contactless measurement system for the spatially resolved assessment of oxygen saturation). Ph.D. thesis, RWTH Aachen University, Aachen, 2010
59. N. Blanik, B. Venema, V. Blazek, S. Leonhardt, *Clin. Technol.* **44**, 5 (2014)
60. C.H. Blackley, *Hay Fever: Its Causes, Treatment and Effective Prevention: Experimental Researches*, 2nd edn. (Baillière, Tindall & Cox, London, 1880)
61. B. Przybilla, K.C. Bergmann, J. Ring, *Praktische allergologische Diagnostik (Allergy Diagnostic)*, 1st edn. (Steinkopff-Verlag, Darmstadt, 2000)
62. F. Ruëff, K.C. Bergmann, K. Brockow, T. Fuchs, A. Grübl, K. Jung, L. Klimek, H. Müsken, O. Pfaar, B. Przybilla, H. Sitter, W. Wehrmann, German Society for Allergology and Clinical Immunology, *Pneumologie* **65**(08), 484 (2011)
63. H. Pijnenborg, L. Nilsson, S. Dreborg, *Allergy* **51**(11), 782 (1996)

64. A.M. Opazo Saez, F. Mosel, J. Nurnberger, U. Rushentsova, M. Gossl, A. Mitchell, R.F. Schafers, T. Philipp, R.R. Wenzel, *Br. J. Clin. Pharmacol.* **59**(5), 511 (2005)
65. C.F. Clough, A.R. Bennett, M.K. Church, *Br. J. Dermatol.* **138**(5), 806 (1998)
66. T.W. Ridler, S. Calvard, *IEEE Trans. Syst. Man Cybern.* **8**, 630 (1978)
67. C. Janus, Funktionelle Erkennung und Vermessung von Ulcera und allergischen Hautreaktionen in Einzelaufnahmen und PPGI Bildsequenzen (Functional detection and measurement of ulcers and allergic skin reactions in images and PPGI video sequences). Ph.D. thesis, RWTH Aachen University, Aachen, 2008
68. V. Blazek, in *Studies in Skin Perfusion Dynamics – Photoplethysmography and Its Applications in Medical Diagnostics*, ed. by V. Blazek, V.J. Kumar, S. Leonhardt, M.M. Rao (Springer, New Delhi, 2016)

# Chapter 3

## Multimodal Image Fusion for Cardiac Resynchronization Therapy Planning



Sophie Bruge, Antoine Simon, Nicolas Courtial, Julian Betancur, Alfredo Hernandez, François Tavard, Erwan Donal, Mathieu Lederlin, Christophe Leclercq, and Mireille Garreau

**Abstract** Cardiac resynchronization therapy (CRT) has shown its efficiency to treat patients with left-sided heart failure, however with 30% of them not responding to the therapy. One way to optimize CRT is to pre-operatively plan the implantation of the CRT device and especially the positioning of the stimulation lead pacing the left ventricle (LV), which is implanted through the coronary veins. Indeed, it has been shown that this lead should target LV sites with a late mechanical activation and without fibrosis. Additional imaging modalities should therefore be part of CRT's planning, in order to describe the anatomy, mechanical activation, and tissue characteristics of the LV. We developed a full workflow to process, register, and fuse CT images, ultrasound (US) images, and MRI, including cine-MRI and late gadolinium enhancement (LGE) MRI. It results in a 3D patient-specific model, describing the anatomy of the LV and of the coronary veins, the electro-mechanical delays, and the presence of fibrosis. The process includes a semi-automatic segmentation of CT images to extract the LV cavity and the veins. 2D US images are processed using speckle tracking echography (STE) to estimate the mechanical strains. LGE-MRI is segmented to extract macroscopic fibrosis. All these images are registered using CT as the anatomical reference. Registration methods have thus been developed to register STE to CT, LGE to cine-MRI, and cine-MRI to CT. This whole process furnishes to the physician, before the CRT implantation, a patient-specific 3D model representing all the information needed to select the most appropriate LV pacing sites. Results obtained on patients undergoing CRT are presented.

---

S. Bruge · A. Simon (✉) · N. Courtial · J. Betancur · A. Hernandez · F. Tavard · E. Donal  
M. Lederlin · C. Leclercq · M. Garreau  
Univ Rennes, CHU Rennes, Inserm, LTSI – UMR 1099, Rennes, France

Université de Rennes 1, LTSI, Rennes, France  
e-mail: [antoine.simon@univ-rennes1.fr](mailto:antoine.simon@univ-rennes1.fr)

**Keywords** Cardiac imaging · Multimodal imaging · Registration · Fusion · Cardiac Resynchronization Therapy · Planning

### 3.1 Introduction

Multimodal imaging has the ability to provide enhanced descriptions of organs by combining descriptors related to anatomy, function, and metabolism. Considering cardiac imaging, many different modalities are clinically used, including computed tomography (CT) imaging, magnetic resonance imaging (MRI), ultrasound (US) imaging, and nuclear imaging. All these modalities provide complementary information, opening the way towards a combined analysis of heart multiphysics that may be useful to improve the diagnosis of cardiac pathologies, plan and assist their treatment, and perform its follow-up.

Chronic heart failure (HF), affecting an estimated 26 million people worldwide [1], corresponds to the heart's inability to pump enough blood to fulfill the body's needs. Cardiac dyssynchrony, i.e., spatial inhomogeneity in timing of contractions, is frequently observed in these patients and leads to a poor outcome if left untreated. Cardiac resynchronization therapy (CRT) is a non-pharmacological treatment based on the implantation of a pacemaker with leads stimulating the heart. Generally, a biventricular pacing is used, with the implantation of three leads: two endocardial leads in the right atrium and ventricle, and one transvenous lead to pace the left ventricle (LV) [19]. CRT has shown its efficiency to treat patients with left-sided heart failure associated with dyssynchrony despite pharmacological therapy [23]. However, the percentage of non-responders remains high: about 30% [37]. A suboptimal position of the LV lead, that is the most difficult one to implant, may be one factor explaining non-response. Indeed, in current practice, the LV stimulation site is selected during the implantation, based on the per-operative angiographic images providing a very poor description of the left ventricle and of the coronary venous access.

On the other hand, it has been shown that cardiac sites with well-defined specific characteristics are better responders to the therapy [4, 10]. Especially, stimulating the site associated with the latest mechanical contraction improved patient outcome [28]. On the contrary, stimulating a fibrotic tissue (i.e., scarred tissue with degraded contractility) is associated with non-response to CRT [35]. In this context, generating an enhanced description of the heart would allow the clinicians to select the most appropriate pacing sites in order to plan the implantation. This description should include the mechanical contraction, the tissular properties but also a description of the LV anatomy and of the coronary veins which are used to implant the LV lead. These descriptions result from different imaging modalities, which have thus to be registered and fused.

Few works of the literature addressed the combination of multiple pre-operative modalities to plan CRT. This combination has mostly been done by using, independently for each modality, a division of the cardiac wall in segments (i.e., a 17-segment bulls-eye representation [11]) [2, 5, 13], thus providing a limited spatial accuracy. Some teams proposed to use a landmark-based registration to combine 3D echography and CT [33], or 2D echography, CT, and SPECT [31]. It provides more accurate characterizations, but is dependent on the selection of well-defined landmarks in the images. Performing an automatic registration method is challenging since the considered modalities are highly different in terms of dimension (2D vs 3D, static vs dynamic), resolution (e.g.,  $0.4 \times 0.4 \times 0.6$  mm in CT versus  $1.8 \times 1.8 \times 4$  mm in cine-MRI in our case), represented information, and since the considered organ, the heart, is submitted to fast deformations, related to the cardiac contraction but also to respiration. It therefore needs the development of specific methods adapted to the characteristics of both the organ and the studied modalities.

We thus have developed a workflow to fuse multimodal cardiac images (i.e., CT, MRI and US) to generate, pre-operatively, a patient-specific model of the LV including different characteristics useful to plan CRT interventions. This model includes the anatomy of the LV and of the coronary veins, the mechanical contraction of the wall, and its tissular characteristics in terms of macroscopic fibrosis.

The global workflow is presented in Fig. 3.1. It is based on multimodal data processing, including the segmentation of CT images to extract the LV and veins, fibrosis characterization based on LGE-MRI, and processing of echographic data

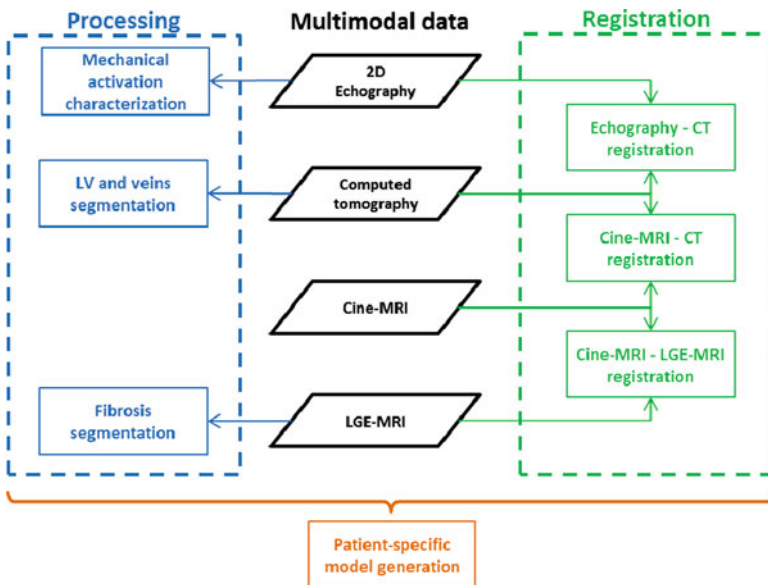


Fig. 3.1 Multimodal image analysis workflow

using speckle tracking echography to characterize the mechanical activation. Then, all these images are registered. These different steps have been previously presented in different publications [7–9, 32]. In this chapter, we summarize these processing and show how they can be integrated to generate a patient-specific 3D model which can help the clinician to select the optimal site(s) by considering the sites localized close to a vein, associated with a large mechanical delay and with the absence of fibrosis. The different processing steps are described below.

## 3.2 Multimodal Image Processing

The first step of the proposed workflow is to extract the descriptors of interest by processing the acquired images, namely the anatomy in CT images, mechanical activation in echography, and fibrosis in MRI. Table 3.1 summarizes the main characteristics of the acquired images.

### 3.2.1 Segmentation of LV and Veins in CT Images

CT imaging, because of its high spatial resolution, remains the reference modality for the anatomical description of the heart, especially considering the coronaries.

The considered CT images were acquired with a multislice computed tomography scanner (General Electric, LightSpeed VCT 64- slice system). Iodine contrast product was injected to enhance the left heart inner cavities (100 and 150 cm<sup>3</sup> being at 300 mg/ml or 350 mg/ml). The acquisitions were retrospectively synchronized on the ECG, providing dynamic 3D+t images (10 or 20 phases describing the cardiac cycle). Since the contrast of the cavities is high, a simple region growing enables to segment the left cavities (atrium and ventricle). In case of segmentation leaks due to limited contrast, a manual correction was used to separate the cavities from neighboring structures.

**Table 3.1** Main characteristics of the considered images (img/CC: images per cardiac cycle; \*: in STE, the considered resolution is the average distance between the landmarks)

	CT	US (STE)	LGE-MRI	cine-MRI
Dimension	3D+t	2D+t	3D	3D+t
Spatial resolution	0.4 × 0.4 × 0.6 mm	3 mm*	1.4 × 1.4 × 10 mm	1.8 × 1.8 × 4 mm
Temporal resolution	10–20 img/CC	50–60 img/CC	–	35 img/CC
Extracted information	Anatomy (LV, veins)	Mechanical contraction	Tissue characterization (fibrosis)	Intermediate registration



The segmentation of the veins is much more challenging, but required since the LV lead implantation is done through the venous network. However, these structures are small, with a low contrast and with a variable anatomy among patients. Moreover, they are very close to arteries, making them difficult to identify. Many works have been proposed in the literature for the segmentation of vessels in MR or CT imaging [21]. However, most of them are focused on the arteries, which present a higher contrast than the veins. Moreover many methods fail to segment the vessels of medium and low diameter, which are of interest for the implantation. We thus used a semi-automatic process [9] including, for each slice containing a specific vein (coronary sinus, great cardiac vein, middle cardiac vein, posterior vein, or left marginal vein): the manual selection of a region of interest; a filtering to enhance tubular structures; a thresholding to identify the tubular objects; a connexity based object identification considering either the largest object or the one related an object previously segmented in the neighboring slices. In case of missing segments, the vein was finally interpolated.

*Manual Selection of a Region of Interest* For each vein, the user defined a 2D region of interest on a slice selected such that the vein is visible. It is then extended to a volume of interest by including the three superior and inferior slices.

*Tubular Structures Filter* The VOI was filtered using the Frangi filter [12], a filter based on the Hessian matrix of the image intensity, intended to enhance the tubular structures. In order to detect vessels of different sizes, a multi-scale approach was used by filtering the VOI with a set of Gaussian filters of different sizes (standard deviation in the range [1, 3] pixels). For each pixel, the highest value resulting from the different Gaussian smoothing was retained.

*Thresholding and Connexity Based Object Identification* The resulting filtered ROI was thresholded using an interactively selected threshold  $T$ . The resulting binary region was analyzed to keep either the largest region (if the current slice is the first one to be processed), or the region connected to the vein segmented in the previous slice.

*Interpolation of the Vein* In some cases, the whole vein could not be extracted using the previous process and some intermediate parts were missing between two segmented parts. Then, an interpolation was used to estimate the missing segment, based on the discretization of the contour using regularly spaced points and their interpolation with cubic splines.

### ***3.2.2 Characterization of the Mechanical Activation Using Speckle Tracking Echography***

Despite the increased attention gained by MRI for cardiac function assessment [14], the measurement of dyssynchrony remains mainly performed using echography, and especially with speckle tracking [10]. By tracking acoustic markers (speckles)

in ultrasound images, speckle tracking echography (STE) provides a mechanical description of the LV contraction in terms of strain curves.

Transthoracic echocardiography (Vivid7, GE Healthcare, Horten, Norway) was acquired at rest. 2D acquisitions were realized using two- and four-chamber apical views over a cardiac cycle. On each view, the endocardium wall was manually segmented on diastole by the expert and tracked using speckle tracking (General Electric ECHOPAC workstation). The strain curves, computed on regularly spaced points on the endocardium, were then automatically computed by the speckle tracking software, and exported. Different descriptors can then be extracted from these strain curves, especially the maximal strain value, to identify areas with low contractility, and the delay between the peak of the QRS complex and the maximal strain (electro-mechanical delay) to identify the delayed segments.

### ***3.2.3 Characterization of Fibrosis in LGE-MRI***

LGE-MRI enables to identify macroscopic fibrosis (i.e., replacement of myocytes after cell damage) by using a gadolinium contrast agent injection and by imaging the increased amount of gadolinium in fibrous tissue [25].

LGE- and cine-MRI were acquired using cardiac SENSE coils (Philips Achieva®, Philips Medical Systems, Best, The Netherlands). Breath-hold cine (bTFE sequence) and LGE (TFE) were acquired for SAX and long axis views (2CH,4CH), using retrospective ECG synchronization. Both inversion recovery (IR) and phase-sensitive IR (PSIR) techniques were used to acquire LGE. 12 slices were acquired for SAX and 3–5 for 2CH/4CH. Multiview LGE was acquired 5–10 min after gadolinium injection (0.1 mmol/kg of Dotarem Guerbet, Roissy, France), at mid-diastole. 16 slices were acquired for SAX and 12 for 2CH/4CH.

If needed, motion artifacts were corrected using an in-house developed software presented in [7].

In order to segment fibrosis areas in LGE images, the inner and outer contours of the myocardium were firstly manually roughly segmented. Then, a fuzzy c-means algorithm was applied to the myocardium and blood pool to associate, to each voxel, a probability to belong to the gadolinium-enhanced class [18]. The membership probability was then automatically thresholded on the myocardium by using the threshold value providing the most stable output [3].

## **3.3 Multimodal Image Registration**

Once all the images have been processed, they were registered and fused to generate the patient-specific 3D model incorporating all the descriptors. The CT image, providing the best spatial resolution, was considered as the anatomical reference.

MRI and STE were therefore registered towards it. Since these three modalities embed dynamic data's acquisition (cine sequence in MRI), the proposed registration process takes advantage of all the available information by combining a temporal synchronization with the spatial registration, thus enabling to register all the phases of the dynamic images in a single process.

### ***3.3.1 STE to CT Registration***

Few works have been proposed in the literature for cardiac multimodal registration considering 2D [24] or 3D US data [22, 27]. The goal of these works is mainly to compare pre- and per-operative data during surgical gestures guided by US [36], or to combine complementary descriptors to help in diagnosis [34]. The temporal synchronization of data is often the first problem to solve. Some works use the ECG, by considering only one instant related to the same cardiac phase [20], whereas others use a dynamic registration relying on an interpolation process [16, 34]. Then, to perform the geometrical matching, some authors considered either iconic methods based on mutual information [17], or geometrical methods based on geometrical landmarks [15, 30], or modelling methods based on the simulation of US images from CT data [34].

We developed a method based on Fourier descriptors to handle differences in spatial resolution and dynamic time warping (DTW) [29] to deal with differences of cardiac rates and ECG sampling frequencies.

The dynamic geometry of the ventricle was available in both STE and CT with a 2D dynamic contour for STE and a 3D dynamic surface for CT. The proposed process combined, in an iterative way, synchronization and registration [7, 32] (cf. Fig. 3.2a). At each iteration, the position of the echographic acquisition plane, expressed in the CT image coordinate system, was refined. This position enabled to generate a cut of the CT dynamic surface, resulting to a dynamic contour. The registration metric, used to express the quality of the registration, was thus defined between the two dynamic contours, from CT and from STE. In order to handle the differences between both contours (i.e., differences in smoothness), they were expressed in terms of Fourier descriptors (maximum order: 50). They were then synchronized by using DTW applied to the Fourier decompositions of both 2D dynamic contours. The final registration metric was, after synchronization, the sum of the differences of the Fourier descriptors.

### ***3.3.2 LGE-MRI to CT Registration***

LGE-MRI was registered to CT images by considering cine-MRI as an intermediate (cf. Fig. 3.2b). Indeed, cine-MRI is consistent with LGE-MRI and, by including the

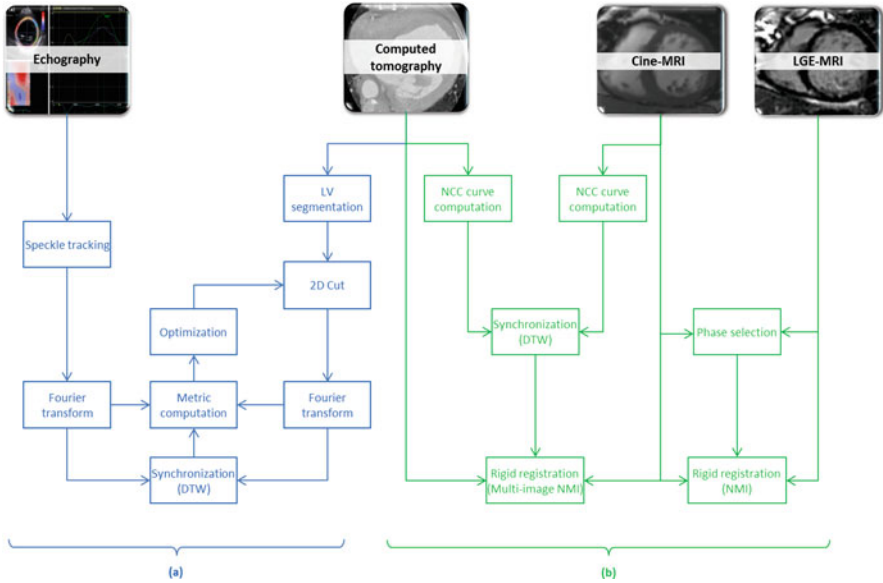


**Fig. 3.2** Multimodal image registration; (a) STE to CT registration; (b) LGE-MRI to CT registration

temporal dimension, provides more information than LGE-MRI for the registration towards CT images. LGE-MRI was rigidly registered towards the closest phase in cine-MRI by using normalized mutual information (NMI).

The registration of cine-MRI and CT is challenging mainly because of the temporal synchronization. If the ECG is used during the acquisition of both images, it may be deformed by the MRI magnetic field and is not always available after the acquisition.

Thus, cine-MRI and CT images were registered in two steps [8]: (1) temporal synchronization based on image information; (2) rigid registration of the synchronized sequences using a multi-image metric.

The temporal synchronization was performed by computing normalized cross-correlation (NCC) curves of input image sequences. One NCC curve was firstly computed for each image sequence, defined by the normalized cross-correlation between the first image of the sequence and each image of the same sequence. The two resulting curves have proven to globally describe the cardiac dynamics in dynamic CT and cine-MRI [6, 26]. The nonlinear synchronization of corresponding cardiac dynamics was then estimated by warping the time axes of these curves, using a DTW procedure. A multi-image rigid registration procedure, using normalized mutual information (NMI) as the metric, was finally used to align dynamic CT and cine-SAX (short axis) with synchronized cardiac dynamics.

### 3.4 Patient-Specific 3D Model Generation

The patient-specific model results from the registration of STE and LGE-MRI towards the planning CT image. Thus, the anatomical description (LV endocardium and veins) is enhanced by the mechanical activation (delay to the peak of strain and peak amplitude, defined on the 2D ultrasound acquisition planes) from STE and by segmented fibrosis provided by LGE-MRI.

The 2D mechanical descriptors have been represented by spheres, positioned on the endocardium along the US acquisition planes, and whose color represents the associated value. Considering the fibrosis, it is represented using a 3D volume corresponding to the localization and extent of fibrosis in the myocardium.

### 3.5 Results

The different steps presented above have been evaluated:

- on simulated data: for STE to CT registration [32];
- on real data:
  - with manually positioned fiducial markers: for cine-MRI to CT registration [8];
  - with reference geometrical transform: for LGE-MRI to cine-MRI registration [7];
  - with an expert qualitative assessment: for CT segmentation [9], for fibrosis segmentation [7], and STE to CT registration [32].

Further evaluations could be performed, especially considering CT and fibrosis segmentations, by comparing the results with manual delineations from experts.

Hereafter, the results obtained on the real data of two patients undergoing a CRT procedure are presented. All the processing results, including CT and MRI segmentations, STE processing and images registrations have been validated by an clinical expert. All the images have been acquired 2 days before the CRT implantation (day D-2) and processed the day before (D-1), in order to be presented to the cardiologist before the implantation.

Figures 3.3, 3.4, and 3.5 illustrate the workflow's different steps for the first patient. Figure 3.3 shows one slice of the CT image and the segmentation result with the left cavities (ventricle and atrium) and the veins. The veins of interest for the LV lead implantation are represented in green, the others in blue. Figure 3.4 presents the echographic image and the speckle tracking result. Figure 3.5 illustrates the MRI data (cine-MRI and LGE-MRI) and the result of the fibrosis segmentation process.

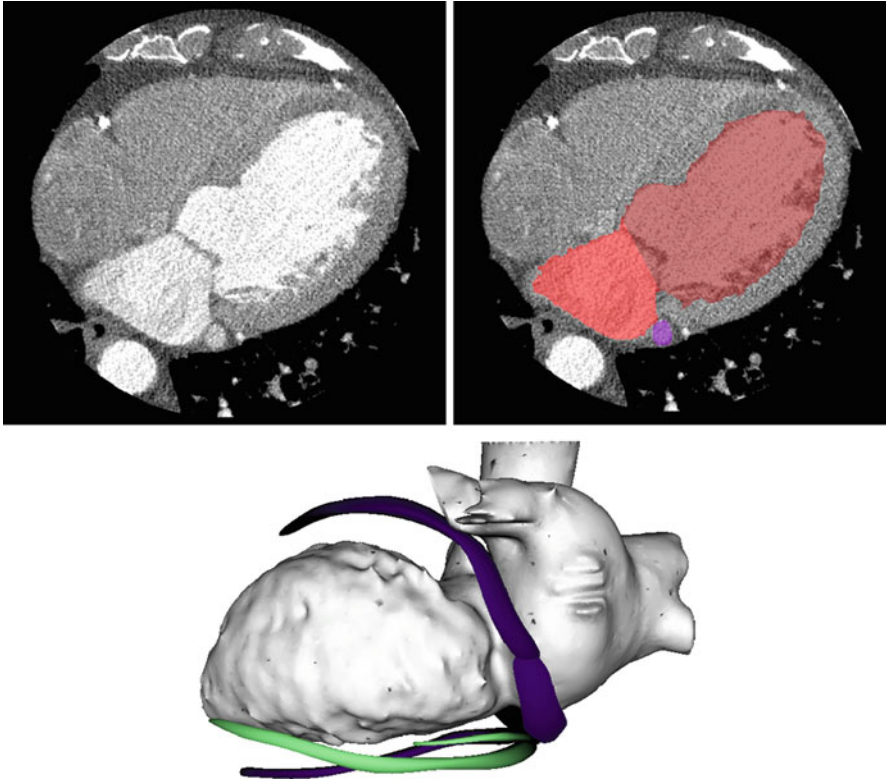


**Fig. 3.3** CT segmentation: example of one original slice and segmentation result (same slice and in 3D). Top-right: the segmented cavities are represented in red and the segmented vein in purple. Bottom: the veins of interest for the LV lead implantation are represented in green, the others in blue

The developed registration workflow results in the illustrated models in Figs. 3.6 and 3.7 for the two patients. While the first patient has a large area of fibrosis, which has to be avoided for the left lead implantation, the second patient shows no tissular defects. The model thus enables the clinician to identify the cardiac sites accessible through a venous access and associated with no fibrosis and with a delayed mechanical contraction.

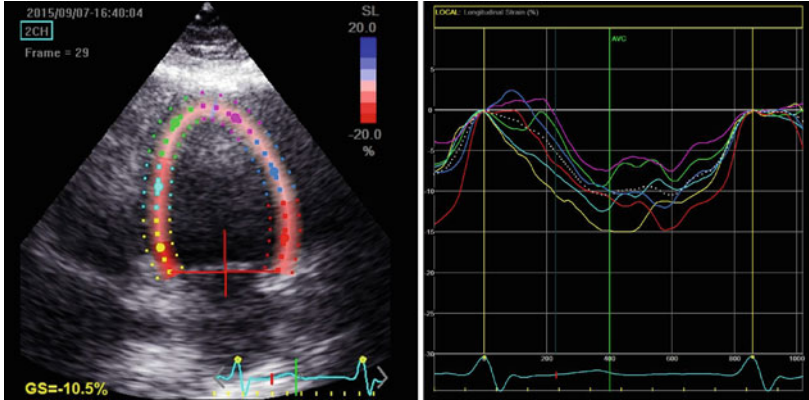


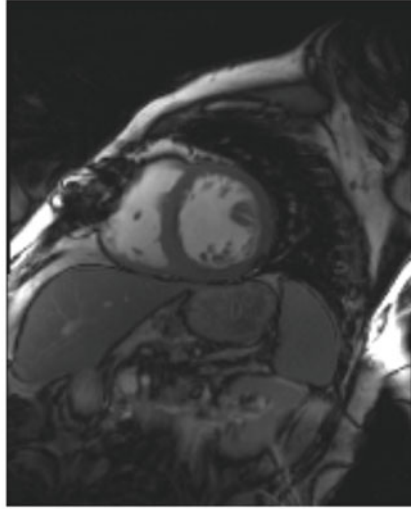
**Fig. 3.4** Echographic data: example of one 2D image and of the associated strain curves estimated with STE. Left: acquired image (four-chamber apical view) with the associated manual segmentation and, in color, cardiac segments; Right: strain curves associated with the segments

### 3.6 Conclusion

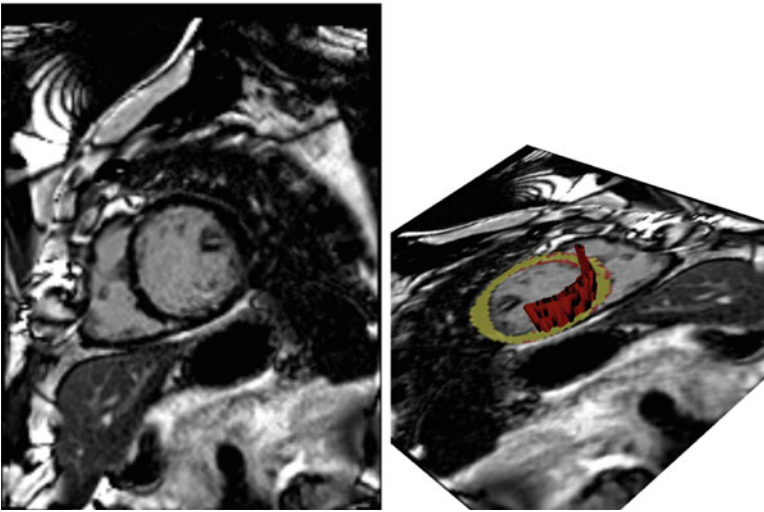
Multimodal cardiac imaging, by combining complementary descriptors (e.g., anatomical, mechanical, and tissular), has the ability to provide an improved characterization of the heart which may be useful in the management of cardiac diseases. However, some specific processes including segmentation, characterization, registration, and fusion have to be developed, evaluated, and combined to provide data management workflows adapted to the clinical needs and requirements.

In this work, we developed a workflow to assist the clinicians in planning CRT procedures. It involves the processing and registration of CT, MRI, and STE images, and the generation of a pre-operative patient-specific model. This model provides different information needed to define cardiac sites likely to respond positively to the stimulation: anatomical description of the left ventricle and the veins to assess the venous access, mechanical contraction to assess the delayed sites, and fibrosis detection to avoid the sites with poor tissular characteristics for CRT.

This process has been implemented in clinical conditions. It should allow the clinician to target the best pacing sites and to evaluate their accessibility through the venous network. This project needs further clinical evaluation, e.g., by evaluating if the proposed planning platform enables to reduce the intervention time and the rate of non-responding patients.



(a)



(b)

**Fig. 3.5** (a) Example of one cine-MRI slice; (b) example of one LGE-MRI slice, with the associated manual delineation of the myocardium and resulting segmented fibrosis displayed in 3D



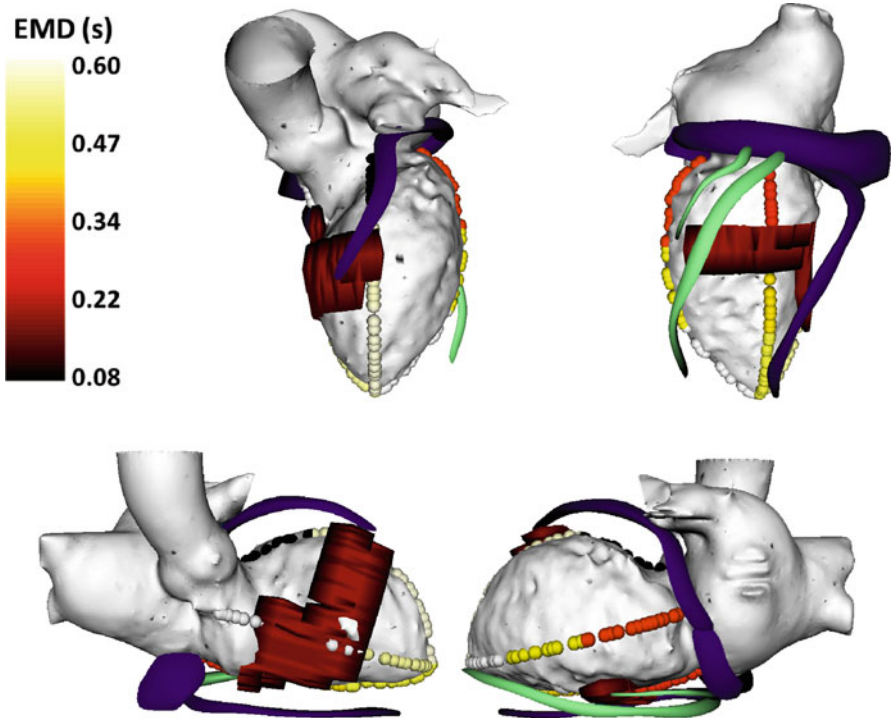


**Fig. 3.6** Generated model for the first patient. It includes: the left cavities and the veins (green: veins of interest for the LV lead implantation); the fibrosis (in dark red); the electro-mechanical delays (EMD, with spheres colored according to the colorbar)

In the future, this workflow may be tuned and enriched to be extended to other pathologies and interventional gestures, such as the ablation of ventricular tachycardia or of atrial fibrillation.

**Acknowledgements** This work was supported by the French National Research Agency (ANR) in the framework of the Investissement d'Avenir Program through Labex CAMI (ANR-11-LABX-0004). It was conducted in part in the experimental platform TherA-Image (Rennes, France), supported by Europe FEDER.

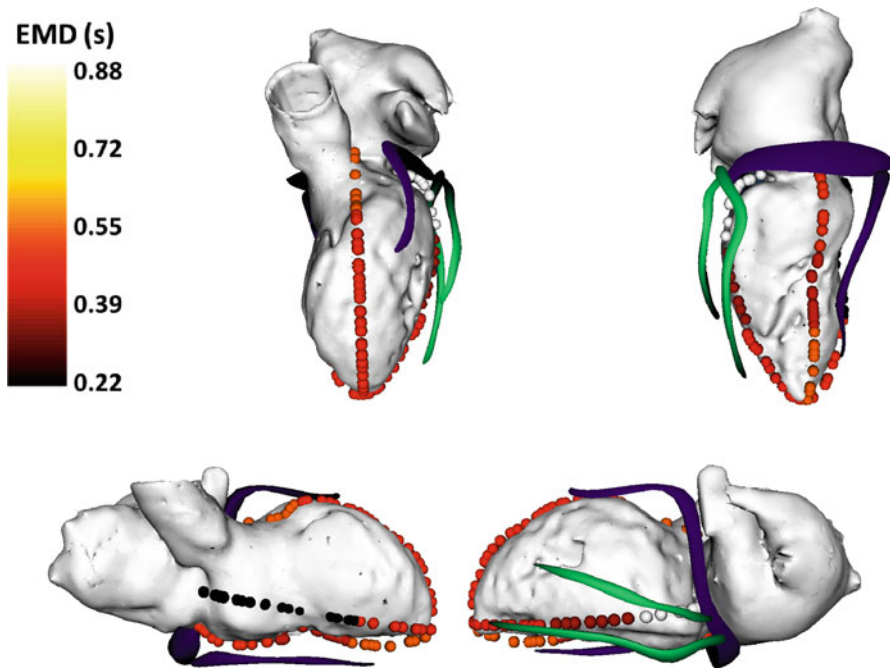


**Fig. 3.7** Generated model for the second patient. It includes: the left cavities and the veins (green: veins of interest for the LV lead implantation); the electro-mechanical delays (EMD, with spheres colored according to the colorbar); no fibrosis was detected in LGE-MRI

## References

1. A.P. Ambrosy, G.C. Fonarow, J. Butler, O. Chioncel, S.J. Greene, M. Vaduganathan, S. Nodari, C.S. Lam, N. Sato, A.N. Shah, M. Gheorghiad, The global health and economic burden of hospitalizations for heart failure: lessons learned from hospitalized heart failure registries. *J. Am. Coll. Cardiol.* **63**(12), 1123–1133 (2014)
2. Z. Bakos, H. Markstad, E. Ostefeld, M. Carlsson, A. Roijer, R. Borgquist, Combined preoperative information using a bullseye plot from speckle tracking echocardiography, cardiac CT scan, and MRI scan: targeted left ventricular lead implantation in patients receiving cardiac resynchronization therapy. *Eur. Heart J. Cardiovasc. Imaging* **15**(5), 523–531 (2014)
3. N. Baron, N. Kachenoura, P. Cluzel, F. Frouin, A. Herment, P. Grenier, G. Montalescot, F. Beygui, Comparison of various methods for quantitative evaluation of myocardial infarct volume from magnetic resonance delayed enhancement data. *Int. J. Cardiol.* **167**(3), 739–744 (2013)
4. J.M. Behar, S. Claridge, T. Jackson, B. Sieniewicz, B. Porter, J. Webb, R. Rajani, S. Kapetanakis, G. Carr-White, C.A. Rinaldi, The role of multi modality imaging in selecting patients and guiding lead placement for the delivery of cardiac resynchronization therapy. *Expert. Rev. Cardiovasc. Ther.* **15**(2), 93–107 (2017)
5. M. Bertini, D. Mele, M. Malagù, A. Fiorencis, T. Toselli, F. Casadei, T. Cannizzaro, C. Fragale, A. Fucili, E. Campagnolo et al., Cardiac resynchronization therapy guided by multimodality cardiac imaging. *Eur. J. Heart Fail.* **18**(11), 1375–1382 (2016)

6. J. Betancur, A. Simon, F. Tavard, B. Langella, C. Leclercq, M. Garreau, Segmentation-free MRI to CT 3d registration for cardiac resynchronization therapy optimization, in *Computing in Cardiology Conference (IEEE, Piscataway, 2012)*, pp. 701–704
7. J. Betancur, A. Simon, E. Halbert, F. Tavard, F. Carré, A. Hernández, E. Donal, F. Schnell, M. Garreau, Registration of dynamic multiview 2D ultrasound and late gadolinium enhanced images of the heart: application to hypertrophic cardiomyopathy characterization. *Med. Image Anal.* **28**, 13–21 (2016)
8. J. Betancur, A. Simon, B. Langella, C. Leclercq, A. Hernández, M. Garreau, Synchronization and registration of cine magnetic resonance and dynamic computed tomography images of the heart. *IEEE J. Biomed. Health Informatics* **20**(5), 1369–1376 (2016)
9. S. Bruge, A. Simon, M. Lederlin, J. Betancur, A. Hernandez, E. Donal, C. Leclercq, M. Garreau, Multi-modal data fusion for cardiac resynchronization therapy planning and assistance, in *2015 37th Annual International Conference of the IEEE Engineering in Medicine and Biology Society (EMBC) (IEEE, Piscataway, 2015)*, pp. 2391–2394
10. P. Carità, E. Corrado, G. Pontone, A. Curnis, L. Bontempi, G. Novo, M. Guglielmo, G. Ciaramitaro, P. Assennato, S. Novo et al., Non-responders to cardiac resynchronization therapy: insights from multimodality imaging and electrocardiography. A brief review. *Int. J. Cardiol.* **225**, 402–407 (2016)
11. M.D. Cerqueira, N.J. Weissman, V. Dilsizian, A.K. Jacobs, S. Kaul, W.K. Laskey, D.J. Pennell, J.A. Rumberger, T. Ryan, M.S. Verani et al., Standardized myocardial segmentation and nomenclature for tomographic imaging of the heart. *Circulation* **105**(4), 539–542 (2002)
12. A.F. Frangi, W.J. Niessen, K.L. Vincken, M.A. Viergever, Multiscale vessel enhancement filtering, in *Medical Image Computing and Computer-Assisted Intervention (MICCAI) (Springer, Berlin, 1998)*, pp. 130–137
13. O. Goitein, J.M. Lacomis, J. Gorcsan, D. Schwartzman, Left ventricular pacing lead implantation: potential utility of multimodal image integration. *Heart Rhythm* **3**(1), 91–94 (2006)
14. B. Heydari, M. Jerosch-Herold, R.Y. Kwong, Imaging for planning of cardiac resynchronization therapy. *JACC: Cardiovasc. Imaging* **5**(1), 93–110 (2012)
15. J. Hong, K. Konishi, H. Nakashima, S. Ieiri, K. Tanoue, M. Nakamuta, M. Hashizume, Integration of MRI and ultrasound in surgical navigation for robotic surgery, in *World Congress on Medical Physics and Biomedical Engineering*, pp. 3052–3055 (2007)
16. X. Huang, N. Hill, J. Ren, G. Guiraudon, T. Peters, Intra-cardiac 2D US to 3D CT image registration, in *SPIE Medical Imaging*, vol. 6509, pp. 65092E–1 (2007)
17. X. Huang, J. Moore, G. Guiraudon, D. Jones, D. Bainbridge, J. Ren, T. Peters, Dynamic 2D ultrasound and 3D CT image registration of the beating heart. *IEEE Trans. Med. Imaging* **28**(8), 1179–1189 (2009)
18. N. Kachenoura, A. Redheuil, A. Herment, E. Mousseaux, F. Frouin, Robust assessment of the transmural extent of myocardial infarction in late gadolinium-enhanced MRI studies using appropriate angular and circumferential subdivision of the myocardium. *Eur. Radiol.* **18**(10), 2140–2147 (2008)
19. C. Leclercq, S. Cazeau, P. Ritter, C. Alonso, D. Gras, P. Mabo, A. Lazarus, J. Daubert, A pilot experience with permanent biventricular pacing to treat advanced heart failure. *Am. Heart J.* **140**(6), 862–870 (2000)
20. M. Ledesma-Carbayo, J. Kybic, M. Desco, A. Santos, M. Suhling, P. Hunziker, M. Unser, Spatio-temporal nonrigid registration for ultrasound cardiac motion estimation. *IEEE Trans. Med. Imaging* **24**(9), 1113–1126 (2005)
21. D. Lesage, E.D. Angelini, I. Bloch, G. Funka-Lea, A review of 3D vessel lumen segmentation techniques: models, features and extraction schemes. *Med. Image Anal.* **13**(6), 819–845 (2009)
22. F. Li, P. Lang, M. Rajchl, E. Chen, G. Guiraudon, T. Peters, Towards real-time 3D US-CT registration on the beating heart for guidance of minimally invasive cardiac interventions, in *SPIE Medical Imaging*, pp. 831615–831615 (2012)

23. C. Linde, W.T. Abraham, M.R. Gold, M.S.J. Sutton, S. Ghio, C. Daubert, Randomized trial of cardiac resynchronization in mildly symptomatic heart failure patients and in asymptomatic patients with left ventricular dysfunction and previous heart failure symptoms. *J. Am. Coll. Cardiol.* **52**(23), 1834–1843 (2008)
24. T. Mäkelä, P. Clarysse, O. Sipila, N. Pauna, Q. Pham, T. Katila, I. Magnin, A review of cardiac image registration methods. *IEEE Trans. Med. Imaging* **21**(9), 1011–1021 (2002)
25. N. Mewton, C.Y. Liu, P. Croisille, D. Bluemke, J.A. Lima, Assessment of myocardial fibrosis with cardiovascular magnetic resonance. *J. Am. Coll. Cardiol.* **57**(8), 891–903 (2011)
26. D. Perperidis, R.H. Mohiaddin, D. Rueckert, Spatio-temporal free-form registration of cardiac MR image sequences. *Med. Image Anal.* **9**(5), 441–456 (2005)
27. E. Puyol-Antón, M. Sinclair, B. Gerber, M.S. Amzulescu, H. Langet, M. De Craene, P. Aljabar, P. Piro, A.P. King, A multimodal spatiotemporal cardiac motion atlas from MR and ultrasound data. *Med. Image Anal.* **40**, 96–110 (2017)
28. S. Saba, J. Marek, D. Schwartzman, S. Jain, E. Adelstein, P. White, O.A. Oyenuga, T. Onishi, P. Soman, J. Gorcsan, Echocardiography-guided left ventricular lead placement for cardiac resynchronization therapy results of the speckle tracking assisted resynchronization therapy for electrode region trial. *Circ. Heart Fail.* **6**(3), 427–434 (2013)
29. H. Sakoe, S. Chiba, Dynamic programming algorithm optimization for spoken word recognition. *IEEE Trans. Acoust. Speech Signal Process.* **26**(1), 43–49 (1978)
30. A. Savi, M. Gilardi, G. Rizzo, M. Pepi, C. Landoni, C. Rossetti, G. Lucignani, A. Bartorelli, F. Fazio, Spatial registration of echocardiographic and positron emission tomographic heart studies. *Eur. J. Nucl. Med. Mol. Imaging* **22**(3), 243–247 (1995)
31. A. Sommer, M.B. Kronborg, B.L. Nørgaard, S.H. Poulsen, K. Bouchelouche, M. Böttcher, H.K. Jensen, J.M. Jensen, J. Kristensen, C. Gerdes et al., Multimodality imaging-guided left ventricular lead placement in cardiac resynchronization therapy: a randomized controlled trial. *Eur. J. Heart Fail.* **18**(11), 1365–1374 (2016)
32. F. Tavard, A. Simon, C. Leclercq, E. Donal, A.I. Hernández, M. Garreau, Multimodal registration and data fusion for cardiac resynchronization therapy optimization. *IEEE Trans. Med. Imaging* **33**(6), 1363–1372 (2014)
33. F. Tournoux, R.C. Chan, R. Mancke, M.D. Hanschumacher, A.A. Chen-Tournoux, O. Gérard, J. Solis-Martin, E.K. Heist, P. Allain, V. Reddy et al., Integrating functional and anatomical information to guide cardiac resynchronization therapy. *Eur. J. Heart Fail.* **12**(1), 52–57 (2010)
34. W. Wein, A. Khamene, D. Clevert, O. Kutter, N. Navab, Simulation and fully automatic multimodal registration of medical ultrasound, in *Medical Image Computing and Computer-Assisted Intervention (MICCAI)* (Springer, Berlin, 2007), pp. 136–143
35. J.A. Wong, R. Yee, J. Stirrat, D. Scholl, A.D. Krahn, L.J. Gula, A.C. Skanes, P. Leong-Sit, G.J. Klein, D. McCarty et al., Influence of pacing site characteristics on response to cardiac resynchronization therapy. *Circ. Cardiovasc. Imaging* **6**(4), 542–550 (2013)
36. Q. Zhang, R. Eagleson, T. Peters, Real-time visualization of 4D cardiac MR images using graphics processing units, in *IEEE International Symposium on Biomedical Imaging: Nano to Macro*, pp. 343–346 (2006)
37. Q. Zhang, Y. Zhou, C.-M. Yu, Incidence, definition, diagnosis, and management of the cardiac resynchronization therapy nonresponder. *Curr. Opin. Cardiol.* **30**(1), 40–49 (2015)

# Chapter 4

## CFD-Based Postprocessing of CT-MRI Data to Determine the Mechanics of Rupture in Abdominal Aortic Aneurysms



Tejas Canchi, Eddie Y. K. Ng, Ashish Saxena, and Sriram Narayanan

**Abstract** Multimodality imaging techniques are becoming the norm in medical imaging. Using a combination of techniques, clinicians can make a more informed diagnosis. In the case of abdominal aortic aneurysms (AAA), a combination of CT and MRI imaging techniques is used to diagnose and subsequently decide on surgical intervention. Clinicians use a maximum transverse diameter metric of 55 mm to recommend surgery in AAA patients based on the images obtained. However, the clinical metric by itself is not sufficient to prognose rupture. Hence, a mechanics-based approach can be employed to extract biomechanical parameters such as wall shear stress and principal stresses to predict rupture well in advance. With the application of computational fluid dynamics (CFD), these parameters can be estimated from a fluid–structure interaction (FSI)-based analysis of the abnormal aorta. Patient-specific geometry and boundary conditions such as velocity, pressure, and material properties are used in these methods. In this chapter, an FSI-based approach to study the rupture mechanics of AAA is discussed in detail. Subsequently, the need of studying AAA in Asian population is outlined and a case study is presented on a patient-specific model to illustrate the mechanics-based approach in predicting rupture in AAA. Results from the case study reveal that the maximum transverse diameter is not the sole determinant of AAA rupture risk. Hence, mechanics-based method supplements the image-based techniques for better patient management.

**Keywords** Abdominal aortic aneurysm · Multimodal imaging · CFD · Rupture risk assessment · Patient-specific

---

T. Canchi · E. Y. K. Ng (✉) · A. Saxena  
School of Mechanical and Aerospace Engineering, Nanyang Technological University, Singapore, Singapore  
e-mail: [mykng@ntu.edu.sg](mailto:mykng@ntu.edu.sg)

S. Narayanan  
Department of General Surgery, Tan Tock Seng Hospital, Singapore, Singapore

## 4.1 Abdominal Aortic Aneurysms (AAA): Causes and Its Rupture

According to the World Health Organization, an estimated 17.5 million people died from cardiovascular diseases (CVDs) in 2012. This is equivalent to 31% of all global deaths during that year [1]. CVDs are the leading cause of death globally except for Africa [2]. There are several risk factors that are believed to contribute to the development of cardiovascular disease. Some examples of these risk factors are physical inactivity, unhealthy diet, cholesterol, raised blood pressure and hypertension, obesity, smoking, etc. [3]. These risk factors may trigger certain adverse conditions within the vascular system such as stenosis and aneurysms. CVDs are diagnosed using an array of laboratory tests and imaging studies. Cardiac magnetic resonance imaging (MRI), chest X-ray, echocardiography (ECG), and computed tomography (CT) are some of the common imaging methods that are commonly used for diagnosis in clinical settings [4].

Aneurysm is a type of CVD that is prevalent in the aorta, the main artery (blood vessel carrying oxygenated blood) that pumps blood to all the parts of the body. Aneurysms in the cardiovascular system are abnormal dilations of a specific region of the aorta. It can be formed at several locations along the aorta that stretches from the exit of the heart down to the iliac bifurcation, leading to weakening of the wall and eventually rupture. This can be attributed to several pathophysiological, biomechanical, and genetic factors that aid in the genesis, growth, and eventual rupture. Once diagnosed, clinicians use size metrics corresponding to the type of aneurysm in recommending surveillance or surgery.

### 4.1.1 Types of Aneurysms

There are several types of aneurysms that occur in the body. The types that have highest incidence are described below.

- (a) *Cerebral aneurysm*: Cerebral aneurysm (also known as intracranial aneurysm) is a dilation of a weak region of the blood vessel in the brain. The dilation results in a balloon shaped aneurysm. Rupture of this dilation releases blood in to the subarachnoid space of the brain causing a hemorrhage. Cerebral aneurysms are asymptomatic unless there is a large dilation or rupture. Cerebral aneurysms generally occur in the area around the circle of Willis. This area is a junction of arteries that supply the brain with nutrition. Hence, this is a susceptible area for the weakening of the arterial wall. The likely causes of a cerebral aneurysm include advanced age, smoking, atherosclerosis, high blood pressure, or possible injury to the blood vessel. The diagnosis may be carried out using one or more imaging techniques, namely, CT scans, cerebral angiographies, or MRI. Surgical intervention is done through clipping of the dilated region or

endovascular coiling where a catheter coil is inserted into the dilated region preventing entry of blood. Cerebral aneurysms can be of two types: saccular or fusiform. In a saccular aneurysm, the dilation is on one side of the artery like a hanging fruit. On the other hand, in a fusiform aneurysm, the entire artery dilates along the transverse direction.

- (b) *Thoracic aneurysm*: It is a type of aneurysm where the thoracic aorta dilates to a diameter of more than 4.5 cm. Thoracic aneurysm diameters may go up to a value of 65 mm [5]. The thoracic aorta is composed of the ascending aorta, descending aorta, and the aortic arch. The aneurysms may occur in any of these segments and in some cases in all of them. Patients with thoracic aortic aneurysms may also have an abdominal aortic aneurysm. Sixty percent of thoracic aortic aneurysms involve the aortic root and/or ascending aorta, 40% involve the descending aorta, 10% involve the arch, and 10% involve the thoracoabdominal aorta (with some involving >1 segment) [6]. The etiology, natural history, and treatment of thoracic aneurysms differ for each of these segments. Aneurysms in the ascending aorta grow up to 60 mm where it is prone to rupture risk. Similarly, for descending aortas, the critical size is 70 mm [7]. CT and MR angiographies are generally used in the diagnosis of thoracic aneurysms.
- (c) *Abdominal Aortic Aneurysms (AAA)*: It is a localized enlargement of the abdominal aorta. Under this condition, the diameter of the aorta enlarges by 50% or more of its normal size [8]. AAA has caused 1.3% of all deaths among men aged 65–85 years in developed countries. It is listed as the 13th most common form of mortality in the Western world. Men are at a higher risk of developing AAA, almost four times more likely, as compared to women. The risk of women developing AAA increases with their age, where they tend to have this condition at an older age than men [9]. AAA is known to be a silent killer as diagnosis is mostly accidental and no symptoms are exhibited before rupture, and hence mortality is high.

### 4.1.2 Causes of AAA

Although the main cause of AAA remains unclear, it has been considered to be caused by a complex interaction among several risk factors, which are genetic, biomechanical, and pathophysiological. Within the risk factors, there are some factors that have shown a more direct connection to the development of AAA. Those factors are acute infection (brucellosis), chronic infection (tuberculosis), inflammatory disease, and connective tissue disorder. These factors change the level of collagenase and elastase. By doing so, they may indirectly lead to the weakening of the aortic wall. Normal aging and hypertension can also weaken the wall of the aorta [10]. Atherosclerosis affects the endothelium of the aortic wall leading to its weakening. Over a period and under the pressure of blood flow, an aneurysm can develop at a weak region of the abdominal aorta. Studies have shown that by

**Table 4.1** Percentage incidence of various diseases reported at Texas Heart Institute

Cause	Percentage incidences (%)
Atherosclerosis	69.5
Medial cystic degeneration	8.9
Congenital disease	6.0
Annuloaortic ectasia	3.7
Myxomatous degeneration	3.0
Marfan syndrome	2.7
Trauma	2.2
Infection	1.0
Other	2.3

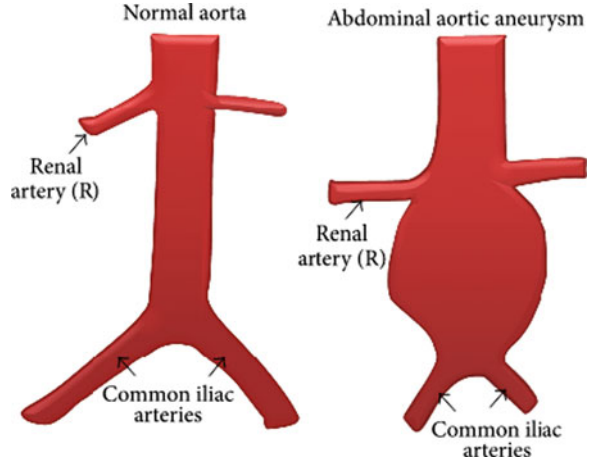
having a higher mean blood pressure, the risk of AAA formation increases. The expansion rate of an aneurysm is another aspect that needs to be considered to determine a suitable time for surgical intervention. Once initiated, it has been seen that the expansion rate of an AAA is exponential [11]. Due to this, there would be major implications in healthcare delivery. A list of other condition which can be possible causes of AAA has been tabulated by Texas Heart Institute based on available patient data [12] (Table 4.1).

### 4.1.3 Rupture in AAA

AAA is an asymptomatic disease commonly occurring in male patients who are 55 years and above in age [13]. The aneurysm is most commonly formed at the aortic site between the lower renal artery and the iliac bifurcation. The infrarenal aorta dilates to more than two times its original diameter that leads to weakening of the arterial wall and eventually to rupture (Fig. 4.1). Pathophysiological and biomechanical factors contribute to the rupture of the AAA. These include advanced age, greater height, coronary artery disease, atherosclerosis, high cholesterol levels, hypertension [14], and smoking [15, 16]. Rupture risk of AAA has always been linked to their size. The clinical metric used for surgical intervention is the maximum transverse diameter (DAAA). Being the diameter of the AAA lumen, DAAA is measured along the central lateral axis. Currently, the decision to surgically intervene is made based on the maximum transverse diameter of the aneurysm, with the threshold being 55 mm [17]. Surgical intervention in the form of the Endovascular Aneurysm Repair (EVAR) procedure involves insertion of a stent graft to restore the structural integrity of the aorta. However, there are numerous cases where patients with a small AAA (maximum diameter of less than 55 mm), still had their aneurysms ruptured. Conversely, large aneurysms having maximum transverse diameters of the order of 75 mm have not ruptured [18].



**Fig. 4.1** Normal abdominal aorta and Abdominal Aortic Aneurysm



When there is an aneurysmal dilation, there is a change in shape thereby altering the flow physics within the lumen. The flow of blood induces shear stress on the aortic wall, known as the wall shear stress (WSS). The WSS in combination with the structural stresses (coupled stresses) induced at the wall lead to further weakening of the wall, and eventually to rupture. Rupture of the wall occurs when the coupled stresses due to the interaction between the aortic wall and blood flow exceeds the strength of the wall. Therefore, imaging-based biomechanical modeling can aid clinicians to predict the risk of rupture by considering parameters such as the wall shear stress and the principal stress.

#### **4.1.4 AAA Incidence in the Asian Population**

There have been numerous studies quantifying the incidence of AAA in the Caucasian population. Retrospective studies have looked at the Asian demographic in several locations to bring out the incidence of AAA in the Asian population. Li et al. [19] reported prevalence of AAA considering 56 studies. The prevalence in Asians was 0.5% as against 2.2% and 2.5% for American and European patients, respectively. This has been corroborated by Guo and Zhang [20], where in a study covering 23,810 patients, the prevalence was seen to be 0.11%. The incidence in Chinese men was 0.18%, whereas it was 0.07% in Chinese women. Other studies done earlier in Japan reported incidence of about 0.36% [21, 22], while in Korea it has been seen to be 0.55% [23]. In a study done in Malaysia, Yii [24] reported that among 123 patients in the Sarawak region of Borneo, incidence among high-risk males and females were 25.6 and 7.6, respectively, per 100,000. In the Caucasian population, a similar metric has shown to range from 3.0 to 117.2 per 100,000.

## 4.2 AAA Rupture Analysis Using Computational Methods

Computational method-based analysis on AAA can be performed using solid mechanics, fluid mechanics, or a combination of these methods, known as fluid–structure interaction [25–28]. Computational solid mechanics based equations have been used to quantify stress development in the arterial wall [29–32]. Initial research considered either only the fluid or the solid mechanics of the AAA separately, using CFD and finite element analysis (FEA) methods. Since the arterial wall is not rigid, it responds to the blood flow in the artery. Therefore, fluid–structure interaction (FSI) is a suitable approach to derive a physiologically accurate solution. This was first investigated by Di Martino et al. [33] using an arbitrary Eulerian Lagrangian (ALE) method to accurately determine an FSI solution. Additional studies carried out by Scotti et al. [34, 35] that considered the movement of the wall, estimated the stress values to be 20% more than a rigid simulation. Applying a varying wall thickness also increased the von Mises stress in the aneurysm model. This was reinforced by Papaharilaou et al. [36], where the authors have reported a 12.5% difference in peak stress when a decoupled FSI solution was incorporated. Figueroa et al. [37] formulated a coupled momentum method (CMM) for FSI problems using the stabilized FEM. Investigating the flow physics in the AAA under rest and exercise conditions, the authors have quantified the changes in stress. It was observed that during exercise, the deformation of the wall is no longer occurring in a radial expansion and contraction fashion, but rather as a net motion forward and backwards due to the much larger inertial forces exerted on the wall by the impinging blood stream. In an FSI study, Li and Kleinstreuer [38] observed that a large neck angle of the aneurysm may cause strong irregular vortices in the AAA lumen and may influence the wall stress distribution by increasing it as much as 40%.

As has been seen from prior studies, FSI analysis provides a more realistic evaluation of the stresses induced in AAA. It provides insight into the mechanics of rupture by considering both the structural and fluid solutions as against exclusively one of them, or even the use of only maximum transverse diameter as a metric to determine rupture. In the following sections, several steps involved in solving an FSI problem are described in brief. Further, a case study is included, wherein implementation of these steps on an Asian patient is demonstrated. A discussion on the results so obtained to bring out the importance of employing mechanics-based methods in studying AAA rupture risk is also presented.

## 4.3 Model Preparation

As shown in Fig. 4.2, a three-dimensional (3D) model is supposed to be reconstructed from the Computed tomography (CT) images of the patient’s abdominal aorta. Following on, image segmentation would be done on the CT images to convert the patient 2D aorta geometry into 3D models using image reconstruction

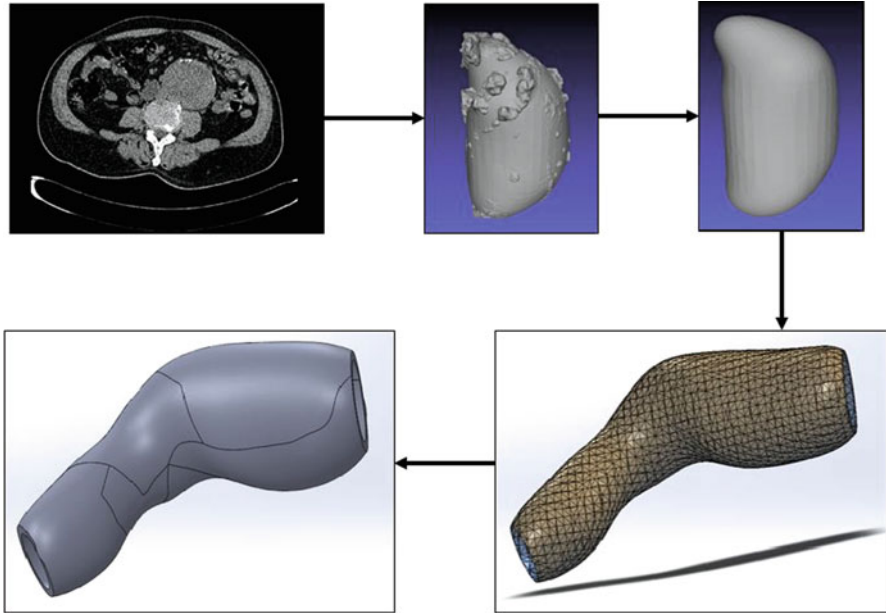


**Fig. 4.2** Geometry reconstruction—from 2D CT images to final model through segmentation

techniques. However, the converted 3D model contains artifacts due to manual segmentation, and hence the surface of the aorta is not suitable for meshing. Therefore, this model must go through refinement using MeshLab to smoothen the features of the aorta. The resultant model is a mesh file without a thickness. This model file must be converted from a mesh file to a Structural Solidworks Part File to be used in both ANSYS Structural and Fluent.

### **4.3.1** *Image Extraction: CT Images*

The most effective method of performing a CT scan is the helical (spiral) scan, where the source of X-rays and the detector rotate around a common axis over a slip ring and the patient lying on a table is made to move along the same axis of rotation [39]. Despite the risk of radiation-induced malignancy, a CT scan is one of the most preferred imaging tools because of its excellent spatial and temporal resolution which allows for an accurate reconstruction of the thin transverse sections of abdominal aortas or other similar geometries [40]. For AAA diagnosis, the most widely accepted method is contrast enhanced CT scanning [41, 42]. With the helical rotation of the detector and the translational movement of the patient, a series of 2D images (in slice mode) are consecutively acquired along the length of the aorta. These series of images are then digitally processed to make a 3D model as described in the next section.

### ***4.3.2 Image Segmentation***

To convert 2D CT images to a 3D model, image segmentation software such as MIALite is used. A threshold-based segmentation method is used, which extracts the geometry based on the contrast level in the CT images. First, all the 2D CT images are loaded onto MIALite. Next, the lower and upper contrast threshold level is defined. Following this process, MIALite requires the user to define the seed region to segment the model and define a block region beyond which the seed would not be allowed to propagate. Finally, the seed will begin to propagate within the region. This process is followed for all the image slices in the region of interest, which ultimately results in a 3D mesh model.

### ***4.3.3 Mesh Model Refinement***

The 3D mesh file generated by MIALite has artifacts on the model which are not smooth and may consist of extra regions that are not related to the aorta. These extra regions result from the poor contrast between the aorta and the surrounding region in the CT images. To obtain a more accurate aorta model, the 3D mesh file from MIALite will have to undergo a series of refinements in a software application such as MeshLab [43]. Within MeshLab, the unwanted region on the 3D model are trimmed and smoothed, using Poisson or Gaussian filters. From Fig. 4.2, it can be observed that the unedited model consists of a lot of debris and uneven surfaces, whereas the refined model is a smooth surface suitable for meshing.

### ***4.3.4 Conversion of Mesh Model File for Analysis Compatibility***

After the refinement process, the resulting 3D model is a mesh model file that does not contain a thickness. Given that ANSYS Structural does not support such a geometry file, a file type conversion is required. A plugin within Solidworks™ (Dassault Systemes Corporation, Waltham, MA) called Scanto3D can be used to convert the 3D mesh file into a Solidworks™ part file which is supported by ANSYS Structural. To do this, firstly, the mesh model must be loaded in Solidworks™ using the Scanto3D plugin. The surfaces can then be created based on the mesh model through the surface wizard function. Next, the mesh model is deleted, and the remaining surfaces undergo a series of surface merging and trimming operations. This is done to achieve a physiologically accurate geometry. Lastly, a wall thickness is introduced to the geometry to model the structural mechanics. Figure 4.2 shows the final model with surfaces created from the mesh model.

## 4.4 Numerical Methodology

### 4.4.1 Governing Equations

The properties of blood in the simulations can be assumed to be Newtonian and incompressible. The Newtonian assumption for blood has been seen to be consistent for large arteries [44]. The inlet flow should be taken as pulsatile to be physiologically accurate. Fluid–structure coupling of the aneurysmal wall motion and blood flow can be done using the arbitrary Lagrangian Eulerian (ALE) method. The incompressible continuity and the Navier–Stokes equations in ALE form can be expressed as

$$\nabla \cdot u = 0 \quad (4.1)$$

$$\rho_f \left( \frac{\partial u}{\partial t} + ((u - u_g) \cdot \nabla) u \right) = -\nabla p + \mu \nabla^2 u \quad (4.2)$$

where  $\rho_f$ ,  $p$ ,  $u$ , and  $u_g$  are the fluid density, the pressure, the fluid velocity, and the moving coordinate velocity, respectively. In the ALE formulation, the term  $(u - u_g)$ , which is the relative velocity of the fluid with respect to the moving coordinate velocity, is added to the conventional Navier–Stokes equations to account for movement of the mesh [45]. The values of  $\rho_f$  and  $\mu$  can be taken as  $1060 \text{ kg/m}^3$  and  $0.0035 \text{ Pa}\cdot\text{s}$  for blood. The SIMPLE method [46] can be used with a time step calculated from the patient-specific heart rate for the transient fluid solution. The transient structural solver and the fluid solver can be used in the ANSYS Workbench suite.

### 4.4.2 Boundary Conditions: Phase Contrast Magnetic Resonance Imaging (PC-MRI)

PC-MRI is used to extract the inlet velocity boundary conditions to solve the governing partial differential equations in Sect. 4.3.1. The patient-specific inlet and outlet boundary conditions are applied through a user-defined function (UDF) script in ANSYS [47]. The walls are bounded by a no-slip condition. An FSI interface should be defined at the inner wall of the aneurysm lumen through the system coupling function of ANSYS Workbench. For the arterial wall, the density can be taken as  $1120 \text{ kg/m}^3$  [48]. By assuming isotropic elasticity, the value of the Young's modulus can be taken as  $4.5 \text{ MPa}$  and Poisson's ratio to be  $0.45$  [49].

### 4.4.3 Mesh Generation—Independence Studies

To solve the governing equations, the reconstructed geometry is required to be meshed. Since the governing equations are coupled to solve the fluid and structure models simultaneously, meshing should be done separately for the fluid and structural parts. For this, firstly the internal fluid part is meshed and then the walls with thickness are meshed using a commercial meshing software such as ICEM or ANSYS workbench mesher. The meshed geometry is then used in the coupled system to solve the FSI problem. As a part of the verification process, different mesh sizes should be investigated to prove the mesh independence of the solver. To do so, the problem should be solved over different meshes, ranging from coarse to fine and a solution parameter such as wall shear stress should be considered to calculate the error between consecutive meshes. A mesh with no significant change in the calculated error is chosen for use in the simulation.

## 4.5 Case Study

### 4.5.1 Background

In the case study presented, CT angiographic images from a patient with AAA were obtained from the IRB-approved vascular database of Tan Tock Seng Hospital, Singapore. CTA images reveal that the patient had developed a small aneurysm with a DAAA of 35 mm. The obtained patient CT images were subjected to a series of segmentation steps using the open source application MIALite™. The resulting geometry was then smoothed using MeshLab. The resulting *.stl* file was exported to SolidWorks (Dassault Systemes Corporation, Waltham, MA) wherein a constant thickness of 2 mm was added to make it suitable for the FSI problem.

Meshing was carried out using the commercial software ICEMCFD in ANSYS Workbench 16.1 (Canonsburg, PA) (Fig. 4.3). The intraluminal thrombus (ILT) was not considered in this geometric model. A tetrahedral mesh was created for the structural wall and a volumetric hexahedral mesh for the fluid part. Three meshes of element count 0.80, 2.02, and 3.34 million are created to perform the mesh independence study. In the present study, the inlet and outlet boundary conditions were defined to be pulsatile with waveforms being extracted from literature as shown in Fig. 4.4 [47]. The integral wall shear stress in the fluid was chosen as the parameter of interest. The variation of the integral wall shear stress was recorded for three cardiac cycles and compared in the different mesh sizes as shown in Fig. 4.5.

From Table 4.2, it can be noted that the percentage error from the coarse mesh to normal mesh is 4.16% in the integral wall shear stress, while there is no error between normal and fine mesh. Therefore, the 2.02 million element mesh was used for the final simulations.

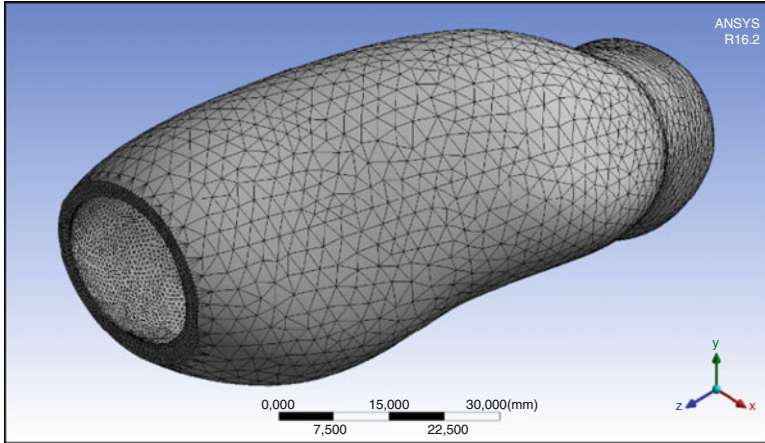


**Fig. 4.3** Structural mesh of AAA geometry from the sample patient

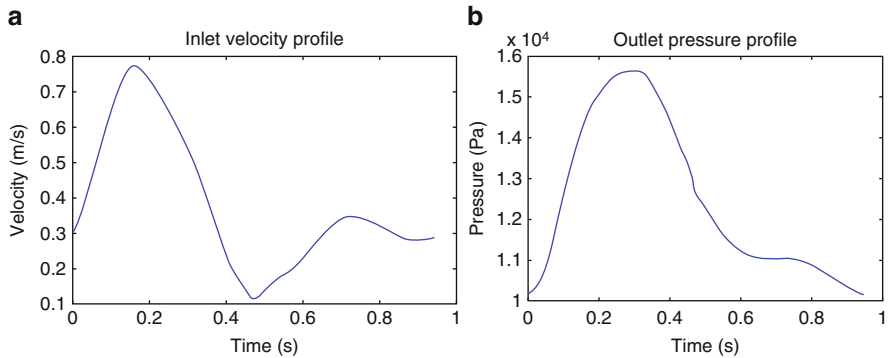


**Fig. 4.4** (a) Inlet velocity boundary condition waveform. (b) Outlet pressure boundary condition waveform

## 4.5.2 Results and Discussion

The present study is an attempt to estimate the mechanics of rupture of AAA using the FSI method. FSI analysis of AAA will aid in this pursuit and eventually improve point of care technologies for the patients. The arterial wall being a nonrigid entity is subject to interaction with the fluid flow and vice versa. Hence, to incorporate the deformation of arterial wall under blood flow, this problem requires an FSI solution to investigate the effect of the moving arterial wall in the estimation of rupture risk. Clinical measurements were available for the patient from records. Pressure data at the inlet to the AAA, lumen neck, and center of the lumen were available for comparison. But these were numerical values as against waveforms as shown in Table 4.3. Hence, a steady flow simulation was carried out for validation using these

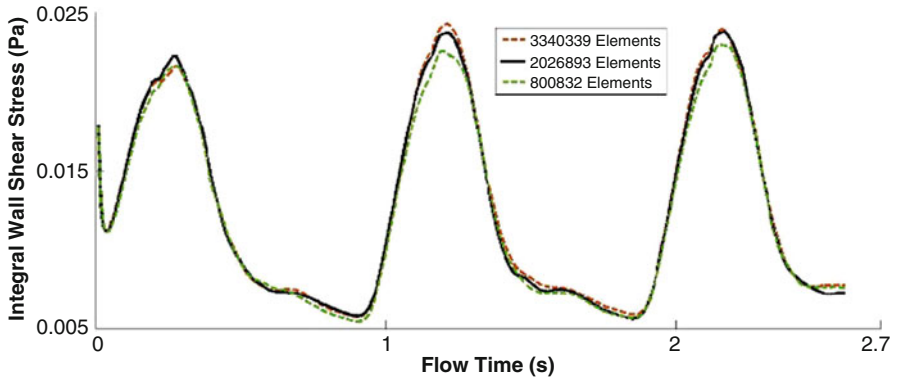


**Fig. 4.5** Integral wall shear stress variation for three mesh sizes (Pa)

**Table 4.2** Wall shear stress for the mesh independent study

Mesh size	Number of elements (millions)	Maximum integral wall shear stress at systole of third cardiac cycle (Pa)	Percentage difference to normal mesh
Fine	3.34	0.024	0%
Normal	2.02	0.024	0%
Coarse	0.80	0.023	4.16%

**Table 4.3** Validation comparison

Patient 1	Simulation pressure (Pa)	Measurement pressure (Pa)	Error (%)
Inlet	12,990	12,665.62	2.56
At lumen neck	12,970	12,932.27	0.29
Center of the lumen	13,000	13,065.59	0.50

parameters. The location below the renal artery was the inlet plane to the AAA. The validation showed that the error percentages are well within limits. The highest error in simulation was 2.56% at the inlet.

The deformation, maximum principal stress, and maximum shear stress were extracted in the structural domain while the integral wall shear stress was the parameter of interest in the fluid domain. Also, the velocity streamlines and pressure distribution over the arterial wall was quantified in each patient. FSI simulations were carried out for three cardiac cycles measuring 0.9 s each. The plots were generated at systole in the third cardiac cycle. This was done to damp out any initial transients resulting from the computational method.

Using the failure theories of mechanics, namely, the maximum principal stress theory and maximum shear stress theory, the parameters causing a significant effect on the rupture risk of the AAA are first principal stress and wall shear stress. In the maximum principal stress theory, the material would fail if the maximum principal



stress induced exceeds the maximum normal strength of the material. As per the maximum shear stress theory, the material would fail if the maximum shear stress suffered exceeds the maximum allowable shear stress.

Hence, it is important to observe the results of the maximum shear and principal stresses in the structural domain to comment on the rupture risk. In the same manner, for a strongly coupled solution, the wall shear stress induced in the fluid domain would be important, affecting the results in the structural domain.

#### 4.5.2.1 First Principal Stress (Structural Domain)

The first principal stress is a suitable metric to determine the peak stress that is being induced in the arterial wall. Principal stresses are the normal stresses acting on the arterial wall. The forces acting on the arterial wall is the pressure load from the fluid, and hence the principal stresses are the indicators of the stress distribution that may lead to rupture of the abdominal aortic wall. The location of the highest principal stresses on the arterial wall is usually seen to be in the antero-distal region of the AAA lumen. Figure 4.6 shows the distribution of the first principal stresses in the patient studied. As seen from the figure, the regions of maximum principal stress induced in the patient are clearly marked out as the ones in red. From structural failure theories, we can deduce that these regions may be most susceptible to rupture. The principal stresses developed in the present patient's aorta are in the same range as those induced in Caucasian aortas (0.2–0.4 MPa). For the patient under study, a maximum principal stress of 0.3 MPa is deduced from the FSI simulation results.

**Fig. 4.6** Spatial distribution of first principal stresses at the AAA wall (Pa)

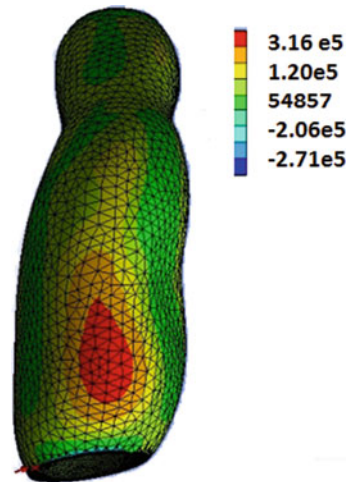
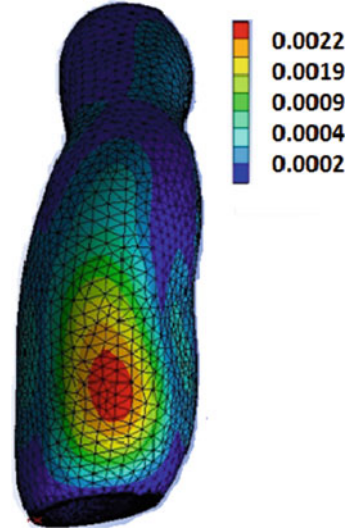


**Fig. 4.7** Spatial distribution of the AAA wall displacement (m)



#### 4.5.2.2 Structural Deformation

This study accounts for the interaction between the fluid and the structure considering the arterial wall as a nonrigid entity. The ALE method, which involves a strongly coupled solution, exchanges the structural deformation value with the fluid in every time step. Therefore, the structural deformation value is an important parameter in this simulation. As shown in Fig. 4.7, the maximum deformation of the arterial wall is 0.0022 m and its location are aligned with the location of the maximum principal stresses. As the arterial wall is weakened during the progression of the disease, the deformation at the site of the high principal stress promotes the tendency to rupture.

#### 4.5.2.3 Wall Shear Stress (WSS) (Fluid Domain)

Wall shear stress is induced by the fluid on the arterial wall. The values of WSS are extracted from the fluid solution in the FSI simulation. Being challenging to quantitatively measure the WSS *in vivo*, CFD-based computational methods make an attractive choice. Figure 4.8 shows the induced WSS in the patient. The induced peak WSS on the arterial wall is 18.74 Pa. The location of peak wall shear stress is not at the same location as that of the peak first principal stress. It is also clear from the pressure distribution that the sites of integral wall shear stress and the pressure are correlated. This is in agreement with the work of Boyd et al. [50], where it is reported that low wall shear stresses dominate sites of rupture in AAA.

**Fig. 4.8** Spatial distribution of WSS (fluid) at the arterial wall (Pa)

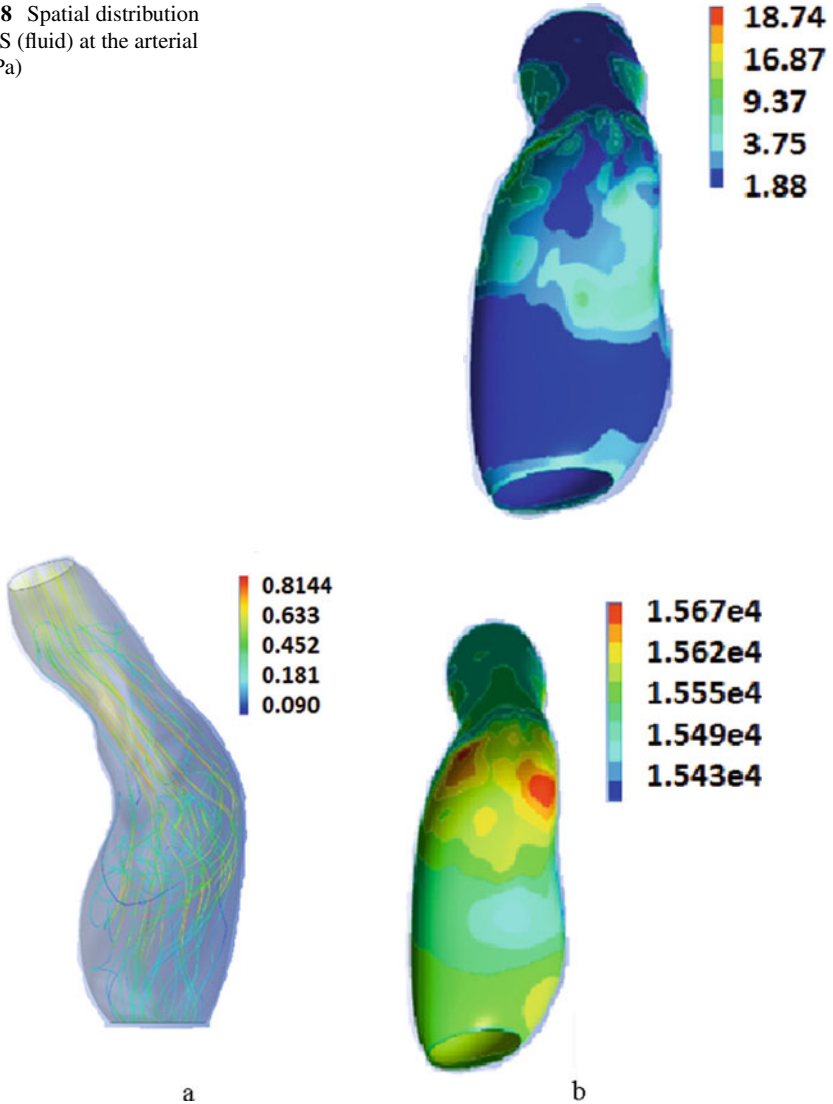


**Fig. 4.9** (a) Velocity streamlines in the fluid domain (m/s). (b) Pressure distribution in the fluid domain (Pa)

#### 4.5.2.4 Velocity and Pressure (Fluid Domain)

Velocity streamlines extracted from the simulation (Fig. 4.9a) provide insight into how the fluid is inducing pressure on the arterial wall. The changed geometry of the diseased aorta as compared to the healthy aorta induces vorticity in the fluid. Flow vortices that are formed at the beginning of the cycle due to the geometry of the

aneurysm migrate distally as the flow decelerates from peak systolic conditions to diastole. Initially, there is attached flow near the proximal end of the aneurysm but by peak systole there is a separation of the vortices from the wall. As the fluid moves from the proximal to the distal region of the AAA model, owing to a relatively less visible neck region and a lower lumen curvature, this effect is found to be less dominating in smaller aneurysms.

Figure 4.9b shows the distribution of pressure over the arterial wall as computed in the fluid domain. When compared to the structural stress distribution, it is observed that the sites of the highest structural stresses are not the same as those having irregular vortical flow or those with high fluid WSS. One possible reason could be the nonrigid treatment of the arterial wall that induces nonuniform stress distributions due to the pulsatile nature of flow in the lumen.

### 4.5.3 *Limitations*

There are a few limitations to this study. The inlet and outlet boundary conditions used have been extracted from literature and are not patient specific. While nonuniform wall thickness values could affect the stress distribution on the arterial wall, use of a constant wall thickness is another limitation of the present study. A nonlinear material model is expected to improve the accuracy of the response of the arterial wall. Nevertheless, an FSI-based solution is an important step towards determining the actual interaction between the arterial wall and blood flow, which will assess rupture risk in an Asian AAA. A more detailed patient-specific model, inclusive of an FSI modeling approach, can further enrich AAA rupture risk prediction.

## 4.6 **Conclusions**

In this chapter, an FSI-based AAA rupture risk evaluation method is described. This method employs both fluid and structural-based models to study the biomechanics of a patient specific abdominal aortic aneurysm. A brief account on AAA rupture prognosis and its prevalence in Asian population is provided. This study is the first of its kind to aim at establishing the biomechanical parameters for Asian AAA. As established from literature, the incidence of AAA in Asian population is low; however, owing to its prevalence, it is important to establish a biomechanical model for the Asian population specific AAA. This can be done using an FSI-based computational method that incorporates the movement of the arterial wall and its interaction with the blood flow in the AAA lumen. As part of case study, an FSI analysis of an Asian AAA patient is presented. A two-way FSI problem was formulated based on boundary conditions extracted from literature. To carry out an evaluation on the mechanics of rupture in the patient model, biomechanical stress parameters such as maximum first principal stress and total deformation in

the structural domain, and integral wall shear stress along with pressure and velocity distributions in the fluid domain were analyzed. Incorporating the biomechanics in the prognosis could be a step forward in minimizing the risk of surgical intervention and bringing down the healthcare costs for AAA patients.

## References

1. World Health Organization, Cardiovascular Diseases (2015) [Online]. Available: <http://www.who.int/mediacentre/factsheets/fs317/en/>. Accessed 19 July 2017
2. S. Mendis, P. Puska, S. Mendis, P. Puska, B. Norrving (eds.), *Global Atlas on Cardiovascular Disease Prevention and Control* (World Health Organization, Geneva, 2011)
3. D.A. Vorp, Biomechanics of abdominal aortic aneurysm. *J. Biomech.* **40**(9), 1887–1902 (2007)
4. A. Mandal, Cardiovascular Disease Diagnosis (2012). [Online]. Available: <http://www.news-medical.net/health/Cardiovascular-Disease-Diagnosis.aspx>. Accessed: 19 July 2017
5. J.A. Elefteriades, A. Sang, G. Kuzmik, M. Hornick, Guilt by association: paradigm for detecting a silent killer (thoracic aortic aneurysm). *Open Hear.* **2**(1), e000169 (2015)
6. E.M. Isselbacher, Thoracic and abdominal aortic aneurysms. *Circulation* **111**(6), 816–828 (2005)
7. R. Erbel, H. Eggebrecht, Aortic dimensions and the risk of dissection. *Heart* **92**(1), 137–142 (2006)
8. K. Shimizu, R.N. Mitchell, P. Libby, Inflammation and cellular immune responses in abdominal aortic aneurysms. *Arteriosclerosis, thrombosis, and vascular biology* **26**(5), 987–994 (2006)
9. J.E. Starr, V. Halpern, Abdominal aortic aneurysms in women. *J. Vasc. Surg.* **57**(4 Suppl), 3S–10S (2013)
10. L.C. Brown, J.T. Powell, Risk factors for aneurysm rupture in patients kept under ultrasound surveillance. UK Small Aneurysm Trial Participants. *Ann. Surg.* **230**(3), 287–289 (1999)
11. J. Cronenwett et al., Actuarial analysis of variables associated with rupture of small abdominal aortic aneurysms. *Surgery* **98**, 472–783 (1985)
12. J. Livesay, G. Messner, W. Vaughn, Milestones in treatment of aortic aneurysm milestones in the treatment of aortic aneurysm. *Texas Hear. Inst. J.* **32**(2), 130–134 (2005)
13. S.S. Raut, S. Chandra, J. Shum, E.A. Finol, The role of geometric and biomechanical factors in abdominal aortic aneurysm rupture risk assessment. *Ann. Biomed. Eng.* **41**(7), 1459–1477 (2013)
14. J. Earle Estes, Abdominal aortic aneurysm: a study of one hundred and two cases. *Circulation* **II**, 258–264 (1950)
15. E.L. Chaikof et al., The care of patients with an abdominal aortic aneurysm: The Society for Vascular Surgery practice guidelines. *J. Vasc. Surg.* **50**(4 Suppl), S2–S49 (2009)
16. F.A. Lederle, D.B. Nelson, A.M. Joseph, Smokers' relative risk for aortic aneurysm compared with other smoking-related diseases: a systematic review. *J. Vasc. Surg.* **38**, 329–334 (2003)
17. J.T. Powell, Mortality results for randomised controlled trial of early elective surgery or ultrasonographic surveillance for small abdominal aortic aneurysms. *Lancet* **352**, 1649–1655 (1998)
18. R.C. Darling, C.R. Messina, D.C. Brewster, L.W. Ottinger, Autopsy study of unoperated abdominal aortic aneurysms. The case for early resection. *Circulation* **56**, 161–164 (1977)
19. X. Li, G. Zhao, J. Zhang, Z. Duan, S. Xin, Prevalence and trends of the abdominal aortic aneurysms epidemic in general population—a meta-analysis. *PLoS One* **8**(12), 1–11 (2013)
20. W. Guo, T. Zhang, Abdominal aortic aneurysm prevalence in China. *Endovasc. Today.* (February), 76–82 (2014)

21. K. Adachi, T. Iwasawa, T. Ono, Screening for abdominal aortic aneurysms during a basic medical checkup in residents of a Japanese rural community. *Surg. Today* **30**(7), 594–599 (2000)
22. S. Ishikawa et al., The characteristics of screened patients with abdominal aortic aneurysms. *Int. Angiol.* **20**, 74–77 (2001)
23. S.H. Oh et al., Routine screening for abdominal aortic aneurysm during clinical transthoracic echocardiography in a Korean population. *Echocardiography* **27**(10), 1182–1187 (2010)
24. M.K. Yui, Epidemiology of abdominal aortic aneurysm in an Asian population. *ANZ J. Surg.* **73**(6), 393–395 (2003)
25. H. Li, K. Lin, D. Shahmirzadi, FSI Simulations of Pulse Wave Propagation in Human Abdominal Aortic Aneurysm: The Effects of sac geometry and stiffness. *Biomedical Engineering and Computational Biology.* **7**, 25–36 (2016) doi:[10.4137/BECB.S40094](https://doi.org/10.4137/BECB.S40094)
26. B. Trachet et al., An animal-specific FSI model of the abdominal aorta in anesthetized mice. *Ann. Biomed. Eng.* **43**(6), 1298–1309 (2015)
27. D. Bianchi, E. Monaldo, A. Gizzi, M. Marino, S. Filippi, G. Vairo, A FSI computational framework for vascular physiopathology: a novel flow-tissue multiscale strategy. *Med. Eng. Phys.* **47**, 25–37 (2017)
28. S. Lin, X. Han, Y. Bi, S. Ju, L. Gu, Fluid-structure interaction in abdominal aortic aneurysm: effect of modeling techniques. *Biomed Res. Int.* **2017** (2017)
29. J.F. Rodríguez, C. Ruiz, M. Doblaré, G.A. Holzapfel, Mechanical stresses in abdominal aortic aneurysms: influence of diameter, asymmetry, and material anisotropy. *J. Biomech. Eng.* **130**(2), 21023 (2008)
30. T. Christian Gasser, An irreversible constitutive model for fibrous soft biological tissue: a 3-D microfiber approach with demonstrative application to abdominal aortic aneurysms. *Acta Biomater.* **7**(6), 2457–2466 (2011)
31. J. Tong, T. Cohnert, P. Regitnig, G.A. Holzapfel, Effects of age on the elastic properties of the intraluminal thrombus and the thrombus-covered wall in abdominal aortic aneurysms: Biaxial extension behaviour and material modelling. *Eur. J. Vasc. Endovasc. Surg.* **42**(2), 207–219 (2011)
32. J.F. Rodriguez, G. Martufi, M. Doblare, E.A. Finol, The effect of material model formulation in the stress analysis of abdominal aortic aneurysms. *Ann. Biomed. Eng.* **37**(11), 2218–2221 (2009)
33. E.S. Di Martino et al., Fluid-structure interaction within realistic three-dimensional models of the aneurysmatic aorta as a guidance to assess the risk of rupture of the aneurysm. *Med. Eng. Phys.* **23**(9), 647–655 (2001)
34. C.M. Scotti, J. Jimenez, S.C. Muluk, E.A. Finol, Wall stress and flow dynamics in abdominal aortic aneurysms: finite element analysis vs. fluid-structure interaction. *Comput. Methods Biomech. Biomed. Engin.* **11**(3), 301–322 (2008)
35. C.M. Scotti, A.D. Shkolnik, S.C. Muluk, E.A. Finol, Fluid-structure interaction in abdominal aortic aneurysms: effects of asymmetry and wall thickness. *Biomed. Eng. Online* **4**(1), 64 (2005)
36. Y. Papaharilaou, J.A. Ekaterinaris, E. Manousaki, A.N. Katsamouris, A decoupled fluid structure approach for estimating wall stress in abdominal aortic aneurysms. *J. Biomech.* **40**(2), 367–377 (2007)
37. C. Figueroa, I. Vignon-Clementel, K. Jansen, T. Hughes, C. Taylor, in *A New Formulation to Model Blood Flow and Vessel Motion in Large, Patient-Specific Models of the Cardiovascular System*. Proceedings of the 2005 Summer Bioengineering Conference (2005), pp. 1402–1403
38. Z. Li, C. Kleinstreuer, A comparison between different asymmetric abdominal aortic aneurysm morphologies employing computational fluid-structure interaction analysis. *Eur. J. Mech. B. Fluids* **26**(5), 615–631 (2007)
39. K.J. Mortele, J. McTavish, P.R. Ros, Current techniques of computed tomography: helical CT, multidetector CT, and 3D reconstruction. *Clin. Liver Dis.* **6**(1), 29–52 (2002)
40. S.W. Stavropoulos, S.R. Charagundla, Imaging techniques for detection and management of endoleaks after endovascular aortic aneurysm repair. *Radiology* **243**(3), 641–655 (2007)

41. R. Scott, The place of screening in the management of abdominal aortic aneurysm. *Scand. J. Surg.* **97**(2), 136–138 (2008)
42. H. Hong, Y. Yang, B. Liu, W. Cai, Imaging of abdominal aortic aneurysm: the present and the future. *Curr. Vasc. Pharmacol.* **8**(6), 808–819 (2010)
43. P. Cignoni et al., in *MeshLab: An Open-Source Mesh Processing Tool*. Sixth Eurographics Ital. Chapter Conf. (2008), pp. 129–136
44. C.R. Ethier, C.A. Simmons, *Introductory Biomechanics: From Cells to Organisms* (Cambridge University Press, Cambridge, 2007)
45. T. Canchi et al., A review of computational methods to predict the risk of rupture of abdominal aortic aneurysms. *Biomed. Res. Int.* **2015**, 1–12 (2015)
46. S. Patankar, *Numerical Heat Transfer and Fluid Flow* (Hemisphere Publishing Corp., Washington, DC, 1980)
47. E. Soudah, E.Y.K. Ng, T.H. Loong, M. Bordone, U. Pua, S. Narayanan, CFD modelling of abdominal aortic aneurysm on hemodynamic loads using a realistic geometry with CT. *Comput. Math. Methods Med.* **2013**, 472564 (2013)
48. S. Pasta et al., Difference in hemodynamic and wall stress of ascending thoracic aortic aneurysms with bicuspid and tricuspid aortic valve. *J. Biomech.* **46**(10), 1729–1738 (2013)
49. G. Giannakoulas et al., A computational model to predict aortic wall stresses in patients with systolic arterial hypertension. *Med. Hypotheses* **65**(6), 1191–1195 (2005)
50. A.J. Boyd, D.C.S. Kuhn, R.J. Lozowy, G.P. Kulbisky, Low wall shear stress predominates at sites of abdominal aortic aneurysm rupture. *J. Vasc. Surg.* **62**(5), 1–7 (2015)

# Chapter 5

## Human Head Modelling Simulation Applied to Electroconvulsive Therapy



Marília Menezes de Oliveira, Bo Song, Tony Ahfock, Yan Li, and Paul Wen

**Abstract** Transcranial electrical stimulation includes electrical stimulation techniques used to treat neurological conditions. Computational human head modelling has been used to investigate diverse cases of therapies and treatments. In this chapter, 3D realistic human head models constructed from magnetic resonance images are presented for applications in electroconvulsive therapy (ECT). This technique uses low frequency and applies high amplitude current for a short period. Due to the high currents used in ECT, electrical stimulation may generate heat as per the Joule effect. Therefore, the bio-heat transfer equation coupled to the Laplace equation is implemented in a computational head model to investigate the effect of temperature due to ECT electrical stimulation. Diverse thermophysical parameters and electrode configurations are considered. The results show that, from the thermal point of view, the brain is safe and no increase in temperature is detected. Temperature rises mainly in external layers of head, such as scalp and skull while the inclusion of fat layer will influence temperature behavior. Apart from that, the inclusion of thermal anisotropic conductivity does not significantly influence temperature rise; however, electrical conductivity is an important factor to consider.

**Keywords** ECT · Temperature · FEM · Anisotropy · Human head model

### 5.1 Introduction

The human brain is always incognito and it is common to find people with some kind of neurological issues, where frequently, the problem is unknown and the treatment

---

M. M. Oliveira (✉)

The University of Sydney, Sydney, NSW, Australia

University of Southern Queensland, Darling Heights, QLD, Australia

e-mail: [marilia.menezes@sydney.edu.au](mailto:marilia.menezes@sydney.edu.au)

B. Song · T. Ahfock · Y. Li · P. Wen

University of Southern Queensland, Darling Heights, QLD, Australia

© Springer Nature Switzerland AG 2018

M. Abreu de Souza et al. (eds.), *Multi-Modality Imaging*,

[https://doi.org/10.1007/978-3-319-98974-7\\_5](https://doi.org/10.1007/978-3-319-98974-7_5)



is difficult. Pharmacotherapy is normally used to treat brain diseases; nevertheless, this is not always effective, and can sometimes cause other problems. Another type of treatment that has been used for decades is transcranial electrical stimulation (tES) [1–11], where a stimulus is delivered to the scalp or inside the head, directly to the brain. As in all kinds of treatment, side effects may also occur, but studies and practices have demonstrated promising and efficient results in many cases.

Transcranial electrical stimulation has been used to treat neurological diseases for many years. These therapies range from noninvasive techniques, such as transcranial direct current stimulation (tDCS) [12, 13], which applies low intensity direct current to the scalp; and invasive techniques, such as deep brain stimulation (DBS) [6], where electrodes are implanted in specific regions of the brain. A variety of therapies have been developed over time. Each one of them has its own unique and fundamental characteristics, while they vary in intensity, duration, frequency, and continuity, among other factors.

One of these treatments, which has been used since the 1930s [8], is known as electroconvulsive therapy (ECT). There are many polemics in the use of this technique, because whereas some people say that this technique can treat and help extreme cases of neurological diseases, others say that this technique is too aggressive, with significant side effects thus its use should be ceased.

Electroconvulsive therapy is an intervention used to treat a variety of psychiatric conditions. These disorders include depression (unipolar and bipolar), schizophrenia, bipolar mania (and mixed) states, catatonia, and schizoaffective disorder [14]. This therapeutic intervention applies an electric voltage or current to the scalp through electrodes [9]. The induced electric field is typically widespread and reaches deep brain regions [15]. The patient should receive a muscle relaxant and general anesthesia before the procedure. The stimulation is generated in cycles that vary from 0.5 to 8 second (s) of duration, the frequency fluctuates between 20 and 120 Hz, and the pulse currents diverge from 500 to 900 mA [14]. The entire procedure can be concluded in approximately 10 minutes.

Stimulus waveform, electrode placement, and stimulus dosage are factors and parameters that should be considered for the practice of ECT. The waveforms used are the sine wave, partial sine wave, brief pulses, and ultra-brief pulses. Each waveform differs in its efficiency to deliver seizures. The leading edge of each phase of the waveform is responsible for neuronal depolarization and seizure induction [14]. Seizure threshold may be estimated by determining the minimal electrical dose necessary to elicit a generalized seizure of a specified minimum duration [16]. Electrode placement and stimulus dosage parameters are also important to maximize efficacy and tolerability [9, 14]. These factors can affect the clinical outcome [14].

All these techniques use electrical current input and, in the case of electroconvulsive therapy high current is used, so particular care should be taken. As we know, when electrical current passes through a conductor, heat is generated. Temperature ( $T$ ) increases due to Joule heating and metabolic responses which are a result of electrical stimulation of tissues [4, 6]. Electrical stimulation-induced changes in temperature can profoundly affect tissue function [6]. Moreover, metabolic response occurs in the human head as a result of electrical stimulation. This heat

is distributed over body regions by blood circulation and is carried by conduction to the body surface [17]. Both effects, Joule heat and metabolic response, are causes of temperature increase [4, 6].

This study aims to investigate the distribution of temperature due to high electrical stimulation used in ECT treatments. For that, magnetic resonance imaging (MRI) data is used through which the issues of structural head model details are addressed. Finite element methods (FEM) possess the ability to consider complex geometries and anisotropic behavior without discretization errors. Taking this into account, the commercially available FE package COMSOL Multiphysics<sup>®</sup> is used to generate and map the thermal and electric field distributions. An extensive variation of models is created, altering different parameters and configurations in order to evaluate the increase in temperature. The models consider the inhomogeneous and anisotropic thermal and electrical conductivity along the tissues. Beyond that, they establish a safe input on current threshold and also the effect of biological properties is analyzed. Likewise, the chapter covers the development and construction of a realistic human head model (RHM).

## 5.2 Development of Human Head Model

The realistic human head model is developed based on MRI. Here, a detailed description is provided because of the complexity of the process and the model.

### 5.2.1 *Magnetic Resonance Images*

Before the 1980s, computerized tomography (CT) was the only technique available to clinicians to study the human brain. It used radiation doses and was insensitive to many types of lesions. After the 1980s, MRI was introduced in preference to CT scans.

MRI is a widely accepted imaging technique used to study and analyze the brain. This technique applies a strong magnetic field through an object. The idea is to align the protons of water and thus be able to map different tissues. In short, during the creation of an MRI, magnetic field gradients are applied and a coordinate system is encoded onto the object, causing the generation of an MR image [18]. It is known that each tissue contains a different quantity of water which is also what provides the contrast in the images. For instance, the brain contains more water in its constitution compared to the skull, a bone structure. The research, at present recognizes MR techniques as being safe to the human body.

Different types of images constitute the MRI: proton density (PD); T1-weighted (T1w), and T2-weighted (T2w). PD, also known as spin density, relates to the concentration of MRI-visible protons in tissue. Most of them are localized in water

and, practically, they can be seen when the acquisition has a short TE (Echo Time) and long TR (Repetition Time). If the tissue has edema, normally it will have an increase in PD, and after the treatment, a reduction in PD occurs [19]. Changes in PD are often correlated to T1w changes. The signals of T1w are usually inversely associated to the longitudinal relaxation time T1 in a nonlinear way. Biophysical properties of tissues are intrinsic to T1w. The importance of T1w is for tissue characterization, contrast agent uptake studies and to measure blood volume and perfusion. In normal tissues, T1w values are associated to macromolecule concentration, water binding, and water content. Therefore the contrast in the brain is caused by myelin making white matter (WM) have a shorter T1w than grey matter (GM) [20]. On the other hand, T2w describes the process decay of the nuclear signal, determining for how long it is possible to measure the nuclear signal. It is used mainly for qualitative diagnostic purposes [18].

## ***5.2.2 MRI Image Processing for Model Construction***

In order to develop 3D geometries from MRI images, it is necessary to follow a systemic process. A brief explanation of the procedure is shown in Fig. 5.1. The first step is the registration of images, where the T1 and T2 images need to be registered together. There are a few software packages capable of accomplishing the task, like FMRIB's Software Library (FSL) [21], 3D Slicer, MedInria, and ScanIP. FSL and ScanIP have been utilized throughout our work. Afterwards, it is necessary to conduct segmentations of the image. In this procedure, different types of tissues are identified and masks are created. Once the tissues and regions of interest are recognized and segmented, they are put together to construct the 3D geometry. Furthermore, through FE (Finite Element), the meshes are generated. Then the meshed model is ready to be exported to an FE software package, where the physics of the problem is applied and calculations are carried out. Finally, the results need to be further treated in a postprocess technique. The whole procedure is shown in the flowchart below.

### **5.2.2.1 Image Registration**

Within MRI datasets, the reconstruction of a 3D volume from the 2D images datasets is realized in order to obtain a correct 3D visualization and morphometric analysis [22], thus recognizing a model-based object. In this process, a technique called image registration is required to align images. The images are mapped spatially and in relation to intensity. The purpose of this is that they stay in the same coordinate plane while if there are any differences or feature overlaps, they are easier to visualize [23].

Methods of registration are characterized by four distinctive components and their diverse combinations. The four components are feature space, search space,

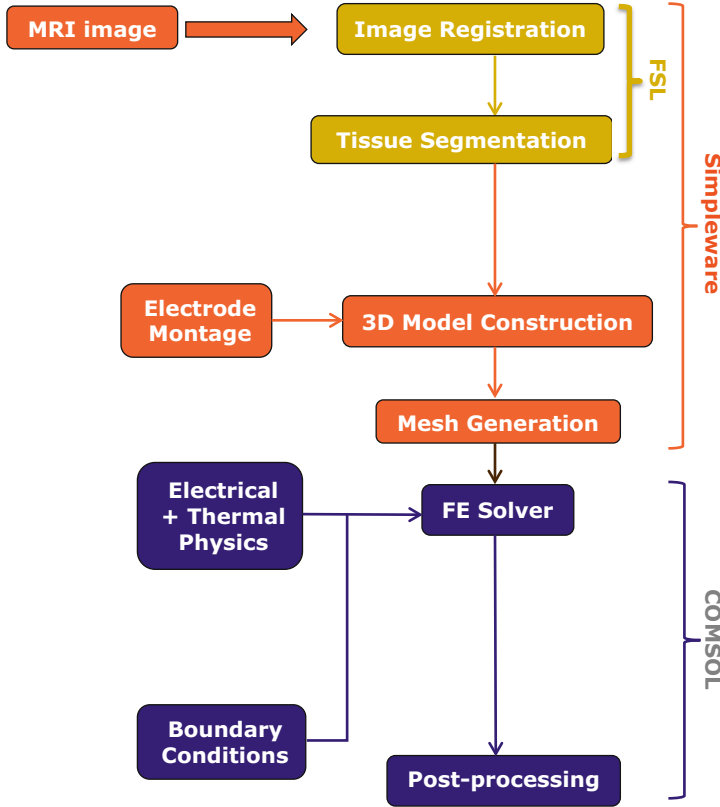


Fig. 5.1 Flowchart showing the development of a realistic head model

search strategy, and similarity metric. The *feature space* is the step used to find common features among the images that can help to align the landmarks. The *search space* is the type of transformation  $T(x)$ ,  $f(x) = g(T(x))$ , which should be used in order for two images to be aligned. It is a mapping of locations correlating the points of one image to new locations in another image. There are different types of transformation that can be chosen, such as rigid body, rotation plus translation, affine, projective, perspective and global polynomial. The type of transformation selected will influence the algorithm's registration nature. The *search strategy* defines the type of technique or method (linear programming techniques, relaxation method, etc.) that is going to be used during each step, after the first transformation is defined. Tied in with the search strategy comes the *similarity metric*, where a quantification of the transformations is realized. In this step the differences between the transformed source image and the target image will be quantified, with different choices available in attempt to achieve that, such as mean-squared error and correlation [23, 24].

In short, a reference image and a floating image (image to be registered according to the reference image) are defined. A similarity function is evaluated among the images; hereafter an optimization algorithm evaluates the best transformation function, which will transform the floating image. If the result is acceptable, the registration is complete, otherwise, a new transformation is performed [22].

Within FSL, two main functions may be used for the registration process. Both are fully automated tools, robust and accurate for brain image registration: the FMRIB's linear image registration tool—FLIRT, and the FMRIB's nonlinear image registration tool—FNIRT [25]. These functions perform an alignment with the MNI152 space.

### 5.2.2.2 Tissue Segmentation

Image segmentation is intended to classify an image into homogeneous regions. These regions need to have a semantical meaning, boundaries that do not overlap and similar attributes, like texture, intensity, color and depth.

The tissue segmentation of MRI is going to divide and specify tissue types and anatomical structures. In the brain, one of the most important features for its segmentation is the intensity. There are a few methods which can be used to segment the brain, such as manual segmentation, methods based on intensity, atlas and surface, and hybrid segmentation methods [26].

Prior to the MRI segmentation and besides the image registration and the brain extraction, it is important to realize the bias field correction (intensity inhomogeneity). It is a low-frequency artifact that causes a variation in the smooth signal intensity within tissues of the same physical properties. This is generated due to spatial inhomogeneity of the magnetic field. The FMRIB's automated segmentation tool—FAST, from FSL, does the bias field correction and realizes generic tissue-type segmentation.

### 5.2.3 Realistic Head Modelling Development

A realistic head model is used in this research. The geometry is built based on an MRI acquired from the available database *BrainWeb* [27]. The images are based on the average of 27 co-registered MRI data from the same subject, generated by an MRI simulator. The images have a resolution of  $1 \text{ mm}^3$  isotropic voxel and contain  $181 \times 181 \times 217$  slices in the transverse, sagittal, and coronal axes. The T1 was generated using SFLASH with  $TR = 18 \text{ ms}$  (repetition time), flip angle  $= 30^\circ$  and  $TE = 10 \text{ ms}$  (echo time). The T2 was acquired using dual echo spin echo, late echo with  $TR = 3300 \text{ ms}$ , flip angle  $= 90^\circ$  and  $TE = 35 \text{ ms}$  (dual echo spin echo) and  $120 \text{ ms}$  (late echo). PD was obtained with dual echo spin echo, early echo with  $TR = 3300 \text{ ms}$ , flip angle  $90^\circ$ , and  $TE = 35 \text{ ms}$  and  $120 \text{ ms}$  [28]. In this case, the

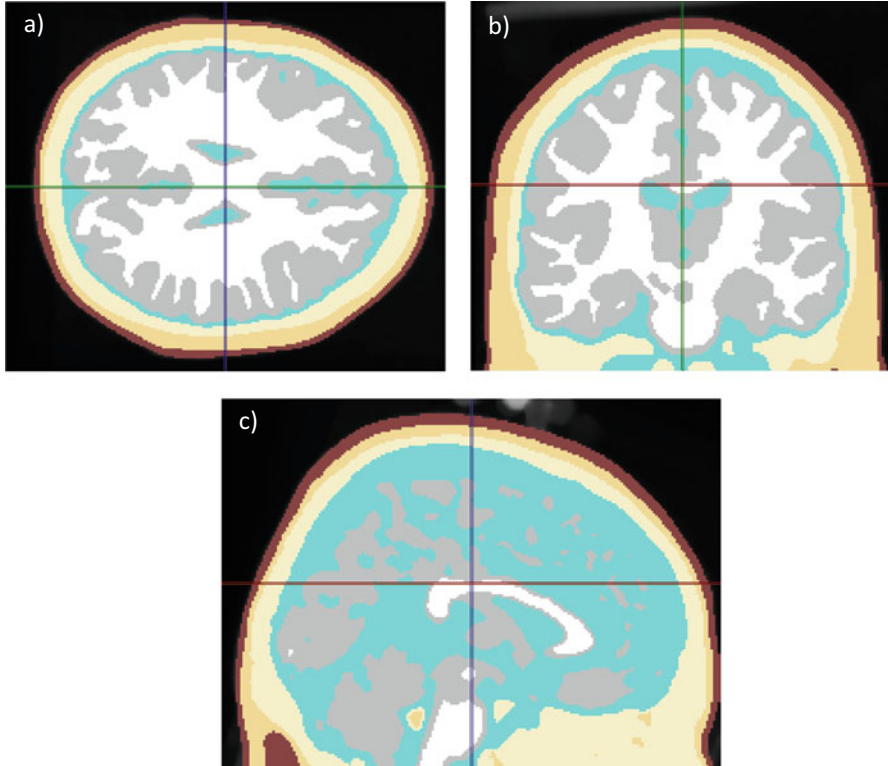


**Fig. 5.2** Model RHM\_06, segmentation of six tissue layers for the images acquired from Brainweb; (a) transversal, (b) coronal, and (c) sagittal planes

head model generated consists of six tissue layers: scalp, fat, skull, cerebrospinal fluid (CSF), GM, and WM. Figure 5.2 shows segmentation of these tissues.

In the head model development, prior to the registration of images, a reorientation and a brain extraction through the FSL function `fsloreorient2std` and BET (Brain Extraction Tool) [29] are conducted. The purpose is to put the images in the same space coordinate and to separate brain regions from non-brain regions that are going to help in the registration and segmentation steps. Also, the skull stripping is realized using BET. FAST and BET are used to generate the following masks: scalp, skull, CSF, GM, and WM. Afterwards, the FLIRT tool is used. The T1 image is selected as the reference image and the T2 is the floating image. The transformations applied are rigid-body and affine. Posteriorly, fat is semiautomatically generated using the ScanIP module from Simpleware 4.3 (Simpleware Ltd.).

In the tissue segmentation, semiautomatic tools from FSL and Simpleware are used employed. T1 images are used to identify and segment scalp, fat, skull, CSF, GM, and WM, while T2w and PD are used to classify inner skull and CSF boundaries.

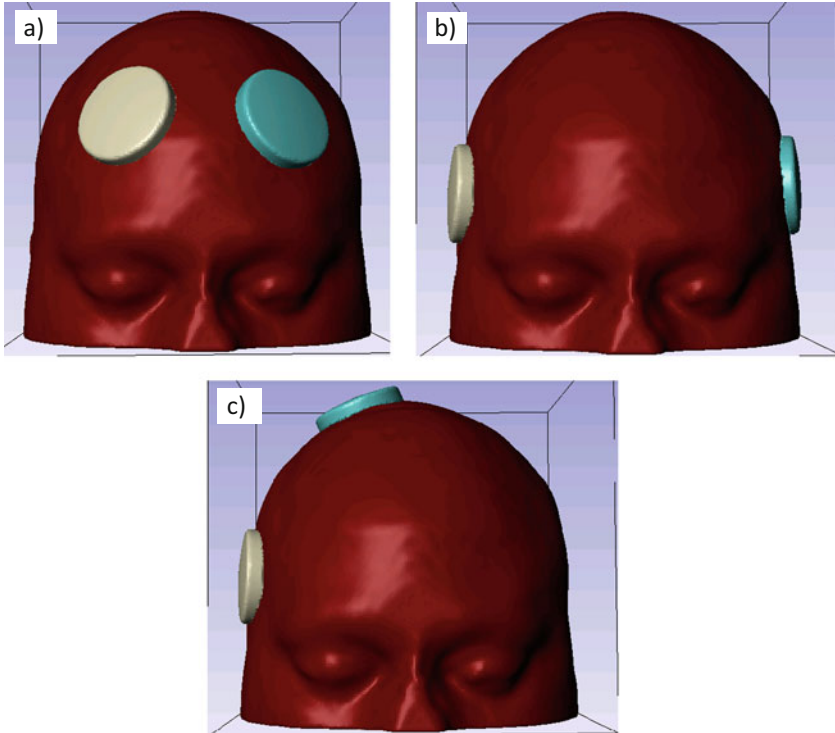


**Fig. 5.3** ECT electrode montage: (a) bifrontal—BF, (b) bilateral frontotemporal—BL and (c) right unilateral—RUL

Once the tissues had been segmented, six in this model, several semiautomatic and manual corrections needed to be done. At first, a CAD+ module (Simpleware Ltd.) was employed to construct all the tissue masks as a whole head model. Thereafter, the masks are exported to ScanIP, where automatic image processing techniques are used to correctly place one tissue adjacent to another and further smoothen the layers. Techniques such as dilate, erode, Gaussian filter, and FloodFill are applied. Later on, some manual corrections are required to remove any floating islands.

#### 5.2.4 *Electrode Modelling*

Three conventional electrode configurations (BF, BL, and RUL) normally employed during the practice of ECT are modelled (Fig. 5.3). They are constructed within CAD+. The mask of the electrodes is subtracted from the scalp mask, allowing for the electrodes to be geometrically placed over the scalp tissue.

BF and BL placements are bilateral stimulation, whereas RUL is unilateral. The electrodes are built in the software CAD+ (Simpleware Ltd.). Steel is considered

as the electrode material. The placements of the electrodes are as follows: for BF electrode configuration, both electrodes are localized 5 cm above the outer angle of the orbit, parallel to the sagittal plane [9]; for BL, both electrodes are positioned 2.5 cm above the midpoint of the line that connects external canthus and tragus, at the frontotemporal position [2, 9, 14]; and for RUL, the electrodes are positioned on the right hand side of the head, one 2.5 cm to the right of vertex (active) and the other in the same position as right BL placement [9].

The electrolyte gel is largely displaced when the electrodes are pressed against the scalp. Its aim is to stabilize the impedance of the electrode-scalp interface [9]. This is already considered in the computational model. Thus, in this study, the gel is not directly modelled.

### 5.2.5 Mesh Generation

The generation of a mesh is the prerequisite to apply the finite element method. It represents a discretized geometry being expressed into small units of simple shapes. In the models generated in this work, it also represents the electric and thermal properties of the head volume conductor. The mesh is generated using the package Simpleware utilizing the tetrahedral technique. To choose the size of the mesh, a convergence analysis was conducted.

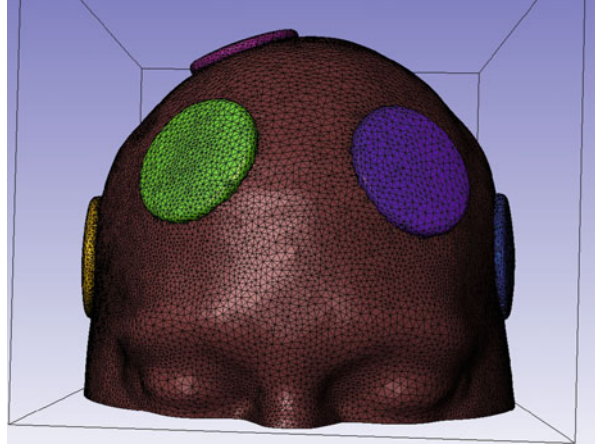
The mesh was generated under the umbrella of ScanIP. A convergence analysis was conducted. The chosen mesh has the compound coarseness set to  $-22$ , which has the following parameters: characteristic lengths with target minimum and maximum edge length of 2.04 and 4.96 mm respectively and target maximum error (distance re-meshed surface is allowed to move from original mesh) of 0.1 mm; surface constraints with a surface change rate of 44 and a target number of elements across a layer of 0.78; volume elements generation with an internal change rate of 30 and quality optimization cycles of 5; an additional quality improvement with metric scaled Jacobian of 0.1; and maximum off-surface distance, being, fraction of local edge lengths of 0.2. These specifications generate meshes that consist of approximately two million tetrahedral elements. Figure 5.4 shows an image of the mesh generated, on the external layer and the electrodes. Finally, the mesh model file is exported to COMSOL, where the physics and boundary conditions are applied. Each model took approximately 17 min to run on a 32 GB RAM, Quad-Core, Quadro GPU enabled laptop workstation.

## 5.3 Applications

Applications of a realistic human head model using ECT are shown in this section. Anisotropic thermal and electrical conductivities within the skull layer are applied, in order to examine their influences and to analyze the effect of heat transfer on the



**Fig. 5.4** Mesh generated for RHM, showing scalp and electrodes position



brain region due to ECT. The problems are defined for both isotropic and anisotropic versions of a realistic head model using the finite element method. The solutions are computed using the COMSOL package and the results are evaluated by showing the temperature behavior within the tissues. Additionally, it is shown how the magnitude and spatial distribution of temperature are affected through biological properties and ECT stimulation parameters are examined. The model used is composed of six types of tissues: scalp, fat, skull, CSF, GM, and WM. The volumetric mesh comprises about two million tetrahedral elements.

### 5.3.1 Volume Conductor Model

When frequency is low, from direct current (DC) to 10 kHz, biological material exhibits strong resistivity behavior. Therefore, Maxwell's equation can be simplified to the quasi-static approximation [30–33]. According to Ohm's law and supposing electric field strength,  $E$ , throughout a passive volume conductor model, it results in the Laplace partial differential equation:

$$\nabla \cdot (-\sigma \nabla V) = 0 \quad \text{or} \quad \nabla \cdot \begin{bmatrix} \sigma_{xx} & \sigma_{xy} & \sigma_{xz} \\ \sigma_{yx} & \sigma_{yy} & \sigma_{yz} \\ \sigma_{zx} & \sigma_{zy} & \sigma_{zz} \end{bmatrix} \begin{bmatrix} \partial V / \partial x \\ \partial V / \partial y \\ \partial V / \partial z \end{bmatrix} = 0 \text{ in } \Omega \quad (5.1)$$

where  $\sigma$  and  $V$  are the electrical conductivity and the scalar electric potential respectively in a volume of  $\Omega$ .

The electrical conductivity is a scalar number in the case of isotropic volume conductors. For anisotropic conductors,  $\sigma$  is a tensor, where it is possible to consider its preferential directions of current flow [30, 33].

**Table 5.1** Thermophysical and electrical properties of tissues

	$k$ (W/(m K))	$\sigma$ (S/m)	$\rho$ (kg/m <sup>3</sup> )	$c_p$ J/(kg K)	$Q_m$ (W/m <sup>3</sup> )	$\omega_b$ (1/s)
Scalp	0.39	0.465	1125	3150	363	0.00143
Fat	0.21	4.06e−2	911	2348	464.61	7.7436e−6
Skull	See Table 5.2	See Table 5.2	1850	1300	70	1.43e−4
CSF	0.60	1.654	1000	4200	0	0
GM	0.565	0.33	1035.5	3680	16,229	1.3289e−2
WM	0.503	0.65	1027.4	3600	4517.9	3.6956e−3

Pennes [34] formulated a simplified bio-heat transfer equation (BHTE), with the assumption that heat transfer in tissues occurs in the capillaries and they are in good thermal balance with the surrounding tissues. BHTE is heat conduction, with specific terms for the generation of heat, due to blood perfusion and to metabolic heat. The equation is shown below:

$$\rho c \frac{\partial T}{\partial t} = \nabla (k \nabla T) + \omega \rho_b c_b (T_a - T) + Q_m \quad (5.2)$$

where  $\rho$ : density (kg/m<sup>3</sup>),  $c$ : heat capacity (J/(kg °C)),  $k$ : thermal conductivity (W/(m °C)),  $T$ : temperature (°C),  $T_a$ : arterial blood temperature (°C),  $\omega_b$ : blood perfusion rate (1/s),  $Q_{met}$ : metabolic heat source (W/m<sup>3</sup>), and the subscript  $b$  denotes blood [4, 35, 36]. The term from the left side is related to the rate of stored energy into the tissue mass that balances the equation. The first term from the right side is related to the rate of input and output energy; the second term is an additional amount related to heat transfer from blood flow, which is the energy added or removed due to the convective blood flow into and out of the tissue; the last term is the generation of metabolic heat [37, 38].

The BHTE combined with the Laplace equation (Eq. 5.3) is used as the physics and as equations to solve the current models. The electrical and the thermophysical properties [4, 17, 39] for the scalp, fat, skull, CSF, GM, and WM are shown in Table 5.1.

$$\rho c \frac{\partial T}{\partial t} = \nabla (k \nabla T) + \omega \rho_b c_b (T_a - T) + Q_m + \nabla \cdot (\sigma \nabla V) \quad (5.3)$$

Initial and boundary conditions are assigned for the thermal and electrical physics. For the thermal physics, convection occurs in the external boundaries, defined as:

$$-k \cdot \frac{\partial T}{\partial n} = h \cdot (T_{amb} - T), \quad (5.4)$$

where  $h$  is  $4 \text{ W/m}^2 \text{ }^\circ\text{C}$  and  $T_{\text{amb}}$  is  $24 \text{ }^\circ\text{C}$ . The interfaces between the layers are governed by conduction. Initial temperature is equal to  $36.7 \text{ }^\circ\text{C}$  and the parameters for blood perfusion are assigned as  $\rho_b = 1050 \text{ kg/m}^3$ ,  $c_b = 3600 \text{ J/(kg }^\circ\text{C)}$  and  $T_a = 36.7 \text{ }^\circ\text{C}$  [4].

For the electrical physics, the external boundaries are considered electrically insulated and are represented by Neumann BC,  $n \cdot (\sigma \nabla V) = 0$ . The inner boundaries are ruled by the continuity of the normal component of the current density between regions of different conductivity.

Moreover, the external surface of the anode is assigned Dirichlet ( $V = V_0$  volts) BC, where  $V_0$  is the input potential set as the rms value of a biphasic brief pulse of  $111.11 \text{ Hz}$  (models from Sect. 5.3.2) or  $120 \text{ Hz}$  (models from Sect. 5.3.3) and  $1 \text{ ms}$  width pulse, and the amplitude is equivalent to  $900 \text{ mA}$  total current injection. This DC signal has been considered due to lengthy extensive computations which may expend to more than  $18 \text{ h}$  in each single case.

In comparison, the external surface of the cathode is assigned Dirichlet ( $V = 0 \text{ V}$ ) BC. Dirichlet BC is chosen for the active electrode due to limitations of the software when thermal and electrical physics are applied together.

The three conventional electrode configurations (BF, BL, and RUL) are modelled as described in Sect. 5.2.4, with  $\sigma = 9.8 \times 10^5 \text{ (S/m)}$  and  $k = 42 \text{ (W/(m K))}$  [40, 41].

### 5.3.2 Anisotropy Skull Conductivity

Some regions of the head present anisotropic electrical conductivity [42–45]. The expression that gives the anisotropic electrical conductivity is found in the literature and is usually given in local coordinates as:

$$\sigma_{\text{skull}} = \begin{bmatrix} \sigma_T & 0 & 0 \\ 0 & \sigma_T & 0 \\ 0 & 0 & \sigma_R \end{bmatrix} \quad (5.5)$$

where  $\sigma_{\text{SKULL}}$  is a second rank symmetric tensor ( $\sigma_{\text{SKULL}}^T = \sigma_{\text{SKULL}}$ ) and positive definite, and  $\sigma_T$  and  $\sigma_R$  represent the conductivity in tangential and radial direction, respectively.

There are certain methods and approaches to calculate the electrical conductivity from the diffusion weighted MRI. The approach used here is the volume constraint (VC) [45] which considers that eigenvalues must retain their geometric mean, and thus, the volume of the conductivity tensor:

$$\frac{4}{3}\pi\sigma_R(\sigma_T)^2 = \frac{4}{3}\pi\sigma_{\text{iso}}^3. \quad (5.6)$$

A linearity between thermal conductivity tensor and electrical conductivity tensor is found in the literature [46]. The model for the relationship between electrical and thermal conductivity is based on the effective medium approach for two-phase anisotropic media. The relationship of the effective transport tensor to the microstructure is written as:

$$\frac{[\alpha_{\text{eff}}]}{\alpha_e} = [R^{(i)}][P_\alpha] \quad (5.7)$$

where  $\alpha$  denotes either thermal or electrical conductivity; the subscripts eff and e denote tensors to the microstructure and transport coefficients in the host phase (basic interstitial matrix), respectively;  $[R^{(i)}]$  is a concatenated series containing microstructure information; and,  $[P_\alpha]$  is a concatenated series of  $\alpha$ . Therefore, it is possible to obtain a cross-property relationship between the two transport tensors:

$$\kappa_v = a_1 (\sigma_v \pm c_1) \quad (5.8)$$

where  $\kappa_v$  and  $\sigma_v$  are the eigenvalues of the thermal conductivity tensor and electrical conductivity tensor, respectively, while  $a_1$  and  $c_1$  are numerical constants.

Taking into account this linear relationship (Eq. 5.8) between electrical and thermal conductivity tensors, a correlation based on VC (Eq. 5.6) was imposed to calculate the radial and tangential anisotropy conductivity. Similarly, the volume of the thermal conductivity tensor is maintained, given that the geometric mean of the eigenvalues is preserved, i.e.,

$$\frac{4}{3}\pi k_R(k_T)^2 = \frac{4}{3}\pi k_{\text{iso}}^3. \quad (5.9)$$

This assumption was made due to insufficient information on thermal anisotropy conductivity of the head [40]. The VC is used to set up the eigenvalues for the electrical and thermal anisotropic cases, Eqs. 5.6 and 5.9, respectively.

The known common isotropic thermal and electrical conductivities, valued as  $k = 0.53$  W/m K and  $\sigma = 0.0132$  S/m [47] are considered respectively. Four different anisotropic ratios [45] are chosen and they are shown in Table 5.2.

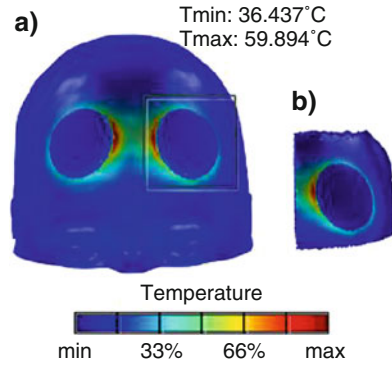
**Table 5.2** Values used to simulate the skull. Units of  $k$  and  $\sigma$  in W/m K and S/m, respectively [40]

Ratio	Skull Tensor eigenvalues			
	Thermal		Electrical	
	$k_R$	$k_T$	$\sigma_R$	$\sigma_T$
1:1 (iso)	0.53	0.53	0.0132	0.0132
1:2	0.335	0.67	8.3e-3	1.6646e-2
1:5	0.181	0.905	4.5e-3	2.2607e-2
1:10	0.114	1.14	2.8438e-3	2.8438e-2
1:100	0.0245	2.45	6.1269e-4	6.1269e-2

**Table 5.3** Thermophysical and electrical properties of the scalp for interface electrode-skin study [41]

	$k$	$\sigma$	$Q_m$	$\omega_b$
	(W/(m K))	(S/m)	(W/m <sup>3</sup> )	(1/s)
Scalp	0.33–0.45	0.255–0.465	0–363	0–1.43e–3

**Fig. 5.5** Model showing the electrode montage: (a) BF, and delimiting by the black box the (b) ROI. The color map represents temperature



### 5.3.3 Interface Between Electrode and Skin

For the simulations in this section the properties of scalp and the inclusion of fat layer were analyzed. For the isotropic case, the range of scalp electrical and thermal conductivities is varied, according to Table 5.3. All other thermophysical values are considered as in Table 5.1.

Firstly, neither the blood perfusion nor the metabolic activity is considered. Therefore, in the first iteration,  $\omega_b$  and  $Q_b$  are zero for all tissue layers. Afterwards, a study of how the convection of blood regulates the temperature was performed. In this case,  $\omega_b$  scalp varied from 0 to 0.00143. Furthermore, the effect of fat is analyzed. The fat thickness in this model is 3.75 mm. For this purpose, a model without a fat layer is constructed. With the intention of retaining the same mesh and properties of the model, the fat layer is assigned scalp properties.

### 5.3.4 Measures for Analysis

The maximum temperature ( $T_{\max}$ ) with respect to time is selected as one of the measures for analysis. A radial line, starting from the position where  $T_{\max}$  happened, is used to study the behavior of temperature. Afterwards, a case of “no-stimulation” (no electrical input current) is conducted and compared with the case of input current using the graphical distribution of temperature profiles. Furthermore, a region of interest (ROI) (Fig. 5.5) is specified to evaluate the temperature near the electrodes.

The relative error (RE) of  $T$  is also employed to provide the relative difference between isotropic and corresponding anisotropic solutions. This statistical measure-

ment is defined as below:

$$RE = \sqrt{\frac{\sum_{i=1}^n (T_i^{\text{iso}} - T_i^{\text{aniso}})^2}{\sum_{i=1}^n (T_i^{\text{aniso}})^2}} \quad (5.10)$$

where  $n$  is the number of samples in the respective ROI and  $T^{\text{iso}}$  and  $T^{\text{aniso}}$  the  $i$ th component of  $T$  in the isotropic and anisotropic cases, respectively [9].

## 5.4 Results Analysis

### 5.4.1 Behavior of Temperature for Isotropic Cases

Firstly, the behavior of temperature against time was evaluated. Analysis showed that the region near the electrode, on the scalp, is where  $T_{\text{max}}$  occurred. For the three electrode montages, the location where  $T_{\text{max}}$  occurred and their behavior against time was evaluated, as can be seen in Fig. 5.6a. The behavior is of a first order system, increasing exponentially with time, where  $T_{\text{max}}$  occurred on the scalp layer, at the end of the stimulation period.

Afterwards, the  $T_{\text{max}}$  in each layer was considered. The results of  $T_{\text{max}}$  at the time of 8 s for all tissue layers, isotropic case and the three electrode montages are shown in Table 5.4. The layers which had a higher temperature increase were the external ones, fat and scalp, with a variation rise of 5–29 °C. The intermediate layers of skull and CSF had a variation increase of 1–3.9 °C. The internal layers of GM and WM had a temperature rise of 0.06–0.34 °C. The changes in temperature rise depend on the electrode montage used for the model. As an example, the behavior

**Fig. 5.6**  $T_{\text{max}}$  for isotropic models (a) for whole head, the three electrode configurations: BF, BL, and RUL; and for BL electrode montage showing each tissue layer (b) scalp, fat, skull, CSF, GM, and WM

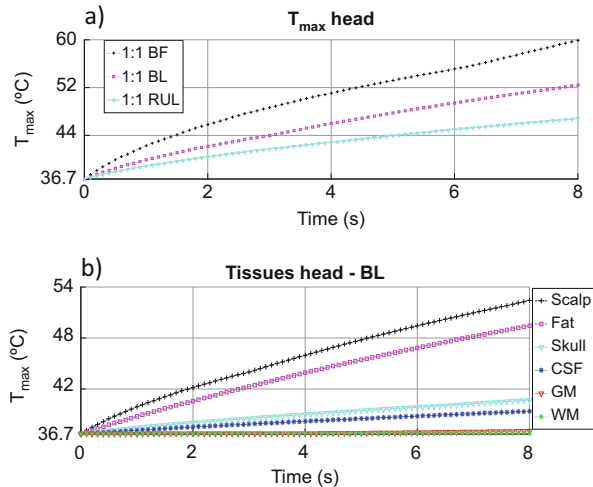


**Table 5.4** RHM isotropic case,  $T_{max}$  in each tissue layer at  $t = 8$  s

Isotropic	RHM		
	BF	BL	RUL
Scalp	59.89	52.43	46.80
Fat	50.76	49.44	44.39
Skull	38.84	40.68	38.61
CSF	38.07	39.38	37.91
GM	36.81	37.05	36.88
WM	36.76	36.80	36.77

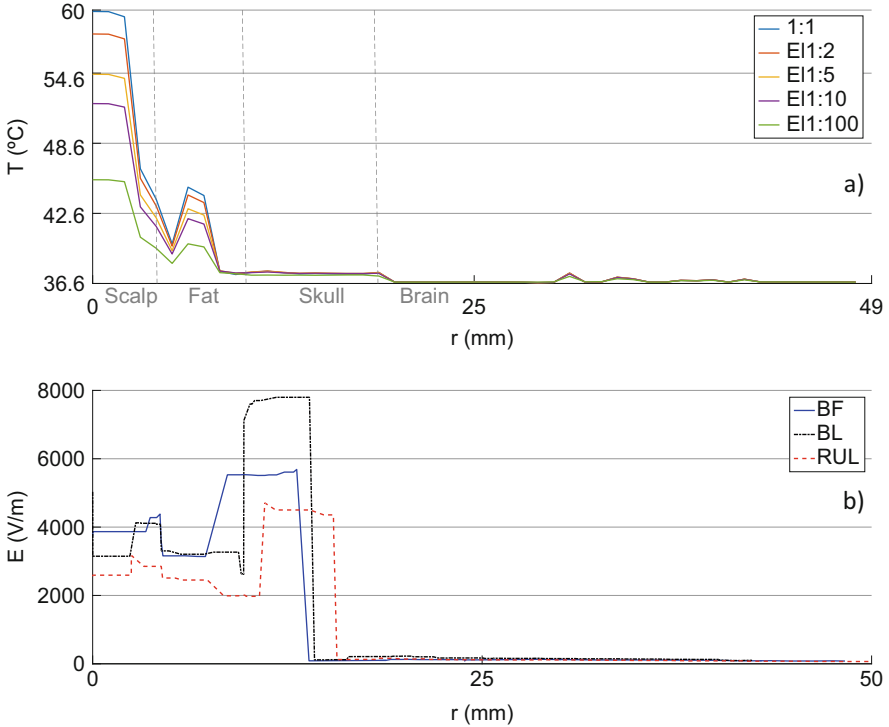


**Fig. 5.7** Distribution along a radial direction starting from the position where  $T_{max}$  occur, at 8 s. (a) Temperature for BF electrode montage, isotropic (1:1) and four electrical (EI) anisotropy ratios (1:2, 1:5, 1:10, 1:100). The grey dashed lines represent boundaries among tissues, first: scalp-fat, second: fat-skull, third: skull-brain; and (b) E-field, isotropic, BF, BL, RUL [40]

of temperature against time of each tissue layer, for the BL configuration can be seen from Fig. 5.6b. It is clear to notice that the inner layers do not vary greatly in temperature.

In order to study and analyze the behavior of temperature due to the electrical stimulation throughout the model, a radial line starting from  $T_{max}$  and passing along all tissue layers was used. The starting point is at  $T_{max}$  because it is expected that the surrounding regions will also have influence and rise in temperature. From Fig. 5.7a it can be seen the behavior for BL case. The external layers have an

increase in temperature, and as long as it penetrates to deeper layers, the temperature approaches the reference temperature. The E-field profile from the same radial direction, for the three electrode montages, isotropic case, is shown on Fig. 5.7b. The higher E-fields appear at BF and BL configurations, for the external and internal layers, respectively.

### **5.4.2 Temperature Behavior Under Skull Anisotropy Influence**

The behavior of temperature was analyzed when considering anisotropy on the skull layer. Four anisotropic ratios were considered, as according to Table 5.2. These models were compared to the isotropic models. Three different sets of anisotropy were modelled: thermal skull anisotropy (Sect. 5.4.2.1), electrical skull anisotropy (Sect. 5.4.2.2) and thermal and electrical skull anisotropy combined together (Sect. 5.4.2.3).

#### **5.4.2.1 Thermal Skull Anisotropy**

When considering thermal skull anisotropy, a variation in temperature happened on the skull layer (Table 5.5) in addition to a small change at CSF and GM. Additionally, a slight difference appeared in the fat layer when modelling with BF configuration. As long as the tangential to radial skull thermal conductivity increases, a change in temperature would occur. The behavior also differs based on the electrode configuration used. Temperature dropped at fat, skull, and CSF; however it increased at GM, for BF montage. For BL configuration, temperature decreased at skull and increased at CSF as well as GM. For RUL placement, the temperature behavior was altered. At GM, temperature rose; at CSF, temperature had a decrease at small tangential to radial conductivity, while it increased at a higher ratio (1:100); lastly at skull, temperature rose at a small ratio (1:2), and afterwards, as the ratio increased, temperature declined.

Comparing the isotropic case with the thermal anisotropic cases, a temperature variation of 0.016, 0.575, 0.088, and 0.037 °C occurred at fat, skull, CSF, and GM, respectively. The electrode configuration that experienced greater fluctuation was the BL, when compared to BF and RUL. Also, a rise of 0.35 °C occurred at GM when compared with “no-stimulation” model.

#### **5.4.2.2 Electrical Skull Anisotropy**

Varying electrical anisotropy in the skull (Table 5.5) caused a variation in temperature in all tissue layers of the head model. Increasing the tangential-radial electrical conductivity ratio there was a decrease in temperature for almost all BF and BL



**Table 5.5**  $T_{max}$  in the skull layer for all cases: isotropic conductivity—1:1; and skull anisotropic conductivity (thermal—Th, electrical—El, electrical and thermal—ElTh)—ratios 1:2, 1:5, 1:10, and 1:100

	Skull								
	BF			BL			RUL		
	Th	El	ElTh	Th	El	ElTh	Th	El	ElTh
1:1	38.84			40.68			38.61		
1:2	38.81	38.87	38.84	40.63	40.31	40.24	38.63	38.75	38.76
1:5	38.74	38.77	38.70	40.52	39.84	39.69	38.62	38.80	38.80
1:10	38.67	38.64	38.53	40.41	39.51	39.31	38.61	38.79	38.79
1:100	38.45	38.28	38.14	40.11	38.73	38.44	38.51	38.93	38.84

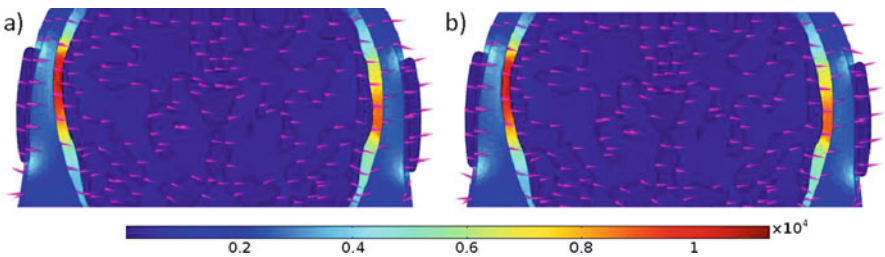


**Fig. 5.8** E-field distribution in a nonhomogeneous medium along axial plane for BL electrode configuration. The magenta arrows represent current density. (a) Isotropic and (b) El1:10

cases. The exception was in the inner cases (GM and WM) of BF in which the temperature rose instead. For RUL configuration, in the external layers of scalp and fat, the temperature ascended until the ratio 1:10 and it dropped in the other ratios. A climb in temperature occurred in the WM, CSF, and skull layers. A fall of temperature also happened in the GM. Comparing the results of GM with “no-stimulation” results, the temperature rose by 0.2 °C.

A behavior of temperature distribution can be seen in the graph of Fig. 5.7a. It shows along a radial line for the BF case that, as long as the electrical anisotropy ratio increases, the temperatures in the external layers drop.

Figure 5.8 shows the E-field distribution and current density path for two different cases, isotropic and ratio 1:10 of electrical anisotropy. It was found that isotropic cases have high E-field intensity and stronger current density than electrical anisotropy. This behavior was noticed for BL and BF electrode montages; whereas, for RUL, the contrary occurred. The outcome endorses the results of temperature shown in Table 5.5.

### 5.4.2.3 Electrical and Thermal Skull Anisotropy

Applying electrical and thermal skull conductivity together resulted to similar figures as those when only electrical conductivity was applied. The main variation

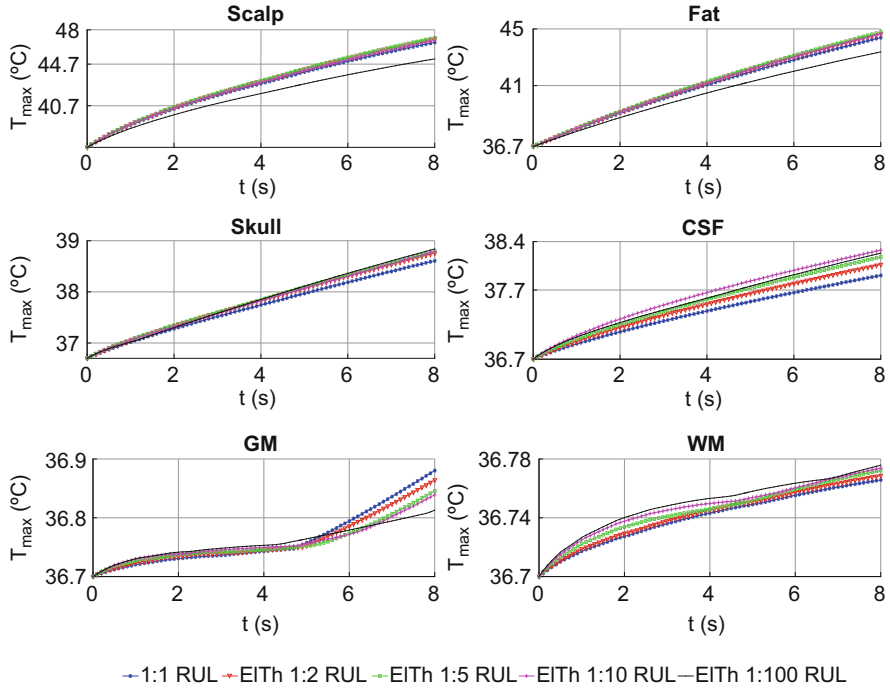


**Fig. 5.9**  $T_{max}$  comparison among isotropic (1:1) and electrical and thermal anisotropic (different ratios: 1:2, 1:5, 1:10, 1:100), for all tissue layers, RUL electrode montage

was on the skull layer itself where the temperature had a small drop. Overall, this is the layer where the fluctuation of temperature is higher and more evident when applying anisotropy conductivity. The results of skull peak temperature for different conductivity ratios and electrode montages are shown in Table 5.5.

Figure 5.9 displays graphs of  $T_{max}$  versus time at each tissue layer, for RUL configuration, making a comparison among isotropic and four ratios of electrical and thermal skull anisotropy. In general, as long as the anisotropy ratio increases, the temperature also increases. The exception is the GM layer, which the opposite occurs; and the higher ratio of 1:100 that in the external layers has a drop in temperature.

A graphical comparison for the isotropy case and the three different anisotropy conductivities for ratio 1:10, in the skull layer, for BF montage is shown in Fig. 5.10. The higher temperature is considering isotropy case, 38.97 °C; and the variation from the other settings are from 0.008% to 0.474%.

The delimited ROI (Fig. 5.5b) was used to calculate the temperature RE (Eq. 5.10). The temperature RE for all realistic models is displayed in Fig. 5.11. Temperature rose provided that the anisotropy ratio rose. In that way, the higher temperature variation is at ratio 1:100, particularly if electrical anisotropy was applied. As analyzed previously, thermal anisotropy did not have much variation

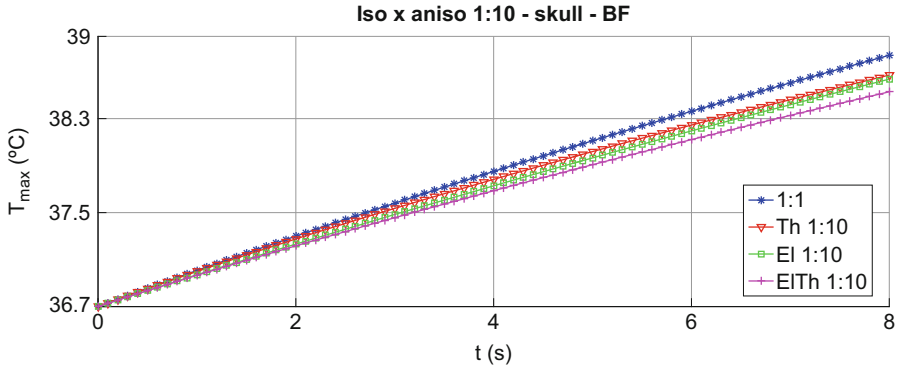


**Fig. 5.10**  $T_{max}$  of skull as a function of time showing a comparison among isotropy and anisotropy at ratio 1:10 (thermal (Th), electrical (EI), and electrical and thermal (EITH)), BF electrode configuration

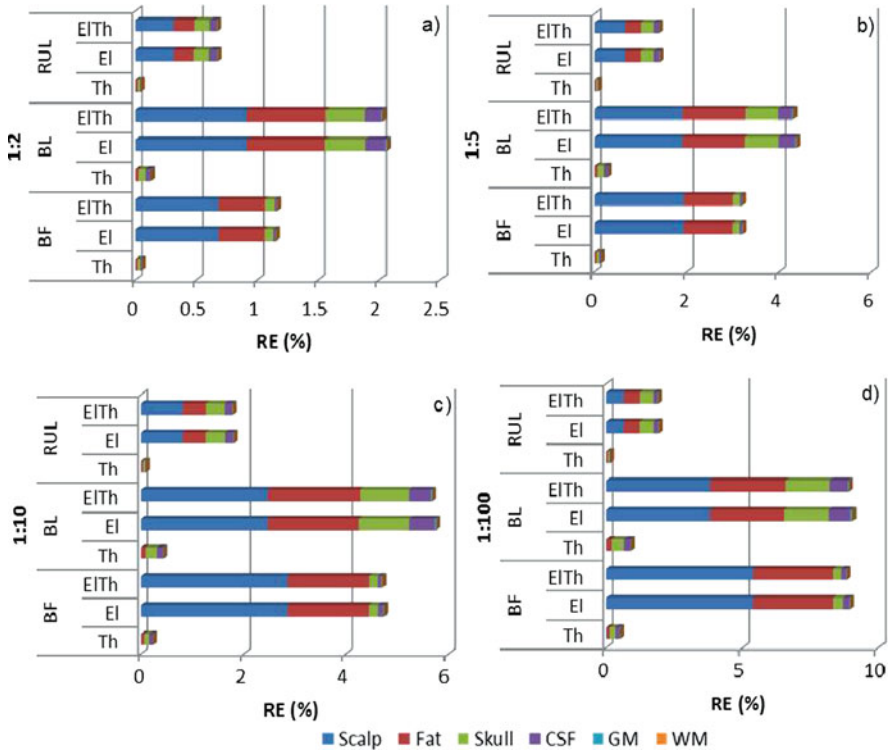


**Fig. 5.11** Temperature RE (%) of anisotropic (a) 1:2, (b) 1:5, (c) 1:10, and (d) 1:100 models from ROI; thermal (Th), electrical (EI) and thermal + electrical (EITH), for BF, BL, and RUL. Each color relates to one head tissue, scalp (dark blue), fat (red), skull (green), CSF (purple), GM (light blue), and WM (orange) [40]

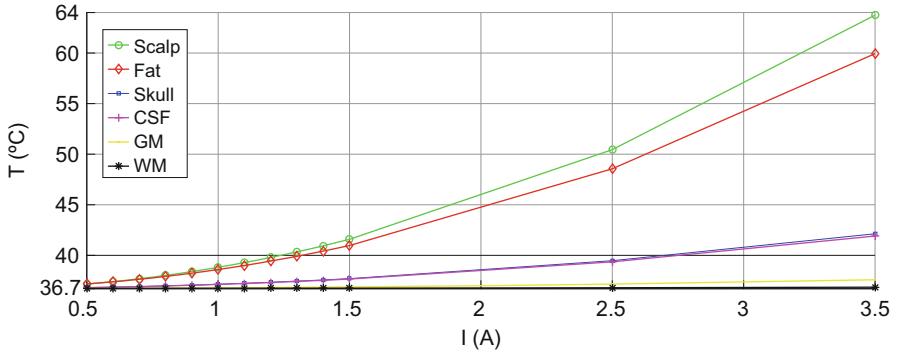


**Fig. 5.12**  $T_{max}$  behavior for different input current in each tissue layer, BL at  $t = 8$  s

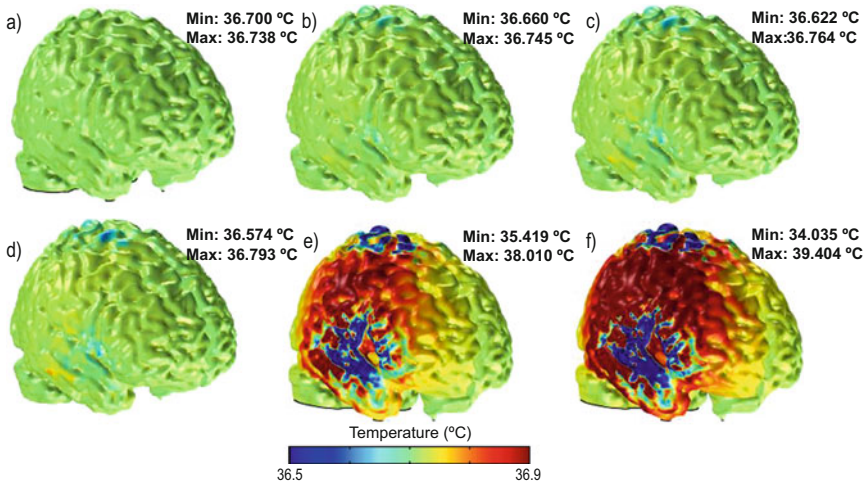


**Fig. 5.13** Distribution of temperature on GM surface, RUL at  $t = 8$  s, for cases: (a) “no-stimulation,” (b) 0.6 A, (c) 0.8 A, (d) 1.0 A, (e) 2.5 A, and (f) 3.6 A

in temperature. Also, high temperature dissimilarities occur in the external layers; whereas only a small variation transpired in the inner layers. Regarding the electrode montages, the greater temperature variation occurred for BL configurations.

#### 5.4.2.4 Threshold of Input Current

In order to find the thermally safe current threshold, a broader range of input currents was considered. This range varied from 0.4 to 3.6 A. It included normal ECT limits and extrapolated values. Figures 5.12 and 5.13 depict the behavior of temperature at the different current inputs and the temperature profile, respectively, for BL and RUL montage at 8 s. There is an increase in temperature when the input current

is higher. The layers affected the most are the external ones. Scalp reaches 40 and 41 °C at 1.23 and 1.40 A respectively; fat reaches 40 and 41 °C at 1.31 and 1.50 A respectively, for BL at  $t = 8$  s. GM temperature will only reach 38 °C if the applied current is equal to 1.75 A for BL; 2.48 A for RUL and 3.33 A for BF electrode configuration.

### ***5.4.3 Effect of Biological Properties on Induced Temperature Variation***

The models considered in this section emphasize the effect of biological properties during the induced temperature variation, especially the thermal and electrical conductivity. Furthermore, the influence of blood perfusion, metabolic heat and the fat layer are analyzed. The models are isotropic and the thermophysical and electrical parameters are related to Table 5.3 [41] for scalp, and Table 5.1 for other tissue layers, or as mentioned in the text.

#### **5.4.3.1 Temperature Distribution and Peak of Temperature, No Blood Perfusion, No Metabolic Heat**

In this section, at first, the influence of ECT electric heat solely was measured, without considering the influence of either metabolic heat or blood perfusion. In this case, these parameters were assigned as zero value for all tissue layers. For that, two different cases were considered, where electrical and thermal conductivity of scalp differed. The first one kept the thermal conductivity in a fixed value ( $k = 0.39$  W/m K) and varied the electrical conductivity ( $\sigma = 0.255$ – $0.605$  S/m); and the second one was the opposite, the electrical conductivity was fixed ( $\sigma = 0.39$  S/m) and thermal conductivity changed ( $k = 0.33$ – $0.45$  W/m K).

The external layer experienced the biggest increase in temperature due to the electrical stimulation. When considering thermal conductivity as constant, the peak temperature change by 0.66 °C for BL, 1.55 °C for RUL and 2.49 °C for BF (Fig. 5.14a and Table 5.6-I); and when considering electrical conductivity as constant the variation was of 1.27 °C for BL, 0.71 °C for RUL and 2.12 °C for BF, as shown in Fig. 5.14b and Table 5.6-II. According to the results, it is possible to analyze that if thermal and electrical conductivity decreases, the temperature rises.

#### **5.4.3.2 Temperature Distribution and Peak of Temperature with Blood Perfusion and Metabolic Heat**

Temperature in the head is balanced by blood perfusion and metabolic heat. In order to demonstrate the influence of blood convection, different models were created.

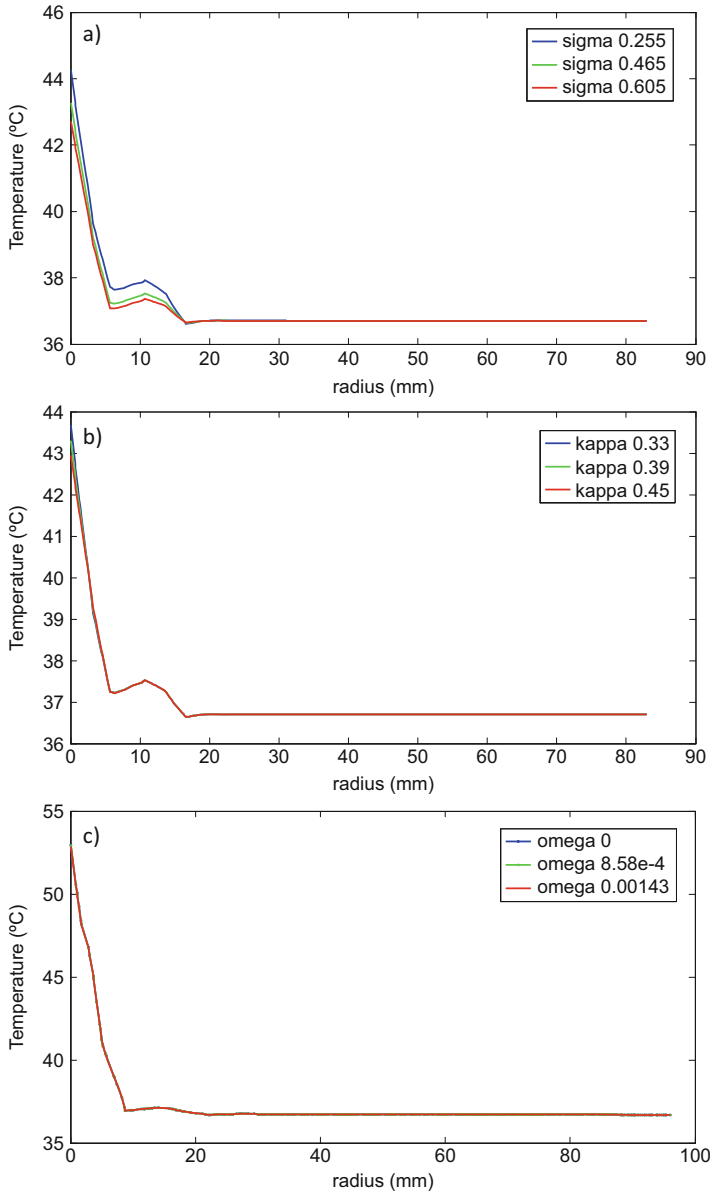


**Fig. 5.14** Temperature distribution along radius of model after ECT stimulation. The profile begins where peak temperature occurs. (a) Temperature versus scalp electrical conductivity ( $\sigma$ —sigma), for RUL electrode montage; the thermal conductivity ( $k$ —kappa) was fixed at 0.39 W/m K and blood perfusion and metabolic heat are absent. (b) Temperature versus scalp thermal conductivity, for RUL electrode montage; the electrical conductivity was fixed at 0.465 S/m and blood perfusion and metabolic heat are absent. (c) Temperature versus blood perfusion, for BF electrode montage; the scalp electrical and thermal conductivity are fixed at 0.465 S/m and 0.39 W/m K, respectively. Only slight variations cause graphs to superimpose [41]

In these ones, the values of thermal and electrical conductivities on scalp were considered fixed, equal to  $k = 0.39$  W/m K and  $\sigma = 0.465$  S/m, respectively; metabolic heat was included with the value of  $363$  W/m<sup>3</sup>; blood perfusion ranged between 0 and 0.00143 1/s; and the blood temperature was set as  $36.7$  °C. With these configurations, for the case that  $\omega = 0.00143$  1/s, the maximum temperature was of 46.81, 43.25 and 52.89 °C, for BL, RUL and BF, respectively (Fig. 5.14c and Table 5.6-III) [41]. Comparing with the results for the models without blood perfusion and metabolic heat (Table 5.6-I and II), it was a decrease of 0.07% to 0.13% in the peak temperature.

### 5.4.3.3 Influence of Fat Layer and Blood Perfusion on the Peak Temperature

The influence of the fat layer was explored. For these cases, four different models were created, for each electrode configuration. The fat layer was included in two models, one considered the blood perfusion whereas the other did not; similarly, on the remaining two models, the blood perfusion was taken into consideration on one of them but not in the other with the fat layer being disregarded. For the latter, the fat layer was modelled as scalp layer ( $\sigma = 0.465$  S/m and  $k = 0.39$  W/m K). The models with blood perfusion were assigned the value of 0.00143 1/s and metabolic heat as  $363$  W/m<sup>3</sup>. Comparing the results for the models with and without fat, a variation of 10–19% occurred. When blood perfusion was not considered the temperatures rose from 0.06% to 0.13%. The results can be found on Table 5.7 [41].

**Table 5.6** Influence of biological parameters on  $T_{\max}$  for BF, BL, and RUL montages

	$\sigma$ (S/m)	$k$ (W/m K)	$\omega_b$ (1/s)	$T_{\max}$ (°C)		
				BF	BL	RUL
I	0.255	0.39	0	54.26	47.13	44.28
	0.465			52.96	46.87	43.28
	0.605			51.77	46.46	42.72
II	0.465	0.33	0	54.14	47.42	43.68
		0.39		52.96	46.87	43.28
		0.45		52.02	46.46	42.28
III	0.465	0.39	0	52.96	46.87	43.28
			$8.54e-4$	52.92	46.83	43.26
			0.00143	52.89	46.81	43.25

**Table 5.7** Effect of fat and blood perfusion on  $T_{\max}$  when ECT stimulation is applied for BF, BL, and RUL

Fat	Blood perfusion	$T_{\max}$ (°C)		
		BF	BL	RUL
<i>y</i>	<i>y</i>	52.89	46.81	43.25
<i>y</i>	<i>n</i>	52.96	46.87	43.28
<i>n</i>	<i>y</i>	42.51	38.35	38.57
<i>n</i>	<i>n</i>	42.53	38.36	38.58

## 5.5 Discussions

The realistic head models presented in this work analyze the behavior of temperature when applying ECT. Thermal and electrical anisotropy skull conductivities were considered and different thermophysical parameters were analyzed. The RHM models were compared with spherical head models (results not shown here), built with equivalent characteristics and configurations. The comparison showed similar results behavior. More information about this comparison can be found elsewhere [40, 48, 49]. As a semi-validation for these models, a resistive-capacitive network model was developed and the comparison can be seen in [40, 48, 49].

### 5.5.1 Isotropic Model and Its Temperature Behavior

ECT practices use of high electrical current during a short period of time. Electrical simulation propagates current along the head, on the path of electrodes. Additionally, it generates heat. The heat influences regions on external tissue layers, on the scalp and fat, close to the electrodes. The constitution of the material influences the propagation of heat; and heat propagation causes changes in temperature. Two reasons can cause change rate: thermal capacitance and heat dissipation. Thermal capacitance and temperature are inversely proportional, so the greater the value of thermal capacitance, the smaller the increase in temperature. Heat dissipation occurs through two mechanisms on the scalp: heat is dissipated through convection to air and through blood perfusion in the internal tissues.

The behavior of temperature in the head is represented through a radial line in Fig. 5.7. Firstly, with time, the electrical stimulation causes a rise in temperature. For the BF case, the  $T_{\max}$  occurs on the scalp, in the region near the electrodes reaching 59.9 °C. Passing through the scalp, a drop in temperature occurs and declining to 46.4 °C at the boundary between scalp and fat. Scalp and fat are neither good thermal nor electrical conductors. The electrical conductivity of the scalp is approximately ten times more than the fat. In addition, there is barely any blood perfusion at the fat layer to act as a convection mechanism. Therefore, a greater drop in temperature of 9.0 °C was noted on the fat layer. Afterwards, when analyzing the skull, a small rise of 0.2 °C occurred. At this layer, there is still a growth in the current density, but only with small magnitude, which does not cause a temperature increase. At the inner layers, CSF, GM, and WM together work as a heat sink and



the temperature is maintained close to  $36.7\text{ }^{\circ}\text{C}$ . The blood has the ability to balance the temperature and to contain it close to  $T_{\text{ref}}$ . In brief, the electrical stimulation causes an increase in temperature on external layers only and close to the electrodes themselves. The results found in this work agree with Kim et al. [50]. In their study, a microelectrode array was implanted and simulated; the results showed that temperature rose on regions near the device and as it moved further from the device, a drop in temperature followed.

The electrode configuration used in the models is an important factor to consider (Table 5.5 and Fig. 5.11). When the distance between electrodes is smaller, as in BF configuration, the temperature increases. When the montage is unilateral, as in the RUL case, the rise in temperature is smaller. In the same way that electrode configuration and distance between electrodes used have an effect in the E-field, current flow, and current density [9, 51], also have an influence in variation of temperature.

### 5.5.2 *Electrical and Thermal Skull Anisotropy Influences*

Electrical only, thermal only and thermal and electrical combined skull anisotropy were applied to analyze the influence of temperature variation. In general, temperature had a higher variation when considering electrical anisotropy. Thermal anisotropy, for the short period of time simulated, does not have significant influence.

For the models with electrical skull anisotropy the behavior of temperature is different according to the electrode montage used. For BF configuration, when the electrodes are closer to each other, the greater effect of temperature rise is on the external layers of scalp and fat, while on the inner layers the influence is smaller. On the other side, for the BL montage (configuration further away from each other), the internal layers presented a greater impact. This behavior is due to the E-field. Temperature rises according to the magnitude and direction of E-field (Fig. 5.7b). The E-field path is from the active electrode to the reference electrode. When the electrodes are closer to each other (BF) the E-field flows mainly through the external layers; in the scalp and fat layers the effect of current shunting occurs, reducing the E-field in the internal layers, not contributing to temperature rise. When the electrodes are far from each other (BL), a stronger flow happened through the inner tissues, causing also an increase in temperature. For RUL montage, temperature rise occurs only in the skull and fat layers. When increasing the ratio of  $\sigma$ , the E-field decreases (Fig. 5.8) and, consequently, so does the temperature. Similarly, in the study conducted by Elwassif et al. [6], a voltage-controlled circuit, varying the electrical conductivity of WM caused a variation on the E-field, therefore, in the temperature.

In other areas of study, such as cornea and radiofrequency ablation, it is also possible to find the relation among  $T_{\text{max}}$  and anisotropic ratio. In the study undertaken by Berjano et al. [52] with cornea, it was stated a direct relation between

the anisotropic ratio used and the temperature profile. They also specified that the result of temperature at a position is inversely proportional to the value of  $k$  used in that specific time and position. Likewise, the study of Watanabe et al. [53] in radiofrequency ablation showed similar results.

A resistance-capacitance network is another technique that can be used to represent the BHTE. During a short period of time, as in ECT practice, the thermal capacitances work as a short circuit that allows thermal charge. In that case, the effect of thermal conductance is reduced, as the capacitances are not fully charged. Hence, thermal anisotropy has an insignificant effect on the behavior of temperature. On the other side, if the system comes to reach steady-state (not real for ECT case), the thermal capacitance behaves as an open circuit and the resistances plays the major role. In such cases, thermal anisotropy affects temperature distribution and should be considered in the model. For some thermotherapy techniques and implanted electronic devices [50] like thermal ablation, transcutaneous electrical nerve stimulation and DBS [5], thermal anisotropy should be applicable.

### ***5.5.3 Extrapolation of Input Current***

The conventional current used as an ECT input is among 0.5 and 0.9 A. As the point was to analyze the behavior of temperature, this input was extrapolated. Therefore, only as a simulation experiment, the tested currents varied from 0.4 until 3.6 A (Figs. 5.12 and 5.13). Previous results showed that the temperature has a higher increase in the external layers, when compared to the internal layers. Are there, thus, any increase in temperature in the internal layers with these high inputs?

It is known that temperatures bigger than 40 °C cause damage in tissues and when above 41 °C, tissue ablation occurs [6]. For the normal ECT current, these temperatures occur only on the external layers. If the temperature of the brain reaches 38 °C, it may suffer changes in cell excitability, network function, and blood–brain barrier function [6]. From our experimental input current, in order for the brain temperature reaches 38 °C, the input current needed to be higher than 1.75 A. As previously stated, high currents like this is not used in real ECT practice. Therefore, from the thermal point of view, the brain is safe when ECT is applied. Higher temperatures only occur at scalp and fat, as mentioned in the work of Swartz [54]. To further solidify the results, a sensitivity analysis was realized by varying the parameters of scalp, thermal and electrical conductivity, and the inclusion or not of blood perfusion, metabolic heat, and the fat layer.

### ***5.5.4 Temperature Distribution Considering the Effect of Biological Properties in a Realistic Model***

The realistic head models in this study also analyzed the temperature distribution generated due to electrical stimulation, taking into account the effect of biological

properties, thermal and electrical conductivity, blood perfusion and metabolic heat, and the inclusion or not of a fat layer [41].

A study by Elwassif et al. [6] modelled the WM as a cylinder in a DBS simulation. They demonstrated that the peak temperature rises when the value of  $\sigma$  increases and  $k$  is maintained at a fixed value. The geometry they used was one-layer only and no adjacent tissues were taken into account. In part, our results agree with their study. However, we analyzed the scalp temperature, considering a realistic model with diverse tissues and convection to ambient. These can explain the differences found among the results.

The electrode configuration used affects the behavior and intensity of the E-field [9, 51]. Similar conduct occurred in the present study. BF configuration which has the smallest distance between electrodes showed stronger E-field, and consequently, strongest peak temperature.

For the different electrode configuration used it is important to consider safety limits [4]. As shown in the present study, despite no influence occurring in brain temperature, scalp and fat layers demonstrated different temperature variation according to the electrode montage applied.

The peak temperature is influenced by the inclusion of metabolic heat and blood perfusion. The presence of these parameters enabled Joule heat to be convected out of the tissue layers, triggering peak temperature drop [6]. In our results, that same behavior occurred. However, the decrease in temperature is only as far as 0.13%, which equates to less than 2.5 times the drop in temperature found in Elwassif et al. [6], despite the tissue layers observed exhibiting distinctly different properties.

The inclusion of fat into the model increases scalp current density [55], consequently increasing the temperature. Fat has an electrical conductivity ten times smaller than scalp electrical conductivity. Moreover, current chooses the least resistive path to flow. Thus, it causes a shrinkage of the effective cross-sectional area of the current preferential path in the scalp [55]. Consequently, it is important to consider the fat layer in a thermal-electrical human head model.

## 5.6 Conclusions

The development of a realistic human head model from MRI images is covered. A brief explanation about MRI and the image process used to construct the head model is provided. The main procedures such as image registration, tissue segmentation, mesh generation and computation are also explained.

This work analyzes the profiles of temperatures arising during electroconvulsive therapies when anisotropic thermal and electrical conductivities are considered in the skull layer. The work was conducted using RHM, with six layers. The results from the head models show that current ECT practice is safe and no harm is caused to the brain from a thermal point of view. An increase in temperature occurs only in external layers, in specific regions, mainly near the electrodes, in the scalp and fat. The brain will only be affected if currents higher than 1.75 A are applied (not

a practical ECT current). The electrode montage influences temperature behavior. Anisotropic thermal conductivity does not influence the findings significantly; however, skull electrical anisotropy is an important aspect to consider. Moreover, the inclusion of blood perfusion leads to slight drop in peak temperature. Finally, the inclusion of fat is highly recommended in order to achieve more realistic results.

## References

1. A. Cancelli, C. Cottone, F. Tecchio, D.Q. Truong, J. Dmochowski, M. Bikson, A simple method for EEG guided transcranial electrical stimulation without models. *J. Neural Eng.* **13**, 036022 (2016)
2. S. Casarotto, P. Canali, M. Rosanova, A. Pigorini, M. Fecchio, M. Mariotti, A. Lucca, C. Colombo, F. Benedetti, M. Massimini, Assessing the effects of electroconvulsive therapy on cortical excitability by means of transcranial magnetic stimulation and electroencephalography. *Brain Topogr.* **26**, 326–337 (2013)
3. J.-J. Chen, L.-B. Zhao, Y.-Y. Liu, S.-H. Fan, P. Xie, Comparative efficacy and acceptability of electroconvulsive therapy versus repetitive transcranial magnetic stimulation for major depression: a systematic review and multiple-treatments meta-analysis. *Behav. Brain Res.* **320**, 30–36 (2017)
4. A. Datta, M. Elwassif, M. Bikson, Bio-heat transfer model of transcranial DC stimulation: comparison of conventional pad versus ring electrode. *Conf. Proc. IEEE Eng. Med. Biol. Soc.* **2009**, 670–673 (2009)
5. M.M. Elwassif, A. Datta, A. Rahman, M. Bikson, Temperature control at DBS electrodes using a heat sink: experimentally validated FEM model of DBS lead architecture. *J. Neural Eng.* **9**, 046009 (2012)
6. M.M. Elwassif, Q. Kong, M. Vazquez, M. Bikson, Bio-heat transfer model of deep brain stimulation-induced temperature changes. *J. Neural Eng.* **3**, 306–315 (2006)
7. A. Fertoni, C. Miniussi, Transcranial electrical stimulation what we know and do not know about mechanisms. *Neuroscientist* (2016). pii:1073858416631966.
8. B. Guleyupoglu, P. Schestatsky, D. Edwards, F. Fregni, M. Bikson, Classification of methods in transcranial Electrical Stimulation (tES) and evolving strategy from historical approaches to contemporary innovations. *J. Neurosci. Methods* **219**, 297–311 (2013)
9. W.H. Lee, Z.-D. Deng, T.-S. Kim, A.F. Laine, S.H. Lisanby, A.V. Peterchev, Regional electric field induced by electroconvulsive therapy in a realistic finite element head model: influence of white matter anisotropic conductivity. *Neuroimage* **59**, 2110–2123 (2012)
10. A.V. Peterchev, T.A. Wagner, P.C. Miranda, M.A. Nitsche, W. Paulus, S.H. Lisanby, A. Pascual-Leone, M. Bikson, Fundamentals of transcranial electric and magnetic stimulation dose: definition, selection, and reporting practices. *Brain Stimul.* **5**, 435–453 (2012)
11. T. Wagner, A. Valero-Cabre, A. Pascual-Leone, Noninvasive human brain stimulation. *Annu. Rev. Biomed. Eng.* **9**, 527–565 (2007)
12. A. Datta, V. Bansal, J. Diaz, J. Patel, D. Reato, M. Bikson, Gyri-precise head model of transcranial direct current stimulation: improved spatial focality using a ring electrode versus conventional rectangular pad. *Brain Stimul.* **2**, 201–207 (2009)
13. S. Shahid, P. Wen, T. Ahfock, Numerical investigation of white matter anisotropic conductivity in defining current distribution under tDCS. *Comput. Meth. Prog. Biomed.* **109**, 48–64 (2013)
14. R.D. Weiner, *The Practice of Electroconvulsive Therapy: Recommendations for Treatment, Training, and Privileging: A Task Force Report of the American Psychiatric Association* (Amer. Psych. Assoc., USA, 2002)
15. M.A. Rosa, S.H. Lisanby, Somatic treatments for mood disorders. *Neuropsychopharmacol.* **37**, 102–116 (2012)

16. H.A. Sackeim, J. Long, B. Luber, J.R. Moeller, I. Prohovnik, D. Devanand, M.S. Nobler, Physical properties and quantification of the ECT stimulus: I. Basic principles. *J. ECT* **10**, 93–123 (1994)
17. D. Fiala, K.J. Lomas, M. Stohrer, A computer model of human thermoregulation for a wide range of environmental conditions: the passive system. *J. Appl. Physiol.* **87**, 1957–1972 (1999)
18. P.A. Boulby, F.J. Rugg, in *Quantitative MRI of the Brain*, ed. by P. Tofts. T2: The Transverse Relaxation Time (John Wiley & Sons Ltd., Chichester, 2003)
19. P.S. Tofts, in *Quantitative MRI of the Brain: Measuring Changes Caused by Disease*, ed. by P. Tofts. PD: Proton Density of Tissue Water (John Wiley & Sons Ltd., Chichester, 2003)
20. P.A. Gowland, V.L. Stevenson, in *Quantitative MRI of the Brain: Measuring Changes Caused by Disease*, ed. by P. Tofts. T1: The Longitudinal Relaxation Time (John Wiley & Sons Ltd., Chichester, 2003)
21. S.M. Smith, M. Jenkinson, M.W. Woolrich, C.F. Beckmann, T.E. Behrens, H. Johansen-Berg, P.R. Bannister, M. DE Luca, I. Drobnjak, D.E. Flitney, Advances in functional and structural MR image analysis and implementation as FSL. *Neuroimage* **23**, S208–S219 (2004)
22. V. Positano, in *Advanced Image Processing in Magnetic Resonance Imaging*, ed. by L. L. V. P. M. F. Santarelli. Image Registration in MRI (Taylor & Francis Group, LLC, Boca Raton, 2005)
23. P.J. Kostelec, S. Periaswamy, Image registration for MRI. *Mod. Signal Process.* **46**, 161–184 (2003)
24. L.G. Brown, A survey of image registration techniques. *ACM Comput. Surv.* **24**, 325–376 (1992)
25. M. Jenkinson, P. Bannister, M. Brady, S. Smith, Improved optimization for the robust and accurate linear registration and motion correction of brain images. *Neuroimage* **17**, 825–841 (2002)
26. I. Despotović, B. Goossens, W. Philips, MRI segmentation of the human brain: challenges, methods, and applications. *Comput. Math. Methods Med.* **2015**, 1–23 (2015)
27. M.N.I. McConnell Brain Imaging Center, McGill University. BrainWeb: Simulated brain database. <http://www.bic.mni.mcgill.ca/brainweb/>
28. B. Aubert-Broche, A.C. Evans, L. Collins, A new improved version of the realistic digital brain phantom. *Neuroimage* **32**, 138–145 (2006)
29. S.M. Smith, Fast robust automated brain extraction. *Hum. Brain Mapp.* **17**, 143–155 (2002)
30. S. Bai, C. Loo, S. Dokos, A review of computational models of transcranial electrical stimulation. *Crit. Rev. in Biomed. Eng.* **41**, 21–35 (2013)
31. M. Ferdjallah, F. Bostick, R. Barr, Potential and current density distributions of cranial electrotherapy stimulation (CES) in a four-concentric-spheres model. *IEEE Trans. Biomed. Eng.* **43**, 939–943 (1996)
32. J. Malmivuo, R. Plonsey, *Bioelectromagnetism: Principles and Applications of Bioelectric and Biomagnetic Fields* (Oxford University Press, Oxford, 1995)
33. S.S. Shahid, Numerical Investigation of Transcranial Direct Current Stimulation on Cortical Modulation. PhD Thesis, University of Southern Queensland (2013).
34. H.H. Pennes, Analysis of tissue and arterial blood temperatures in the resting human forearm. *J. Appl. Physiol.* **1**, 93–122 (1948)
35. L. Bezerra, M.M. Oliveira, T. Rolim, A. Conci, F. Santos, P. Lyra, R. Lima, Estimation of breast tumor thermal properties using infrared images. *Signal Process.* **93**, 2851–2863 (2013)
36. K.M. Silay, C. Dehollain, M. Declercq, in Numerical Analysis of Temperature Elevation in the Head Due to Power Dissipation in a Cortical Implant. *EMBC-IEEE Ann. Int. Conf.* pp. 951–956 (2008)
37. S.A. Berger, W. Goldsmith, E.R. Lewis, *Introduction to Bioengineering* (Oxford University Press, USA, 1996)
38. M.M. Christian, S.L. Firebaugh, A.N. Smith, COMSOL thermal model for a heated neural micro-probe. *Proc. COMSOL Conf.* (2012).
39. P.A. Hasgall, E. Neufeld, M.C. Gosselin, A. Klingenböck, N. Kuster, IT'IS Database for thermal and electromagnetic parameters of biological tissues (2014)

40. M.M. Oliveira, P. Wen, T. Ahfock, Heat transfer due to electroconvulsive therapy: Influence of anisotropic thermal and electrical skull conductivity. *Comput. Meth. Prog. Biomed.* **133**, 71–81 (2016)
41. M.M. Oliveira, P. Wen, T. Ahfock, Bio-heat transfer model of electroconvulsive therapy: Effect of biological properties in induced temperature variation. *EMBC-IEEE Ann. Int. Conf. IEEE* (2016)
42. J. De Munck, The potential distribution in a layered anisotropic spheroidal volume conductor. *J. Appl. Phys.* **64**, 464–470 (1988)
43. G. Marin, C. Guerin, S. Baillet, L. Garnero, G. Meunier, Influence of skull anisotropy for the forward and inverse problem in EEG: simulation studies using FEM on realistic head models. *Hum. Brain Mapp.* **6**, 250–269 (1998)
44. S.P. van den Broek, F. Reinders, M. Donderwinkel, M. Peters, Volume conduction effects in EEG and MEG. *Electroencephalogr. Clin. Neurophysiol.* **106**, 522–534 (1998)
45. C. Wolters, A. Anwander, X. Tricoche, D. Weinstein, M. Koch, R. Macleod, Influence of tissue conductivity anisotropy on EEG/MEG field and return current computation in a realistic head model: a simulation and visualization study using high-resolution finite element modeling. *Neuroimage* **30**, 813–826 (2006)
46. B.S. Khundrakpam, V.K. Shukla, P.K. Roy, Thermal conduction tensor imaging and energy flow analysis of brain: A feasibility study using MRI. *Ann. Biomed. Eng.* **38**, 3070–3083 (2010)
47. W.H. Lee, Z. Liu, B.A. Mueller, K. Lim, B. He, Influence of white matter anisotropic conductivity on EEG source localization: Comparison to fMRI in human primary visual cortex. *Clin. Neurophysiol.* **120**, 2071–2081 (2009)
48. M.M. Oliveira, P. Wen, T. Ahfock, S.S. Shahid, A preliminary study about the distribution of temperature due to electrical stimulation in ECT (*Int. Conf. Complex Med. Eng.*, Taipei, Taiwan, 2014)
49. M.M. Oliveira, *Human head temperature and electric field investigations under ECT*, PhD Thesis, University of Southern Queensland, (2017)
50. S. Kim, P. Tathireddy, R. Normann, F. Solzbacher, Thermal impact of an active 3-D micro-electrode array implanted in the brain. *IEEE Trans. Neural Syst. Rehabil. Eng.* **15**, 493–501 (2007)
51. S. Bai, C. Loo, A. Al Abed, S. Dokos, A computational model of direct brain excitation induced by electroconvulsive therapy: comparison among three conventional electrode placements. *Brain Stimul.* **5**, 408–421 (2012)
52. E.J. Berjano, J. Saiz, J.M. Ferrero, Radio-frequency heating of the cornea: Theoretical model and in vitro experiments. *IEEE Trans. Biomed. Eng.* **49**, 196–205 (2002)
53. H. Watanabe, N. Yamazaki, Y. Kobayashi, T. Miyashita, M. Hashizume, M.G. Fujie, in Temperature Dependence of Thermal Conductivity of Liver Based on Various Experiments and a Numerical Simulation for RF Ablation. *EMBC-IEEE Ann. Int. Conf. IEEE 2010*. pp. 3222–3228 (2010)
54. C.M. Swartz, Safety and ECT stimulus electrodes: I. Heat liberation at the electrode-skin interface. *J. ECT* **5**, 171–175 (1989)
55. S. S. Shahid, P. Wen, T. Ahfock, in Effect of fat and muscle tissue conductivity on cortical currents—A tDCS study. *2011 IEEE/ICME Int. Conf. Complex Med. Eng.* pp. 211–215 (2011)

# Chapter 6

## Use of Photon Scattering Interactions in Diagnosis and Treatment of Disease



**Robert Moss, Andrea Gutierrez, Amany Amin, Chiaki Crews, Robert Speller, Francesco Iacoviello, Paul Shearing, Sarah Vinnicombe, and Selina Kolokytha**

**Abstract** This chapter looks at photon scattering applications in medicine. In the energy range of interest there are two types of scattering events, incoherent (Compton) and coherent (Rayleigh) scattering, and this chapter looks at how these events can be usefully used in the diagnosis and treatment of disease. In the first part we present an overview of Compton cameras for gamma imaging in the context of proton beam therapy, where they can be used for proton range verification. Proton beam therapy is currently in need of range verification for quality assurance and to improve treatment efficacy and safety. We will first briefly introduce potential methods for in vivo proton range verification, of which prompt gamma imaging is a promising example. We describe the process of gamma emission during proton irradiation, as well as the challenges of its detection and interpretation. The use

---

R. Moss · A. Gutierrez · C. Crews · R. Speller  
Department of Medical Physics & Biomedical Engineering, University College London,  
London, UK  
e-mail: [robert.moss@ucl.ac.uk](mailto:robert.moss@ucl.ac.uk); [a.gutierrez@ucl.ac.uk](mailto:a.gutierrez@ucl.ac.uk); [chiaki.crews.10@ucl.ac.uk](mailto:chiaki.crews.10@ucl.ac.uk);  
[r.speller@ucl.ac.uk](mailto:r.speller@ucl.ac.uk)

A. Amin  
John Radcliffe Hospital, Oxford, UK  
St Bartholomew's Hospital, London, UK  
e-mail: [amany.amin@ouh.nhs.uk](mailto:amany.amin@ouh.nhs.uk)

F. Iacoviello · P. Shearing  
Electrochemical Innovation Lab, Department of Chemical Engineering, University College  
London, London, UK  
e-mail: [f.iacoviello@ucl.ac.uk](mailto:f.iacoviello@ucl.ac.uk); [p.shearing@ucl.ac.uk](mailto:p.shearing@ucl.ac.uk)

S. Vinnicombe  
The Breast Unit, Cheltenham, Gloucestershire Hospitals NHS Foundation Trust, Gloucester, UK  
The University of Dundee, Dundee, UK  
e-mail: [sarah.vinnicombe@nhs.net](mailto:sarah.vinnicombe@nhs.net)

S. Kolokytha (✉)  
Empa, Centre for X-Ray Analytics, Swiss Federal Laboratories for Materials Science  
and Technology, Dübendorf, Switzerland

of Compton camera for prompt gamma imaging has advantages over other gamma detectors since it does not require mechanical collimators and has a typical field of view of  $180^\circ$ . The Compton camera's principle of operation and design criteria for prompt gamma imaging are described, as well as image reconstruction techniques such as back-projection and stochastic origin ensemble.

The second part of the chapter presents tissue diffraction, based upon coherent scattering as a diagnostic tool. X-ray diffraction (XRD) is a technique which can be used to calculate the atomic or molecular structure of a material by measuring X-ray scattering profiles. While XRD has been a longstanding tool in analytical and materials science, this section reviews the relatively new application of XRD to the differentiation of healthy and cancerous tissue and how the results compare to conventional histopathology. As well as outlining the typical signatures expected of different tissue types, the hardware and data processing requirements will be discussed, particularly in the context of the trade-offs that would need to be considered in the design and development of a clinically deployable system.

**Keywords** Compton scattering · Imaging · Coherent scattering · X-ray diffraction · Tissue analysis

## 6.1 Introduction to Photon Scattering

Photon scattering (elastic and inelastic) is often considered a problem in the medical applications of ionising radiation beams. For example, in diagnostic radiology scattered photons generate a featureless background upon which the useful information is superimposed. This is a situation that can mean that the ratio of scattered photons to primary radiation can exceed 10 in some diagnostic X-ray examinations. The net effect is to reduce the contrast-to-noise ratio and hence make the detection of subtle features more difficult. Hence, a series of techniques have been introduced to reduce the effects of scattered radiation in imaging techniques [1]. The use of ionising radiation in the treatment of disease requires well defined beams of radiation, as anything that detracts from the designed shape of a treatment beam will mean that unintended tissues are being irradiated. Scatter will contribute to the off-target radiation, but with higher energies employed in treatment, the scatter is generated in the forward direction which generally helps mitigate its undesirable effects.

However, scattered radiation fields can be usefully exploited [2] and this chapter looks at medical applications of both inelastic and elastic scattering. The kinematics of inelastic or Compton scattering links the angle at which photons are scattered to their initial energy and the energy deposited in the interaction. The probability of inelastic scattering taking place depends upon the electron density and physical density of the material through which the beam is passing. Thus, knowing the incident energy and the energy lost in an appropriate detector system allows



scattering angles to be calculated, enabling maps of source locations to be generated. These detector systems are called Compton cameras—described in detail later in this chapter—and have been used to study these parameters in a number of medical investigations. Bone quality metrics have been developed by making estimates of physical density [3, 4] and the measurement of electron density in mixed tissue samples has been used to characterise breast cancer [5]. One of the advantages of studying inelastic as opposed to elastic scattering is that the former occurs at the higher X-ray energies most commonly used in medical investigations.

Elastic or Rayleigh scattering is most predominant in soft tissues at low X-ray energies in the range most frequently used in mammographic examinations. Two approaches have been investigated in the use of elastic scattering: measurements of total scattered intensity, and measurements of the interference patterns generated after elastic scattering, i.e. the recording of X-ray diffraction patterns. The total scattered intensity has a dependence upon the atomic number of the material through which the beam is passing as well as the physical density. Hence combining elastic and inelastic scatter measurements allows the effective atomic number of tissues to be determined and this has been applied in the study of breast tissue [6]. Recording X-ray diffraction information from biological tissues has been undertaken to study both crystalline and amorphous materials. Calcified tissues (bone [7, 8] and urinary calculi [9]) provide well defined diffraction data with sharp peaks due to their crystalline nature, but the more amorphous tissues such as breast [10–12] and liver [13] provide diffraction profiles made up of one or more broad, often overlapping, peaks. It is these amorphous biological materials with more challenging X-ray diffraction signatures that are the subject of the X-ray diffraction study described below.

## 6.2 Prompt Gamma Imaging During Proton Beam Therapy Using Incoherent Scattering

The use of incoherent scattering interactions is mainly used in nuclear medicine, specially for positron emission tomography (PET) and single photon emission computed tomography (SPECT). Imaging of prompt gamma during proton beam therapy is a relatively new technique that can potentially be used for treatment verification. In this section we present prompt gamma imaging during proton beam therapy using Compton cameras. We first discuss the concept of using prompt gamma detection for proton range verification and the principle of operation of Compton cameras. At the end of the section, we focus on Stochastic Origin Ensemble (SOE) image reconstruction, the most widely used technique for prompt gamma imaging. SOE has the advantage of being computationally fast, which makes it ideal for real-time imaging.

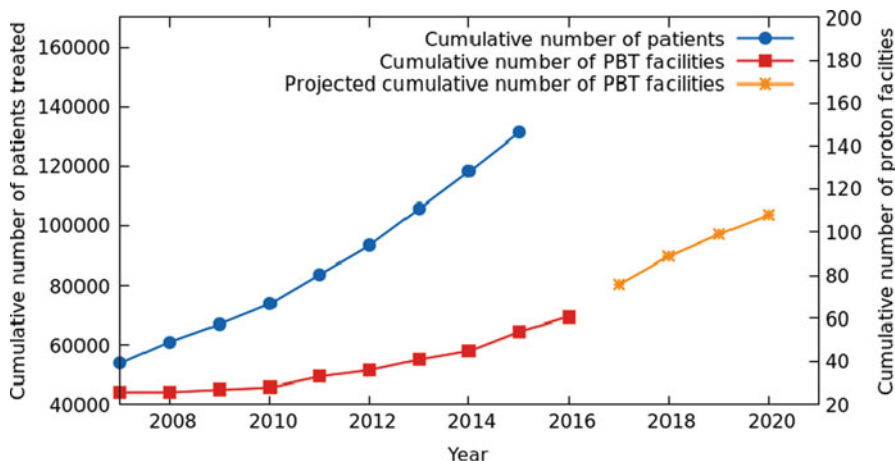


**Fig. 6.1** Cumulative number of patients treated (left axis) and cumulative number of operational proton beam facilities (right axis) since 2007. The projected cumulative number of PBT facilities (right axis) from 2017 to 2020 is an estimate from the existing information of facilities under construction and in the planning phase. Data was extracted from [www.ptcog.ch](http://www.ptcog.ch), the Particle Therapy Co-Operative Group in April 2017

### 6.2.1 *In Vivo Proton Range Verification*

Worldwide, the number of proton beam therapy (PBT) facilities for cancer treatment has been increasing exponentially. The increasing demand is not surprising since proton beam therapy has considerable clinical benefits over photon therapy. Protons deposit most of their energy in a localised volume, the so-called Bragg peak, sparing surrounding healthy tissue and critical organs the effects of radiation. Figure 6.1 shows the cumulative number of treated patients and the cumulative number of operational proton beam facilities since 2007.

PBT is particularly suitable for pediatric cancers, as well as brain, head and neck cancers. Unfortunately, the full potential of PBT has been limited by uncertainties associated with patient immobilisation and setup, organ motion, anatomical and physiological changes of the patient, dose calculation (e.g. artefacts in computed tomography images and stopping power conversion), and beam delivery [14]. These uncertainties could compromise the treatment, resulting in under-dosing the tumour and/or over-dosing healthy tissues as illustrated in Fig. 6.2.

*In vivo* real-time proton range verification is highly desirable for clinical application. Online monitoring of dose delivery would allow real-time quality assurance of treatment and help to prevent long-term adverse side-effects compromising the health and well-being of the patient. Several approaches have been proposed and are currently being investigated; a review by Knopf and Lomax can be found in [15]. The difficulty of proton range verification relies on the fact that protons are typically completely absorbed in the human tissue. For this reason, some direct

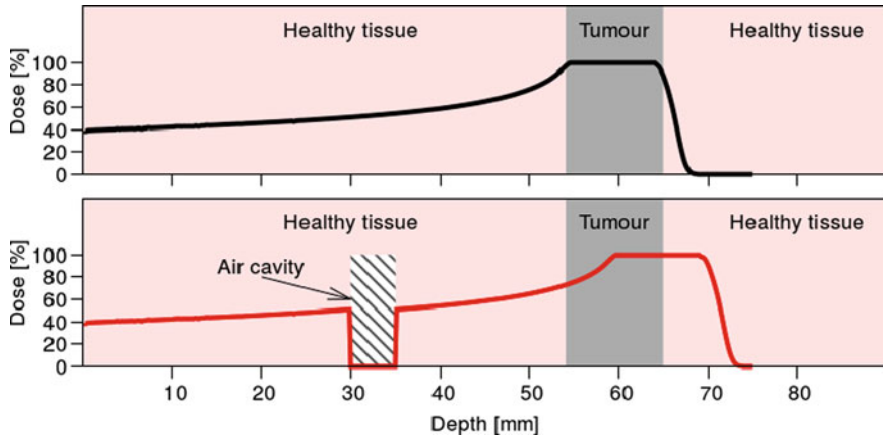


**Fig. 6.2** Illustration of the localized energy deposition in a tumour with a spread-out Bragg peak (SOBP) (top image) and the effect of proton range uncertainties when an air cavity is present in the proton path (bottom image). The bottom image illustrates the influence of proton range uncertainties where the tumour is under-dosed and the healthy tissue is over-dosed

methods for range and dose verification would be rather invasive, for example using implantable dosimeters [16–19]. On the other hand, indirect methods make use of, for example, the detection of secondary particles created from the interaction of the protons through tissue. Prompt gamma rays are emitted during proton irradiation of tissue and will be the scope of this chapter part. Also, acoustic waves are produced as the protons' energy is deposited and can potentially be used to determine the proton range [20–23]. This technique combined with other techniques, such as optoacoustic tomography, is also under investigation [24].

A wide range of gamma-ray energies is emitted during proton irradiation. Particularly, there are two principal mechanisms through which the majority of gamma rays are created:

1. Coincident 511 keV gamma rays are produced by positron emitting isotopes (e.g.  $^{11}\text{C}$ ,  $^{13}\text{N}$  and  $^{15}\text{O}$ ) created during nuclear reactions between the protons and nuclei in the tissue material. Positron annihilations are detected using positron emission tomography (PET). The half-life for the beta decay of the isotopes range between 2 and 20 min. This technique can be performed both during and after proton beam treatment, but requires a PET device inside the treatment room. Also, due to transport of the isotopes in the blood stream (the wash-out effect), the distribution of activity in the tissue changes over time. Monte Carlo simulations are used to correct those changes [25]. A summary review of PET for proton range verification by Studenski and Xiao can be found in [26].
2. Some protons undergo nuclear interactions with nuclei in the tissue. As a result of nuclear excitation, prompt gamma rays are emitted within a few nanoseconds. The energy of prompt gamma rays typically ranges from 2 to 10 MeV and the energy spectrum is dominated by specific nuclear de-excitation of carbon

**Table 6.1** Main prompt gamma energies emitted when using  $^{16}\text{O}$  and  $^{12}\text{C}$  targets

Target	Emitter	$E_\gamma$ (MeV)
$^{16}\text{O}$	$^{16}\text{O}$	6.13
		6.92
		7.12
		2.74
	$^{12}\text{C}$	4.44
$^{12}\text{C}$	$^{15}\text{N}$	5.27
	$^{12}\text{C}$	4.44
	$^{11}\text{C}$	2.00

Note that 4.44 MeV corresponding to  $^{12}\text{C}$  nuclear de-excitation is present in both targets. Data extracted from [28]

(4.44 MeV) and oxygen (6.13 MeV). Another dominant gamma line in the spectrum is the one produced by neutron capture of hydrogen, with an energy of 2.2 MeV. Neutrons are produced in the tissue after nuclear interactions in the tissue. If it is a passively scattered beam, neutrons are produced in the nozzle of the beamline.

## 6.2.2 Prompt Gamma Emission

Protons undergo inelastic interactions with nuclei in the tissue. Nuclei excited in the collisions de-excite to the ground state in less than a few nanoseconds by emitting prompt gamma rays, which have energies that are characteristic of the elemental composition of the tissue. Table 6.1 shows the main prompt gamma energies expected during tissue irradiation. Figure 6.3 shows the simulated energy spectrum of gamma rays leaving a plastic phantom irradiated by a 150 MeV proton beam using Geant4 simulation toolkit [27] (proton energies in PBT ranges between 60 and 230 MeV). The peaks correspond to the discrete nuclear transitions, while the background is mainly bremsstrahlung photons from electrons. The latter originate from atomic interactions between protons and atoms of the tissue. In addition to gamma emission, a substantial number of neutrons are produced during proton irradiation. The neutrons can also produce prompt gamma rays via neutron capture reactions.

Prompt gamma rays are emitted along the path of the primary protons and are correlated with the Bragg curve. Prompt gamma imaging for range verification was first proposed by Stichelbaut and Jongen in 2003 [29] and in 2006, Ming et al. performed the first experimental demonstration of the correlation between prompt gamma rays and the Bragg peak [30].

However, prompt gamma emission does not directly match the delivered dose: prompt gamma rays are created through nuclear interactions while the Bragg peak is mostly the result of electromagnetic interactions. Prompt gamma yield typically increases near the end of the beam path, with a sudden drop when the primary proton

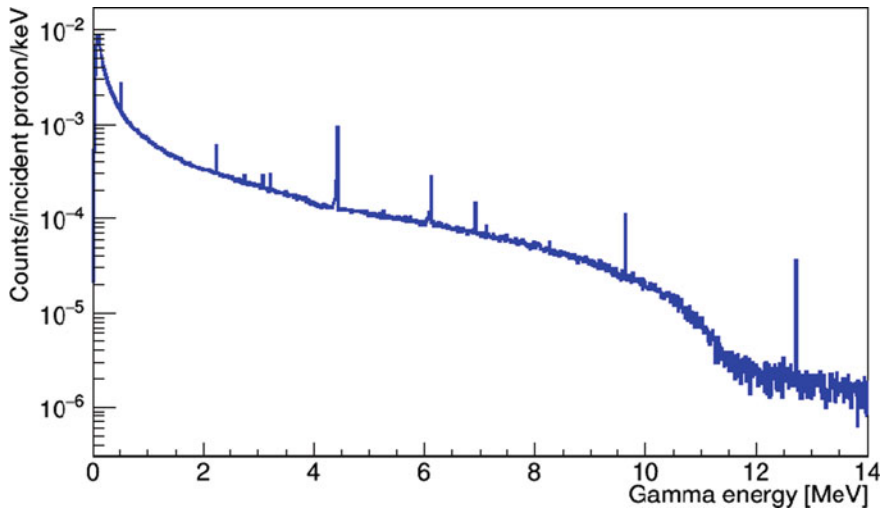


**Fig. 6.3** Simulated energy of gamma rays leaving a plexiglass phantom ( $20 \times 20 \times 20 \text{ cm}^3$ ) when irradiated by 150 MeV proton (Geant4 v.10.02.p01 and physics list QGSP\_BERT\_HP\_LIV). Table 6.1 shows the characteristic prompt gamma energies

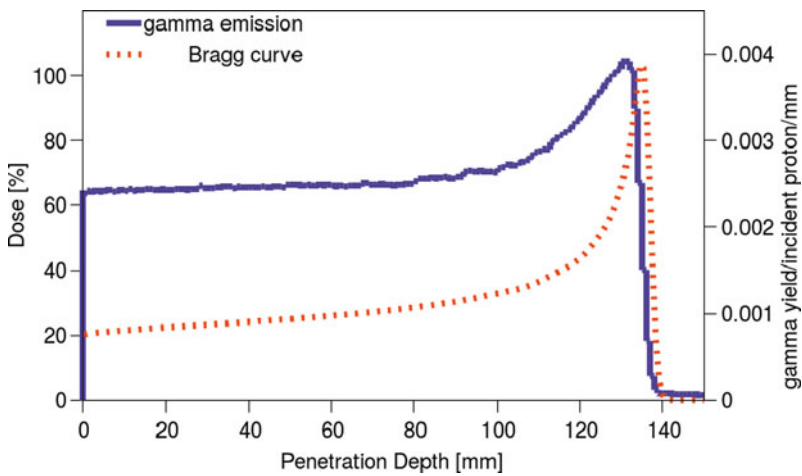


**Fig. 6.4** Simulation of 150 MeV protons irradiating a plexiglass phantom (Geant4 v.10.02.p01 and physics list QGSP\_BERT\_HP\_LIV). Proton dose (left axis) as a function of the penetration depth (Bragg curve) and the corresponding gamma emission (right axis) are shown

energy is below the reaction threshold. Figure 6.4 shows an example of gamma yield as a function of the penetration depth. To date, application of this technique relies on the relative change of the prompt gamma emission rather than inferring the absolute range of protons.

The difficulty of prompt gamma detection lies in developing a device with high detection efficiency in the 2–10 MeV range. Several detectors have been investigated: pinhole and knife-edge collimator cameras [31–33], multi-slit collimator cameras [34–36], two-stage [37–39] and triple-stage Compton cameras [40–42]. In addition, due to the high neutron background, the time-of-flight technique has been developed and demonstrated to efficiently discriminate between prompt gamma rays and secondary fast neutrons [43].

In 2016 a first clinical test of range verification during proton beam therapy was performed in a patient with a knife-edge camera from IBA. Richter et al. demonstrated the potential to improve the precision of particle therapy with this technique [44].

### 6.2.3 Compton Camera Principle of Operation

Compton cameras have been developed and used for a variety of applications, including astrophysics, industrial imaging, radioactive waste management and medical imaging.

Compton cameras were first proposed for medical application in 1974 [45] and were first built and tested for medical use by Singh and Doria [46] for single photon emission computed tomography (SPECT), as a replacement for the conventional mechanical parallel collimator in front of a position sensitive detector.

Compton cameras have the advantage over mechanical collimators of having a wider field of view and detecting a larger number of gamma rays (due to the absence of an absorber/mechanical collimator). Therefore, Compton cameras can have increased sensitivity with an improved signal-to-noise ratio and shorter detection times [45].

Compton cameras exploit Compton scattering kinematics to track back the position of the gamma-ray source. Figure 6.5 shows the Compton scattering principle where an incident photon scatters off an electron at rest.

Using the energy and momentum conservation, the relationship between initial photon energy ( $E_\gamma$ ), the scattered photon energy ( $E_{\gamma'}$ ), and the scattering angle ( $\theta$ ) can be given as:

$$\cos \theta = 1 - m_e c^2 \left[ \frac{1}{E_{\gamma'}} - \frac{1}{E_\gamma} \right], \quad (6.1)$$

where  $m_e$  is the electron rest mass and  $c$  is the speed of light.

Compton cameras are composed of two detector layers: a scatterer where the recoil electron is detected and an absorber where the scattered photon is completely absorbed by photoelectric effect or multiple scattering processes. Some Compton cameras have been optimised with multiple layers (e.g. multiple scatterers for better image resolution or multiple absorbers for high energy photons).

**Fig. 6.5** Illustration of Compton scattering

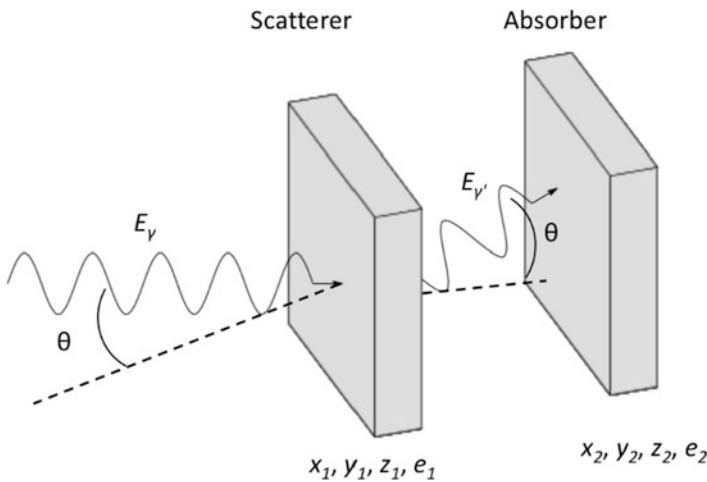
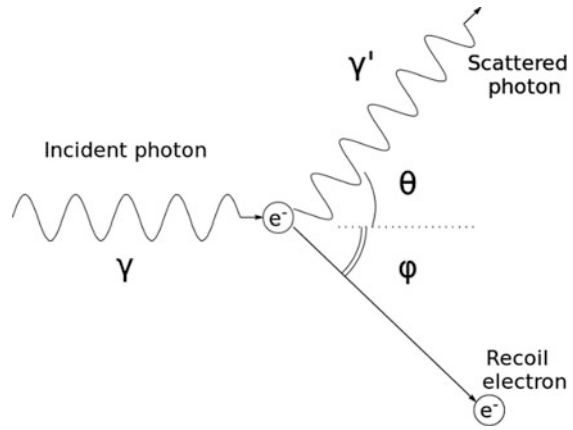


**Fig. 6.6** Illustration of the Compton camera principle.  $(x_1, y_1, z_1)$  is the detected position of the recoil electron in the scatter layer and  $e_1$  is its detected energy.  $(x_2, y_2, z_2)$  is the detected position in the absorber layer and  $e_2$  is the energy of the absorbed photon (measured through secondary electrons)

Both layers are position sensitive to extract the direction of the scattered photon, as illustrated in Fig. 6.6. Also, the energies of the recoil and absorbed electrons ( $e_1$  and  $e_2$ , respectively) have to be accurately detected. From Eq. (6.1), the scattering angle can be translated in terms of the detected quantities:

$$\cos \theta = 1 - m_e c^2 \left[ \frac{1}{e_2} - \frac{1}{e_1 + e_2} \right], \tag{6.2}$$

where  $E_\gamma = e_1 + e_2$  and  $E_{\gamma'} = e_2$ . With this information, the source of the incident photon can be constrained to lie on a conical surface.

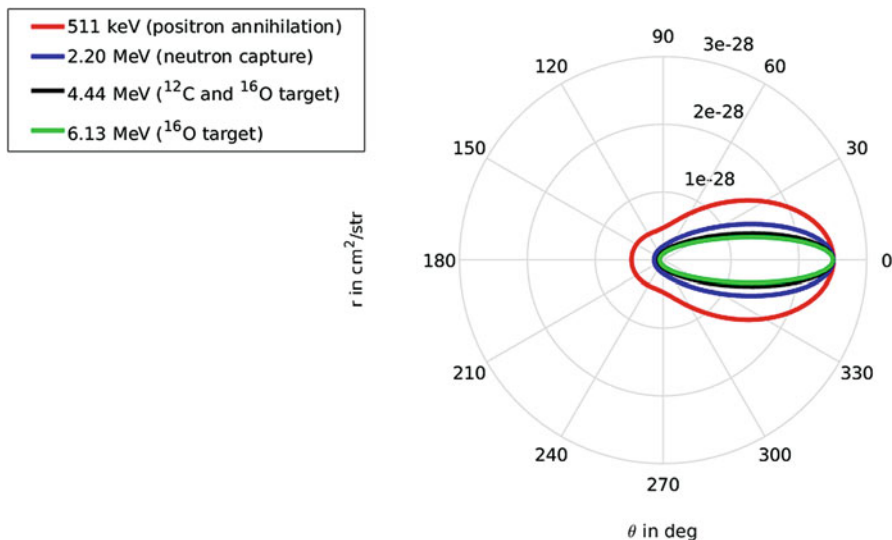


**Fig. 6.7** Differential cross section of photon scattering in Germanium using Klein–Nishina formula [46]

### 6.2.4 Design Criteria

A Compton camera is position and energy sensitive. Simultaneous events need to be detected in coincidence so the information can be used to reconstruct the conical surface of each set of events. The material and thickness of the layers are optimised to increase the probability of a scattering interaction in the scatterer while avoiding multiple scattering. The second layer is typically optimised to increase the probability of full absorption of the scattered photon. Another parameter for optimisation is the distance between the layers and the sensitive area of the detector. Such optimization for prompt gamma imaging has been studied in [40, 41].

Another criterion to take into account is the differential cross section of photon scattering. It is desired that photons in the first layer will be scattered forward so they can be detected by the second layer. The scattering angle depends on the photon energy and the scattering material, as reflected in the Klein–Nishina formula [46]. Figure 6.7 shows the differential cross section using Klein–Nishina formula in Germanium. For low energy photons, backscattering is more pronounced, while prompt gamma rays in the range of MeV are more likely to be scattered in the forward direction.



### 6.2.5 Compton Camera Image Reconstruction Principle

The image reconstruction principle consists of using coincidence events (one from the scatterer and one from the absorber) and reconstructing the corresponding conical surfaces using the scattering angle  $\theta$  and the direction of scattering (cone direction axis) in the field of view of the detector [47]. If the distance between the photon source and the detector is known, a 2D image can be reconstructed by overlapping multiple conical surfaces at the appropriate axial distance as illustrated in Fig. 6.8. Figure 6.9 (left) shows an image reconstruction using a few events from a point source placed at the origin of the image. This analytical algorithm is called back-projection [45, 48]. When using an adequate number of events, an image can be reconstructed as shown in Fig. 6.9 (right).

**Fig. 6.8** Illustration of the back-projection of two conical surfaces from two photon events. The photon source is imaged using the conical surface overlapping

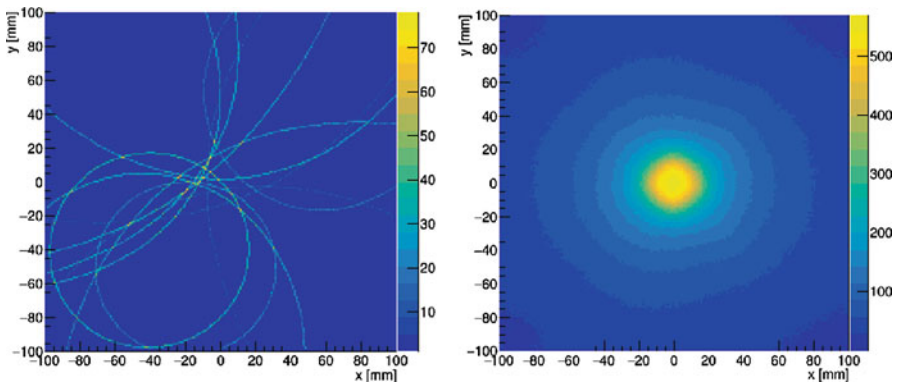
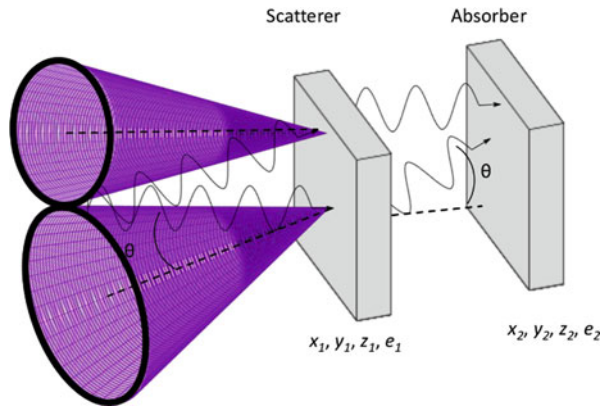


**Fig. 6.9** Example of the resulting image using back-projection algorithm from a simulated point source. In the left, a few tens of events are back-projected so the Compton cones are overlapping. In the right, the resulting reconstructed source with around 100,000 events is presented

Analytical algorithms achieve image reconstruction in an acceptable time for clinical application, although statistical methods, such as iterative algorithms, have great potential to improve the quantitative accuracy of the reconstructed image. An overview of existing image reconstruction algorithms for Compton camera can be found in [49].

Widely used iterative algorithms are, for example, Maximum-Likelihood Expectation-Maximisation (MLEM), List-Mode MLEM and Ordered Subset Expectation Maximisation (OSEM) [50–53], where the latest two are more computing time efficient. Multi-threading and GPU calculation are generally necessary to achieve acceptable reconstruction timing [54–56].

Another iterative algorithm growing in popularity for prompt gamma imaging with a Compton camera is the Stochastic Origin Ensemble (SOE) and will be presented in the next section.

### ***6.2.6 Stochastic Origin Ensemble (Iterative Algorithm)***

The popularity of the Stochastic Origin Ensemble (SOE) is due to the shorter computing time required compared to other iterative algorithms and an image quality comparable to MLEM [57]. The SOE method was derived by Sitek and tested for PET [58]. The algorithm is based on the Markov Chain Monte Carlo method and a rigorous mathematical analysis can be found in [58]. SOE was later demonstrated with a Compton Camera by Andriy et al. [59, 60].

The SOE algorithm does not require back- and forward-projections, nor voxelization of the image space. Instead, images are defined as set of potential origins. For each event, a potential origin is randomly selected in the corresponding conical surface. A probability density matrix is obtained by voxelizing the image space and including events that are currently positioned in each individual voxel. The iterations are performed by randomly generating a new event position. The new position is always accepted if the density is higher at that new given position and the density is updated accordingly. At the end of the desired number of iterations, a voxelized image is generated. SOE has been tested with point sources, see example in Fig. 6.10. Also, the image quality using SOE algorithm can be further improved by implementing resolution recovery [60]. Since Compton cameras have limited spatial and energy resolution, this technique consists of allowing to slightly shift off the respective conical surface during the random position generation. It was shown that resolution recovery improves the quality of images (similar quality as when using a perfect detector) and can be implemented with little computational cost [60].

Mackin et al. used SOE algorithm for prompt gamma imaging with simulated data. It was observed that the prompt gamma distal falloff can be reconstructed within  $\pm 0.6$  mm [61]. Also, multi-threading and GPU acceleration have also been implemented to speed up the image reconstruction [62].

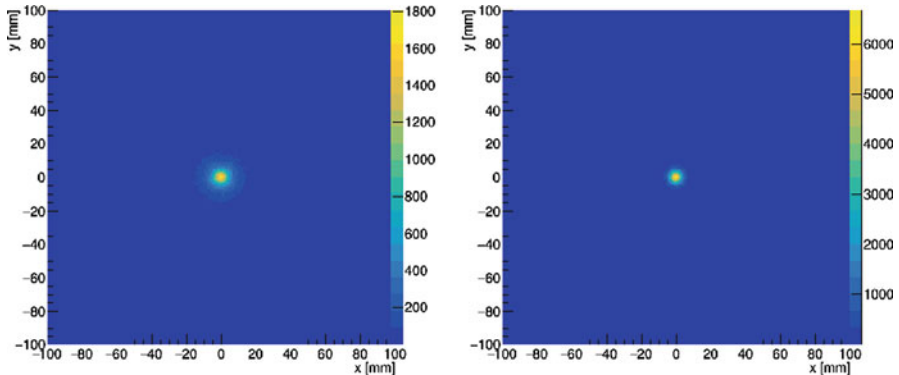


**Fig. 6.10** Image reconstruction of a point source using SOE algorithm after 10 iterations (left) and after 100 iterations (right). The data was simulated using Geant4 v.10.02.p01 and physics list QGSP\_BERT\_HP\_LIV, and 1 mm detector resolution

### 6.3 Volume Analysis of Breast Tissue vs 2D Histopathology—The Role of Coherent Scattering and Tissue Diffraction in Breast Cancer Diagnosis and Management

#### 6.3.1 Introduction to X-Ray Diffraction of Tissue

Breast cancer is the most common form of cancer with over 508,000 women dying globally in 2011 due to breast cancer [63]. Recent research has highlighted the importance of tumour-associated stroma in breast cancer initiation and progression [64]. A major component of such stroma is abnormal collagen, the amount and orientation of which can directly influence epithelial growth and transition as well as response to neoadjuvant therapy. However, conventional X-ray imaging is unable to interrogate stromal collagen and the development of a technique that could identify abnormal collagen could have profound impact on breast cancer diagnosis and treatment.

Early breast cancer treatment usually involves breast conserving surgery (BCS) where the cancerous tissue is removed from the patient. Histopathological analysis is carried out on the excised tissue postoperatively. The tissue is prepared for microscopic analysis starting with dissection of the fresh sample, chemical fixation to prevent decay, further dissection and sampling of regions of interest, processing of the tissue into paraffin wax and production of stained microscope slides. The purpose of the analysis is to delineate and classify the tumour, particularly to ensure that all of the cancerous material has been removed. Where cancerous tissue is found at the edge of the resected tissue, the patient may be required to undergo further treatment.

Histopathological analysis relies on examining a thin (4  $\mu\text{m}$  thick) slice of tissue based on its micro-structure (cellular scale) through the use of optical microscopy. However, changes in the nano-scale structure associated with disease [65] can also be used to discriminate between different tissue types hence suggesting that X-ray diffraction (XRD) signatures can also be used for this purpose. This creates several transformative opportunities. Since X-rays are penetrating radiation they can be used to look at thick sections of tissue and hence could be used to enhance the mammographic examination.

X-ray diffraction (XRD) is a well-established technique which is used to analyse the atomic or molecular structure of materials. Diffraction occurs when X-rays are coherently and elastically scattered from different atomic or molecular layers within a material separated by a distance ( $d$ ). Scattered X-rays constructively interfere at certain scattering angles ( $2\theta$ ), where Bragg's Law is satisfied, giving rise to intense cones of radiation.

$$n\lambda = 2d \sin(\theta) \quad (6.3)$$

Where  $n$  is the order of diffraction (taking on values 1, 2, 3, ... although all the results shown in this work are for  $n = 1$ ) and  $\lambda$  is the wavelength of the radiation. Thus, measurements of the set of " $d$ " values that satisfy Eq. (6.3) can be used to characterise the structure of the material.

### 6.3.2 Trade-Offs in Diffractometer Design and the Pixelated Diffraction Approach

To undertake these measurements Eq. (6.3) can be satisfied using two basic approaches. Angular dispersive X-ray diffraction (ADXRD) uses a monoenergetic beam of X-rays and collects scattered intensities over a wide range of scattering angles either by moving both the source and a single detector or having a fixed geometry and using a pixelated detector. A pixelated detector is a large area sensor that is divided into an array of active pixels. Each pixel records information, total intensity or an energy spectrum and images are formed by displaying the recorded information. The alternative approach of energy dispersive X-ray diffraction (EDXRD) uses a polyenergetic beam of X-ray photons, a fixed scattering angle and an energy dispersive detector. In general ADXRD will provide better specificity in the diffraction data but is usually slower in acquiring the data and uses a system that is best suited to a research laboratory environment. On the other hand, EDXRD can provide results more rapidly in a very compact and adaptable format as there are no moving parts. The two approaches are shown schematically in Fig. 6.11.

A recent development in detector technology called HEXITEC [66] has enabled the advantages of *both* X-ray diffraction techniques to be merged using a hybrid approach called pixelated X-ray diffraction (PixD) [67, 68] and has been demonstrated in a compact system [70]. Figure 6.12 shows how a hybrid methodology is achieved using a pixelated, energy dispersive detector.

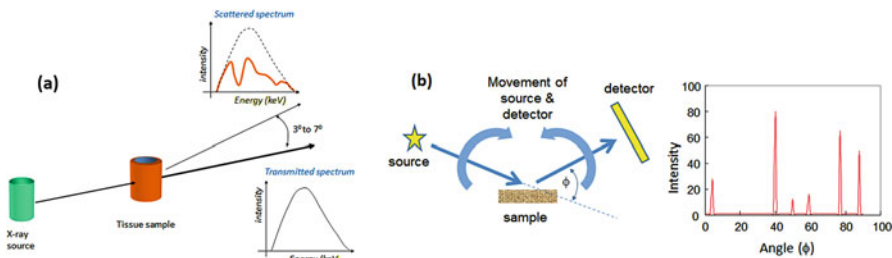


**Fig. 6.11** Possible approaches to X-ray diffraction measurements. (a) shows a typical arrangement for EDXRD where a polyenergetic X-ray beam is used. The source, sample and detector are fixed so that the scattered spectrum can be measured. The scattered or diffractive spectrum will change as the detector is moved away from the straight through or transmitted position. (b) shows a typical arrangement for ADXRD where a monochromatic X-ray beam is used. Both the source and detector move over a range of angles so that different scattering angles ( $\phi$ ) are created. Note that  $\phi = 2\theta$  where  $\theta$  is given in Eq. (6.1)

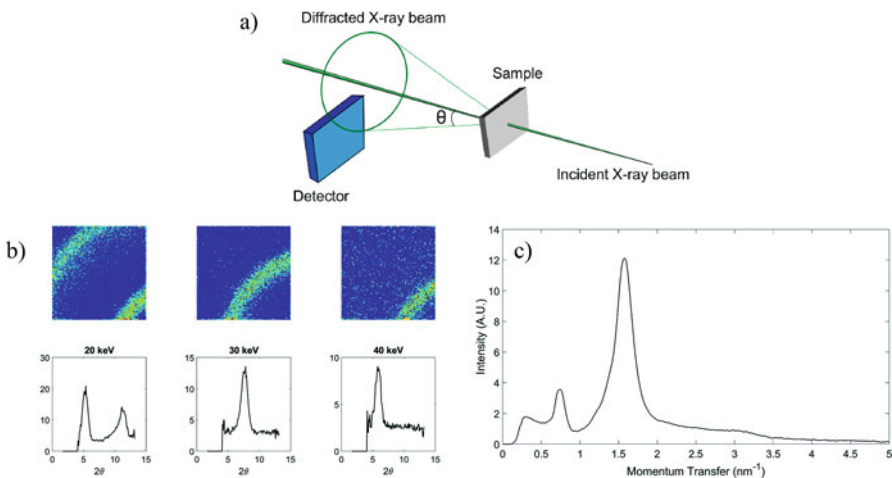


**Fig. 6.12** Pixellated diffraction. (a) shows the arrangement of the pixellated detector with respect to the X-ray beam. In this position the detector records one quadrant of the diffraction profile and avoids saturation from the intense direct X-ray beam. (b) shows typical data sets displayed for narrow energy windows of 20, 30 and 40 keV along with the radially integrated profiles. Although shown as data relating to a single energy, these data are collected at the same time by the Hexitec sensor and sorted into these displays post-acquisition. (c) shows the summed profiles after conversion to momentum transfer. In practice each pixel has a known position in the array and hence scattering angle. Thus, each detected energy spectrum can be converted to a spectrum in momentum transfer and then summed

Figure 6.12a shows the physical arrangement of the equipment. Knowing the positions of the sensor, X-ray beam and sample allows a scattering angle to be assigned to each pixel in the sensor array. The polyenergetic X-ray beam interacts with the sample, producing high intensity cones of radiation where the

Bragg equation is satisfied. These are recorded by the energy resolving, pixellated detector—the resulting images at a few selected energies are shown in Fig. 6.12b. These data demonstrate how the cones of radiation move to smaller scattering angles as the energy increases. Radially summing these images leads to the profiles also shown in Fig. 6.12b where the vertical axis is directly related to “intensity” for these energy selected profiles. Looking again at Eq. (6.3) it can be seen that by rearrangement, the important structural parameter “ $d$ ,” or in this case reciprocal of “ $d$ ” can be expressed as  $(E/hc)\sin(\theta)$  and this quantity is referred to as momentum transfer. Thus, expressing diffraction profiles as intensity of scattered X-rays against momentum transfer means that measurements made with any diffraction system can be compared on the same set of axes. More importantly for pixelated diffraction this gives the opportunity to combine all the data recorded both in terms of energy and scattering angle into a single diffraction profile for a material. This powerful technique means that when only a few events are recorded at any given energy or scattering angle they can be combined to form a high quality diffraction signature for the sample. Thus, good diagnostic quality data can be captured in timeframes compatible with clinical applications.

### 6.3.3 Hardware for Pixelated and Non-pixelated Diffraction

For ADXRD the X-ray source is typically a copper target tube operated with  $k$ -edge filters to monochromate the beam such that only the  $k_{\alpha}$  line (energy of 8.038 keV) is used. Other options are available but the combination of target material and filter are chosen to provide a monochromatic beam. Measurements are often made in the reflection mode as shown in Fig. 6.11, as the beam energy is insufficient to penetrate thick samples. A range of detectors have been used but generally do not need spectroscopic properties. In most ADXRD systems the source and detector are scanned over a range of angles in order to construct a diffraction pattern based on where the detector crosses the cones of diffraction. An alternative approach is to have a fixed large area detector and a stationary, pencil beam of radiation. In this case a full diffraction pattern is formed on the detector and this is then interpreted to form the typical diffraction profile of the sample.

Typical X-ray sources for medical EDXRD are tungsten target sources operated up to 80 kV. This provides a broad range of photon energies with a maximum intensity in the 30–40 keV range and considering practical arrangements of equipment  $5^{\circ}$  scattering allows access to typical tissue ‘ $d$ ’ values. To detect the scattered beam that contains the diffraction information energy resolving detectors are required. Typically HPGc detectors with energy resolution of a few 100s eV might be used but these need to be operated at liquid nitrogen temperatures (c. 77 K) for successful suppression of dark current. Alternatives are the use of CdTe or CdZnTe detectors that have poorer energy resolution (typically around 1 keV) but can be successfully operated at room temperatures. In choosing a suitable detector the angular resolving capability of the system should also be considered. Collimators are often used to

restrict the scattering volume. Restricting that volume reduces the detected photon intensity (for a given source power) and hence increases the noise in the recorded diffraction profile. Thus to give acceptable statistical quality in the data with X-ray source power available in many laboratory sources the collimation needs to be relaxed. Under these conditions it is often the case that better detector energy resolution will not yield significant improvements in diffraction profile definition and the CdTe or CdZnTe options are suitable.

While EDXRD usually consists of a single detector, the PixD method relies on the sophisticated HEXITEC CdTe detector which consists of a 1 mm CdTe single crystal sensor bonded to an application specific integrated circuit (ASIC) which offers square pixellation [66]. In this case, the HEXITEC detector is configured to have  $80 \times 80$  pixels at  $250 \mu\text{m}$  pitch. The CdTe sensor offers excellent efficiency for photons up to 100 keV. Since the small pixels provide good angular resolution (for samples up to about 10 mm thick), there is no need to use detector-side collimation, which means a greater fraction of the available X-ray flux can be used, allowing data to be collected in much shorter time scales compared to AD or EDXRD alone.

### ***6.3.4 Volume Analysis of Breast Tissue vs 2D Histopathology***

As an example of the power of tissue diffraction measurements we have chosen to discuss one of its applications in breast cancer treatment. Early breast cancer treatment usually involves surgery, chemotherapy and radiotherapy. Chemotherapy and radiotherapy are used to shrink a tumour and prevent cancerous cells spreading prior to surgery and to kill any remaining cancer cells close to the site of the primary tumour post-surgery. However, despite advances in modern personalised treatments the recurrence rates at the site of the primary tumour are generally around 20–40% [70]. Thus implying that not all the tumour was removed. The most common approaches to surgery include complete breast removal (mastectomy) or breast conserving surgery (lumpectomy). Current practice is to take a wide local excision (WLE) that includes the tumour and an appropriate margin. It is still a current discussion as to what constitutes a safe margin but there is generally a conflict between removing the minimum tissue to give a good cosmetic result and sufficient tissue to ensure complete removal [71]. Margins of a few millimetres are typical. Following surgery the excised tissue is sent for analysis to check that the whole tumour has been removed. The conventional approach to postoperative tissue analysis is to prepare microscope slides, generally using a 4–10  $\mu\text{m}$  thick slice of tissue and to investigate a limited portion of the excised tissue in ‘areas of interest’ as selected by the oncologist/pathologist. This process has several potential problems:

- By selecting a limited portion of the sample to investigate there is a real possibility that some important parts are not analysed.



- Histopathology is labour intensive and represents a significant workload if many tissue sections are looked at.
- Histology takes time—typically 10 days. During this period the patient anxiously awaits the result.
- If a positive margin is found the patient needs to be recalled for further surgery.
- The excised tissue and its associated tumour is a three dimensional structure and using a 2D technique means the full volumetric analysis will be compromised.

Building up a 3D assessment for the pathology of the excised tissue through the use of multiple 2D slices is not really required. What is important is to investigate the outer 1 mm of tissue over the whole surface of the excised material to see if any tumour remains. If this outer ‘shell’ is clear then there is confidence that the whole tumour has been successfully removed as it is contained within the WLE. As transmission X-ray diffraction is an additive technique all points along the X-ray path within the scattering volume defined by the incident and scattered beam will contribute to the detected signal. Thus if the sample is made up of two materials, for example tumour and normal tissue, then the diffraction profile will be a summation of the profiles from both materials. The weighting attached to each profile will depend upon how much of each material is present, what the materials are and the X-ray spectrum. However, simply the *presence* of both materials can be inferred from the measured diffraction profile. Thus, provided the diffraction profile from tumour is different from other tissues that might be present, making measurements across the surface of the WLE will reveal the presence of tumour, that is, a so-called positive margin will have been found and further surgery will be needed. Potentially these measurements could be made in theatre at the time of the initial surgery. The ability to characterise a whole tissue sample without needing to carefully prepare and select a limited portion would improve cancer treatment both in terms of reducing the cost and burden on the treating centre and in improving patient outcome.

### 6.3.5 *Diffraction Profiles from Breast Tissue*

There have been a number of studies of tissue diffraction [72–74]. The work by Kidane et al. [75] looked at classifying breast tissue according to its diffraction profile and the results are shown in Fig. 6.13. In these plots the vertical axis has been scaled to give the *differential coherent scattering coefficient*,  $\mu$  but can be directly related to the intensity of scattered photons.

It can be seen that the different tissue types have different profiles which has been explained by the way cancer disturbs the normal arrangement of the collagen molecules in breast stroma [76]. Less organised structures tend to move the diffraction peak to larger values of momentum transfer as can be seen in the case of carcinoma. As only short-range order exists in amorphous materials such as breast tissue, the peaks are not as sharp as might be expected in more crystalline



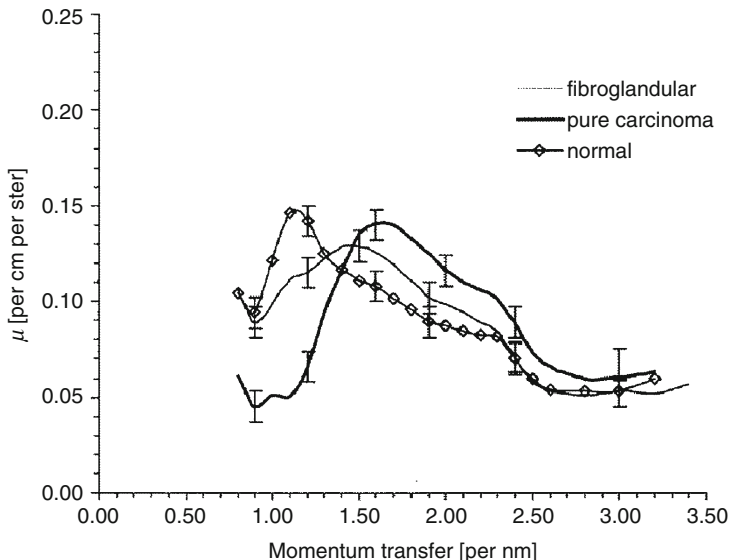


**Fig. 6.13** Diffraction data for different breast tissue types displayed as the differential coherent scattering coefficient,  $\mu$ . This coefficient describes the probability that coherent scattering, leading to diffraction effects, will take place. Taken from Kidane et al. [63]

samples (see Fig. 6.11 for example). However, there are statistical methods that can be used to separate these different diffraction signals.

To demonstrate the potential of tissue diffraction to WLE inspection for positive margins a tissue sample is shown in Fig. 6.14. The sample ( $\sim 40 \times 40 \times 5$  mm, formalin-fixed) came from a patient who had authorised the use of their tissue for scientific research. Data were collected using a pixelated diffraction instrument (miniPixD [69]) and measurements were made at regularly spaced positions across the whole sample.

Figure 6.14a shows the measurement positions overlaid on a high resolution transmission X-ray image of the sample. A statistical analysis technique called principal component analysis (PCA) was used to reveal the similarities and differences between the shapes of the diffraction profiles, that is, the differences as shown in Fig. 6.13. The points in Fig. 6.14a have been colour-coded to indicate the results of the PCA analysis. Since the diffraction profile is driven by the atomic and molecular structure of the material being analysed, we infer that the colour-code can be used to discriminate tissue types. In this example green implies adipose-like tissue and blue tumour-like tissue with colours in between representing mixtures of these tissues. This has been compared to the 2D histological analysis as is normally carried out on a slice from the top surface of the sample, and a microCT data set created using a Nikon XT H 225 System. Slices from the 3D microCT data set are shown in Fig. 6.14b and using the results of the conventional histological analysis have been colour coded so that the tumour is shown in red. Following through the

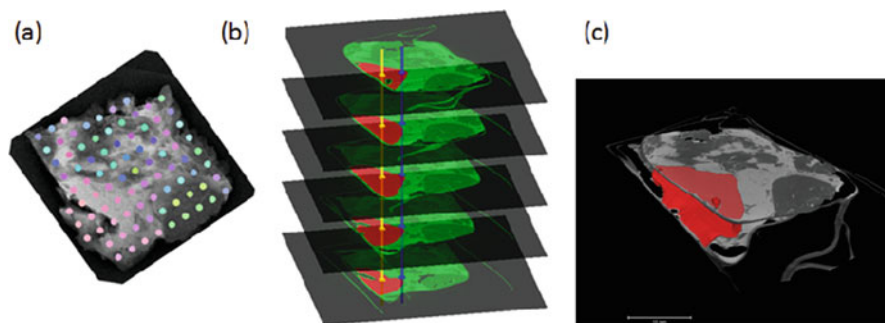


**Fig. 6.14** MicroCT and diffraction results from a  $40 \times 40 \times 5$  mm WLE. (a) shows a high resolution X-ray transmission image with the colour coded diffraction results overlaid at the points of measurement. See text for explanation of colour code. (b) and (c) are the microCT images with the tumour, following histopathology analysis, shown in red—(b) shown as separate slices and (c) shown as a surface rendered 3D volume

stack of slices it can be seen that the tumour outline changes both in total area and in shape. If, as is the case in conventional histology, decisions were taken using a single slice then errors in the assumed ‘safe margin’ might occur. Looking at the colour coded diffraction data (red/pink in the region identified as tumour and yellow/blue elsewhere) it can be seen that near the border of the tumour the colour coding changes—sometimes indicating a colour close to that associated with the tumour region and sometimes a colour closer to the normal or fatty regions of the sample. These subtle colour changes are indicating the fact that along a given ray-path through the sample there is a mix of tissue types, and it is only when the colour becomes clearly that associated with normal tissue that we can be sure that there is no contribution from tumour. Two of the X-ray-paths associated with the diffraction data are shown in Fig. 6.14b. It can be seen that only the yellow one takes a path that is exclusively tumour. The blue ray-path contains both tumour and other tissues. These observations change the position of the border between tumour and normal tissue and allow for the 3D nature of tissue types to be taken into account without the need to slice the tissue.

### **6.3.6 Applications of Diffraction Approaches in Medical and Security Areas**

It can be seen that X-ray diffraction is a powerful technique for analysing material types and can be packaged in a way to make clinical applications of the technique possible. It can play a role in enhancing imaging techniques such as mammography where image guided analysis could enable real-time characterisation of suspicious regions. It has also been shown that it can identify fake or sub-standard pharmaceuticals without destroying the sample.

In the security field it can identify illicit drugs in cargo and passenger luggage and can also identify explosives in baggage scanning scenarios.

## References

1. P.P. Dendy, B. Heaton, *Physics for Diagnostic Radiology*, Medical Science Series (IoP Publishing, UK, 1999), p. 122
2. R.D. Speller, J.A. Horrocks, Photon scattering – a ‘new’ source of information in medicine and biology? *Phys. Med. Biol.* **36**, 1 (1991)
3. T. Koliqliatis, J. Kalef-Ezra, R.D. Speller, M.J. Mooney, J. Litsas, Compton scatter densitometry in bone: influence of the anatomical site. *Phys. Med.* **14**, 73 (1998)
4. M.A. Kumakhov, A.F. Gamaliy, V.N. Vasiliev, M.Y. Zaytsev, K.V. Zaytseva, A.A. Markelov, Y.V. Ozerov, Scattered X-rays in medical diagnostics. *SPIE* **5943**, 210 (2005)
5. M. Antoniassi, A.L.C. Conceicao, M.E. Poletti, Characterization of breast tissues using Compton scattering. *Nucl. Instrum. Methods Phys. Res., Sect. A* **619**, 375 (2010)
6. M. Antoniassi, A.L.C. Conceicao, M.E. Poletti, Study of effective atomic number of breast tissues determined using the elastic to inelastic scattering ratio. *Nucl. Instrum. Methods Phys. Res., Sect. A* **652**, 739 (2011)
7. M. Georgiadis, M. Guizar-Sicairos, A. Zwahlen, A. Trussel, O. Bunk, R. Muller, P. Schneider, 3D scanning SAXS: a novel method for the assessment of bone ultrastructure orientation. *Bone* **71**, 42 (2015)
8. N. Tamura, P.U. Gilbert, X-ray microdiffraction of biominerals. *Methods Enzymol.* **532**, 501 (2013)
9. C. Dawson, J.A. Horrocks, R. Kwong, R.D. Speller, H.N. Whitfield, Low-angle X-ray scattering signatures of urinary calculi. *World J. Urol.* **14**, S43 (1996)
10. S. Sidhu, G. Falzon, S.A. Hart, J.G. Fox, R.A. Lewis, K.K.W. Siu, Classification of breast tissue using a laboratory system for small-angle x-ray scattering (SAXS). *Phys. Med. Biol.* **56**, 6779 (2011)
11. B. Ghamraoui, L. Popescu, Non-invasive classification of breast microcalcifications using X-ray coherent scatter computed tomography. *Phys. Med. Biol.* **62**, 1192 (2017)
12. C. Sosa, A. Malezan, M.E. Poletti, R.D. Perez, Compact energy dispersive X-ray microdiffractometer for diagnosis of neoplastic tissues. *Radiat. Phys. Chem.* **137**, 125 (2017)
13. W. Elsharkawy, W. Elshemey, Quantitative characterization of fatty liver disease using X-ray scattering. *Radiat. Phys. Chem.* **92**, 14 (2013)
14. H. Paganetti, Range uncertainties in proton therapy and the role of Monte Carlo simulations. *Phys. Med. Biol.* **57**, R99–R117 (2012)
15. A.-C. Knopf, A. Lomax, In vivo proton range verification: a review. *Phys. Med. Biol.* **58**, R131–R160 (2013)
16. H.-M. Lu, A potential method for in vivo range verification in proton therapy treatment. *Phys. Med. Biol.* **53**, 1413–1424 (2008)
17. H.-M. Lu et al., Investigation of an implantable dosimeter for single-point water equivalent path length verification in proton therapy. *Med. Phys.* **37**, 5858–5866 (2010)
18. B. Gottschalk et al., Water equivalent path length measurement in proton radiotherapy using time resolved diode dosimetry. *Med. Phys.* **38**, 2282–2288 (2011)
19. E.H. Bentefour et al., Effect of tissue heterogeneity on an in vivo range verification technique for proton therapy. *Phys. Med. Biol.* **57**, 5473–5484 (2012)
20. L. Sulak et al., Experimental studies of the acoustic signature of proton beams traversing fluid media. *Nucl. Instrum. Methods* **161**, 203–217 (1979)
21. Y. Hayakawa et al., Acoustic pulse generated in a patient during treatment by pulsed proton radiation beam. *Radiat. Oncol. Investig.* **3**, 42–25 (1995)

22. W. Assmann et al., Ionoacoustic characterization of the proton Bragg peak with submillimeter accuracy. *Med. Phys.* **42**(2), 567–574 (2015)
23. M. Ahmad et al., Theoretical detection threshold of the proton-acoustic range verification technique. *Med. Phys.* **42**(10), 5735–5744 (2015)
24. S. Kellnberger et al., Ionoacoustic tomography of the proton Bragg peak in combination with ultrasound and optoacoustic imaging. *Sci. Rep.* **6**, 29305 (2016). <https://doi.org/10.1038/srep29305>
25. K. Parodi et al., Patient study of in vivo verification of beam delivery and range, using positron emission tomography and computed tomography imaging after proton therapy. *Int. J. Radiat. Oncol. Biol. Phys.* **68**, 920–934 (2007)
26. M.T. Studenski, Y. Xiao, Proton therapy dosimetry using positron emission tomography. *World J. Radiol.* **2**, 135–142 (2010)
27. S. Agostinelli et al., Geant4 – a simulation toolkit. *Nucl. Instrum. Methods Phys. Res., Sect. A* **506**, 250–303 (2003)
28. J.M. Verburg et al., Simulation of prompt gamma-ray emission during proton radiotherapy. *Phys. Med. Biol.* **57**, 5459–5472 (2012)
29. F. Stichelbaut, Y. Jongen, in *Verification of Prompt Beam Position in the Patient by the Detection of Prompt Gamma-Rays Emission*. 39th Meeting In the Particle Therapy Cooperative Group, San Francisco (2003)
30. C.H. Min et al., Prompt gamma measurements for locating the dose falloff region in the proton therapy. *Appl. Phys. Lett.* **89**, 183517 (2006)
31. D. Kim et al., Pinhole camera measurements of prompt gamma-rays for detection of beam range variation in proton therapy. *J. Korean Phys. Soc.* **55**, 1673–1676 (2009)
32. V. Bom et al., Real-time prompt gamma monitoring in spot-scanning proton therapy using imaging through a knife-edge-shaped slit. *Phys. Med. Biol.* **57**, 297–308 (2012)
33. J. Smeets et al., Prompt gamma imaging with a slit camera for real-time range control in proton therapy. *Phys. Med. Biol.* **57**, 3371–3405 (2012)
34. C.H. Min et al., Development of array-type prompt gamma measurements system for in vivo range verification in proton therapy. *Med. Phys.* **39**, 2100–2107 (2012)
35. J. Krimmer et al., Collimated prompt gamma TOF measurements with multi-slit multi-detector configurations. *J. Instrum.* **10**, P01011 (2015)
36. J. Smeets et al., Experimental comparison of knife-edge and multi-parallel collimators for prompt gamma imaging of proton pencil beams. *Front. Oncol.* **6**, 156 (2016)
37. M. Frandes et al., A tracking Compton-scattering imaging system for hadron therapy monitoring. *IEEE Trans. Nucl. Sci.* **57**, 144–150 (2010)
38. F. Roellinghoff et al., Design of a Compton camera for 3D prompt gamma imaging during ion beam therapy. *Nucl. Instrum. Methods Phys. Res., Sect. A* **648**, S20–S23 (2011)
39. C. Golnik et al., Tests of a Compton imaging prototype in a monoenergetic 4.44 MeV photon field – a benchmark setup for prompt gamma-ray imaging devices. *J. Instrum.* **11**, P06009 (2016)
40. S.W. Peterson et al., Optimizing a 3-stage Compton camera for measuring prompt gamma rays emitted during proton radiotherapy. *Phys. Med. Biol.* **55**, 6841–6856 (2010)
41. D. Robertson et al., Material efficiency studies for a Compton camera designed to measure characteristic prompt gamma rays emitted during proton beam radiotherapy. *Phys. Med. Biol.* **56**, 3047–3059 (2011)
42. J.C. Polf et al., Imaging of prompt gamma rays emitted during delivery of clinical proton beams with a Compton camera: feasibility studies for range verification. *Phys. Med. Biol.* **60**, 7085–7099 (2015)
43. P. Cambraia Lopes et al., Time-resolved imaging of prompt-gamma rays for proton range verification using a knife-edge slit camera based on digital photon counters. *Med. Phys. Biol.* **60**, 6063–6085 (2015)
44. R.W. Todd, J.M. Nightingale, D.B. Everett, *Nature* **251**, 132–134 (1974)
45. M. Singh, D. Doria, An electronically collimated gamma camera for single photon emission computed tomography. Part II: Image reconstruction and preliminary measurements. *Med. Phys.* **10**, 427–435 (1983)

46. O. Klein, Y. Nishina, Über die Streuung von Strahlung durch freie Elektronen nach der neuen relativistischen Quantendynamik von Dirac. *Z. Phys.* **52**(11–12), 853–868 (1929)
47. S.J. Wilderman et al., Fast algorithm for list mode back-projection of Compton scatter camera data. *IEEE Trans. Nucl. Sci.* **45**, 957–962 (1998)
48. S.E. King, A solid-state Compton camera for three-dimensional imaging. *Nucl. Instrum. Methods Phys. Res., Sect. A* **353**, 320–323 (1994)
49. B. Smith, Reconstruction methods and completeness conditions for two Compton data models. *J. Opt. Soc. Am. A* **22**, 445–459 (2005)
50. T. Hebert et al., Three-dimensional maximum likelihood reconstruction for an electronically collimated single-photon-emission imaging system. *J. Opt. Soc. Am. A* **7**, 1305–1313 (1990)
51. S.J. Wilderman et al., Improved modeling of system response in list mode EM reconstruction of Compton scatter camera images. *IEEE Trans. Nucl. Sci.* **48**, 111–116 (2001)
52. L. Han et al., Statistical performance evaluation and comparison of a Compton medical imaging system and a collimated Anger camera for higher energy photon imaging. *Phys. Med. Biol.* **53**, 7029–7045 (2008)
53. S.M. Kim et al., Fully three-dimensional OSEM-based image reconstruction for Compton imaging using optimized ordering schemes. *Phys. Med. Biol.* **55**, 5007–5027 (2010)
54. V.-G. Nguyen et al., GPU-accelerated 3D Bayesian image reconstruction from Compton scattered data. *Phys. Med. Biol.* **56**, 2817–2836 (2011)
55. J. Cui et al., in *Fast and Accurate 3D Compton Cone Projections on GPU Using CUDA*. Proc. IEEE Nucl. Sci. Symp. Med. Imag. Conf. (NSS/MIC) (2011), pp. 2572–2575
56. V.-G. Nguyen, S.-J. Lee, GPU-accelerated iterative reconstruction from Compton scattered data using a matched pair of conic projector and backprojector. *Comput. Methods Prog. Biomed.* **131**, 27–36 (2016)
57. A. Andreyev et al., Fast image reconstruction for Compton camera using stochastic origin ensemble approach. *Med. Phys.* **38**, 429–438 (2011)
58. A. Sitek, Representation of photon limited data emission tomography using origin ensemble. *Phys. Med. Biol.* **53**, 3201–3216 (2008)
59. A. Andreyev et al., in *Stochastic Image Reconstruction Method for Compton Camera*. Proc. IEEE Nucl. Sci. Symp. Conf. Record (NSS/MIC) (2009), pp. 2985–2988
60. A. Andreyev et al., Resolution recovery for Compton camera using origin ensemble algorithm. *Med. Phys.* **43**, 4866–4876 (2016)
61. D. Mackin et al., Evaluation of stochastic reconstruction algorithm for use in Compton camera imaging and beam range verification from secondary gamma emission during proton therapy. *Phys. Med. Biol.* **57**, 3537–3553 (2012)
62. F.X. Avila-Soto et al., in *Parallelization for Fast Image Reconstruction Using the Stochastic Origin Ensemble Method for Proton Beam Therapy*. REU Site: Interdisciplinary Program in High Performance Computing (2015)
63. <http://www.who.int/cancer/detection/breastcancer/en/index1.html>
64. P.P. Provenzano et al., Collagen density promotes mammary tumor initiation and progression. *BMC Med.* **6**, 11 (2008)
65. L. Cherkezyan et al., Nanoscale changes in chromatin organization represent the initial steps of tumorigenesis: a transmission electron microscopy study. *BMC Cancer* **14**, 189 (2014)
66. L. Jones et al., HEXITEC ASIC—a pixellated readout chip for CZT detectors. *Nucl. Instrum. Methods Phys. Res., Sect. A* **604**, p34–p37 (2009)
67. D. O’Flynn et al., Explosive detection using pixellated X-ray diffraction (PixD). *J. Instrum.* **8**, P03007 (2013)
68. C. Christodoulou et al., Multivariate analysis of pixelated diffraction data. *J. Instrum.* **6**, C12027 (2011)
69. R. Moss et al., miniPixD: a compact sample analysis system which combines X-ray imaging and diffraction. *J. Instrum.* **12**, P02001 (2017)
70. F.J. Fleming et al., Intraoperative margin assessment and re-excision rate in breast conserving surgery. *Eur. J. Surg. Oncol.* **30**, 233–237 (2004)

71. M.S. Moran et al., Society of Surgical Oncology – American Society for Radiation Oncology consensus guideline on margins for breast-conserving surgery with whole-breast irradiation in stages I and II invasive breast cancer. *Int. J. Radiat. Oncol. Biol. Phys.* **88**, 553–564 (2014)
72. J.K. Pijanka et al., A wide-angle X-ray fibre diffraction method for quantifying collagen orientation across large tissue areas: application to the human eyeball coat. *J. Appl. Crystallogr.* **46**, 1481–1489 (2013)
73. S. Pani et al., Characterization of breast tissue using energy-dispersive X-ray diffraction computed tomography. *Appl. Radiat. Isot.* **68**, 1980–1987 (2010)
74. F.B. de la Cuesta et al., Coherent X-ray diffraction from collagenous soft tissues. *Proc. Natl. Acad. Sci. U. S. A.* **106**, 15297–15301 (2009)
75. G. Kidane et al., X-ray scatter signatures for normal and neoplastic breast tissues. *Phys. Med. Biol.* **44**, 1791–1802 (1999)
76. M. Costa et al., Diagnosis applications of non-crystalline diffraction of collagen fibres: breast cancer and skin diseases. *Lect. Notes Phys.* **776**, 265–280 (2009)

# Chapter 7

## Digital Breast Tomosynthesis: Systems, Characterization and Simulation



Anastasios Konstantinidis, Selina Kolokytha, and Andria Hadjipanteli

**Abstract** Digital breast tomosynthesis (DBT) is an advanced imaging application for breast cancer detection, which makes use of a number of 2D X-ray projection images over a limited angular range to reconstruct quasi 3D reconstruction images. As such, first an introduction to digital X-ray tomosynthesis is given, after which existing limited angle tomosynthesis methods are presented. In the next section DBT geometry and its development to date is discussed. Details are given on geometries currently available from different manufacturers, and recent advances. Part of this section presents the available relevant reconstruction methods. Next, we look into the DBT detectors and their performance evaluation. Current DBT detectors are based on amorphous silicon (a-Si) and amorphous selenium (a-Se) thin film transistor (TFT) technology. However, complementary metal-oxide-semiconductor (CMOS) active pixel sensor (APS) digital X-ray detectors have the potential to replace a-Si:H TFT detectors in DBT in the near future, due to a smaller pixel pitch, low electronic noise, faster frame rate and negligible image lag. The performance of current DBT detectors is evaluated mainly by: automatic exposure control performance, response function, noise analysis, detector element failure, and system projection modulation transfer function (MTF). Following this we discuss image quality measurements, because they are essential for the evaluation and optimization of DBT systems. They should represent relevant clinical tasks, such as the detection of microcalcifications and masses in mammographic backgrounds. Currently the CDMAM phantom is used for contrast-detail analysis (i.e., the required threshold contrast to detect discs of various diameters) of the reconstructed images. The TOR MAM phantom can also be used to score the visualization of discs, filaments

---

A. Konstantinidis

Diagnostic Radiology and Radiation Protection Service, Christie Medical Physics and Engineering, The Christie NHS Foundation Trust, Manchester, UK

S. Kolokytha (✉)

Empa, Centre for X-Ray Analytics, Swiss Federal Laboratories for Materials Science and Technology, Dübendorf, Switzerland

A. Hadjipanteli

Medical School, University of Cyprus, Nicosia, Cyprus

© Springer Nature Switzerland AG 2018

M. Abreu de Souza et al. (eds.), *Multi-Modality Imaging*,

[https://doi.org/10.1007/978-3-319-98974-7\\_7](https://doi.org/10.1007/978-3-319-98974-7_7)

and specks for various contrast levels. The parameter  $Z$ -resolution is used to assess the inter-plane spread of reconstruction artifacts associated with 1 mm diameter aluminum spheres (contained in a specific three-dimensional phantom). Furthermore, the system MTF in the  $x$ - $y$  plane is used to take into account all sources of blurring in the DBT system: detector MTF, additional sources of unsharpness and the reconstruction algorithm. The final part of the chapter describes image simulation methods for DBT optimization. Briefly, DBT is currently under consideration for its use in breast cancer screening in Europe, in combination with 2D mammography or alone. Several parameters (such as image acquisition parameters, detector response, system geometry, radiation dose, and image processing and reconstruction algorithms) are studied for their effect on image quality and the investigation of the optimum use of DBT. Traditionally, large clinical trials are required to evaluate these parameters over a large number of women. Such trials are time consuming, expensive and require irradiating asymptomatic women. Alternatively, several research groups use virtual clinical trials (based on image simulation methods) to optimize DBT parameters in fast, radiation-free, and cost-effective ways. This part of the chapter reviews several simulation methods in DBT and the applications in evaluating its effectiveness.

**Keywords** Digital breast tomosynthesis · Breast cancer detection · Image quality · DBT detectors · DBT performance · Image simulation

## 7.1 Introduction to Digital X-Ray Tomosynthesis

The term “tomosynthesis” was first defined by Grant in 1972 by combining the two Greek words “tomos” and “synthesis” [1]. Tomos (τόμος) means a section, a slice or a cutting. The word synthesis (σύνθεσις) describes the process which combines together two or more preexisting elements, resulting in the formation of something new [2]. Tomosynthesis is an advanced X-ray application, used mainly in medical imaging, which makes use of a number of two-dimensional (2D) X-ray projection images over a given angular range to reconstruct quasi three-dimensional (3D) reconstruction images. This technique combines the advantages of conventional computed tomography (CT), that is, full 3D image reconstruction at the cost of high dose, and 2D planar radiography which utilizes low dose but is limited by overlapping objects (e.g., tissue superposition). To perform a tomosynthesis image acquisition, the X-ray tube is moved over a range of angles about a pivot point (i.e., the isocenter) near the digital X-ray detector to obtain a series of low-dose digital projection radiographs.

Tomosynthesis is a substantial improvement over conventional geometric tomography which was introduced in 1930s [3] and was utilized clinically until the early 1990s [4]. Geometric tomography was used to produce a single slice, representing a plane of interest (also known as in-focus or focal plane), over a continuous exposure by moving the X-ray tube and the detector (originally screen-film and then image



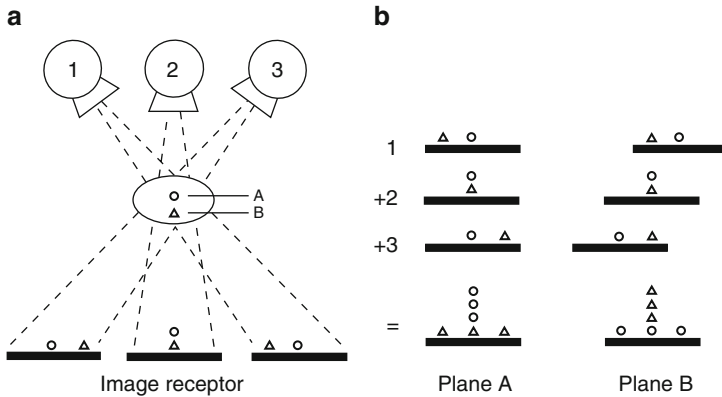


**Fig. 7.1** Principle of shift-and-add tomosynthesis (figure copied with permission from Dobbins III and Godfrey [4])

intensifier) in opposite directions across the patient. All other planes (above and below the focal plane) resulted in low intensity blurry objects in the slice image. Actually these characteristics resulted in the main limitations of this technique: (a) very high patient dose and time are required for acquisition of a volume of data and (b) it cannot completely suppress out of focus (i.e., off-focus) plane details, limiting the detection of details of interest [4]. In the early 1990s CT and magnetic resonance imaging (MRI) replaced conventional geometric tomography in routine clinical practice, due to improved diagnosis at the cost of zero (MRI) or lower (CT) patient dose.

Compared to geometric tomography, tomosynthesis is allowing the retrospective reconstruction of an arbitrary number of planes from a single medium dose acquisition procedure. These planes are reconstructed from a limited number of projection images acquired at varying orientations of the X-ray tube, patient and digital X-ray detector [4]. Tomosynthesis is based on the “shift-and-add” concept (Fig. 7.1), that is, the reconstructed slice images are generated from the summation of a set of shifted projection images acquired at different orientations of the X-ray tube. This method brings structures of a given plane into focus. Figure 7.1a demonstrates the “shift-and-add” concept using a simplified sample. The sample contains two structures (a circle and a triangle) at two different heights above the detector (planes A and B). Planes at different heights  $z$  above the detector can be brought in focus by varying the amount of shifting of the projections before adding them to form the plane. In the example provided the X-ray tube moves to three positions over an object containing the circle in plane A and the triangle in plane B. As the X-ray tube moves, three projection images, containing the two objects in relative positions, are generated (Fig. 7.1a). The three projection images can be shifted and added to bring either plane A or plane B into focus. The projections (1, 2 and 3) for the production of plane A are just added, thus bringing the circle into focus (more circles in the plane produced). The projections (2 and 3) for the production of

plane B are first shifted, in comparison to projection 1, to bring into focus what is located at the height of plan B above the receptor (triangle). If another plane below would be produced, the shifting of projections before their addition would be even bigger. In all cases, the in-focus plane object will emerge while the other will be spread across the image, that is, blurred. This results in lower contrast of in-focus plane objects, because the in- and off-focus objects will occupy the full dynamic range of the image display system. Therefore, several deblurring algorithms have been developed to remove the blurry off-focus plane structures [4].

A successful tomosynthesis system requires a large area detector with high performance at rapid readout. The first tomosynthesis systems were developed in the early 1970s [1, 5, 6] and in the following years a lot of research and development was made using digitized video cameras and image intensifiers [7–9]. However, tomosynthesis was not used in routine clinical practice due to practical technological limitations: (a) noise and pincushion distortion (i.e., an increase in magnification at the periphery of the image) at the edge of the image field corrupted tomographic reconstructions, (b) post-processing could not be applied on the analog signal to remove noise and artifacts and (c) the computing power was very expensive this period [4]. Furthermore, CT was the standard clinical 3D imaging technique since late 1970s. Until the early 1990s several software solutions were suggested to overcome hardware limitations. For example, Kolitsi et al. [10] suggested reconstructing groups of pixels (instead of individual pixels) to significantly reduce the reconstruction time and maintain computer power requirements to a minimum. Nevertheless, in the late 1990s a series of technological developments allowed tomosynthesis to be considered a reliable clinical adjunct to CT: (a) the computing power became cheaper, allowing for many tomosynthesis reconstruction and post-processing algorithms to be applied for the first time and (b) digital flat-panel detectors, based on thin film transistor (TFT) technology, were able to produce digital images of sufficient quality at fast readout frames [4]. Finally, the quality of the reconstructed images and the absorbed dose depend on (a) the angular range and number of projections, (b) the exposure used per projection, and (c) the performance of the used digital X-ray detector and electronics [11].

Digital X-ray tomosynthesis has been used in several diagnostic medical imaging applications, mainly: (a) angiography (e.g., coronary and cerebral angiography, digital subtraction angiography (DSA)), (b) chest imaging, (c) mammography (also known as digital breast tomosynthesis (DBT)), (d) dental applications, and (e) orthopaedic (finger joints and knee) [4]. The following sections of this book chapter focus on DBT: sections 7.2 and 7.3 describe the reconstruction methods and digital X-ray detectors used in DBT, respectively. Section 7.3 also describes the performance of DBT detectors, while section 7.4 is related to the image quality of reconstructed images. Finally, section 7.5 briefly describes the use of image simulation to evaluate the performance of DBT systems.

## 7.2 DBT Geometry, Reconstruction Methods, and Dosimetry

2D digital mammography (also known as full field digital mammography (FFDM)) uses low energy X-rays to image breast and identify possible cancer signs (characteristic masses and microcalcifications) and is currently used as a diagnostic and screening tool. The main disadvantage of 2D mammography is that the overlying and underlying anatomy of the breast are superimposed on pathology, thus obscuring the visualization of abnormalities. DBT is an innovative, quasi 3D X-ray imaging technique, which involves the acquisition of 2D X-ray projections over a limited angular range and their reconstruction to image planes parallel to the detector. Its main advantage over 2D mammography is that it can provide a 3D image of the breast (or image planes), therefore additional breast architectural details. Hence, DBT can potentially provide benefits to the patient, such as eliminating the need for additional mammographic views and reducing recall rates. Furthermore, it can improve the identification of lesion characteristics [12].

Most DBT systems have the same geometry and basic components as that of FFDM units (so their average cost is marginally higher than FFDM and substantially lower compared to CT and MRI). Hence, most DBT systems are capable of 2D and 3D imaging: (a) FFDM acquisition (FFDM image), (b) DBT acquisition and sometimes (c) FFDM and DBT acquisition (combination mode). The system consists of a direct or indirect full field digital detector (see section 7.3), a breast support and compression plate and an X-ray tube mounted on an arm, which is rotated in one plane around the static compressed breast. A series of images is acquired, one at each X-ray tube positioning. The detector can either be static or rotate to maintain its top surface normal to the X-ray tube. There are three common DBT geometries [4, 13], shown in Fig. 7.2: (a) complete isocentric motion with an isocenter located in the center of the breast, (b) partial isocentric motion, that is, the X-ray tube is rotated with angular range and detector moves in perpendicular plane

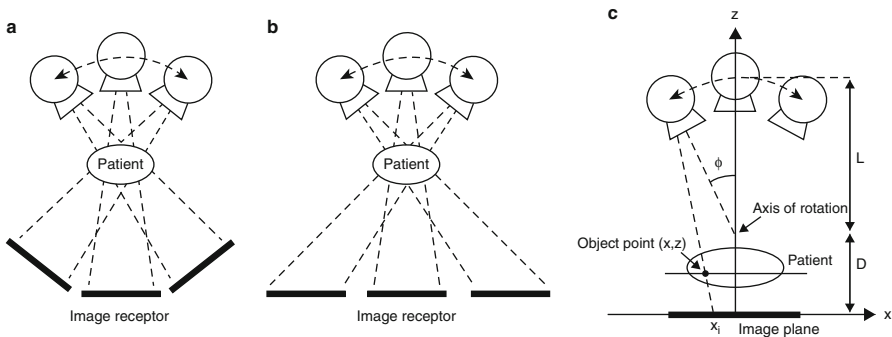


**Fig. 7.2** Tomosynthesis geometries using isocentric motion: (a) complete isocentric motion, (b) partial isocentric motion with moving detector in one plane, (c) partial isocentric motion with stationary detector (figure copied with permission from Dobbins III and Godfrey [4])

and (c) partial isocentric motion, that is, the DBT detector remains stationary while X-ray tube moves around a central axis with an isocenter located above the breast.

Different manufacturers have applied additional modifications to their systems' geometries for optimization. These might include for example a step-and-shoot instead of a continuous motion system, for blurring reduction [14] or a stationary but "rocking detector" (Selenia Dimensions, Hologic, Inc., Bedford, MA). Further investigations in geometry for system optimization have been carried out including a carbon nanotube array of X-ray sources as a replacement of the X-ray tube and rotating gantry [15] and a multislit photon counting linear detector and a collimated X-ray fan beam scanned in an arc across the breast with the center of rotation below the breast (Sectra Microdose, now Philips Healthcare, Best, The Netherlands). Further advances in DBT systems are discussed by Sechopoulos [16, 17].

The series of projections acquired is processed by a reconstruction algorithm which uses the different location in the projections of the same tissues to compute their vertical positions, thereby estimating the 3D distribution of the tissues. Reconstruction methods in DBT are based on either filtered back projection (FBP) or iterative reconstruction algorithms, such as simultaneous algebraic reconstruction technique (SART) and maximum likelihood expectation maximization (MLME).

The most commonly known algorithm for DBT reconstruction is FBP. FBP is a two-step process: the projections are first filtered in the frequency domain, and then they are back-projected. The choice of filters in FBP highly affects image quality. Normally the filters in use include the ramp-type and apodization filters. In DBT a slice thickness filter that dampens the impact of the incomplete sampling of the frequency space due to the limited angular range can control the impact of out-of-plane artifacts on image quality [18]. The concept of an additional filter to avoid the zeroing out of the low frequencies by the ramp filter has also been investigated [19].

Iterative reconstruction methods form an image using the acquired data by solving an inverse problem and using multiple iteration steps. Algebraic methods that have been investigated for reconstruction in DBT include SART [20], which have been shown to perform worse than back projection in homogeneous phantom reconstruction but better in realistic structured phantom reconstruction. Matrix inversion tomosynthesis was introduced for DBT by Chen et al. [21] and was shown to be sufficient at removing out of plane artifacts and handling high frequency information, but was also shown to perform poorly with low frequency information. The MLME algorithm forms the most commonly studied method in DBT [22]. With the use of faster computer processors and considering the smaller number of projections in DBT, iterative reconstruction algorithms are in use by several manufacturers (Table 7.1).

Since the female breast is a radiosensitive organ and DBT has been introduced as a screening tool, the radiation absorbed dose to the breast, also known as mean glandular dose (MGD), is of great concern. Currently established dose limits (such as Diagnostic Reference Levels (DRLs)) or recommendations are used in mammography. Similar dose levels should be pursued in DBT, although they should not compromise clinical performance [24]. Dose levels vary between clinics (e.g., DRLs are typically country or region specific) and used DBT systems.

**Table 7.1** Specifications and geometry of currently available or in development DBT systems [16, 23]

DBT system	GE Healthcare SenoClaire	GE Healthcare Pristina	Hologic Selenia Dimension	IMS Giotto TOMO	IMS Giotto Class	Philips MicroDose Scanning multislit	Planned Clarity 3D	Siemens Mammomat Inspiration	Fujifilm Amulet Innovativity
Type of geometry	Full-field	Full-field	Full-field	Full-field	Full-field	Scanning multislit	Full-field	Full-field	Full-field
Detector conversion type	Indirect	Indirect	Direct	Direct	Direct	Photon counting	Indirect	Direct	Direct
Detector type	Energy integrating	Energy integrating	Energy integrating	Energy integrating	Energy integrating	Photon counting	Energy integrating	Energy integrating	Energy integrating
Detector material	CsI/a-Si:H TFT	CsI/a-Si:H TFT	a-Se TFT	a-Se TFT	a-Se TFT	Si	CsI/a-Si:H TFT	a-Se TFT	a-Se TFT
Detector pixel pitch ( $\mu\text{m}$ )	100	100	70 (binned $2 \times 2$ )	85	85	50 (perpend to motion)	83	85	68 (Hexagonal)
Focal plane pixel size ( $\mu\text{m}$ )	100	100	95–117	90	90	100	83/166	85	50–100/100–150
Detector size ( $\text{cm}^2$ )	$24 \times 30$	$24 \times 30$	$24 \times 29$	$24 \times 30$	$24 \times 30$	21 line detectors, each 24 cm	$24 \times 30$	$24 \times 30$	$24 \times 30$

(continued)

Table 7.1 (continued)

DBT system	GE Healthcare SenoClaire	GE Healthcare Pristina	Hologic Selenia Dimension	IMS Giotto TOMO	IMS Giotto Class	Philips MicroDose Slit Scan	Planned Clarity 3D	Siemens Mammomat Inspiration	Fujifilm Amulet Innovality
Detector motion	Static	Static	Rotating	Static	Static	Continuous Slit Scan	Rotating	Static	Static
X-ray tube target	Mo or Rh	Mo or Rh	W	W	W	W	W	W	W
X-ray tube filter	Mo: 30 $\mu\text{m}$ Rh: 25 $\mu\text{m}$	Mo: 30 $\mu\text{m}$ Ag: 25 $\mu\text{m}$	Al: 700 $\mu\text{m}$	Rh: 50 $\mu\text{m}$ Ag: 50 $\mu\text{m}$	Ag: 50 $\mu\text{m}$	Al: 500 $\mu\text{m}$	Rh: 75 $\mu\text{m}$ Ag: 60 $\mu\text{m}$	Rh: 50 $\mu\text{m}$	Al: 700 $\mu\text{m}$
X-ray tube motion	Step-and shoot	Step-and shoot	Continuous	Step-and shoot	Step-and shoot	Continuous	Continuous Sync-and-Shoot	Continuous	Continuous
Angular range ( $^{\circ}$ )	25	25	15	40	30	11	30	50	15/40
Number of projections	9	9	15	13	11	21	15	25	15
Scan time (s)	7	7	3.7	12	10	3–10	20	25	15
Frame rate (fps)	1.3	1.3	4.1	1.1	1.1	2.1–7.0	0.8	1.0	1.0
Reconstruction method	Iterative	Iterative	FBP	Iterative	Iterative	Iterative	Iterative	FBP	FBP

Furthermore, the provided image quality, which is dose dependent, may vary due to (a) the radiologists' preference or (b) differences in the breast characteristics of the population [24]. DBT dose depends on breast composition (i.e., glandularity) and thickness, X-ray beam quality (i.e., used anode/filter combination at a given tube voltage (kVp)), projection angle, number of projections and motion of the system (i.e., step-and-shoot or continuous). Dance et al. [25] published Monte Carlo-based conversion factors (over a wide range of X-ray spectra, breast thicknesses and glandularities, and projection angles) to estimate tomosynthesis MGD from entrance surface air kerma (ESAK). Maldera et al. [26] performed a dose and image quality assessment for four DBT systems using Dance et al. [25] conversion factors. For PMMA thicknesses in the range 20–70 mm the MGD values ranged from 0.84 to 4.62 mGy. Compared with the respective FFDM units the DBT/FFDM mean dose ratio ranged from 1.1 to 1.9. Nevertheless, all DBT MGD values were below the 2D FFDM dose limits published by the European QC protocol for FFDM [27]. Finally, Svahn et al. [24] compared actual DBT with 2-view FFDM dose levels. The DBT/FFDM dose ratio ranged 0.34–1.0 for 1-view DBT and 0.68–1.17 for 2-view DBT. On the other hand, for DBT combined with 2-view FFDM the dose ratio ranged 1.03–1.5 for 1-view DBT plus FFDM and 2.0–2.23 for 2-view DBT plus FFDM. However, a significant dose reduction (by around 45% for 2-view DBT plus 2-view FFDM) was achieved when 2D views, reconstructed from the DBT images (also known as “synthetic 2D views”), were used instead of FFDM images.

### 7.3 DBT Detectors and Their Performance Evaluation

Digital X-ray detectors used for DBT need to have high spatial resolution to detect microcalcifications and fine details, and low background image noise (also known as electronic noise) for sufficient detection of low contrast masses at low exposures, therefore decreasing the MGD within the breast. In other words, high contrast-to-noise ratio (CNR) at low exposures (given the need to divide the total exposure over several projections) is necessary to detect masses with low patient MGD. Furthermore, DBT detectors need to have fast readout time to keep the total acquisition time of all projections to a minimal image lag and ghosting, which may introduce image artifacts, and minimum reduction in detective quantum efficiency (DQE) at low exposures [16]. The DQE shows the ability of an imaging system to transfer the signal-to-noise ratio (SNR) from its input to the output and combines the effect of spatial resolution, noise, and contrast, which are the most important factors that affect X-ray image quality [28].

Current large area X-ray detectors for DBT are based mainly on thin film transistor (TFT) passive pixel sensor (PPS) technology (also known as flat-panel detectors). TFTs are currently the detector of choice in medical imaging applications because they are high-performing, radiation hard (i.e., electronic components and systems resistant to damage or malfunctions caused by ionizing radiation) and large area (up to 43 cm × 43 cm for general radiography) detectors. They

are either direct (i.e., input X-rays are converted directly to electron charge) or indirect (i.e., incident X-rays are converted to light photons inside a scintillator and subsequently to electron charge inside the digital sensor) conversion X-ray detectors. The direct conversion detectors consist of amorphous selenium (a-Se) photoconductors and TFT technology, which acts as a switch to transfer electron charge from the photoconductor to the readout electronics. The indirect conversion detectors combine scintillators (usually thallium-activated cesium iodide (CsI:TI)) coupled to secondary quantum (i.e., optical photons) detectors (mainly hydrogenated amorphous silicon (a-Si:H) TFT for DBT). The term passive (see PPS) means that the signal from each pixel is transferred onto a common readout bus as a charge. The indirect conversion detectors present poorer spatial resolution due to the light diffusion inside the scintillator. On the other hand, the resolution of a direct conversion detector is limited mainly by the pixel aperture function (also known as sinc function), which corresponds to the shape and size of the active pixel area. The blurring due to charge diffusion inside the photoconductor is minimal.

The pixel pitch of a-Se TFT DBT detectors is in the range 70–85  $\mu\text{m}$ , while the respective of a-Si TFT detectors is around 100  $\mu\text{m}$  [16]. Decreasing the pixel pitch in indirect detectors does not significantly improve spatial resolution (due to optical blurring of the scintillator), while it decreases SNR (due to the reduction of both digital signal and quantum noise (i.e., electronic noise becomes dominant source)) and consequently DQE. The DQE of direct conversion detectors is high at higher spatial frequencies due to increased resolution, even though it might be decreased by the presence of aliasing [29]. TFT detectors have a relatively slow frame rate of 1–4 frames per second (fps) which increases the readout time and total DBT scan time (thus limiting the total number of projections). Faster readout can be achieved with pixel binning, that is, the average of the signal over a certain number of adjacent pixels, usually  $2 \times 1$  or  $2 \times 2$ . The binning mode capability allows a trade-off between spatial and temporal resolutions. In other words, binned mode increases SNR (and subsequently CNR), but with a penalty in the modulation transfer function (MTF) which is a metric of small high contrast objects resolving per spatial frequency. Therefore, it is usually applied on a-Se TFT DBT detectors. Finally, the binning mode results in very small reduction of DQE with decreasing exposure [16]. TFT detectors have large electronic noise (greater than 1000 electrons ( $e^-$ )) which can induce high background image noise. This means that at low exposure levels, electronic noise becomes the dominant source of noise per projection. Hence, higher exposure and MGD is required to detect microcalcifications and masses. Finally, image lag and ghosting may cause image artifacts during the relative fast image acquisition process of DBT. Lag is the residual image charge generated in previous exposed frames that remains in electronics in subsequent frames as offset charge. Ghosting is associated with the change in X-ray sensitivity induced by the X-ray exposure over time. An a-Se TFT DBT detector has around 4–5% image lag and ghosting [30]. TFT detectors have high image lag and ghosting due to the amorphous structure of a-Si or a-Se (i.e., there are electron traps inside these materials).



In the 1990s charge coupled devices (CCDs) were used extensively in medical imaging. CCDs have high sensitivity due to high fill factor and quantum efficiency, leading to small (down to 25  $\mu\text{m}$ ) pixel pitch. Also, CCDs have very low electronic noise (around 10–20  $e^-$ ) because the charge transfer does not introduce any temporal noise. However, the production cost of CCDs is high, which limits their active area to 2–5  $\text{cm}^2$ . Therefore, demagnification of the light signal is essential to allow coverage of the required X-ray field size (around 24  $\text{cm} \times 30 \text{ cm}$  in FFDM and DBT). However, a number of optical photons can be lost in the demagnification stage, which reduces the SNR. Furthermore, CCDs are serial devices, which leads to high electronic noise at high frame rates and subsequently limits their use in DBT. On the other hand, in the early 2000s complementary metal-oxide-semiconductor (CMOS) active pixel sensor (APS) digital X-ray detectors have been considered as an alternative to a-Si:H TFT PPS detectors in medical imaging applications. APS detectors have at least one source follower transistor in each pixel, which buffers and in some cases amplifies the accumulated signal, leading to an improved speed, decreased electronic noise, and high SNR. Since the early 2010s CMOS APS have been studied for DBT [31–37]. Compared to a-Si:H TFT PPS X-ray detectors, CMOS APS offer smaller pixel pitch (40–75  $\mu\text{m}$ ), low electronic noise (usually in the range 50–200  $e^-$ ), faster frame rate (20–30 fps) and a negligible image lag (<0.1%) [38–40]. The high pixel resolution and low noise floor of CMOS APS detectors improves the 2D projection imaging performance, especially at high spatial frequencies (>5 line pairs per millimeter; lp/mm) [32–35, 37]. Furthermore, the analysis of reconstructed tomographic images show benefits of resolving subtle microcalcifications using a 75  $\mu\text{m}$  pixel pitch CMOS APS detector [41, 42]. Hence, CMOS APS X-ray detectors have the potential to replace a-Si:H TFT PPS detectors in DBT in the near future. Table 7.1 shows currently available or in development DBT systems [16, 23].

Quality Control (QC) methods for DBT systems have been recently developed to evaluate (a) the performance of DBT detectors and (b) the image quality of the reconstructed images [23, 43–45]. This section briefly describes the methods used to evaluate the performance of current DBT detectors: (a) Automatic Exposure Control (AEC) performance, (b) response function, (c) noise analysis, (d) detector element failure, (e) uncorrected defective detector elements and (f) system projection MTF. The detector performance tests can be measured in DBT projection images or projection images acquired in  $0^\circ$  angle stationary mode. Further details about these tests can be found in the literature [23, 43–45]. It is difficult to perform absolute analysis of processed DBT images because the relationship between average pixel value and dose in reconstructed images depends on a) the detector response, b) reconstruction algorithm and c) post-processing [26].

It is useful to test the AEC performance, although is not related directly to the performance of a DBT detector, because it indicates whether the projection images consistently use the appropriate exposure parameters for a given breast thickness, leading to low noise levels in the reconstructed images. Optimal exposures for DBT are not yet known, however the AEC performance can be used in determining system stability and for inter-system comparison [45]. The AEC performance can

be implemented through the calculation of CNR (also referred in the literature as signal-difference-to-noise ratio (SDNR)) for different PMMA thicknesses: a 0.2 mm Aluminum (Al), that is, the object of interest, square (10 mm × 10 mm) can be combined with various PMMA, that is, background, plates (20–70 mm with steps of 10 mm) in order to calculate the contrast (i.e., absolute signal difference (in average pixel values) between object and background) to noise (expressed by the standard deviation of the background or the combined object-background standard deviation) ratio. These parameters should be extracted from 5 mm × 5 mm regions of interests (ROIs). It is suggested to combine two background ROIs (on the chest wall and nipple sides of the Al square) to calculate the average pixel value and standard deviation of the background [23, 44, 45]. The relative values of CNR as a function of PMMA thickness can be compared to the FFDM mode of the DBT system or to an FFDM system of the same manufacturer (with similar specifications). However, due to the effects of pixel pitch and image processing, CNR values are not comparable between different DBT systems [45].

The detector response (also known as response function or signal transfer property (STP)) is the relationship of output signal and noise, expressed by the average pixel value and standard deviation, to input signal, that is, the detector air kerma (DAK). The detector response should correspond to the manufacturer's specification. It is suggested to use the first projection image to minimize the influence of lag and ghosting in the measurements. The gradient of the response function, which corresponds to the detector gain, is usually increased for DBT mode compared to FFDM mode. This happens because the DBT detectors have increased sensitivity to improve the SNR (considering that for a linear detector the signal follows Poisson distribution) at lower dose per projection [23].

The noise analysis can be used to quantify the contribution of different noise components to the total image noise. Hence, it can provide additional information on the performance of the DBT system. There are three main noise sources: electronic (or read), quantum (or shot), and structure (or fixed pattern) noise. Electronic noise is defined as any noise source that is not a function of signal. It includes any noise sources independent from the signal level (dark noise, readout noise, amplifier noise, etc.). Quantum noise is the random spatial and temporal variation of the X-ray quanta emitted from the source, following Poisson distribution. It is an uncorrelated source of noise because it differs for individual images taken with the same detector. Structure noise is correlated noise because its pattern remains the same in repeated images taken with the same detector. Structure noise needs to be removed in order to improve the SNR of the X-ray detector. This process, known as flat-field correction, is applied by normalizing or subtraction of the flat-field image. However, due to limited number of images used for the flat-field mask and the associated noise in the mask itself, there is a remnant structure noise. Furthermore, flat-field correction may not be applied to each projection image, leading to some additional structure noise. The first two types of noise have a temporal nature, while structure noise is spatial. Electronic noise is independent of the exposure level, structure noise is proportional with exposure and quantum noise is related to the square root of the exposure, due

to Poisson statistics [28]. Therefore, the noise components can be separated using the following formula:

$$SD^2 = k_e^2 + k_q^2 \cdot PV + k_s^2 \cdot PV^2 \quad (7.1)$$

where SD is the standard deviation in a specific ROI, PV is the average pixel value in the ROI and  $k_e$ ,  $k_q$  and  $k_s$  are the electronic, quantum and structure noise coefficients, respectively.  $SD^2$  can be plotted as a function of detector air kerma. Next, the measured data is fitted using the above equation and the three noise coefficients are determined. This allows determining the detector air kerma range for which quantum noise is the dominant source of noise. A FFDM detector should be operated within this range [46]. However, for DBT detectors quantum noise may not be the largest noise component in individual projection images. Hence, this measurement can be used for reference purposes to ensure stability over time and similar settings/quality on the same model of the DBT system [23]. Noise decomposition can also be applied in the spatial frequency domain. Further details can be found in Monnin et al. [47].

The detector element failure is actually the most recent “bad pixel map” for tomosynthesis mode generated from the DBT system. This map can be different compared to the bad pixel map in FFDM mode due to differences in the readout of the detector (see higher detector gain in the response function paragraph) or pixel binning after readout. Currently it is suggested to use the manufacturer’s limits for each DBT model [23].

The uncorrected defective detector elements test can be performed using the standard test block (i.e., a 45 mm thick PMMA block used to represent a typical load for the DBT system). In particular, five images of this PMMA block should be acquired to determine whether any pixel (within a 5 mm × 5 mm ROI) deviates more than 20% compared to the average pixel value of this ROI. No uncorrected defective detector elements should be visible and any pixel deviation (compared to the average value) should be less than 20% [23].

Finally, the system projection MTF can be used mainly to quantify the blurring in the direction of movement when the DBT system has a continuous X-ray tube motion (i.e., the X-ray tube moves during the exposure of a projection image) [43]. The system MTF measured in the projection images includes the blurring due to focal spot size, focal spot motion and detector MTF. The detector MTF includes the effect of blurring due to the X-ray converter (i.e., photoconductor in direct detectors or scintillator in indirect detectors), pixel pitch (see aperture function), and detector binning. The system MTF measured in 0° angle stationary mode includes the above blurring sources except the focal spot motion. Blurring due to focal spot size and motion depends on the position of the rotating point and the position in the z-direction of the object (i.e., the position above the bucky table). Therefore, the system projection MTF should be measured at a number of positions above the bucky to evaluate blurring at different heights in the reconstructed volume [23, 43]. The system projection MTF can be calculated using the tilted edge method [48]. The process is well described in the European QC Protocol for DBT systems

[23]. It should be noted that an alternative MTF calculation methodology has been suggested recently by the International Electrotechnical Commission (IEC) standard for the evaluation of digital radiographic detectors [49]. This standard has been adapted by researchers for the evaluation of CMOS APS detectors [50].

## 7.4 DBT Image Perception Characterization

Image quality measurements of the reconstructed images are essential for the evaluation and optimization of DBT systems. QC methods have been recently developed to evaluate the image quality of DBT systems [23, 43–45]. Furthermore, an IEC standard for DBT image performance evaluation is currently under development [51]. These image quality measurements should represent relevant clinical DBT tasks, that is, the detection of microcalcifications and masses in mammographic backgrounds. As aforementioned in the previous section, most DBT systems are capable of FFDM and DBT imaging. However, the current FFDM image quality phantoms are not ideal to assess image reconstruction because they do not include mammographic background. New 3D structured phantoms are being suggested in the literature for DBT with some of them including objects for detection tasks [52–57]. A recent publication also suggested the creation of an inhomogeneous breast phantom for dual energy digital mammography [58]. There are also the commercially available DBT phantoms: Agatha (Leeds Test Objects, Leeds, UK) suggested by Jacobs et al. [59], VOXMAM (Leeds Test Objects, Leeds, UK), and BR3D Breast Imaging Phantom (CIRS Ltd., VA, USA). The detection of objects within the developed DBT phantoms can be evaluated via human observers or using model observers (currently under development). These phantoms can be included in for example UK and European protocols [23, 45] when the methods to test system performance will be validated.

At the moment in order to test the stability of image quality in the  $x$ - $y$  plane, 2D FFDM phantoms, such as CDMAM or TOR MAM test objects, can be used to measure subjectively the CNR and resolution. However, since these phantoms have not been designed for DBT, they cannot be used to compare the performance between different DBT models. Figure 7.3 shows the CDMAM 3.4 and TOR MAM test objects.

In Europe, the CDMAM (Contrast Detail phantom for MAMmography) 3.4 phantom (Artinis Medical Systems, Netherlands) is being extensively used to apply contrast detail analysis (which combines the effects of contrast, noise, and resolution on the human observer detectability of low-contrast fine details) in mammography. There are detailed descriptions of how the CDMAM 3.4 phantom can be used to assess mammographic [27] and DBT [23] image quality. Briefly, the CDMAM 3.4 phantom consists of a matrix of 205 square cells with gold disks of varying diameter (from 0.06 to 2.00 mm) and thickness (from 0.03 to 2.00  $\mu\text{m}$ ). Each of the 205 cells contains two discs: one at the center and the other in a randomly selected corner (eccentric disc). Both diameter and thickness ranges are selected

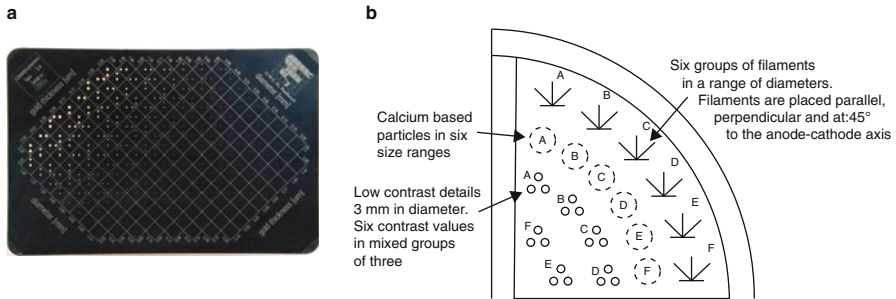


**Fig. 7.3** (a) Image of the Artinis CDMAM 3.4 phantom and (b) layout of the quantitative side of the Leeds TOR MAM test object containing 24 filaments, 6 calcification clusters and 16 discs (figure adapted from Jannetta et al. [60])

to simulate the respective size and contrast ranges for microcalcifications. The CDMAM phantom is used to determine the contrast limit (threshold contrast) or threshold gold thickness for a given disk diameter that corresponds to successful observation of the eccentric disk location. To simulate the detectability of microcalcifications, the details have to be imaged on a background object with a thickness close (in terms of attenuation) to a typical compressed breast. Hence, the CDMAM phantom is usually inserted between two PMMA plates of 20 mm thickness each. The CDCOM software tool [61] can be used to automatically score the CDMAM phantom. However, the use of CDCOM software for reading tomosynthesis images has not been validated by comparison with human reading, as made for FFDM [62]. Therefore, converting the CDCOM results to predicted human values may not be correct. Therefore, the automatic CDMAM analysis can only be used to monitor the stability of DBT image quality [23]. In other words, the predicted human threshold gold thickness results of a DBT system cannot (a) be compared to the FFDM acceptable and achievable limits (suggested by [27]) or (b) be used for performance comparison with another DBT model [23]. The TOR MAM phantom (combined with a 30 mm stack of PMMA) contains three groups of test features: 24 fibres, 6 simulated microcalcification clusters and 16 low contrast plastic discs (in the quantitative side); plus an area designed to give an anthropomorphic impression of a breast parenchymal pattern with overlying microcalcification clusters [63]. Human observers can visually score the detection of these objects, usually between 0 (not visible) and 3 (clearly visible). Hence, the max total score is 144; however the typical score of a DBT detector is usually in the range 65–90. Visual evaluation of TOR MAM is very subjective and likely to vary significantly between observers and between observations by the same observer on different occasions (i.e., interobserver and intraobserver variation, respectively). Therefore, it is recommended to use the TOR MAM phantom to compare the visibility of details against a baseline image [23].

The  $z$ -resolution shows the ability of the DBT system to remove overlying structures (i.e., over the  $z$  direction) and the amount of artifacts due to out of focus

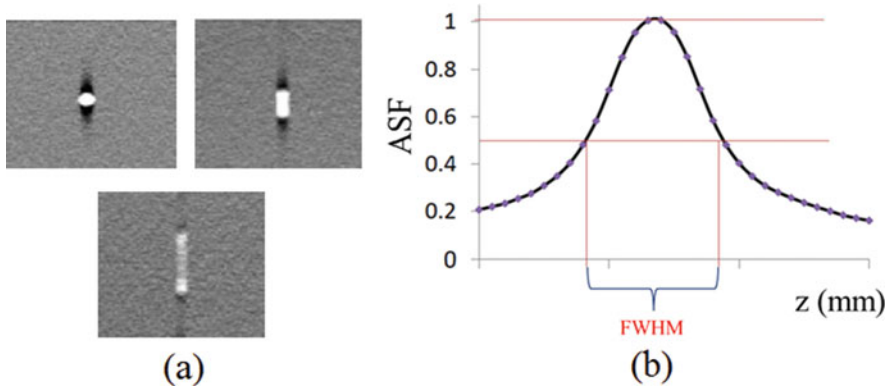


**Fig. 7.4** (a) Artifact images at various focal planes and (b) ASF( $z$ ) curve and FWHM extraction

structures in the image. These artifacts arise from to the incomplete sampling in DBT, due to the limited angular range. In other words, the angular range of a DBT system determines the  $z$ -resolution of the reconstructed images [43]. The greater the angular range the better the position of an object in the  $z$ -direction can be determined. However, this comes at a cost of increased number of projections. It should be mentioned that for a specific angular range, vertical (or  $z$ -) resolution does not improve any further beyond an optimum threshold number of projections. On the other hand, increased number of projections means either higher total exposure to get sufficient image quality or lower image quality for a given exposure (which means reduced exposure per projection and consequently increased impact of electronic noise). Current angular range is  $11\text{--}50^\circ$  and number of projections within  $9\text{--}25$  (see Table 7.1). Because of the incomplete nature of the DBT data it is hard to quantify the  $z$ -resolution. This parameter is typically evaluated by the artifact spread function (ASF), which is the ratio between the contrast of the object outside of the plane of its location (i.e., in adjacent focal planes; off-focus plane) and the contrast of that in focus plane [64]. ASF is plotted as a function of distance from in-focus plane (over the  $z$ -direction). In other words, ASF is the point spread function (PSF) of the DBT system along the  $z$ -plane. Figure 7.4a shows artifact images at various focal planes. It should be noted that ASF is also referred to in the literature as slice sensitivity profile (SSP) [43, 65]. ASF is given by the following formula [64, 66]:

$$\text{ASF}(z) = \frac{I_O(z) - I_{BG}(z)}{I_O(z_0) - I_{BG}(z_0)} \quad (7.2)$$

where  $I_O$  is the intensity (expressed in average pixel value) of the object of interest,  $I_{BG}$  is the intensity of the surrounding background,  $z_0$  is the in-focus plane location of the reconstructed object of interest (i.e., real feature), and  $z$  is an off-focus plane location. The ASF curve as a function of  $z$  has a Gaussian-like shape and full width

at half maximum (FWHM) can be extracted to express  $z$ -resolution. Figure 7.4b shows how FWHM can be extracted from an ASF( $z$ ) curve. It should be mentioned that  $z$ -resolution is coarser compared to  $x$ - and  $y$ -resolutions.

The European QC Protocol [23] describes in detail how to measure the ASF. Briefly, a 5 mm thick PMMA phantom including several 1 mm diameter Al spheres should be combined with six 10 mm thick PMMA slabs placed on the bucky. Three exposures should be made with the 5 mm PMMA phantom (including the Al spheres) in three positions between the PMMA slabs (i.e., between the (a) first and second slab (top position), (b) third and fourth (middle position), and (c) fifth and sixth (bottom position) slab). A visual inspection can be made of the appearance of artifacts and how they change and shift between focal planes (Fig. 7.4a). Furthermore, quantitative measurements can be made by extracting the FWHM (as a measure of  $z$ -resolution) and full width at quarter maximum (FWQM) from the ASF data (Fig. 7.4b). Both FWHM and FWQM values can be used for reference purposes and ensure stability over time and similar settings/quality of the same DBT model.

By definition, the MTF is calculated based on the linear-systems theory [67]. However, the use of linear system theory metric (i.e., linear and shift invariant response) on reconstructed tomosynthesis images is under debate, especially for iterative reconstruction techniques. A linear (or can be linearized) detector transfers the input signal (i.e., detector Air Kerma) linearly, that is, the output signal (expressed in pixel values) is proportional to the input throughout the dynamic range of the detector. A detector is considered shift invariant when its response to an input signal is the same at all locations relative to the pixel matrix. The output of a linear and shift invariant detector in response to any input signal is the convolution of the input with the PSF of the system (along the  $x$ - $y$  plane), which corresponds to the 2D resolution. Currently the European QC Protocol [23] suggests (as an optional test) to calculate the MTF in the  $x$ - $y$  plane to monitor stability of the DBT system and to allow comparison of results obtained from systems of the same model. The MTF in the reconstructed  $x$ - $y$  planes includes the blurring due to focal spot size and motion, detector MTF (i.e., X-ray converter blurring, aperture function and detector binning) and reconstruction algorithm. The MTF in the  $x$ - $y$  plane can be measured using a 25  $\mu\text{m}$  diameter W wire held within two PMMA plates of 5 mm (top) and 10 mm (bottom) thickness. The process is well described in the European QC Protocol [23].

There is a possibility that a part of breast tissue can be missed at the edges of the reconstructed volume. Hence, it is necessary to evaluate the missed tissue at (a) chest wall side and (b) the top and bottom of the reconstructed tomosynthesis image. To evaluate the former, two X-ray rulers (or a phantom with markers) should be positioned on the bucky perpendicular and aligned to the chest wall edge. Next, a tomosynthesis image should be acquired to evaluate the amount of missed tissue. This test indicates if there is any missed tissue between the chest wall edge of the bucky and the chest wall edge of the reconstructed focal plane. To evaluate the latter, a tomosynthesis image should be acquired with small high contrast objects positioned (at the center, near the chest wall edge and in each corner) on the bucky surface. Next, another tomosynthesis image should be acquired with the



small objects attached on the underside of the compression paddle. This allows the observer to check if all objects are brought into focus in focal planes near the bottom and top of the reconstructed images, respectively. Further details are given in the European QC Protocol [23].

As mentioned in the previous section, flat-field correction is applied to remove the structure noise (based on pixel-to-pixel and column-to-column nonuniformities) and possible background trends, such as heel effect and geometric effect. However, remnant structure noise, background trends, and artifacts may be present in the image and affect clinical image quality. A visual inspection of the image may not be sufficient to detect them, so homogeneity tests have been suggested for DBT [23, 65]. It is recommended to position a 45 mm thick PMMA block on the bucky table covering the whole field of view and make an exposure in the clinically used AEC mode. Next, ROIs of 5 mm  $\times$  5 mm can be used in the reconstructed tomosynthesis planes. In each ROI the average pixel value, standard deviation and variance can be calculated and used to generate 2D maps of (a) average pixel value, (b) SNR and (c) variance. The 2D SNR map can be used to indicate background trends. On the other hand, the variance map is very sensitive to artifacts, which is very important because small artifacts may affect the detection of microcalcifications.

Finally, geometric distortion information can be extracted from the three reconstructed images (corresponding to top, middle and bottom positions of a 5 mm PMMA including several 1 mm Al spheres between six 10 mm PMMA slabs) suggested for the measurement of  $z$ -resolution [23]. Analysis software can be used to determine the in-focus plane position of each sphere in the  $x$ ,  $y$  and  $z$  directions. This information can be used to evaluate whether the focal planes are flat or tilted relative to the plane of the bucky surface. Furthermore, it can be used to assess whether there is any distortion or scaling error within the focal planes. Any error should be within the manufacturer's specification.

## 7.5 Evaluating the Performance of DBT Through Simulations

DBT is currently under consideration for its use in breast cancer screening, in combination with 2D mammography or alone. For DBT to be combined with mammography in breast screening it would require the additional dose due to DBT to be justified in terms of mortality and morbidity. For DBT to replace 2D mammography in screening it would have to at least provide the same detectability of cancer lesions with mammography, at similar dose levels. Some studies have shown that the detectability of forms of breast cancer with DBT is slightly lower than with 2D mammography [68], whereas others have claimed that the converse is true [69]. Further investigation on the usefulness of DBT in breast cancer screening in comparison with 2D-mammography is currently ongoing.



There are a number of different DBT systems commercially available. However, each acquires the images for DBT using a different technique and there is no agreement, either between the vendors or in the literature, on the best methodology for image acquisition and reconstruction. The detectability of a lesion in the breast using X-ray imaging depends on the image acquisition methods, radiation dose, image processing, reconstruction algorithms, the physical properties of the breast and the lesion itself. The effect of each parameter on lesion detectability is briefly described below.

The tomographic scan angular range and the number of projections are two of the image acquisition parameters that are expected to affect the detectability of lesions in DBT. By increasing the angular range, depth resolution increases [64]. However, the movement required by the X-ray tube may also increase and, unless the system is step-and-shoot [14], blurring can be introduced due to tube motion and the oblique incidence angle [70]. Wider scan angles need more projections for an adequate sampling of image data and fewer tomosynthesis reconstruction artifacts. However, at a fixed total dose, and with increasing the number of projections, the relative quantum noise in each projection increases. In combination with insufficient angular sampling, the quantum noise can have an effect on the detectability of small-scale signals [71]. Also, electronic noise may become more dominant. Sechopoulos and Ghetti [72] have shown that increasing the number of projections decreases the CNR for microcalcification-like objects.

Another imaging parameter that can affect lesion detectability is the X-ray spectrum. Also, decreasing dose for a fixed geometry increases the relative noise in an image, creating mainly quantum noise-limited images and may lead to a decrease in the detectability of lesions ([73–76]). The effect of image processing and reconstruction algorithms can also greatly affect the visibility of lesions, as discussed in section 7.2 above.

As aforementioned, microcalcifications and masses are two forms of breast cancer that might require different system characteristics for the enhancement of their visibility. Masses do not have a high contrast in comparison with healthy breast tissue when 2D-projected, and can be superimposed by surrounding structures. The separation of overlying structures into planes by DBT can decrease the effect of masses being superimposed by healthy breast tissue. Microcalcifications on the other hand have a higher contrast in comparison with healthy breast tissue, but the visualization of their small size (0.26 mm average calcification diameter in Warren et al. [77]) depends on the resolution and noise in the imaging system.

The establishment of the optimum combination of the above variables for DBT is complicated, due to the large number of variables and the effect they can have on each other. For the investigation of the effect of the variables on lesions detectability, the methods to be used should have settings as similar as possible to the clinical case. Ideally, clinical trials should be used to measure cancer detection for different imaging conditions. However, clinical trials are normally expensive and there are usually ethical issues if there were multiple radiation exposures on the same women.

Alternatively, it is in the interest of several research groups worldwide to use simulation methods to study and optimize DBT systems, and to allow for

a straightforward and meaningful comparison of both against 2D mammography and between the wide range of DBT image acquisition parameters available [78]. Modelling the performance of DBT through simulations normally involves three stages: (1) the development of mathematical breast phantoms, (2) the development of simulated lesion and insertion into the breast phantoms, and (3) the calculation of images using X-ray tracing techniques. Following the simulations conclusions can be drawn on the effectiveness of DBT in breast cancer detection, either through observer studies or through assessment using image quality metrics.

In the subsections below a description is made of the stages described above.

### ***7.5.1 Development of Breast Software Phantoms***

Breast software phantoms developed and used in DBT simulations vary widely in terms of methods of preparation and complexity. They can also be purely mathematical in origin, or derived from clinical images (e.g., patient CT data).

Images of breast-tissue-mimicking material [79, 80] as well as real imaged mastectomy samples [81] have been used to simulate breast. Sechopoulos and Ghetti [72] used fully simulated phantoms of sections of the breast developed from a white noise volume filtered with the square root of an isotropic 3D power law spectrum, reported to be followed by breast tissue in breast CT data. Advanced phantoms of the whole breast formed the models developed by Bliznakova et al. [82–84], which were based on the combinations of 3D geometrical primitives and voxel matrices. Similarly, Bakic et al. [85] developed a model which used a seeded region growing algorithm for the production of the adipose compartments of different shapes and sizes. These provided compact coverage to the adipose region of the phantom. The fibroglandular region had fewer, more widely separated adipose compartments. Skin and Cooper’s ligaments were also simulated.

More recently, Elangovan et al. [86, 87] created breast phantoms by first extracting breast tissue structures from reconstructed DBT planes of real patient images. The extracted structures were de-noised using a series of morphological image operations, scaled and inserted into an empty breast phantom volume containing only skin and adipose tissue. Each phantom was composed of five different tissue types: skin, glandular tissue, adipose tissue, Cooper’s ligaments and blood vessels. The compositions of the adipose tissue, glandular tissue and skin were taken from Hammerstein et al. [88]. The composition of the Cooper’s ligaments and blood vessels were assumed to be that of adult skeletal muscle [89].

Similarly, Li et al. [90] described mathematically defined 3D breast models based on the analysis of segmented clinical CT images. Small- and medium-scale fibroglandular and adipose tissue morphologies were mimicked and medium-scale morphology of each adipose compartment was simulated by a union of overlapping ellipsoids.

An open-source, multimodality breast phantom was also made available by Graff [91]. The production of this phantom was based on the deformations initially

performed on a quadric to form the breast shape. A Voronoi technique was used to produce the initial glandular compartments and a ductal tree structure with terminal duct lobular units grown from the nipple into each compartment. The fat and glandular lobules were created using a Perlin noise function and a vascular tree was grown from the chest muscle into the breast tissue too. Inkjet printing was recently used to fabricate the phantom from the virtual model into a physical breast phantom [92].

Two methods are currently in use for assessing the realism of breast phantoms. The first involves radiologists distinguishing between real breast images and mathematical breast images. The second involves comparison of the statistical properties of simulated images of the phantoms and real images.

### 7.5.2 *Development of Simulated Lesions*

As with the development and use of breast phantoms, breast lesions have also been developed and used with different methods and at different levels of complexity. Normally the lesion and its realism define the DBT assessment method and the quality metric (MTF, CNR, ASF, etc.) to be used in the assessment. Realistic lesions would allow the system to be assessed by observers; quantitative analysis (e.g., MTF) can be carried out if for example a wire represents the lesion in a DBT simulated system [93].

Calcium carbonate particles representing microcalcifications of several sizes have been used in several studies for representing calcifications [72, 79, 80]. In Hadjipanteli et al. [76] one high-resolution microcalcification image volume was chosen from a database of 400 real microcalcification image volumes (breast biopsy samples), which were acquired using a micro-CT system [94]. The attenuation coefficient of each calcification was set as the product of the attenuation coefficient of calcium oxalate and the factor 0.84. This corrects for differences in the attenuation of calcium oxalate and real calcifications (Fig. 7.5) [95].

Masses are normally represented using soft tissue simulated material [72]. Advanced simulated masses were recently developed by Elangovan et al. [86, 96] using diffusion limited aggregation.

Lesions can be inserted into the breast phantoms by voxel replacement. If the original voxel size of the breast phantom is larger than that for the lesions, a limited cubic region around each insertion site can be created at a higher resolution by super sampling the background tissue voxels of the phantom to accommodate the microcalcification clusters.

Cockmartin et al. [97] suggested a hybrid method for both 2D mammography and DBT that combines target objects (i.e., spheres of breast tissue simulating material and microcalcifications) with patient images (i.e., real patient background) without the need for mathematical simulations. In particular, their suggested method takes into account the system sharpness and noise propagation for the target objects, the effect of image processing, reconstruction algorithm and anatomical background in

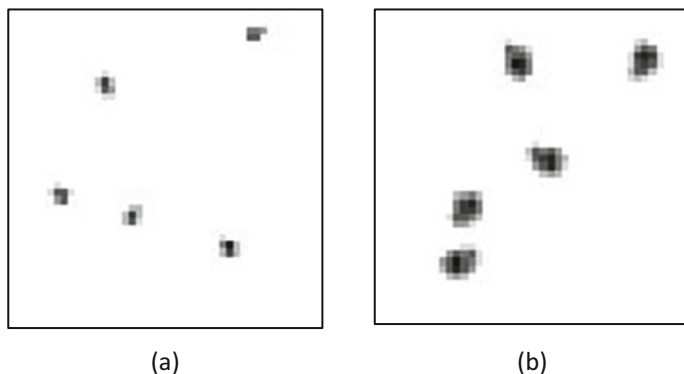


**Fig. 7.5** Example 2D projection images of ( $2.5 \times 2.5 \times 2.5 \text{ mm}^3$  cubic volume) simulated microcalcification clusters with two different diameters before insertion into the simulated images: (a)  $125 \mu\text{m}$  and (b)  $250 \mu\text{m}$  (figure adapted from Hadjipanteli et al. [76])

the detection evaluation of the system. However, it suffers from several limitations, mainly (a) it is device specific (i.e., the findings cannot be applied directly to other DBT systems), (b) their detection task was mainly binary (i.e., the target object was present or absent), (c) it may be time consuming to develop realistic physical target objects, and (d) the variation in the DBT scan angle introduces contrast loss for small objects [97].

### 7.5.3 Calculation of Images Using X-Ray Tracing Techniques

Several simulation frameworks for creating realistic DBT images from voxel breast models have been previously published [98–100]. Images can be created using a projection method (e.g., ray tracing) [101, 102]. If an existing system is to be tested, accurate knowledge of the system parameters is required, which might require collaboration with the manufacturers or experimental measurements. Alternatively, the optimization of systems can be carried out based on variable parameters until the optimum image quality is achieved.

The resultant projection images need to be adjusted to include scatter, detector blur, and other sources of blur and to add any noise associated with the detector during conversion of X-ray flux to an image. Compared to planar imaging, there may be additional challenges to simulating DBT images due to multiple images being acquired at different angles of incidence for the X-ray beam, and additionally lag and ghosting may affect the quality of the images [103].

DBT clinical performance evaluation studies might require changing only a single factor at a time. For example, changing the system geometry: angle and number of projections, allows for the investigation of the effect of geometry only

on lesions detection and can avoid possible confounding effects associated with changes in receptor, pixel size, X-ray spectrum, dose, and other factors.

A “continuous” or a “step-and-shoot” configuration can be tested. In the “continuous” configuration the source movement introduces blurring, and this effect can be incorporated by increasing the focal spot size in the direction of movement in the simulation model. Based on physical measurements of the tube rotation speed and the time of exposure for each projection, made on a system, for the exposure of a breast of a particular thickness, the focal spot length (in the direction of tube movement) can be calculated for different systems. The focal spot width (in the direction perpendicular to the movement of the tube) can also be based on physical measurements. The ray tracing simulation can also include transmission through the grid, if any. The attenuations in the breast support and compression paddle and breast movement could also be taken into account.

The kVp and target/filter materials used in the X-ray simulation might have a great effect on lesions detectability. The X-ray spectra to be used in the simulation (e.g., [104]) can be attenuated by an aluminum thickness to match the calculated and measured real half value layers. Taking into account the heel effect and the amount of noise across the image will make a simulated projection image more realistic.

One important factor to which a lot of emphasis is normally given when simulating breast imaging systems is dose to the breast. For each spectrum to be used in the simulation, the incident air kerma can be calculated at the entrance of the breast and the MGD to be computed using conversion factors from Dance et al. [25, 105]. For a given set of experimental conditions, the X-ray spectrum can be scaled so that the MGD calculated from the incident air kerma matches the required dose value.

To incorporate the effect of scatter in the image, a scatter-to-primary ratio can be introduced in the simulation calculations and multiplied by the average primary signal in the image patch to give the scatter signal to be added. For this a precalculated table can be used and validated as part of the image simulation framework. Care should be taken for using the scatter to primary ratio that corresponds to a particular breast thickness and glandularity.

The image simulation tools should include image degradation tools. These are normally tools which are designed based on experimental measurements made on real systems by various authors [106–109] and in various National Health Service Breast Screening Programme (NHSBSP) reports [110]. Measurements of STP, MTF, noise power spectrum (NPS), and flat-field correction maps could be made on the imaging system that is simulated to adapt the image quality of the simulated images. The above measurements can be used to blur the projection images and then to add noise corresponding to the specific detector pixel size and exposure. Finally, the energy absorbed per unit area in the detector, as calculated in the simulations, can be converted into pixel values, based on detector response measurements (STP). A further analysis and characterization of the currently available systems with a view to improving the existing simulation frameworks was carried out by Mackenzie et al. [103]. This work presented measurements and an in-depth evaluation of the noise, sharpness, lag, and ghosting characteristics of projection images acquired on four

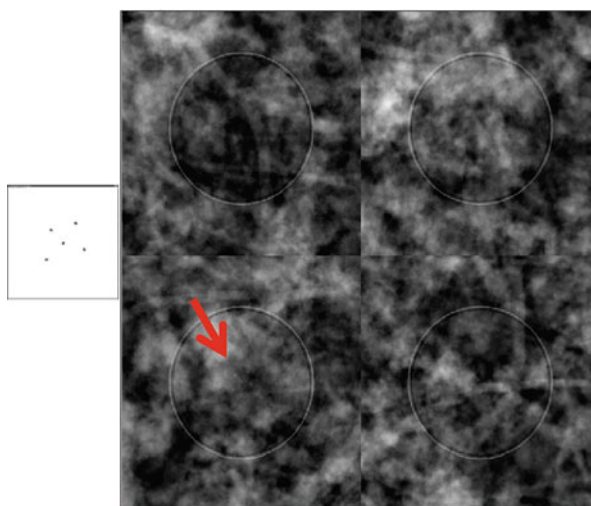
mammographic systems in DBT mode and for comparison purposes, the MTF and noise for planar imaging. It also considered whether further development of the current simulation frameworks is required.

Clinical, commercial or custom-made reconstruction and processing software are used for the processing and reconstruction of images. If commercial or custom-made reconstruction software are used, quantitative analysis (FWHM, CNR, contrast degradation factor (CDF) etc.) and qualitative tests on DBT images reconstructed using different reconstruction software might be needed to find out whether it produces images comparable to those produced by reconstruction and processing software used clinically.

Several studies used different analysis methods for the evaluation of the performance of DBT in detecting breast lesions. Quality metrics, such as CNR, MTF, ASF etc., form one type of evaluation method. Alternatively, the formation of new metrics using the combination of the above quality factors [72] can be used. This type of evaluation method has the advantage that many system configurations can be tested in one study, since it is normally a time efficient method.

Observer studies require observers (radiologists or even nonexperts) to assess the visibility of images. Alternative forced choice (AFC) is one form analysis for of observer studies. The main characteristic of an AFC study is the requirement for a “signal known exactly” and “background known exactly” detection task (Fig. 7.6). Receiver operating characteristics is an alternative method, used extensively in clinical studies, and a comparison with AFC was given by Burgess [111]. Even though observer studies can be a more realistic approach into assessing the detectability of lesions using DBT, the time constraint can put a limit to how many system parameters can be tested.

**Fig. 7.6** Example image displayed for a 4AFC study graphical user interface showing four 2D mammography image patches and the signal cue for a 175  $\mu\text{m}$  microcalcification cluster. The red arrow has been added to the image to indicate which of the four images contains the cluster (figure adapted from Hadjipanteli et al. [76])



## 7.6 Summary

DBT is a new technique and still under development. Several parameters (such as image acquisition parameters, detector response, system geometry, radiation dose, and image processing and reconstruction algorithms) are studied for their effect on image quality and the investigation of the optimum use of DBT. The use of simulations in the evaluation of DBT can provide a lot of flexibility in testing a wide range of system conditions, without the need to expose patients to additional dose. Compared to conventional clinical trials, virtual ones can provide system optimization in fast, radiation free and cost-effective ways. With DBT currently under consideration for its use in breast cancer screening, simulations can help to better understand the areas where DBT can improve breast cancer detection.

## References

1. D.G. Grant, Tomosynthesis: a three dimensional radiographic imaging technique. *IEEE Trans. Biomed. Eng.* **BME-19**, 20–28 (1972)
2. A. Tingberg, X-ray tomosynthesis: a review of its use for breast and chest imaging. *Radiat. Prot. Dosimetry* **139**(1–3), 100–107 (2010)
3. B.G. Ziedses des Plantes, Eine neue methode zur differenzierung in der roentgenographie (planigraphie). *Acta Radiol.* **13**, 182–192 (1932)
4. T. Dobbins III, D.J. Godfrey, Digital X-ray tomosynthesis: current state of the art and clinical potential. *Phys. Med. Biol.* **48**, R65–R106 (2003)
5. J.B. Garrison, D.G. Grant, W.H. Guier, R.J. Johns, Three dimensional roentgenography. *Am. J. Roentgenol.* **105**, 903–908 (1969)
6. E.R. Miller, E.M. McCurry, B. Hruska, An infinite number of laminagrams from a finite number of radiographs. *Radiology* **98**, 249–255 (1971)
7. N.A. Baily, R.L. Crepeau, E.C. Lasser, Fluoroscopic tomography. *Investig. Radiol.* **9**, 94–103 (1974)
8. N.A. Baily, R.A. Keller, C.V. Jakowatz, A.C. Kak, The capability of fluoroscopic systems for the production of computerized axial tomograms. *Investig. Radiol.* **11**, 434–439 (1976)
9. N.A. Baily, T.D. Kampp, Digitized longitudinal tomography. *Investig. Radiol.* **16**, 126–132 (1981)
10. Z. Kolitsi, G. Panayiotakis, V. Anastassopoulos, A. Scodras, N. Pallikarakis, A multiple projection method for digital tomosynthesis. *Med. Phys.* **19**, 1045–1050 (1992)
11. M.J. Yaffe, J.G. Mainprize, Digital tomosynthesis: technique. *Radiol. Clin. North Am.* **52**, 489–497 (2014)
12. S. Destounis, J.L. Gruttadauria, An overview of digital breast tomosynthesis. *J. Radiol. Nurs.* **34**, 131–136 (2015)
13. L.T. Niklason, B.T. Christian, L.E. Niklason, D.B. Kopans, D.E. Castleberry, B.H. Opsahl-Ong, C.E. Landberg, P.J. Slanetz, A.A. Giardino, R. Moore, D. Albagli, M.C. DeJule, P.F. Fitzgerald, D.F. Fobare, B.W. Giambattista, R.F. Kwasnick, J.Q. Liu, S.J. Lubowski, G.E. Possin, J.F. Richotte, C.Y. Wei, R.F. Wirth, Digital tomosynthesis in breast imaging. *Radiology* **205**, 399–406 (1997)
14. E. Shaheen, N. Marshall, H. Bosmans, Investigation of the effect of tube motion in breast tomosynthesis: continuous or step and shoot? *Proc. SPIE* **7961**, 79611E (2011)

15. X. Qian, R. Rajaram, X. Calderon-Colon, G. Yang, T. Phan, D.S. Lalush, J. Lu, O. Zhou, Design and characterization of a spatially distributed multibeam field emission X-ray source for stationary digital breast tomosynthesis. *Med. Phys.* **36**, 4389–4399 (2009)
16. I. Sechopoulos, A review of breast tomosynthesis. Part I. The image acquisition process. *Med. Phys.* **40**, 014301-1–014301-12 (2013)
17. I. Sechopoulos, A review of breast tomosynthesis. Part II. Image reconstruction, processing and analysis, and advanced applications. *Med. Phys.* **40**, 014302-1–014302-7 (2013)
18. T. Mertelmeier, J. Orman, W. Haerer, M.K. Dudam, Optimizing filtered backprojection reconstruction for a breast tomosynthesis prototype device. *Proc. SPIE* **6142**, 61420F (2006)
19. J. Orman, T. Mertelmeier, W. Haerer, Adaptation of image quality using various filter setups in the filtered backprojection approach for digital breast tomosynthesis. *Proc. IWDM*, 175–182 (2006)
20. Y. Zhang, H.P. Chan, B. Sahiner, J. Wei, M.M. Goodsitt, L.M. Hadjiiski, J. Ge, C. Zhou, Tomosynthesis reconstruction using the simultaneous algebraic reconstruction technique (SART) on breast phantom data. *Proc. SPIE* **6142**, 614249 (2006)
21. Y. Chen, J.Y. Lo, J.T. Dobbins III, Importance of point-by-point back projection correction for isocentric motion in digital breast tomosynthesis: relevance to morphology of structures such as microcalcifications. *Med. Phys.* **34**, 3885–3892 (2007)
22. T. Wu, A. Stewart, M. Stanton, T. McCauley, W. Phillips, D.B. Kopans, R.H. Moore, J.W. Eberhard, B. Opsahl-Ong, L. Niklason, M.B. Williams, Tomographic mammography using a limited number of low-dose cone-beam projection images. *Med. Phys.* **30**, 365–380 (2003)
23. R.E. van Engen, H. Bosmans, R. Bouwman, D.R. Dance, P. Heid, B. Lazzari, N.W. Marshall, S. Schopphoven, C. Strudley, M.A.O. Thijssen, K.C. Young, Protocol for the Quality Control of the Physical and Technical Aspects of Digital Breast Tomosynthesis Systems, Version 1.01, EUREF (2016)
24. T.M. Svahn, N. Houssami, I. Sechopoulos, S. Mattsson, Review of radiation dose estimates in digital breast tomosynthesis relative to those in two-view full-field digital mammography. *Breast* **24**, 93–99 (2015)
25. D.R. Dance, K.C. Young, R.E. Engen, Estimation of mean glandular dose for breast tomosynthesis: factors for use with the UK, European and IAEA breast dosimetry protocols. *Phys. Med. Biol.* **56**, 453–472 (2011)
26. A. Maldera, P. De Marco, P.E. Colombo, D. Origgi, A. Torresin, Digital breast tomosynthesis: dose and image quality assessment. *Phys. Med.* **33**, 56–67 (2017)
27. R.E. van Engen, K.C. Young, H. Bosmans, M.A.O. Thijssen, *European Protocol for the Quality Control of the Physical and Technical Aspects of Mammography Screening. Part B: Digital Mammography in European Guidelines for Quality Assurance in Breast Cancer Screening and Diagnosis*, 4th edn. (European Commission, Luxembourg, 2006), pp. 105–165
28. A.C. Konstantinidis, in *X-Ray and Ultrasound Imaging*. Chapter 2.2: Physical Parameters of Image Quality in Comprehensive Biomedical Physics, vol 2 (Elsevier, Amsterdam, The Netherlands, 2014), pp. 49–62
29. E. Samei, Performance of digital radiography detectors: factors affecting sharpness and noise. *Proc. RSNA* **49**, 61 (2003)
30. B. Zhao, W. Zhao, Imaging performance of an amorphous selenium digital mammography detector in a breast tomosynthesis system. *Med. Phys.* **35**, 1978–1987 (2008)
31. S. Naday, E.F. Bullard, S. Gunn, J.E. Brodrick, E.O. O’Tuairisg, A. McArthur, H. Amin, M.B. Williams, P.G. Judy, A. Konstantinidis, Optimised breast tomosynthesis with a novel CMOS flat panel detector. *Proc. IWDM* **428**, 435 (2010)
32. J.G. Choi, H.S. Park, Y. Kim, Y.W. Choi, T.H. Ham, H.J. Kim, Characterization of prototype full-field breast tomosynthesis by using a CMOS array coupled with a columnar CsI(Tl) scintillator. *J. Korean Phys. Soc.* **60**, 521–526 (2012)
33. T. Patel, K. Klanian, Z. Gong, M.B. Williams, Detective quantum efficiency of a CsI-CMOS X-ray detector for breast tomosynthesis operating in high dynamic range and high sensitivity modes. *Proc. IWDM*, 80–87 (2012)



34. C. Zhao, J. Kanicki, A.C. Konstantinidis, T. Patel, Large area CMOS active pixel sensor X-ray imager for digital breast tomosynthesis: Analysis, modeling, and characterization. *Med. Phys.* **42**, 6294–6308 (2015)
35. C. Zhao, A.C. Konstantinidis, Y. Zheng, T. Anaxagoras, R.D. Speller, J. Kanicki, 50  $\mu\text{m}$  pixel pitch wafer-scale CMOS active pixel sensor X-ray detector for digital breast tomosynthesis. *Phys. Med. Biol.* **60**, 8977–9001 (2015)
36. C. Zhao, N. Vassiljev, A. Konstantinidis, R. Speller, J. Kanicki, Three-dimensional cascaded system analysis of a 50  $\mu\text{m}$  pixel pitch wafer-scale CMOS active pixel sensor X-ray detector for digital breast tomosynthesis. *Phys. Med. Biol.* **62**, 1994–2017 (2017)
37. I.M. Peters, C. Smit, J.J. Miller, A. Lomako, High dynamic range CMOS-based mammography detector for FFDM and DBT. *SPIE Med. Imag. Int. Soc. Opt. Photon.* **9783**, 978316 (2016)
38. G. Zentai, in *Comparison of CMOS and a-Si Flat Panel Imagers for X-Ray Imaging*. 2011 IEEE Int. Conf. Imaging Syst. Tech. IST 2011 – Proc. (2011), pp. 194–200
39. A.C. Konstantinidis, M.B. Szafraniec, L. Rigon, G. Tromba, D. Dreossi, N. Sodini, P.F. Liaparinis, S. Naday, S. Gunn, A. McArthur, R.D. Speller, A. Olivo, X-ray performance evaluation of the Dexela CMOS APS X-ray detector using monochromatic synchrotron radiation in the mammographic energy range. *IEEE Trans. Nucl. Sci.* **60**, 3969–3980 (2013)
40. M. Esposito, T. Anaxagoras, A.C. Konstantinidis, Y. Zheng, R.D. Speller, P.M. Evans, N.M. Allinson, K. Wells, Performance of a novel wafer scale CMOS active pixel sensor for bio-medical imaging. *Phys. Med. Biol.* **59**, 3533–3554 (2014)
41. H.S. Park, Y.S. Kim, H.J. Kim, Y.W. Choi, J.G. Choi, Optimization of configuration parameters in a newly developed digital breast tomosynthesis system. *J. Radiat. Res.* **55**, 589–599 (2014)
42. Y.S. Kim, H.S. Park, S.J. Park, S. Choi, H. Lee, D. Lee, Y.W. Choi, H.J. Kim, Characterizing X-ray detectors for prototype digital breast tomosynthesis systems. *J. Instrum.* **11**, P03022 (2016)
43. R.E. van Engen, H. Bosmans, R. Bouwman, D.R. Dance, P. Heid, B. Lazzari, N.W. Marshall, S. Schopphoven, C. Strudley, M.A.O. Thijssen, K.C. Young, A European Protocol for technical quality control of breast tomosynthesis systems. *Proc. IWDM* **8539**, 452–459 (2014)
44. C.J. Strudley, K.C. Young, P. Looney, F. Gilber, Development and experience of quality control methods for digital breast tomosynthesis systems. *Br. J. Radiol.* **88**, 1–11 (2015)
45. NHSBSP Equipment Report 1407, *Routine Quality Control Tests for Breast Tomosynthesis (Physicists)* (Public Health England, London, 2015)
46. R.E. van Engen, K.C. Young, H. Bosmans, B. Lazzari, S. Schopphoven, P. Heid, M.A. Thijssen, A supplement to the European guidelines for quality assurance in breast cancer screening and diagnosis. *Proc. IWDM* **6136**, 643–650 (2010)
47. P. Monnin, H. Bosmans, F.R. Verdun, N.W. Marshall, Comparison of the polynomial model against explicit measurements of noise components for different mammography systems. *Phys. Med. Biol.* **59**, 5741–5761 (2014)
48. E. Samei, M.J. Flynn, An experimental comparison of detector performance for computed radiography systems. *Med. Phys.* **29**, 447–459 (2002)
49. IEC 62220-1-1, *Medical Electrical Equipment – Characteristics of Digital X-Ray Imaging Devices – Part 1-1: Determination of the Detective Quantum Efficiency – Detectors Used in Radiographic Imaging* (International Electrotechnical Commission (IEC), Geneva, Switzerland, 2015)
50. C. Michail, I. Valais, N. Martini, V. Koukou, N. Kalyvas, A. Bakas, I. Kandarakis, G. Fountos, Determination of the detective quantum efficiency (DQE) of CMOS/CsI imaging detectors following the novel IEC 62220-1-1:2015 International Standard. *Rad. Meas.* **94**, 8–17 (2016)
51. IEC 61223-3-6 Ed.1.0 (draft), *Evaluation and Routine Testing in Medical Imaging Departments. Part 3-6: Acceptance and Constancy Tests – Imaging Performance of Mammographic Tomosynthesis Mode of Operation of Mammographic X-Ray Equipment* (International Electrotechnical Commission (IEC), Geneva, Switzerland)

52. G.J. Gang, D.J. Tward, J. Lee, J.H. Siewerdsen, Anatomical background and generalized detectability in tomosynthesis and cone-beam CT. *Med. Phys.* **37**, 1948–1965 (2010)
53. S. Park, R. Jennings, H. Liu, A. Badano, K. Myers, A statistical, task-based evaluation method for three-dimensional X-ray breast imaging systems using variable-background phantoms. *Med. Phys.* **37**, 6253–6270 (2010)
54. A.K. Carton, P. Bakic, C. Ullberg, H. Derand, A.D.A. Maidment, Development of a physical 3D anthropomorphic breast phantom. *Med. Phys.* **38**, 891–896 (2011)
55. N.D. Prionas, G.W. Burkett, S.E. McKenney, L. Chen, L.L. Chenstern, J.M. Boone, Development of a patient-specific two-compartment anthropomorphic breast phantom. *Phys. Med. Biol.* **4293**, 4293–4307 (2012)
56. N. Kiarashi, G.M. Sturgeon, L.W. Nolte, J.Y. Lo, J.T. Dobbins, W.P. Segars, E. Samei, Development of matched virtual and physical breast phantoms based on patient data. *Proc. SPIE* **8668**, 866805-1–866805-6 (2013)
57. L. Cockmartin, N.W. Marshall, G. Zhang, K. Lemmens, E. Shaheen, C. Van Ongeval, E. Fredenberg, D.R. Dance, E. Salvagnini, K. Michielsen, H. Bosmans, Design and application of a structured phantom for detection performance comparison between breast tomosynthesis and digital mammography. *Phys. Med. Biol.* **62**, 758–780 (2017)
58. V. Koukou, N. Martini, G. Fountos, C. Michail, P. Sotiropoulou, A. Bakas, N. Kalyvas, I. Kandarakis, R. Speller, G. Nikiforidis, Dual energy subtraction method for breast calcification imaging. *Nucl. Instr. Methods Phys. Res. A* **848**, 31–38 (2017)
59. J. Jacobs, N. Marshall, L. Cockmartin, F. Zanca, R. van Engen, K. Young, H. Bosmans, E. Samei, Towards an international consensus strategy for periodic quality control of digital breast tomosynthesis systems. *Proc. SPIE* **7622**, 76220G (2010)
60. A. Jannetta, J.C. Jackson, C.J. Kotre, I.P. Birch, K.J. Robson, R. Padgett, Mammographic image restoration using maximum entropy deconvolution. *Phys. Med. Biol.* **49**, 4997–5010 (2004)
61. R. Visser, N. Karssemeijer, Manual CDCOM Version 1.5.2: Software for Automated Readout of CDMAM 3.4 Images (2008)
62. K.C. Young, J.J.H. Cook, J.M. Oduko, H. Bosmans, Comparison of software and human observers in reading images of the CDMAM test object to assess digital mammography systems. *Proc. SPIE* **6142**, 14206 (2006)
63. A.R. Cowen, D.S. Brette, N.J. Coleman, G.J.S. Parkin, A preliminary investigation of the imaging performance of photostimulable phosphor computed radiography using a new design of mammographic quality control test object. *Br. J. Radiol.* **65**, 528–535 (1992)
64. Y.H. Hu, B. Zhao, W. Zhao, Image artifacts in digital breast tomosynthesis: investigation of the effects of system geometry and reconstruction parameters using a linear system approach. *Med. Phys.* **35**, 5242–5252 (2008)
65. R.W. Bouwman, R. Visser, K.C. Young, D.R. Dance, B. Lazzari, R. van der Burght, P. Heid, R.E. van Engen, Daily quality control for breast tomosynthesis. *Proc. SPIE* **7622**, 762241 (2010)
66. T. Wu, R.H. Moore, E.A. Rafferty, D.B. Kopans, A comparison of reconstruction algorithms for breast tomosynthesis. *Med. Phys.* **31**, 2636–2647 (2004)
67. I.A. Cunningham, in *Physics and Psychophysics. Applied Linear-Systems Theory in Handbook of Medical Imaging*, vol 1 (SPIE Press, Bellingham, Washington, 2000), pp. 79–159
68. M.L. Spangler, M.L. Zuley, J.H. Smukin, G. Abrams, M.A. Ganott, C. Hakim, D.M. Chough, R. Shah, D. Gur, Detection and classification of calcifications on digital breast tomosynthesis and 2D digital mammography: a comparison *Am. J. Roentgenol.* **196**, 320–324 (2011)
69. D. Kopans, S. Gavenonis, E. Halpern, R. Moore, Calcifications in the breast and digital breast tomosynthesis. *Breast J.* **17**, 638–644 (2011)
70. J.G. Mainprize, A.K. Bloomquist, M.P. Kempston, M.J. Yaffe, Resolution at oblique incidence angles of a flat panel imager for breast tomosynthesis. *Med. Phys.* **33**, 3159–3164 (2006)

71. I. Reiser, R.M. Nishikawa, Task-based assessment of breast tomosynthesis: effect of acquisition parameters and quantum noise. *Med. Phys.* **4**, 1591–1600 (2010)
72. I. Sechopoulos, C. Ghetti, Optimization of the acquisition geometry in digital tomosynthesis of the breast. *Med. Phys.* **36**, 1199–1207 (2009)
73. E. Samei, R.S. Saunders, J.A. Baker, D.M. DeLong, Digital mammography: effects of reduced radiation dose on diagnostic performance. *Radiology* **243**, 396–404 (2007)
74. L.M. Warren, A. Mackenzie, J. Cooke, R.M. Given-Wilson, M.G. Wallis, D.P. Chakraborty, D.R. Dance, H. Bosmans, K.C. Young, Effect of image quality on calcification detection in digital mammography. *Med. Phys.* **39**, 3202–3213 (2012)
75. P. Timberg, M. Dustler, H. Petersson, A. Tingberg, S. Zackrisson, Detection of calcification clusters in digital breast tomosynthesis slices at different dose levels utilizing a SRSAR reconstruction and JAFROC. *Proc. SPIE* **9416**, 941604 (2015)
76. A. Hadjiipanteli, P. Elangovan, A. Mackenzie, P.T. Looney, K. Wells, D.R. Dance, K.C. Young, The effect of system geometry and dose on the threshold detectable calcification diameter in 2D-mammography and digital breast tomosynthesis. *Phys. Med. Biol.* **62**, 858–877 (2017)
77. L.M. Warren, L. Dummott, M.G. Wallis, R.M. Given-Wilson, J. Cooke, D.R. Dance, K.C. Young, Characterisation of screen detected and simulated calcification clusters in digital mammography. *Proc. IWDWM* **8539**, 364–371 (2014)
78. P.R. Bakic, K.J. Myers, S.J. Glick, A.D.A. Maidment, Virtual tools for the evaluation of breast imaging: state-of-the science and future directions. *Proc. IWDWM* **9699**, 518–524 (2016)
79. H.P. Chan, M.M. Goodsitt, M.A. Helvie, S. Zelaklewich, A. Schmitz, M. Noroozian, C. Paramagul, A.R. Marilyn, A.V. Nees, H.N. Colleen, P. Carson, Y. Lu, L. Hadjiiski, J. Wei, Digital breast tomosynthesis: observer performance of clustered microcalcification detection on breast phantom images acquired with an experimental system using variable scan angles, angular increments and number of projection views. *Radiology* **273**, 675–685 (2014)
80. M.M. Goodsitt, H.P. Chan, A. Schmitz, S. Zelaklewich, T. Santosh, L. Hadjiiski, K. Watcharotone, M.A. Helvie, C. Paramagul, C. Neal, E. Christodoulou, S.C. Larson, P.L. Carson, Digital breast tomosynthesis: studies of the effects of acquisition geometry on contrast-to-noise ratio and observer preference of low-contrast objects in breast phantom images. *Phys. Med. Biol.* **59**, 5883–5902 (2014)
81. A.S. Chawla, J.Y. Lo, J.A. Baker, E. Samei, Optimized image acquisition for breast tomosynthesis in projection and reconstruction space. *Med. Phys.* **36**, 4859–4869 (2009)
82. K. Bliznakova, A. Biznakov, V. Bravou, Z. Kolitsi, N. Pallikarakis, A three-dimensional breast software phantom for mammography simulation. *Phys. Med. Biol.* **48**, 3699–3719 (2003)
83. K. Bliznakova, S. Suryanarayanan, A. Karellas, N. Pallikarakis, Evaluation of an improved algorithm for producing realistic 3D breast software phantoms: application for mammography. *Med. Phys.* **37**, 5604–5617 (2010)
84. K. Bliznakova, I. Sechopoulos, I. Buliev, N. Pallikarakis, BreastSimulator: a software platform for breast X-ray imaging research. *J. Biomed. Graph. Comput.* **2**, 1–14 (2012)
85. P.R. Bakic, C. Zhang, A.D.A. Madiment, Development and characterisation of an anthropomorphic breast software phantom based upon region-growing algorithm. *Med. Phys.* **38**, 3165–3176 (2011)
86. P. Elangovan, D.R. Dance, K.C. Young, K. Wells, Simulation of 3D synthetic breast blocks. *Proc. SPIE* **9783**, 97832E (2016)
87. P. Elangovan, A. Mackenzie, D.R. Dance, K.C. Young, V. Cooke, L. Wilkinson, R.M. Given-Wilson, M.G. Wallis, K. Wells, Design and validation of realistic breast models for use in multiple alternative forced choice virtual clinical trials. *Phys. Med. Biol.* **62**, 2778–2794 (2017)
88. G.R. Hammerstein, D.W. Miller, D.R. White, M.E. Masterson, H.Q. Woodard, J.S. Laughlin, Absorbed radiation dose in mammography. *Radiology* **130**, 485–491 (1979)
89. ICRU, *Report 46: Photon, Electron, Proton and Neutron Interaction Data for Body Tissues. Technical Report* (International Commission on Radiation Units and Measurements, Bethesda, MD, 1992)

90. Z. Li, A. Desolneux, S. Muller, A.K. Carton, A novel 3D stochastic solid breast texture model for X-ray breast imaging. *Proc. IWDM* **9699**, 660–667 (2016)
91. C.G. Graff, A new, open-source, multi-modality digital breast phantom. *Proc. SPIE* **9783**, 9783091 (2016)
92. L.C. Ikejimba, C.G. Graff, S. Rosenthal, A. Badal, B. Ghamraoui, J.Y. Lo, S.J. Glick, A novel physical anthropomorphic breast phantom for 2D and 3D X-ray imaging. *Med. Phys.* **44**, 407–416 (2017)
93. A.W. Tucker, J. Lu, O. Zhou, Dependency of image quality on system configuration parameters in a stationary digital breast tomosynthesis system. *Med. Phys.* **40**, 031917-1–031917-10 (2013)
94. E. Shaheen, C. Van Ongeval, F. Zanca, L. Cockmartin, N. Marshall, J. Jacobs, K.C. Young, D.R. Dance, H. Bosmans, The simulation of 3D microcalcification clusters in 2D digital mammography and breast tomosynthesis. *Med. Phys.* **38**, 6659–6671 (2012)
95. L.M. Warren, A. Mackenzie, D.R. Dance, K.C. Young, Comparison of the X-ray attenuation properties of breast calcifications, aluminium, hydroxyapatite and calcium oxalate. *Phys. Med. Biol.* **58**, 104–113 (2013)
96. P. Elangovan, A. Hadjipanteli, A. Mackenzie, D.R. Dance, K.C. Young, K. Wells, OPTIMAM image simulation toolbox—recent developments and ongoing studies. *Proc. IWDM*, 668–675 (2016)
97. L. Cockmartin, N.W. Marshall, C. Van Ongeval, G. Aerts, D. Stalmans, F. Zanca, E. Shaheen, F. De Keyzer, D.R. Dance, K.C. Young, H. Bosmans, Comparison of digital breast tomosynthesis and 2D digital mammography using a hybrid performance test. *Phys. Med. Biol.* **60**, 3939–3958 (2015)
98. J. Zhou, B. Zhao, W. Zhao, A computer simulation platform for the optimization of a breast tomosynthesis system. *Med. Phys.* **34**, 1098–1109 (2007)
99. S. Young, P.R. Bakic, K.J. Myers, R.J. Jennings, S. Park, A virtual trial framework for quantifying the detectability of masses in breast tomosynthesis projection data. *Med. Phys.* **40**, 51914 (2013)
100. P. Elangovan, L.M. Warren, A. Mackenzie, A. Rashidnasab, O. Diaz, D.R. Dance, H. Bosmans, K.C. Young, K. Wells, Development and validation of a modelling framework for simulating 2D-mammography and breast tomosynthesis images. *Phys. Med. Biol.* **59**, 4275–4293 (2014)
101. R.L. Siddon, Fast calculation of the exact radiological path for a three-dimensional CT array. *Med. Phys.* **12**, 252–255 (1985)
102. B. De Man, S. Basu, Distance-driven projection and backprojection in three dimensions. *Phys. Med. Biol.* **49**, 2463–2475 (2004)
103. A. Mackenzie, N.W. Marshall, A. Hadjipanteli, D.R. Dance, H. Bosmans, K.C. Young, Characterisation of noise and sharpness of images from four digital breast tomosynthesis systems for simulation of images for virtual clinical trials. *Phys. Med. Biol.* **62**, 2376–2397 (2017)
104. J.M. Boone, T.R. Fewell, R.J. Jennings, Molybdenum, rhodium, and tungsten anode spectral models using interpolating polynomials with application to mammography. *Med. Phys.* **24**, 1863–1874 (1997)
105. D.R. Dance, C.L. Skinner, K.C. Young, J.R. Beckett, C.J. Kotre, Additional factors for the estimation of mean glandular breast dose using the UK mammography dosimetry protocol. *Phys. Med. Biol.* **45**, 3225–3240 (2000)
106. N. Marshall, J. Jacobs, L. Cockmartin, H. Bosmans, Technical evaluation of a digital breast tomosynthesis system. *Proc. IWDM* **6136**, 350–356 (2010)

107. T. Olgar, T. Kahn, D. Gosch, Quantitative image quality measurements of a digital breast tomosynthesis system. *Fortschr. Röntgenstrahlen* **185**, 1188–1194 (2013)
108. A. Mackenzie, N. Marshall, D.R. Dance, H. Bosmans, K.C. Young, Characterisation of a breast tomosynthesis unit to simulate images. *Proc. SPIE* **8668**, 86684R1–86684R8 (2013)
109. A. Rodríguez-Ruiz, M. Castillo, J. Garayoa, M. Chevalier, Evaluation of the technical performance of three different commercial digital breast tomosynthesis systems in the clinical environment. *Phys. Med.* **32**, 767–777 (2016)
110. Public Health England (PHE), National Health Service Breast Screening Programme (NHS-BSP), Breast Screening: Professional Guidance (2017). Available at <https://www.gov.uk/government/collections/breast-screening-professional-guidance>
111. A.E. Burgess, Comparison of receiver operating characteristic and forced choice observer performance measurement method. *Med. Phys.* **22**, 643–655 (1995)

# Chapter 8

## Out-of-Core Rendering of Large Volumetric Data Sets at Multiple Levels of Detail



Paulo Henrique Junqueira Amorim, Thiago Franco de Moraes,  
Jorge Vicente Lopes da Silva, and Helio Pedrini

**Abstract** Advances in equipments and techniques for image acquisition have contributed to the availability of massive high-resolution data volumes. Several fields of knowledge have benefited from these technological improvements, such as medicine, geology, biology, fluid dynamics, remote sensing and surveillance, among others. For instance, computed tomography, ultrasonography and magnetic resonance imaging are commonly employed in non-invasive medical diagnosis. More recently, X-ray microtomography imaging techniques have allowed for higher resolution images. The visualization of such large volume data sets using traditional in-core volume rendering has serious limitations, since all data may not fit in the computer's primary memory. To address such a problem, this work presents an architecture for out-of-core volume rendering at multiple levels of detail. Experiments conducted on several data volumes demonstrate the effectiveness of the proposed approach in terms of memory storage and computational time required in the rendering process, signal-to-noise ratio measured at each level of detail for the rendered volumes as well as frame rate during the user's interaction.

**Keywords** Out-of-core architecture · Volumetric visualization · Image compression · Volume rendering

---

P. H. J. Amorim · T. F. de Moraes · J. V. L. da Silva  
Division of 3D Technologies, Center for Information Technology Renato Archer,  
Campinas, SP, Brazil  
e-mail: [paulo.amorim@cti.gov.br](mailto:paulo.amorim@cti.gov.br); [thiago.moraes@cti.gov.br](mailto:thiago.moraes@cti.gov.br); [jorge.silva@cti.gov.br](mailto:jorge.silva@cti.gov.br)

H. Pedrini (✉)  
Institute of Computing, University of Campinas, Campinas, SP, Brazil  
e-mail: [helio@ic.unicamp.br](mailto:helio@ic.unicamp.br)

## 8.1 Introduction

Techniques for volumetric rendering [5, 21, 22, 33, 36, 37] have significantly contributed to the comprehension of massive and complex data. Such tools have assisted researchers in gaining insight into spatial and temporal relationships present in the data.

Several application areas have benefited from volumetric rendering, such as fluid dynamics, medicine, geology, biology and oil and gas exploration, among others. Different types of equipments are employed to acquire the data volumes, according to the application under investigation. Technological advances have allowed the acquisition of data with increasingly larger size and resolution.

Data analysis tasks can become seriously compromised or dependent on the computing system performance in traditional in-core volumetric rendering, since the main memory storage capacity may be insufficient to fit the data.

Some operating systems limit the memory accessible to each process, mainly the ones used in mobile devices [23]. For instance, certain 32-bit operating systems are able to allocate up to a maximum of 2 GBytes to each process. Furthermore, since not only the rendering task is usually executed during the data analysis process, that is, other processing may be simultaneously necessary, the main memory consumption increases due to the generation of temporary data or even duplication of the input data.

Therefore, techniques for efficiently representing massive data sets in the main memory are required, such as out-of-core approaches [45]. Out-of-core methods aim at retrieving data from disk to main memory through powerful image compression techniques and efficient data structures.

The main contribution of this work is to present and discuss an approach to out-of-core rendering of large volumetric data sets in contrast with traditional in-core volume rendering, avoiding the limitation that the entire data may not fit in the main memory.

This paper extends upon the architecture for out-of-core volume rendering developed by Amorim et al. [2], which uses a data structure based on the shell rendering method [47]. Differently from the previous work, our approach employs a 3D wavelet transform combined with the Lempel–Ziv–Markov chain algorithm (LZMA) method [38] to decrease the block sizes to represent the data volumes, which consequently reduces the amount of data traffic between disk and main memory.

The proposed method generates high-quality rendering, whose process is speeded up through graphics processing units. Experimental results obtained with several volumetric data sets, acquired from different types of equipments, are reported and discussed. A comparison between our volume rendering method and ImageVis3D [16] is provided.

The text is organized as follows. Section 8.2 presents some concepts and work related to the research topic. Section 8.3 describes the proposed architecture for out-of-core rendering. Section 8.4 presents the experimental results obtained through the

application of the proposed method to several data sets. Finally, Sect. 8.5 concludes the paper with final remarks and directions for future work.

## 8.2 Background

This section briefly describes some relevant concepts and works related to spatial data structures, volumetric rendering, multi-resolution, memory-mapping file and out-of-core rendering.

### 8.2.1 Spatial Data Structures

Spatial data structures [41] provide efficient mechanisms for storing, retrieving and displaying large amounts of data efficiently. Several types of spatial structures have been developed in the last decades to support data access in different applications.

Octrees [8, 18, 39] are often used to successively partition a three-dimensional volume into octants. The subdivision can be repeated until meeting some stopping criteria or reaching the smallest volume unity (voxel). Each node in an octree partitions the space into eight octants. A node can point to other eight nodes (octant) or be a terminal (leaf) node.

A *kd-tree* [40] is a space-partitioning data structure that organizes points in a *k*-dimensional space. The data structure is a binary tree, where each node is a *k*-dimensional point. *Kd-trees* are widely used in non-structured volumes since empty regions are common in such types of volumes.

A binary space-partitioning (BSP) [19] tree is a structure for representing successive subdivision of a space into convex sets by hyperplanes. A BSP tree is useful in rendering since it allows spatial information about the objects in a scene.

A shell [7, 47] is a structure model for volume rendering that consists of a set of voxels, where each voxel contains a set of attributes for the rendering process. The shell data structure can store the entire 3D volume or only regions on the object surface.

### 8.2.2 Memory-Mapped Files

Memory-mapped file (*mmap*) [12] uses the addressing space for a file to be mapped byte to byte in the virtual memory. The file is considered as if it were a portion of the main memory.

Instead of executing read and write operations as system calls, the virtual memory is altered and the content is automatically updated in the file. The benefit of memory-mapped file is the lazy loading, since only the necessary portions of file are mapped, resulting in low usage of main memory, even for large files.



### 8.2.3 *Levels of Detail*

Level of detail or multi-resolution techniques [9, 24, 42] aim at decreasing the complexity of a 3D object representation as it moves farther from the observer. Such reduction in the visual quality of the object or volume portion with little influence in the rendering process is often unnoticed. Therefore, level of detail techniques can avoid processing and storage of unnecessary data. On the other hand, regions or volume blocks with higher importance can be stored in full resolution.

Techniques based on blocking schemes [20] for efficiently manipulating the data volume have been proposed in the literature. Flat blocking composes volumes or planes with constant-size blocks, whereas hierarchical blocking uses variable block sizes.

### 8.2.4 *Volume Rendering*

Several techniques for interactively rendering structured volume data have been developed over the last decades. In general, they map a set of voxels with scalar values (optical properties) to a bidimensional image. A transfer function is employed to map scalar values in colour and opacity level.

Rendering techniques [15, 37, 46] are commonly classified as image-order or object-order. Image-order starts from an image or plane to shoot rays to volume, whereas object-order follows a certain method for visiting voxels that will compose the final image.

Volume ray casting [10] is an image-order technique. From each pixel of the viewer plane, a ray is shot in volume direction and intercepted voxels have colours and opacities accumulated in a final image. A variation of volume ray casting is the isosurface rendering, where the rays only consider voxel values that satisfy a threshold. Volume ray-casting and isosurface rendering techniques are highly parallelizable, such that it is possible to take advantage of multiple cores of a processor or graphics processing unit (GPU).

Shear-warp [25, 43] is an object-order method, where the volume is sliced in  $x$ ,  $y$  and  $z$  axes. According to viewer position, all slices are shifted to the voxels that are perpendicular to the pixels of the resulting image. These voxels are visited and the colour values and opacity are accumulated in the final image. In case the rendering is performed on the perspective projection, it is necessary to resize the slices.

Texture slicing [14, 48, 49] also samples the volume into slices, which are represented in texture memory from graphical hardware. To create the final image, all planes are overlapped by considering opacity and shading. Similar to the shear-warp technique, it is considered as an object-order method and the volume is sliced in  $x$ ,  $y$  and  $z$  axes. In this case, the volume can be sliced in other directions.

Other rendering techniques are found in the literature, such as splatting [50], fuzzy volume rendering [17], and those based on the Fourier transform [13, 28].

### 8.2.5 Out-of-Core Rendering

Technological advances in medical image acquisition devices have provided substantial increase in the amount of data and image resolution, which makes the data management task very challenging.

Out-of-core rendering approaches [45] are designed to process and display data volumes that are too large to fit into a computer’s main memory. Improvements in graphics processing units (GPU) [6] and availability of multicore processors have allowed more scalable and high-performance graphics architectures. Out-of-core volume rendering based on GPU [4, 34] combined with data compression techniques [1, 27] can be employed to reduce the amount of data among disk, main memory and video memory.

### 8.3 Out-of-Core Architecture

The proposed out-of-core rendering architecture, based on the volume ray-casting technique, aims at maintaining a large portion of the data out of main memory. The diagram shown in Fig. 8.1 illustrates the major components of the proposed architecture. Each stage of the architecture is detailed as follows.

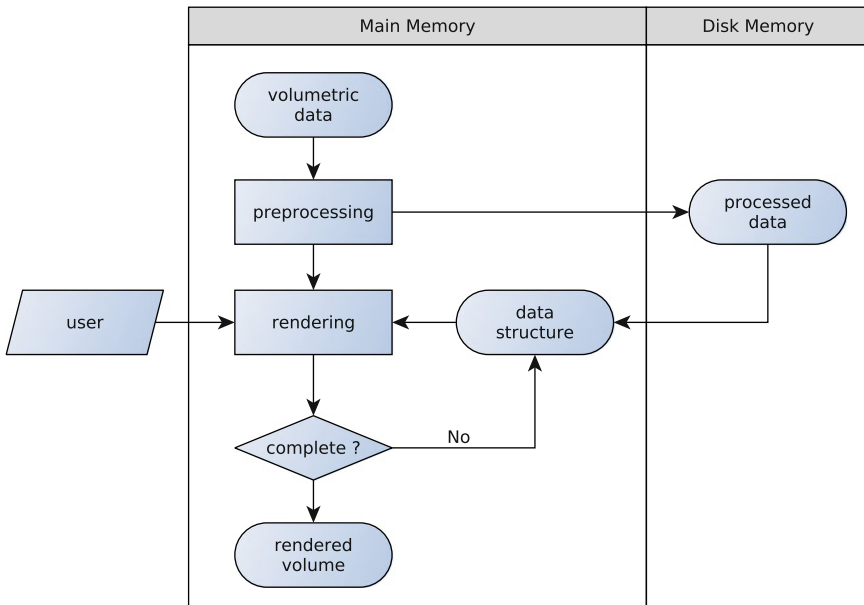


Fig. 8.1 Diagram with the main components of the proposed out-of-core rendering architecture

Data acquired from medical CT, conventional microtomography and synchrotron microtomography are tested in our experiments. However, any other type of volumetric data containing scalar values can be processed by the proposed architecture.

The volume is initially preprocessed in order to represent it in the data structure and resample it if necessary. After user's interaction with the model at a low resolution, blocks are employed in the data structure to perform the rendering at the original resolution. These blocks are demanded in limited amount in order to not overload the main memory.

As the images cannot be loaded entirely in main memory, they are read in portions. Initially, these portions are stored on disks in the form of blocks. The blocks are constructed from a limited number of slices loaded into main memory at a time.

To reduce the amount of data that is transferred between the hard disk and main memory, we apply a wavelet transform to the blocks, extended to three dimensions. The Haar wavelet transform is employed since it presents proper peak signal-to-noise ratio (PSNR) [44], preserving a reconstruction with high degree of fidelity in the decompression stage.

We perform a decomposition level and then the image resulting from the wavelet transform is compressed using the Lempel–Ziv–Markov chain algorithm (LZMA) method [38]. The LZMA is a lossless data compression algorithm that uses a dictionary to produce a stream of symbols encoded through an adaptive binary range encoder.

The preprocessed and stored blocks are mapped into an auxiliary matrix structure in main memory. According to the idea of the shell rendering technique, each position of the array records if the block is mapped or not, the path of the file in the hard disk and the pointer to the mapping when the block is mapped (otherwise, the value is null). The data structure is created from this matrix of preprocessed data.

We use the memory-mapped files (*mmap*) technique to perform the mapping to the main memory of the files present on disk. Some operating systems can map a maximum of 3 GB of data. However, it is known that, in some cases, the total number of blocks can exceed this threshold. To overcome such limitation, we keep a smaller amount of mapped regions. The remaining unmapped portion are indicated (as false) by the state variable. When it is necessary to use blocks that are not mapped, existing mappings are removed and then new blocks are mapped, changing the state variable to true.

The matrix obtained from the preprocessing step is the input to the data structure construction. The blocks are readequated at the time of data structure creation, once blocks can be merged or split due to the subdivision process.

To overcome the overload that may be caused by the transfer of blocks between main memory and hard disk, a volume with low resolution is kept in main memory to be rendered when the user performs operations such as rotation, translation and scaling. After user's interaction, the volume is progressively rendered to its full resolution. If the observer is close to the object, the volume can be rendered at full resolution, whereas if it is far away, lower-resolution blocks can be chosen.

Several rendering techniques were evaluated during the development of our work: volume ray casting [26], shear-warp [25] and texture slicing [48]. The texture slicing, which is based on slices where the observer's view point is not totally perpendicular to the volume, may cause the aliasing effect. In the shear-warp technique, the slices must be displaced so that they are perpendicular to the observer's view point. This may cause additional processing and increase the system overhead. On the other hand, volume ray casting uses rays that are traced from the observer's view point to determine which voxels will be traversed in the data structure. Unlike the previous methods, this technique is not based on slices and may generate high-quality images. Due to these factors, volume ray casting was chosen to compose our methodology.

The rays launched to render the high-resolution model start from the pixels of the bounding box in order to explore the GPU parallelism and prevent the GPU memory from being overloaded. For this reason, the bounding box from the previous step is divided to generate multiple cells. According to our tests, the ideal size of each screen portion is  $16^2$ . These portions are inserted into a queue according to the order of division, which is performed from left to right and from top to bottom.

From each cell, rays are cast to perform the composition step of the volume ray casting. By intercepting each voxel, a test is conducted to determine if its respective block needs to be loaded into the main memory or GPU texture memory. To accelerate this process, we use a dictionary data structure based on hash [11]. This dictionary stores an identifier and block coordinates as key values for the respective block voxel. The identifier is set to 0 if the block is loaded into main memory; if it is loaded into GPU memory, the identifier is set to 1.

A matrix is used to accumulate the partial results obtained by the traversal of rays in the blocks loaded into GPU memory. After a cell is fully rendered, the blocks that are no longer used are unloaded from memory and new blocks are loaded from the hard disk into main memory and then to the GPU memory. This cycle is repeated until the image is fully rendered.

A level-of-detail technique is applied by using two possible strategies. The first uses a threshold distance between the observer and the object. If the value indicates that the observer is close to the object, the complete resolution of the volume is employed, otherwise rendering blocks with lower resolutions is performed through the flat blocking technique. The second scheme takes into consideration the distance from each individual block in relation to the observer, such that the last blocks to be visited by the volume ray casting would be composed of blocks with reduced resolution through the hierarchical blocking technique.

## 8.4 Experimental Results

The experiments were performed on a notebook with Intel Core i5 processor, 6 GB of main memory, hard drive of 500 GB with 5400 rpm, NVidia GeForce GT 520M with 1 GB of VRAM and support for CUDA version 2. The operating system used

**Table 8.1** Characteristics of the data used in the tests

Data set	Imaging modality	Size (voxels)	Depth (bits)	Size
Manix [35]	CT	$512 \times 512 \times 460$	16	240 MB
Melanix [35]	CT	$512 \times 512 \times 1023$	16	630 MB
Material A [29]	$\mu$ CT	$1000 \times 1000 \times 2810$	8	2.8 GB
Material B [30]	$\mu$ CT	$2000 \times 2000 \times 1266$	8	5.1 GB
Bone A [31]	Synchrotron $\mu$ CT	$2048 \times 2048 \times 1420$	8	6.0 GB
Bone B [32]	Synchrotron $\mu$ CT	$2048 \times 2048 \times 1420$	32	23 GB

was Linux Ubuntu 10.13 64-bit version. The algorithms were implemented in C++ programming language and OpenGL package to execute the volume ray-casting technique with the graphical representation of the volumetric data.

We conducted tests on several data sets of varying sizes. Table 8.1 summarizes some characteristics of the data used in our tests. Manix and Melanix files are available in the OsiriX database [35]. Material A [29] and Material B [30] files are available in the Invesalius database [3]. Bone A [31] and Bone B [32] files are available in the MIDAS database. The main focus of our experiments was limited to the preprocessing stage, which is the portion of the proposed architecture that consumes more main memory.

It is possible to observe from Fig. 8.2 that Manix and Melanix data sets with size of 240 MB and 630 MB, respectively, consumed small portions of main memory blocks for all sizes. Thus, it would be possible to preprocess them to perform rendering on mobile devices, which often have limited main memory.

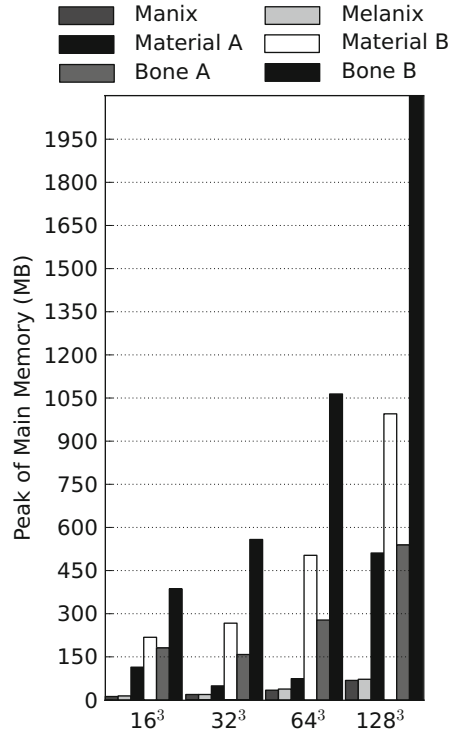
Some works available in the literature apply out-of-core volume rendering methods based on texture slicing or volume ray casting. Figure 8.3 shows a comparison between the two different techniques for the Manix data set. The implementation was carried out through the same tools and same settings for the transfer function; however, the rendering was done in-core since the goal here was to check the quality of the results before considering the out-of-core rendering.

The volume ray-casting technique demonstrated to be superior when compared to texture slicing. From Fig. 8.3a, b, it is possible to observe the aliasing effect on the volumes rendered by the texture slicing technique, whereas such effect does not occur on the volumes rendered by the volume ray casting (Fig. 8.3c, d).

Several tests are conducted on data sets with 5.1, 6.0 and 23 GB. We can conclude that the best size of the blocks in these cases is between  $16^3$  and  $32^3$  voxels, since it is possible to load, preprocess and render them on a personal computer.

Figure 8.4 illustrates the computational time spent during the preprocessing stage with different block sizes for each data set. The computational time required in the preprocessing step for each data set is inversely proportional to the image sizes and block sizes to be generated. Blocks with small sizes produce larger amount of blocks, demanding more accesses to the hard disk. From Fig. 8.4, it is possible to notice that blocks with size  $64^3$  and  $128^3$  require less time than others with larger sizes.

**Fig. 8.2** Tests performed on six data sets, whose blocks have  $16^3$ ,  $32^3$ ,  $64^3$  and  $128^3$  voxels



We measure the maximum amount (peak) of main memory during the preprocessing and interaction stages for different block sizes, whose results are shown in Figs. 8.5 and 8.6, respectively.

The consumption of main memory during the preprocessing and interaction stages is proportional to the block sizes, as shown in Fig. 8.5. This is due to the fact that the original data are stored in several slices. To generate the blocks, we first need to stack all the slices in order to cover the height of the block to be generated, that is, 16 slices will be stacked at a time for a block with size  $16^3$ .

The resolution of each image affects the amount of used memory. Larger resolutions demand more amounts of memory, as shown in Fig. 8.5a–f. Each image of Manix data set (Fig. 8.5a) has  $512 \times 512$  pixels with depth of 16 bits and required 12 MB of memory with blocks with size of  $16^3$ . On the other hand, for the Bone B data set (Fig. 8.5f), each image has resolution of  $2048 \times 2048$  with 32 bits of depth and required a total of 390 MB. A possible alternative is to perform a read operation only in the necessary portions of each image; however, this would take more processing time.

The consumption of main memory was assessed during all the rendering execution. Plots for different block sizes are presented in Fig. 8.6. Similarly to the preprocessing step, the block sizes also affect the consumption of memory during

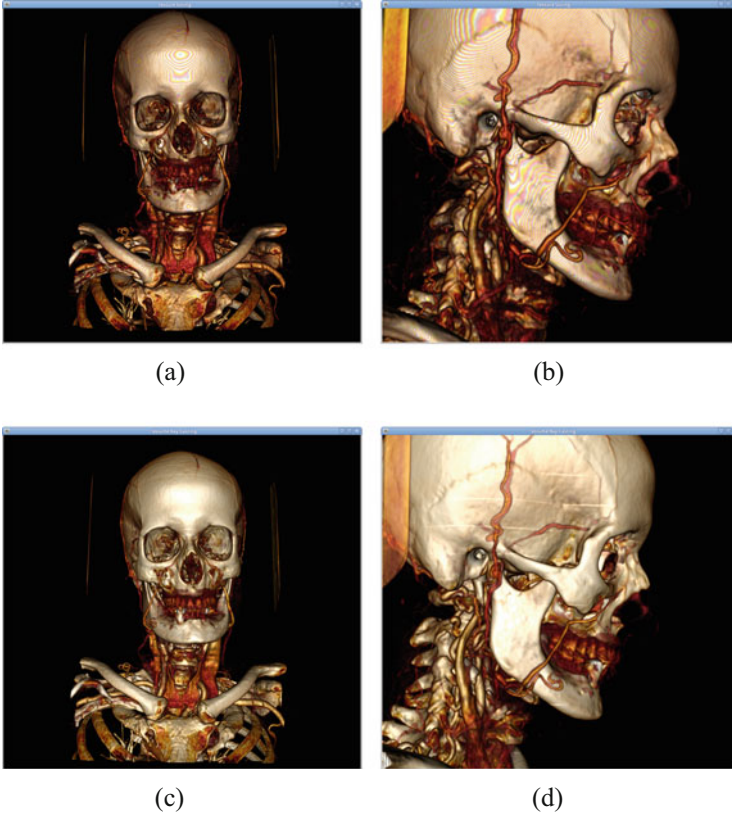
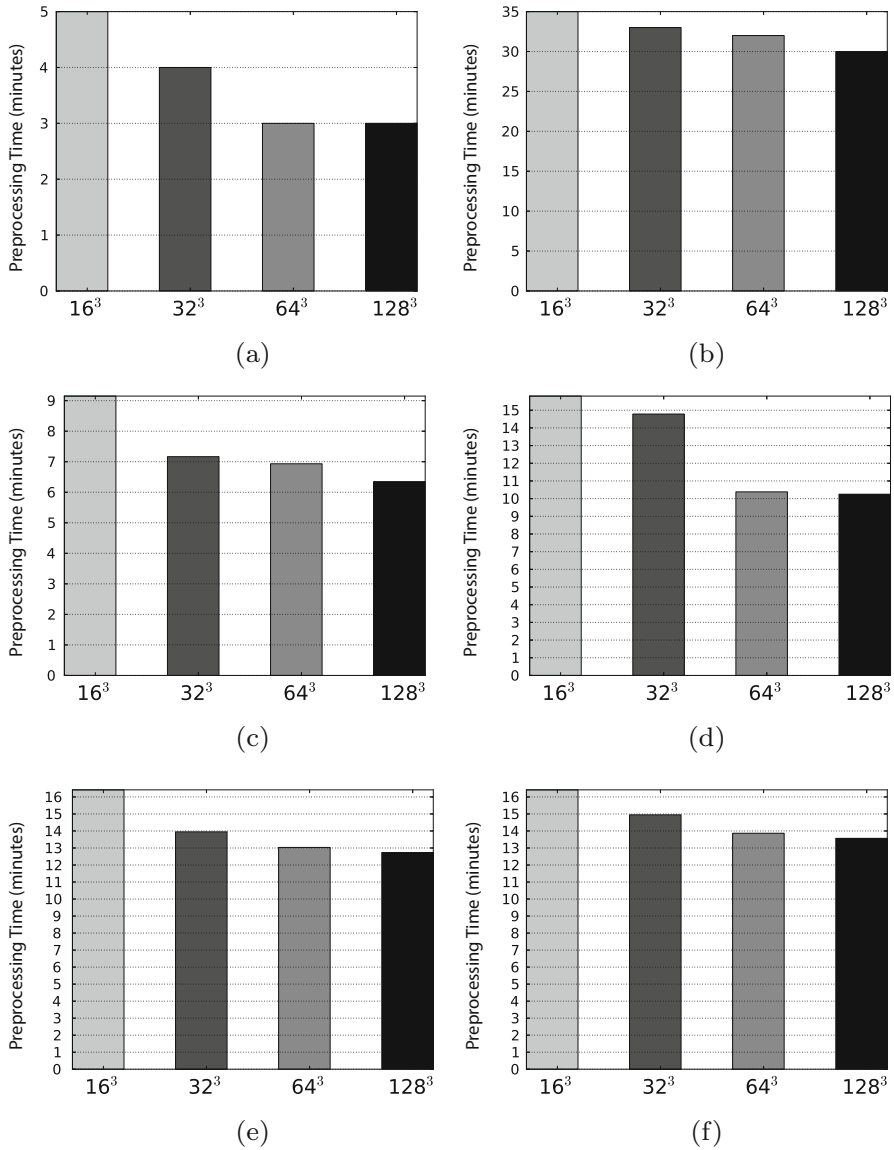


**Fig. 8.3** Comparison for Manix data set rendered through texture slicing and volume ray casting. (a, b) Texture slicing. (c, d) Volume ray casting

the rendering step, according to Fig. 8.6. Models rendered with block size of  $16^3$  required less amount of memory when compared to models rendered with larger size of blocks.

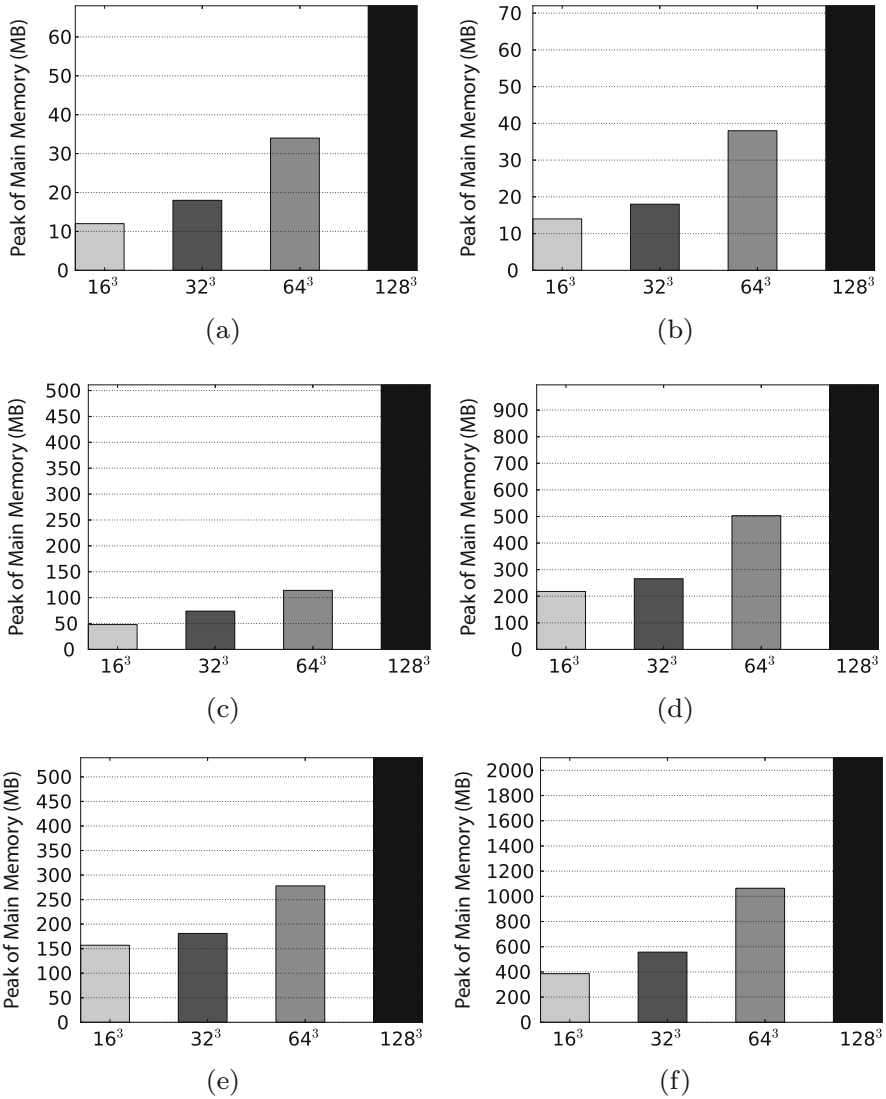
Table 8.2 shows a comparison of the compression results for each data set using wavelet transform in conjunction with LZMA compression method for different block sizes ( $16^3$ ,  $32^3$ ,  $64^3$  and  $128^3$ ). The use of certain block sizes does not reduce the amount of memory required for some data sets. This fact is due to the heterogeneous contents of the data as well as the presence of high-frequency components in the data sets.

Figure 8.7 shows rendering results for different levels of detail, taking the observer's distance into consideration, as described in the methodology section. On the other hand, Figs. 8.8, 8.9, 8.10, 8.11 and 8.12 illustrate the rendering results for 10 levels of details for the respective data sets. To make the comparison



**Fig. 8.4** Time required in the preprocessing step. (a) Manix. (b) Melanix. (c) Material A. (d) Material B. (e) Bone A. (f) Bone B





**Fig. 8.5** Peaks of main memory in the preprocessing step. (a) Manix. (b) Melanix. (c) Material A. (d) Material B. (e) Bone A. (f) Bone B

easier, different scaling factors were applied to the volume while maintaining the same distance from the observer. From these figures, visual differences become imperceptible after level of detail 5. They are only noticed when approximating the volume, as shown in Fig. 8.13.

The calculation of the peak signal-to-noise ratio (PSNR) value is performed at each level of detail for the rendered volumes, whose purpose is to determine if the

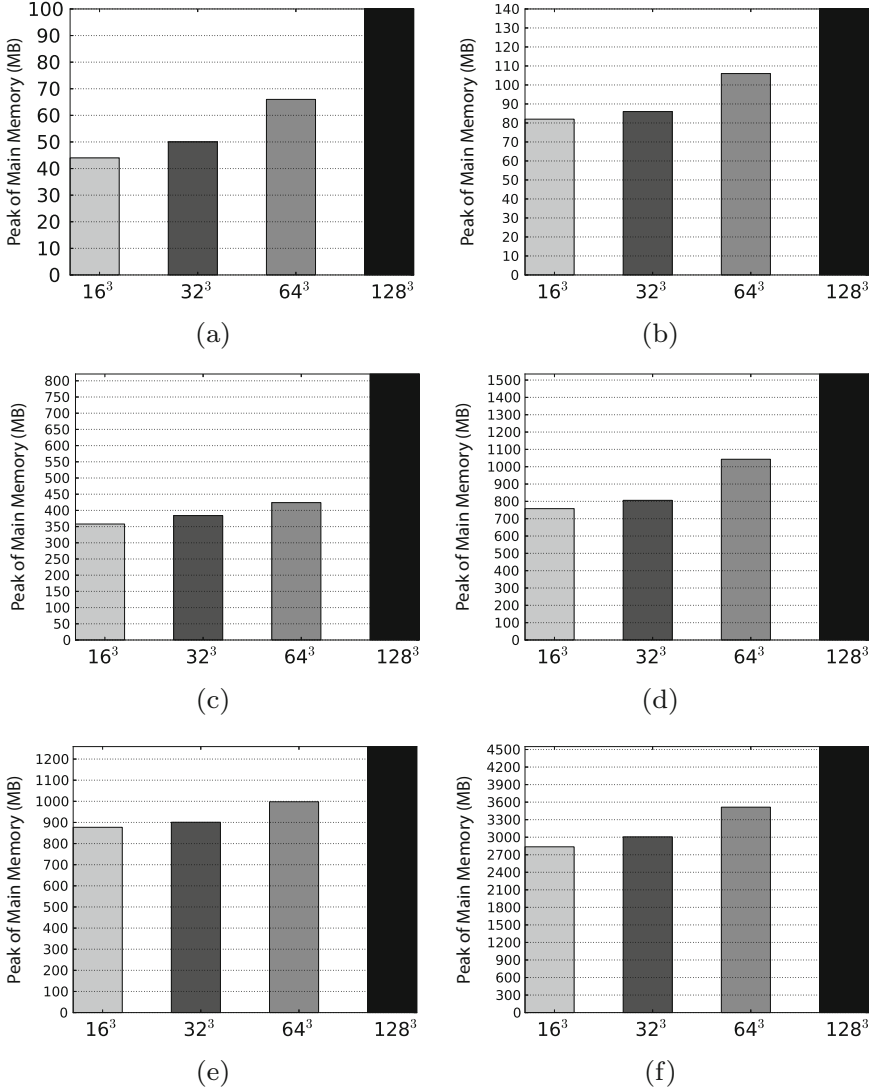


**Fig. 8.6** Peaks of main memory during user interaction. (a) Manix. (b) Melanix. (c) Material A. (d) Material B. (e) Bone A. (f) Bone B

levels of detail for each 10% would be sufficient to represent the models under intermediate resolutions. The PSNR is calculated according to Eq. (8.1) expressed as:

$$\text{PSNR} = 10 \log_{10} \left( \frac{L^2}{\text{MSE}} \right) \quad (8.1)$$

**Table 8.2** Comparison of data compression through wavelet transform with different block sizes

Name	Block size	Non-compressed block size (KB)	Compressed block size (KB)
Manix	$16^3$	8.01	6.67
	$32^3$	61.56	38.66
	$64^3$	460.07	256.56
	$128^3$	3680.07	1978.66
Melanix	$16^3$	7.98	7.26
	$32^3$	63.33	48.52
	$64^3$	506.14	339.59
	$128^3$	3846.47	2372.88
Material A	$16^3$	4.01	3.40
	$32^3$	30.92	24.21
	$64^3$	245.69	160.77
	$128^3$	1948.05	1160.10
Material B	$16^3$	4.03	3.77
	$32^3$	31.61	29.31
	$64^3$	250.50	217.37
	$128^3$	1976.67	1656.65
Bone A	$16^3$	4.03	3.24
	$32^3$	31.63	25.65
	$64^3$	247.03	188.69
	$128^3$	1893.41	1419.35
Bone B	$16^3$	16.03	12.34
	$32^3$	126.29	111.45
	$64^3$	987.90	892.27
	$128^3$	7573.41	7243.44

where  $L$  is the depth of pixels and MSE (mean square error) given by:

$$\text{MSE} = \sum_{band=1}^{band \leq 3} \left( \frac{1}{MN} \sum_{x=0}^{M-1} \sum_{y=0}^{N-1} [I_1(x, y) - I_2(x, y)]^2 \right) / 3 \quad (8.2)$$

where  $I_1$  and  $I_2$  are input images,  $M$  and  $N$  are the image sizes, and *band* represents each one of the three colour channels.

Plots shown in Fig. 8.14 present the PSNR value for each data set rendered through multiple levels of detail. The goal of this experiment is to verify if the resolution reduction compromises rendering quality. For such purpose, PSNR values larger than 20 dB are considered acceptable. Excepted for the plots shown in Fig. 8.14e, f, all first levels of detail (smaller resolutions) are above 20 dB.

Table 8.3 shows the results of frames per second (FPS) rate during the interaction with the volumes at low resolution. The smaller rate (45 FPS) is obtained when the user interacts with the low-resolution Bone B model, which occupied 2.3 GB of main memory, that is, 10% of its original size. Even though this is the smaller rate

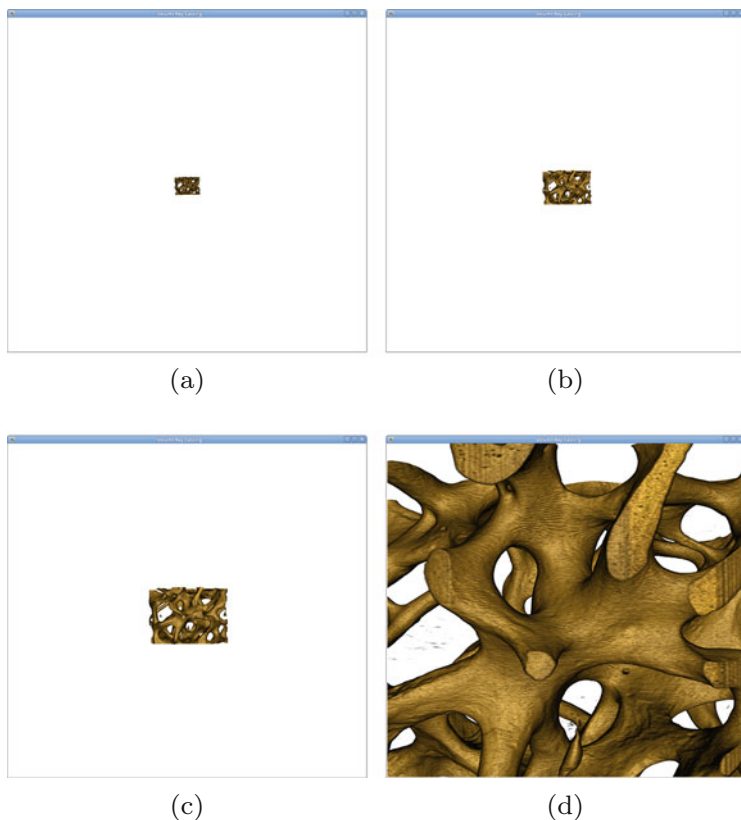


**Fig. 8.7** Comparison among different levels of detail. (a) Level 3. (b) Level 6. (c) Level 8. (d) Level 9

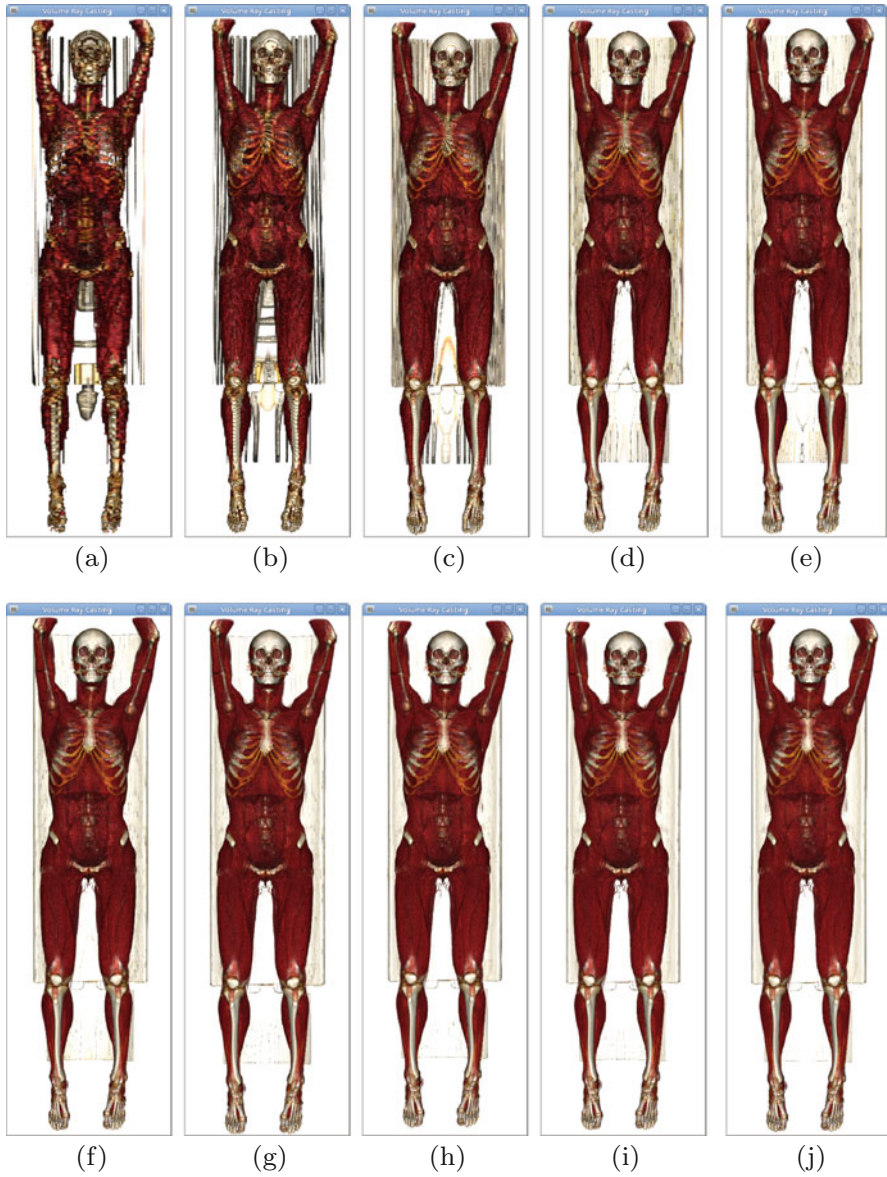
obtained in our experiments, it is above the minimum acceptable for interaction time.

Table 8.4 shows a comparison between our method and ImageVis3D [16] for the peaks of main memory using block size of  $128^3$ .

## 8.5 Conclusions and Future Work

An architecture for out-of-core volume rendering is presented and discussed in this work, which integrates different modules, such as multi-resolution and memory-mapping techniques.

The proposed method is capable of dealing with large volumes using small amount of main memory. Several volumetric data sets, acquired from different types of equipments, were used in our tests.



**Fig. 8.8** Comparison among different levels of detail for the Melanix data set. (a) Level 0. (b) Level 1. (c) Level 2. (d) Level 3. (e) Level 4. (f) Level 5. (g) Level 6. (h) Level 7. (i) Level 8. (j) Level 9

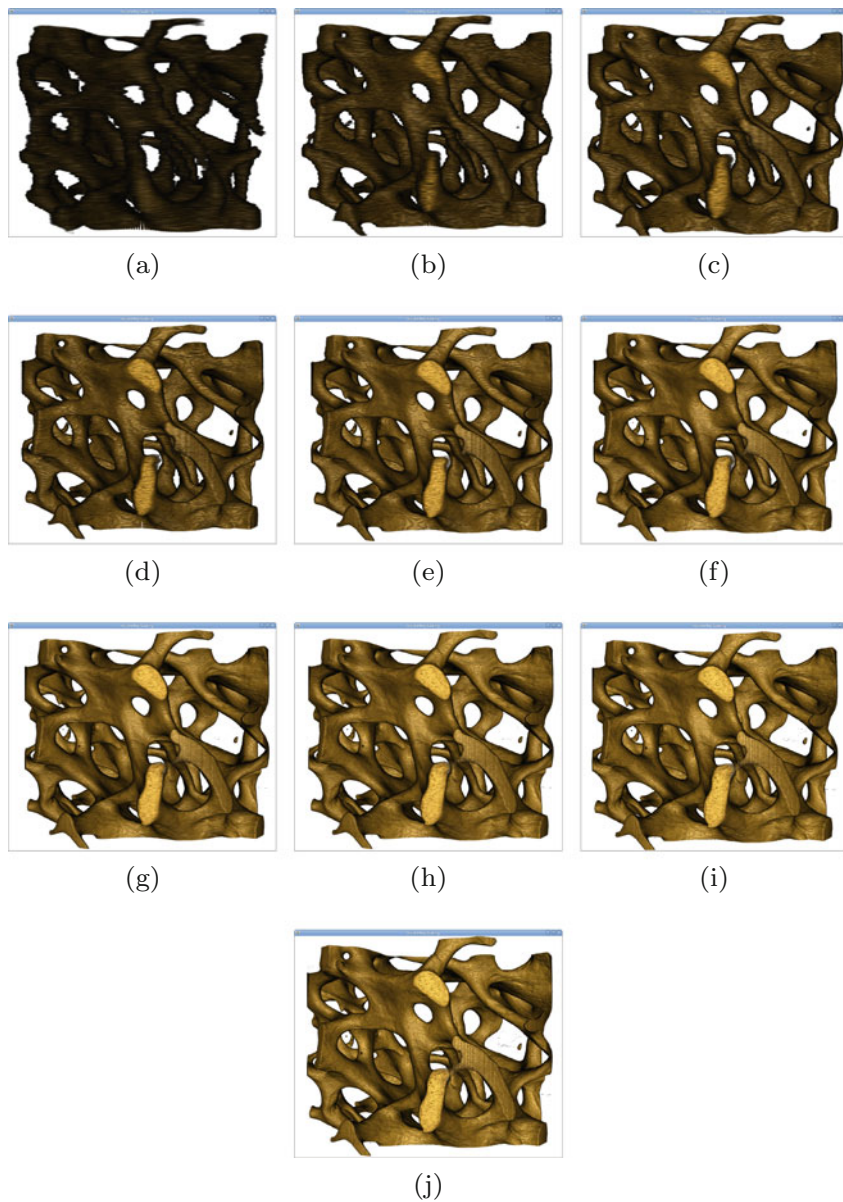


**Fig. 8.9** Comparison among different levels of detail for the Bone B data set. (a) Level 0. (b) Level 1. (c) Level 2. (d) Level 3. (e) Level 4. (f) Level 5. (g) Level 6. (h) Level 7. (i) Level 8. (j) Level 9

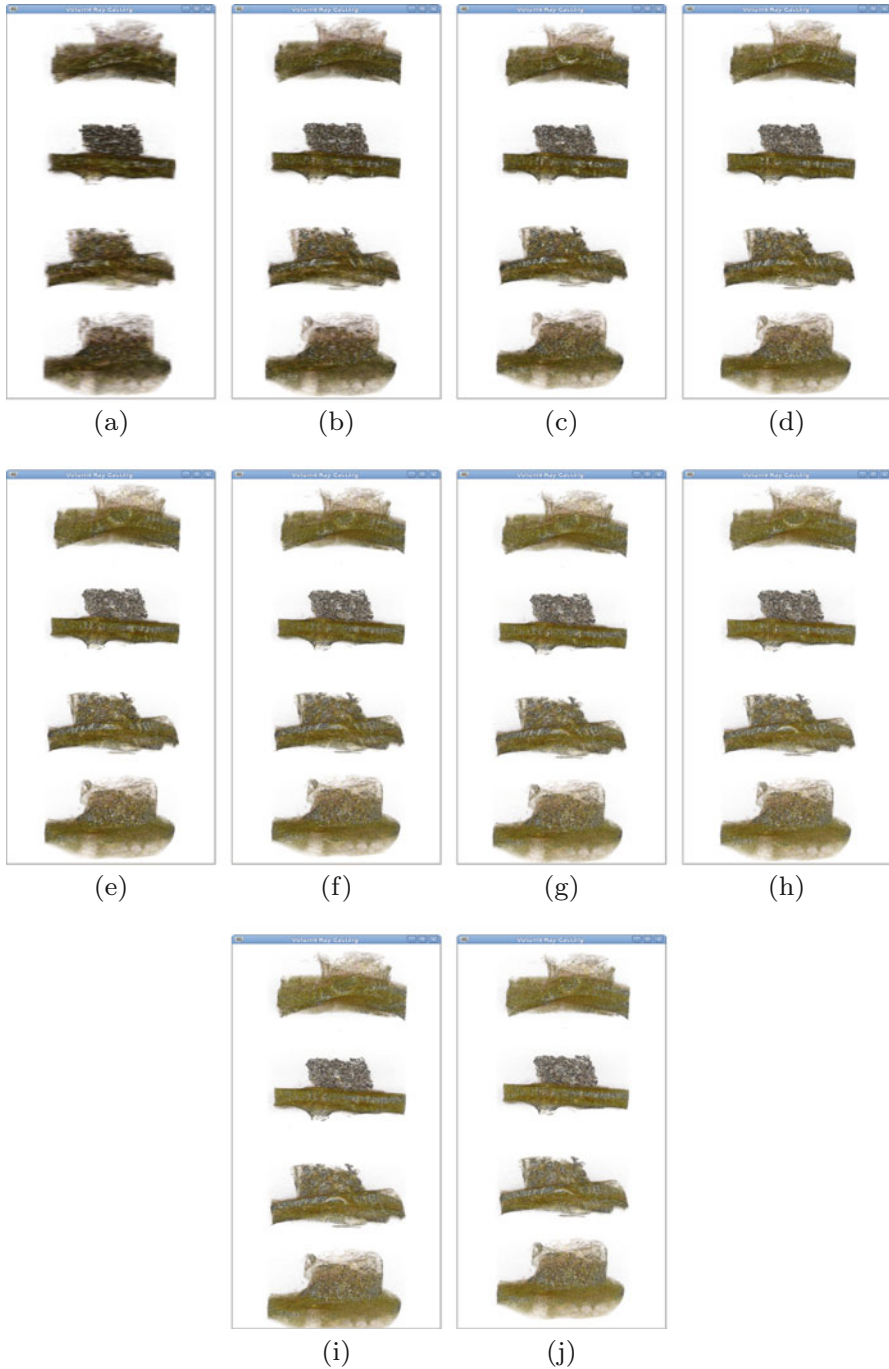


**Fig. 8.10** Comparison among different levels of detail for the Material A data set. **(a)** Level 0. **(b)** Level 1. **(c)** Level 2. **(d)** Level 3. **(e)** Level 4. **(f)** Level 5. **(g)** Level 6. **(h)** Level 7. **(i)** Level 8. **(j)** Level 9



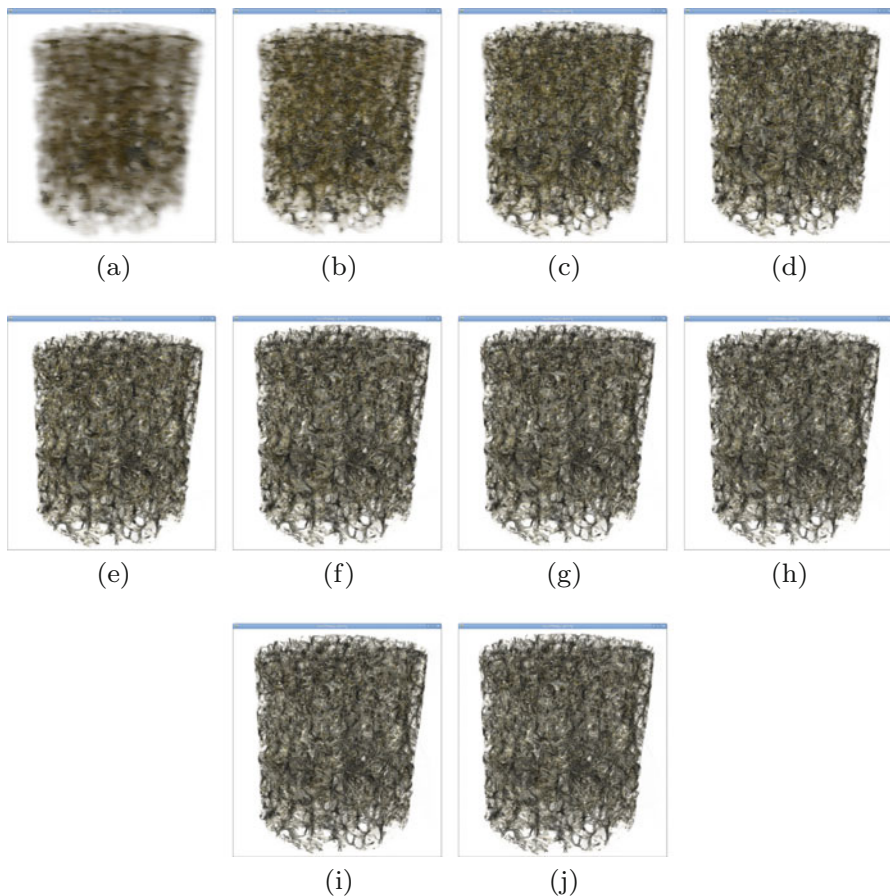


**Fig. 8.11** Comparison among different levels of detail for the Material B data set. (a) Level 0. (b) Level 1. (c) Level 2. (d) Level 3. (e) Level 4. (f) Level 5. (g) Level 6. (h) Level 7. (i) Level 8. (j) Level 9

As directions for future work, the blocks already loaded in main memory could be processed in parallel while searching for the next block to be read into the data structure. We also intend to investigate other data compression methods for exploring volumetric data redundancies.

**Acknowledgements** The authors are grateful to São Paulo Research Foundation (grants FAPESP #2011/22749-8 and #2013/07559-3) and National Council for Scientific and Technological Development (grant CNPq #307113/2012-4) for their financial support to this research. They are also thankful to Cristiane Ibanhes Polo, from the Department of Oral and Maxillofacial Surgery and Traumatology, Faculty of Dentistry, University of São Paulo, Brazil, for providing Materials A and B.



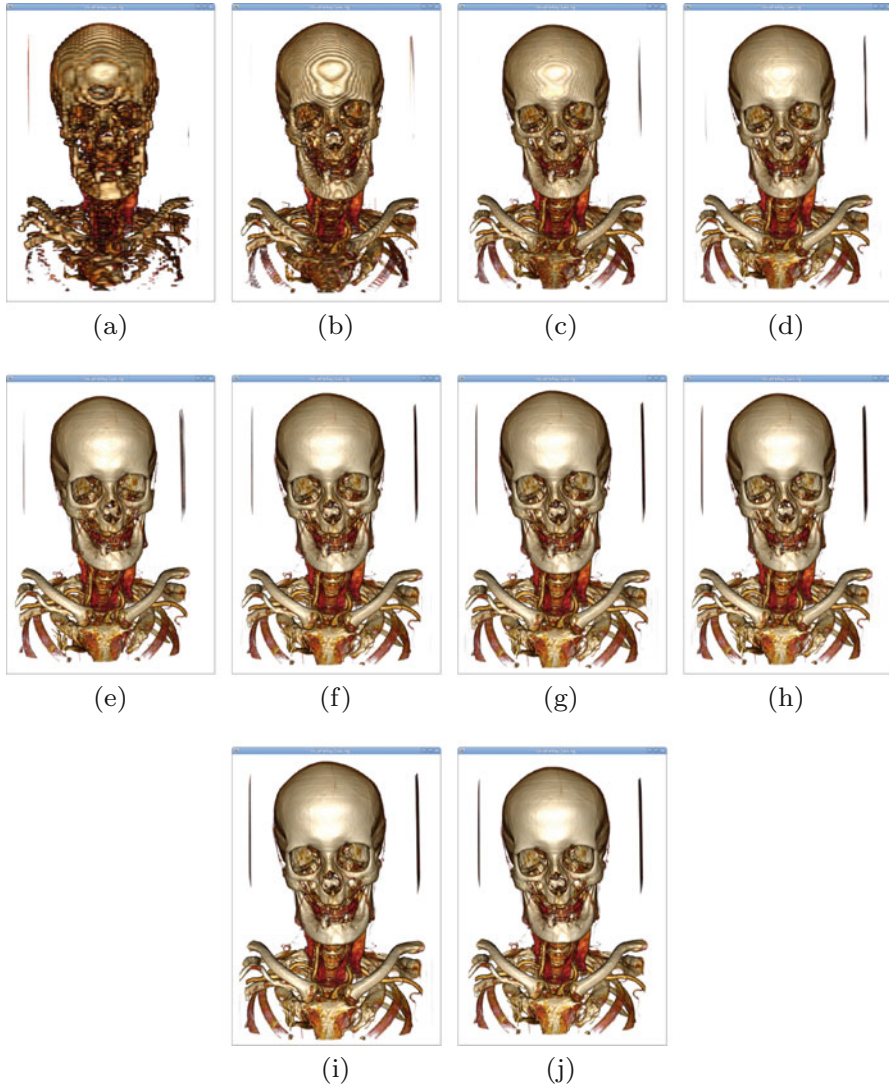


**Fig. 8.12** Comparison among different levels of detail for the Manix data set. **(a)** Level 0. **(b)** Level 1. **(c)** Level 2. **(d)** Level 3. **(e)** Level 4. **(f)** Level 5. **(g)** Level 6. **(h)** Level 7. **(i)** Level 8. **(j)** Level 9

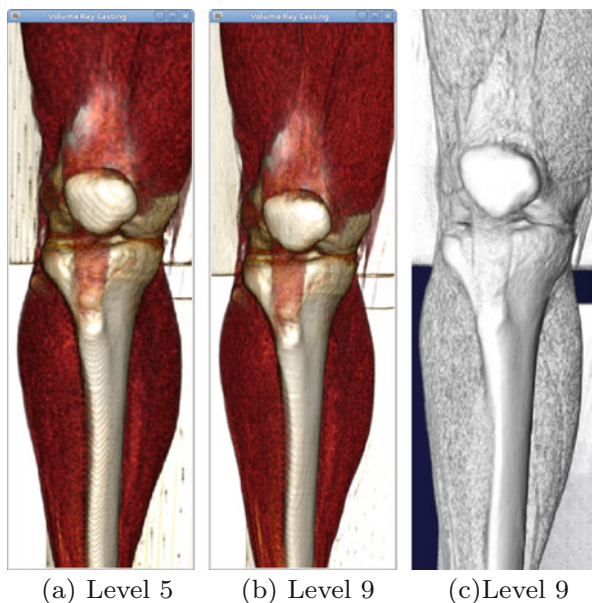


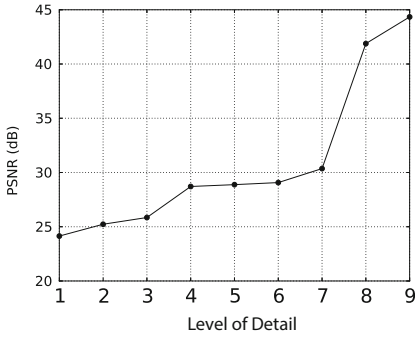
**Fig. 8.13** Comparison of knee region at two levels of detail for the Melanix data set. (a)–(b) proposed method; (c) ImageVis3D [16]

**Table 8.3** Frames per second (FPS) rate during the model interaction

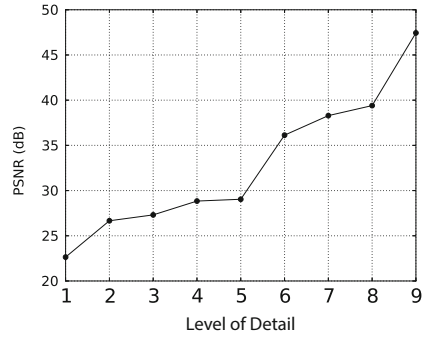
Volume	Frames per second (FPS)
Manix	72
Melanix	68
Material A	65
Material B	59
Bone A	55
Bone B	45

**Table 8.4** Peaks of main memory for block size of  $128^3$  obtained with the proposed method and ImageVis3D [16]

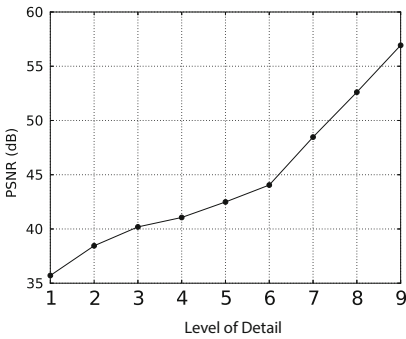
Volume	Proposed	ImageVis3D [16]
Manix	68 MB	185 MB
Melanix	72 MB	188 MB
Material A	511 MB	3300 MB
Material B	995 MB	4100 MB
Bone A	539 MB	4010 MB
Bone B	2100 MB	4190 MB



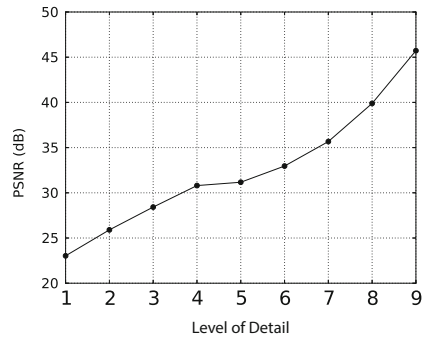
(a)



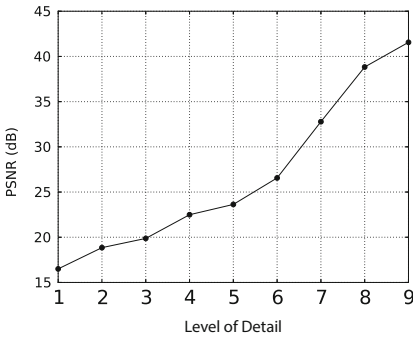
(b)



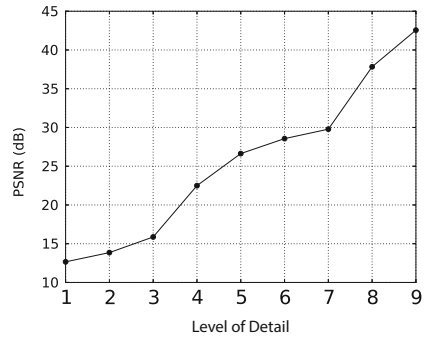
(c)



(d)



(e)



(f)

**Fig. 8.14** Comparison of PSNR for original resolution and intermediate levels of detail. (a) Manix. (b) Melanix. (c) Material A. (d) Material B. (e) Bone A. (f) Bone B

## References

1. A. Agrawal, J. Kohout, G.J. Clapworthy, N.J. Mcfarlane, F. Dong, M. Viceconti, F. Taddei, D. Testi, Enabling the interactive display of large medical volume datasets by multiresolution bricking. *J. Supercomput.* **51**(1), 3–19 (2010)
2. P. Amorim, T. Moraes, J. Silva, H. Pedrini, An out-of-core volume rendering architecture, in *IVECOMAS Thematic Conference on Computational Vision and Medical Image Processing*, Funchal (CRC Press, Boca Raton, 2013), pp. 173–179
3. P. Amorim, T. Moraes, J. Silva, H. Pedrini, InVesalius: an interactive rendering framework for health care support, in *International Symposium on Visual Computing*, Las Vegas (Springer, Berlin, 2015), pp. 45–54
4. J. Baert, A. Lagae, P. Dutré, Out-of-core construction of sparse voxel octrees. *Comput. Graphics Forum* **33**(6), 220–227 (2014)
5. M. Balsa Rodríguez, E. Gobbetti, J.A. Iglesias Guitián, M. Makhinya, F. Marton, R. Pajarola, S.K. Suter, State-of-the-art in compressed GPU-based direct volume rendering. *Comput. Graphics Forum* **33**(6), 77–100 (2014)
6. J. Beyer, M. Hadwiger, H. Pfister, State-of-the-art in GPU-based large-scale volume visualization. *Comput. Graphics Forum* **34**(8), 13–37 (2015)
7. G. Carnielli, A. Falcão, J. Udupa, Fast digital perspective shell rendering, in *XII Brazilian Symposium on Computer Graphics and Image Processing*, Campinas (1999), pp. 105–111
8. H.H. Chen, T.S. Huang, A survey of construction and manipulation of octrees. *Comput. Vis. Graphics Image Process.* **43**(3), 409–431 (1988)
9. Y. Cheng, L. Jiang, X. Ma, J. Xue, Z. Zheng, Multi-resolution texture rendering for medical data, in *Digital Media and Digital Content Management*, Hangzhou (2011), pp. 166–171
10. J.J. Choi, B.-S. Shin, Y.G. Shin, K. Cleary, Efficient volumetric ray casting for isosurface rendering. *Comput. Graphics* **24**(5), 661–670 (2000)
11. T.H. Cormen, C.E. Leiserson, R.L. Rivest, C. Stein, *Introduction to Algorithms* (MIT Press, Cambridge, 2009)
12. D. Dhamdhere, *Operating Systems* (McGraw-Hill Higher Education, New York, 2006)
13. S. Dunne, S. Napel, B. Rutt, Fast reprojection of volume data, in *Proceedings of the First Conference on Visualization in Biomedical Computing*, Atlanta (IEEE, Los Alamitos, 1990), pp. 11–18
14. D. Ellsworth, L.-J. Chiang, H.-W. Shen, Accelerating time-varying hardware volume rendering using TSP trees and color-based error metrics, in *Proceedings of the 2000 IEEE Symposium on Volume Visualization*, Salt Lake City (ACM, New York, 2000), pp. 119–128
15. T. Ertl, *Computer Graphics: Principles and Practice* (Springer, Berlin, 1996)
16. T. Fogal, A. Schiewe, J. Krüger, An analysis of scalable GPU-based Ray-guided volume rendering, in *IEEE Symposium on Large-Scale Data Analysis and Visualization*, vol. 2013 (2013), p. 43. NIH Public Access
17. N. Fout, K.-L. Ma, Fuzzy volume rendering. *IEEE Trans. Vis. Comput. Graph.* **18**(12), 2335–2344 (2012)
18. S.F. Frisken, R.N. Perry, Simple and efficient traversal methods for quadtrees and octrees. *J. Graphics Tools* **7**, 2002 (2002)
19. H. Fuchs, Z. M. Kedem, B.F. Naylor, On visible surface generation by a priori tree structures. *SIGGRAPH Comput. Graphics* **14**(3), 124–133 (1980)
20. M. Hadwiger, P. Ljung, C.R. Salama, T. Ropinski, Advanced illumination techniques for GPU volume raycasting, in *ACM SIGGRAPH Asia Courses* (ACM, New York, 2008)

21. M. Hadwiger, J. Beyer, W.-K. Jeong, H. Pfister, Interactive volume exploration of petascale microscopy data streams using a visualization-driven virtual memory approach. *IEEE Trans. Vis. Comput. Graph.* **18**(12), 2285–2294 (2012)
22. K.H. Höhne, H. Fuchs, S.M. Pizer, *3D Imaging in Medicine: Algorithms, Systems, Applications*, vol. 60 (Springer Science & Business Media, New York, 2012)
23. T. Huang, G. Fox, Collaborative annotation of real time streams on android-enabled devices, in *International Conference on Collaboration Technologies and Systems*, Denver (2012), pp. 39–44
24. E.C. La Mar, B. Hamann, K.I. Joy, Multiresolution techniques for interactive texture-based volume visualization, in *Conference on Visualization: Celebrating Ten Years*, San Francisco (1999), pp. 355–361
25. P. Lacroute, M. Levoy, Fast volume rendering using a shear-warp factorization of the viewing transformation, in *21st Annual Conference on Computer Graphics and Interactive Techniques*, Orlando (ACM, New York, 1994), pp. 451–458
26. M. Levoy, Efficient ray tracing of volume data. *ACM Trans. Graphics* **9**(3), 245–261 (1990)
27. F. Lundell, Out-of-core multi-resolution volume rendering of large data sets. Master's thesis, Linköpings Universitet, 2011
28. T. Malzbender, Fourier volume rendering. *ACM Trans. Graphics* **12**(3), 233–250 (1993)
29. Material A, Software Invesalium (2017), [ftp://ftp.cti.gov.br/pub/dt3d/invesalium/files/pub/data\\_set/npymaterialA.7z](ftp://ftp.cti.gov.br/pub/dt3d/invesalium/files/pub/data_set/npymaterialA.7z)
30. Material B, Software Invesalium (2017), [ftp://ftp.cti.gov.br/pub/dt3d/invesalium/files/pub/data\\_set/npymaterialB.7z](ftp://ftp.cti.gov.br/pub/dt3d/invesalium/files/pub/data_set/npymaterialB.7z)
31. MIDAS, 3D Micro-CT Dataset (2017), <http://www.insight-journal.org/midas/bitstream/view/14533>
32. MIDAS, 3D Micro-CT Dataset (2017), <http://www.insight-journal.org/midas/bitstream/view/14534>
33. T.F. Moraes, P.H. Amorim, J.V. da Silva, H. Pedrini, M.I. Meurer, Medical volume rendering based on gradient information, in *5th Eccomas Thematic Conference on Computational Vision and Medical Image Processing*, Tenerife (CRC Press, Boca Raton, 2015), pp. 181–186
34. D. Nagayasu, F. Ino, K. Hagihara, A decompression pipeline for accelerating out-of-core volume rendering of time-varying data. *Comput. Graphics* **32**(3), 350–362 (2008)
35. OsiriX, DICOM Image Library (2017), <http://www.osirix-viewer.com/resources/dicom-image-library/>
36. F.H. Post, G. Nielson, G.-P. Bonneau, *Data Visualization: The State of The Art*, vol. 713 (Springer Science & Business Media, New York, 2012)
37. D.F. Rogers, R. Earnshaw, *State of the Art in Computer Graphics: Aspects of Visualization*, 1st edn. (Springer Publishing Company, Incorporated, New York, 2014)
38. D. Salomon, *Data Compression: The Complete Reference*, 4th edn. (Springer, London, 2006)
39. H. Samet, Implementing ray tracing with octrees and neighbor finding. *Comput. Graphics* **13**, 445–460 (1989)
40. H. Samet, *The Design and Analysis of Spatial Data Structures*, vol. 85 (Addison-Wesley Longman Publishing Co., Inc., Boston, 1990)
41. H. Samet, *Foundations of Multidimensional and Metric Data Structures*. Data Management Systems (Morgan Kaufmann, Burlington, 2012)
42. M. Scholz, J. Bender, C. Dachsbacher, Real-time isosurface extraction with view-dependent level of detail and applications. *Comput. Graphics Forum* **34**(1), 103–115 (2015)
43. J.P. Schulze, U. Lang, The parallelized perspective shear-warp algorithm for volume rendering. *Parallel Comput.* **29**(3), 339–354 (2003)
44. R. Sharma, M. Garg, Comparative analysis of JPEG DCT, Haar & Daubechies wavelet, fractal for image compression. *Int. J. Adv. Res. Comput. Sci. Softw. Eng.* **4**(1), 1227–1234 (2014)

45. M. Shih, Y. Zhang, K.-L. Ma, J. Sitaraman, D. Mavriplis, Out-of-core visualization of time-varying hybrid-grid volume data, in *IEEE 4th Symposium on Large Data Analysis and Visualization* (2014), pp. 93–100
46. A.C. Telea, *Data Visualization: Principles and Practice* (CRC Press, Boca Raton, 2014)
47. J. Udupa, D. Odhner, Shell rendering. *IEEE Comput. Appl.* **13**(6), 58–67 (1993)
48. A. Van Gelder, K. Kim, Direct volume rendering with shading via three-dimensional textures, in *Symposium on Volume Visualization*, San Francisco (IEEE, Los Alamitos, 1996), pp. 23–30
49. M. Weiler, T. Klein, T. Ertl, Direct volume rendering in OpenGL. *Comput. Graphics* **28**(1), 93–98 (2004)
50. L. Westover, Footprint evaluation for volume rendering. *ACM SIGGRAPH Comput. Graphics* **24**(4), 367–376 (1990)

# Chapter 9

## Geometric and Topological Modelling of Organs and Vascular Structures from CT Data



João Fradinho Oliveira, José Blas Pagador, José Luis Moyano-Cuevas, Francisco Miguel Sánchez-Margallo, and Hugo Capote

**Abstract** Automatic segmentation of organs in CT scans is a field of rising interest for the generation of 3D models that can help surgery planning, training and support during surgical procedures. However, the reconstruction and visualization of 3D models of organs with vascular structures present several modelling problems. In this chapter, we review these problems and describe a methodology that allows for the reconstruction to be automatic. In particular this chapter describes and illustrates: how to transform and extract 3D geometry from sets of planar contours/polygons annotated on DICOM images, a solution for enforcing polygon vertex order consistency, polygon triangulation by *ear clipping* and respective inner angle calculation for irregular polygons, a polygon tiling algorithm for stitching contours in adjacent slices, a file format for storing multiple polygons per slice and support for storing their correspondences with other polygons in other slices. Finally, we show how these algorithms can be used together to build different reconstruction solutions: surface-based reconstruction for organs with simple topology, composite surfaces for organs with branching, single surface with branching and polygon extrusion for topologically complex vascular structures. We conclude by showing how organs and vascular structures can be viewed together using transparency.

---

J. F. Oliveira (✉)

C3i + CIAUD, Instituto Politécnico de Portalegre + Universidade de Lisboa, Lisboa, Portugal  
e-mail: [jfoliveira@ipportalegre.pt](mailto:jfoliveira@ipportalegre.pt); [jfoliveira@fa.ulisboa.pt](mailto:jfoliveira@fa.ulisboa.pt)

J. B. Pagador · J. L. Moyano-Cuevas

Bioengineering and Health Technology Unit, Jesús Usón Minimally Invasive Surgery Center, Cáceres, Spain

e-mail: [jbpagador@ccmijesususon.com](mailto:jbpagador@ccmijesususon.com); [jmoyano@ccmijesususon.com](mailto:jmoyano@ccmijesususon.com)

F. M. Sánchez-Margallo

Jesús Usón Minimally Invasive Surgery Center, Cáceres, Spain

e-mail: [msanchez@ccmijesususon.com](mailto:msanchez@ccmijesususon.com)

H. Capote

Hospital Dr. José Maria Grande, Portalegre, Portugal

e-mail: [Hugo.Capote@ulsna.min-saude.pt](mailto:Hugo.Capote@ulsna.min-saude.pt)

© Springer Nature Switzerland AG 2018

M. Abreu de Souza et al. (eds.), *Multi-Modality Imaging*,

[https://doi.org/10.1007/978-3-319-98974-7\\_9](https://doi.org/10.1007/978-3-319-98974-7_9)

**Keywords** 3D reconstruction · Intraoperative spatial cognitive support · Computed tomography · VTK · IGSTK

## 9.1 Introduction

In recent years, medical imaging has acquired a fundamental role in both diagnosis and treatment of different abdominal pathologies. So it has become an essential tool in surgical planning, intraoperative navigation and clinical follow-up of different pathologies such as tumours.

Medical imaging plays a key role in surgical planning and navigation. In abdominal surgeries, the removal of tumours (i.e. on the liver or on kidney) presents a high complexity which involves risks to the patients. These limitations justify research efforts in this field, mainly developing surgical planning and intraoperative navigation systems that facilitate the surgeon's work to deal with these difficult interventions. So these surgical planning systems are characterized by displaying 3D information of the organ and by providing tools that allow knowing placement and features of key structures involved in the procedure. Additionally, they provide surgeons help to predict possible complications and allow to manage them during the development of the intervention. This important guide is usually built with a combination of preoperative and intraoperative information. These navigation systems reproduce the state of the organ by providing information in real time during the intervention to avoid risks and complications.

A common and fundamental element in the development of these surgical planning and navigation systems is the 3D modelling of organs and anatomical structures.

This introductory section contains two subsections; the first one consists of a broad review of how the segmentation and modelling of anatomical structures from CT images have evolved until today, whilst the second subsection illustrates intrinsic topological and geometrical issues that arise from modelling CT data. We point out that whilst all 3D modelling in this chapter has been carried out from CT planar contours, Meyers suggests that planar contours can be extracted from MRI data by comparing the value in each voxel in a slice with a threshold, and adjusting manually if simple thresholding is not adequate [1]. In Sect. 9.2, a

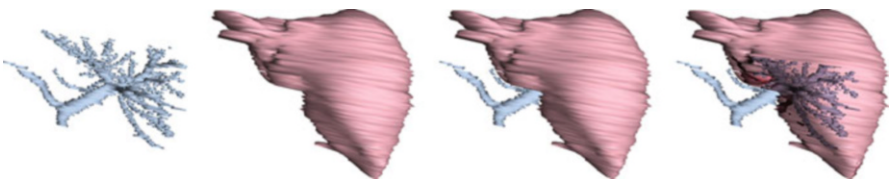


**Fig. 9.1** Modelling and visualization of vascular networks and the liver of a pig (images rendered with a simple OpenGL viewer developed by the authors)



general modelling pipeline is outlined. Each modelling step is described, arising geometric problems are discussed and respective robust solutions are presented. It is the authors' hope that readers can reuse this collection of solutions in their own reconstruction approaches. In Sect. 9.3, modelling steps from Sect. 9.2 are combined to create a volume-based reconstruction solution for vascular networks which does not require topological information. Similarly, in Sect. 9.4, some modelling steps from Sect. 9.2 are combined to create a composite surface reconstruction solution for organs. In the case of the presented reconstructions, the main goal was to provide the visualization of geometric representations based on real data (CT) that enable spatial reasoning tasks preoperatively and intraoperatively as a road-map of anatomical structures. Often surface representations are only the starting point for other applications. For instance, in Nebel's soft tissue deformation work, a volumetric mesh is built by duplicating the 3D scanned surface of human skin to generate three layers of the epidermis, dermis and subcutaneous tissue layers. A finite element method is used to model the different physical properties of the layers, enabling external forces to be applied to deform the skin [2]. In Oliveira et al. body scan animation work [3], automatically extracted skeletons and landmarks are used in conjunction with scanned surface models to create a mapping for smooth surface deformation with motion capture data. Similarly, the reconstructions presented in this chapter could be used to create other representations for other applications such as surgery training with haptic deformation simulation. Finally, in Sect. 9.5, a surface-based reconstruction and a volume-based reconstruction are used together (Fig. 9.1) for visualization in an intraoperative application (Fig. 9.2). Conclusions are presented in Sect. 9.6.

### ***9.1.1 Segmentation of Anatomical Structures***

Image segmentation is the process of partitioning a digital image into different regions or objects with homogeneous or inhomogeneous features, to extract relevant information from it [4]. Segmentation is a basic step in digital image processing as well as being one of the most complex operations. In the field of medical imaging, segmentation is a first and important step in most of the diagnostic and treatment algorithms, and it is a needed preliminary step in other processes such as the volumetric reconstruction of the anatomical structure.

In order to identify organs and pathologies, a clinical specialist usually has to perform a manual segmentation. This procedure is time consuming and results (final segmentation) may suffer from intra-observer and/or inter-observer variability. For this reason, image segmentation has been a research area with many opportunities for the last decades and automatic or semi-automatic algorithms have seen active development for specific target organs and structures. Although general approaches to segmentation are common (algorithms, techniques and concepts), obtained results may have large variations between different organs, due to changes in density, morphology and other image features. In this sense, the focused interest in the

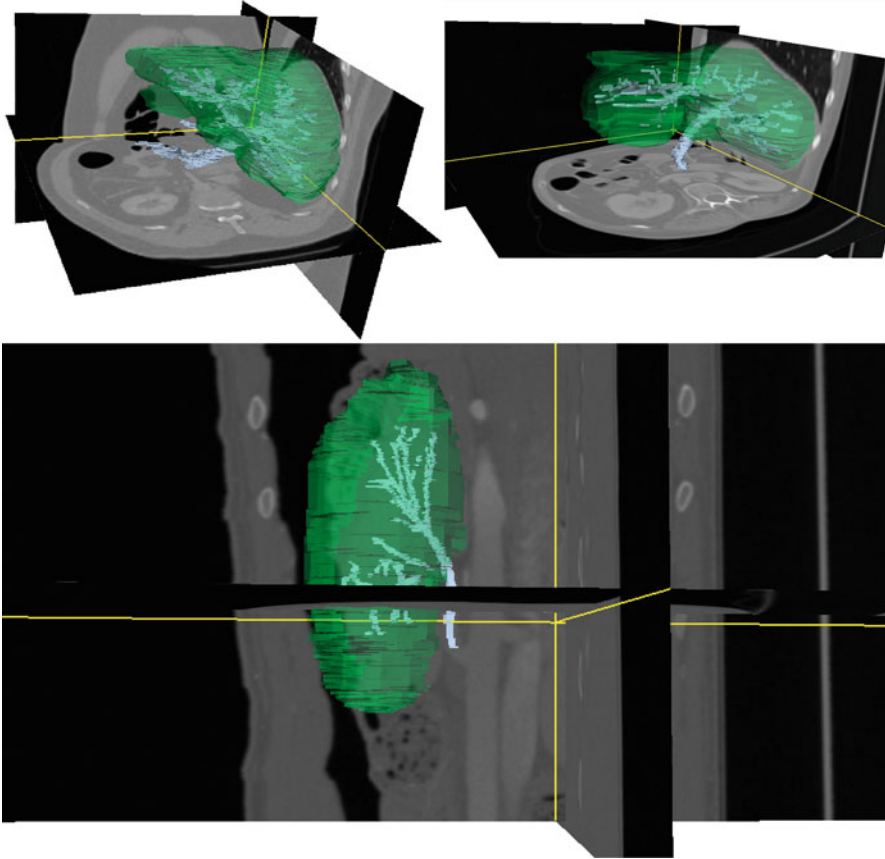


**Fig. 9.2** Volume-based reconstructed models (vascular structures, low-resolution models) and surface-based reconstructed models (organs) visualization in CAS\_Navigate. Top left: two composite surfaces (liver1\_low, liver1b\_low); top right: two composite surfaces (liver2\_low, liver2b\_low); bottom: single surface kidney\_low

abdominal region has produced many practical uses of image segmentation for assisting identification of pathologies in the liver and kidney.

In this section, we will describe the main methods of segmentation for different abdominal organs. Broadly, segmentation methods described in the literature can be classified into three main categories: (1) thresholding and region growing, (2) deformable models and (3) classifier methods.

### 9.1.1.1 Thresholding and Region Growing

Algorithms based on thresholding, that use the intensity grey level or magnitude gradient as features to classify every image's pixel. Hence, the segmentation procedure works by searching for the pixels whose values are greater or less or

are within the ranges defined by these thresholds. Each threshold can be defined manually or automatically. In this sense, the Otsu method is a classic example of an automatic method that uses the histogram to obtain thresholds [5]. On the other hand, region growing algorithms put pixels with similar grey values together as a same region. In contrast to the thresholding method, region growing can use more features than just grey level intensity. In some specific cases, such as kidney segmentation, a combination between region growing and thresholding methods are used [6]. However, Leonardi et al. state that these methods lose effectiveness due to the large overlap of grey level intensity between the kidney and other surrounding tissues and they are very sensitive to initialization parameters. In other cases, such as liver segmentation, similar methods have been used [7], but again similar anatomical structures (in grey levels) and internal variations of the liver itself provoke poor results in these kinds of segmentation approaches [8].

### 9.1.1.2 Deformable Models

Deformable models are curves or surfaces which are used for segmentation in the image domain, these models suffer deformations under the influence of internal and external forces (or energies) to delineate an object's boundary [9]. In these models, internal forces preserve the shape smoothness whilst the external forces modify the shape based on image features until specific desired region boundaries are achieved. In general, two kinds of deformable models can be considered: parametric models (active contour or snake [10, 11], active shape model [12] and active appearance model [13]), and geometrical models based on the level set method [14]. The main idea of the level set method is to implicitly embed the moving contour into a higher dimensional level set function and view the contour as its zero level set [15]. These original methods and modifications of them have been widely described for segmentation of CT medical images with highly accurate results [7, 16, 17]. In the specific case of the liver, there are numerous works that have used the deformable model as the base of their segmentation algorithms [18–20]. In order to achieve accurate liver segmentation, several studies integrated the statistical shape model defined by a training set of shapes for the determination of the external forces of the deformable model [21]. An example of this is the work described by Heimann and Meinzer [22], which were the first to use a shape statistical model to initialize a deformable model method that strives for equilibrium between the internal and external forces, thus segmenting the liver and reducing user interaction. These methodologies have also been applied in the kidney segmentation. Tsagaan and Shimizu described a deformable model for automatic kidney segmentation which is represented by the grey level appearance of the kidney and its statistical information of the shape [23]. In addition, the deformable model has been applied in the segmentation of the internal kidney anatomical structures and their pathologies, such as tumours. Skalski et al. proposed a method based on a hybrid level set algorithm with elliptical shape constraints to segment the kidney, and also its vascular tree and potentially existing tumours [24]. Although these deformable models have been

successfully applied in many medical fields, these methods require additional efforts to improve the accuracy (difference between the anatomical structure identified by the segmentation algorithm and the real anatomical structure, for which common metric are used such as the number of false negatives, false positives, the Dice similarity coefficient, the Jaccard similarity coefficient [25]) in segmentation of the anatomical structures because of difficulties in the initial model estimation and in automatically determining the internal and external forces [15].

### 9.1.1.3 Classifier Methods

Classification methods have also been used for the segmentation of medical images. These segmentation methods can be defined in two main groups: supervised and unsupervised classifiers.

Supervised classifiers are characterized by requiring a previous training step with a set of data which allows to extract structure information. Frequently used supervised classification techniques include linear discriminant analysis (LDA) [26], k-nearest neighbour (kNN) classifiers [27], supervised artificial neural networks (ANN) or support vector machines (SVM) [28]. These algorithms have been widely used for the segmentation of different anatomical structures and different types of medical images [29]. Dağ et al. implemented a kNN classifier [30] to segment the liver from the background and accurate segmentation was achieved by using B-splines. Kalifa et al. used the kNN method to classify different anatomical structures of the kidney in order to evaluate features in kidney transplant procedures [31]. Xu and Suzuki used an LDA classifier in a new method of feature-extraction that segments the liver and the hepatocellular carcinoma with the best result being achieved when the conventional stepwise feature selection used the Wilks' lambda method (HCC) [32]. Dou et al. use the supervised ANN technique for segmentation of the kidney [33]. SVMs, after training with labelled examples, classify data using one or several hyperplanes in an n-dimensional space. In this sense, SVM separates two or more classes and has been applied traditionally to brain images, however, this method has been used to segment different abdominal structures too [34, 35]. An example of this is the work described by Lin et al. who proposed a method based in the SVM to segment gallbladder, liver, kidney, bone and stomach objects [36]. Their method also implements a region growing algorithm as a previous step of the classification. Additionally, SVM algorithms usually implement a mapping function (kernel trick) to reduce the intensive computation required to solve the model.

The main problem of these methods is the sensitivity of these techniques to the initial conditions raised [37]. So in order to achieve high precision of results, it is necessary to take special care with the choice of the training set. In addition, these types of algorithms still require user intervention. Despite these drawbacks, these classifiers stand out for the high accuracy they have shown for segmenting medical imaging when training is appropriate.

In contrast to supervised classifiers, unsupervised classifier try to automatically discover discriminating features without any hints as to what the inputs are [38].

However, the intervention of the user is necessary, in order to make an initial identification of the regions to be classified. In the field of medical imaging, the Fuzzy c-means has been used in the segmentation of abdominal organs and pathologies because this method extracts a lot of information from the original image and it has robust characteristics for ambiguity [39]. In addition, this method has been combined with other methods to improve accuracy and reduce user interaction. Das and Sabut incorporated the Kernel method in the Fuzzy c-means to segment tumour liver in CT images and combined with adaptive thresholding [40]. In another approach, Song et al. used a variation of the kernel-based Fuzzy c-means algorithm (KFCM) including a spatial constraint to segment kidney [41].

Finally, although not related exclusively to segmentation, it is important to note the growing use of deep learning techniques in medical image analysis where these algorithms can be used not only for segmentation but for classification and support decisions of clinicians [42]. Liu et al. [43] report reducing the false negative rate to a quarter of a pathologist when detecting breast cancer metastases in gigapixel microscopy images using a convolutional neural network (CNN) architecture.

In summary, due to the high similarity in grey levels of all abdominal organs and to the anatomical variations between patients and further to the level of noise in different medical images, segmentation of abdominal structures and organs is still a challenging task. For this reason, the *Segmentation of the Liver Competition* proposed for the first time in 2007 in a workshop of the Medical Image Computing and Computer Assisted Interventions (MICCAI) conference is still open nowadays [44, 45].

### ***9.1.2 Intrinsic Topological and Geometric problems***

In Meyers' seminal work the problems of reconstruction from segmented CT planar polygons are categorized into three areas: (1) the correspondence problem, which can be stated as: given any contour on a given slice, finding which contours in adjacent slices correspond or connect to the contour, (2) the contour branching problem, whether a contour splits or joins in an adjacent slice and (3) the triangle tiling problem, finding how to connect/triangulate vertices from corresponding or branching adjacent slice contours [1]. Solving these problems essentially allows to create separate object entities, such as the liver and a vascular network. This, in turn, allows one to calculate the surface area or volume of a given object entity. In contrast, Volume Rendering rasterizes data as global entities, where parts of tissues from various organs are visualized as one entity instead.

The inherent spatial resolution limitation between CT slices gives rise to topological ambiguity questions that make the correspondence problem and the branching problem impossible to solve entirely automatically without error. This spatial limitation also creates geometric problems in tiling. The following subsections describe and illustrate these problems.

### 9.1.2.1 Topological Problems

The spacing between data slices can create branching ambiguity decisions (we refer the reader to Bajaj et al. [46] for a comprehensive review on tiling branching solutions) in the correspondence problem (Fig. 9.3) as shape continuity is difficult to establish. For instance, a distance B between two contours in the same slice can join in the next slice. Whilst a smaller distance A between two contours of the same slice can mean that the structures are separate branches (Fig. 9.4). Furthermore, in

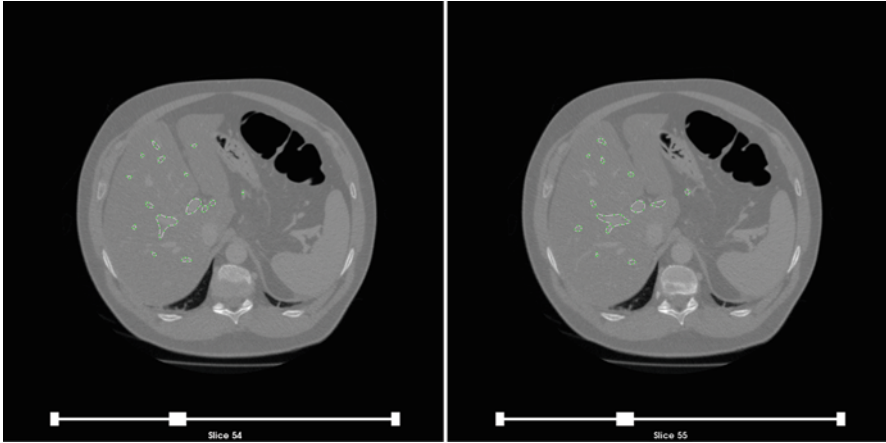


**Fig. 9.3** Correspondence problem—the horizontal distance between contours in slice 54 can indicate that the contours are either separate entities or join in slice 55

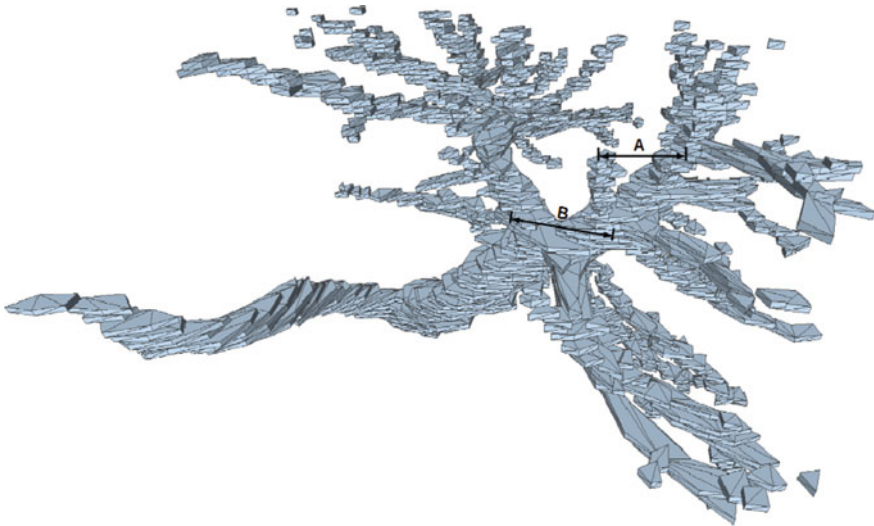


**Fig. 9.4** Branching ambiguity—horizontal contour distance B joins two vascular branches, whereas a smaller horizontal contour distance A represents separate branches

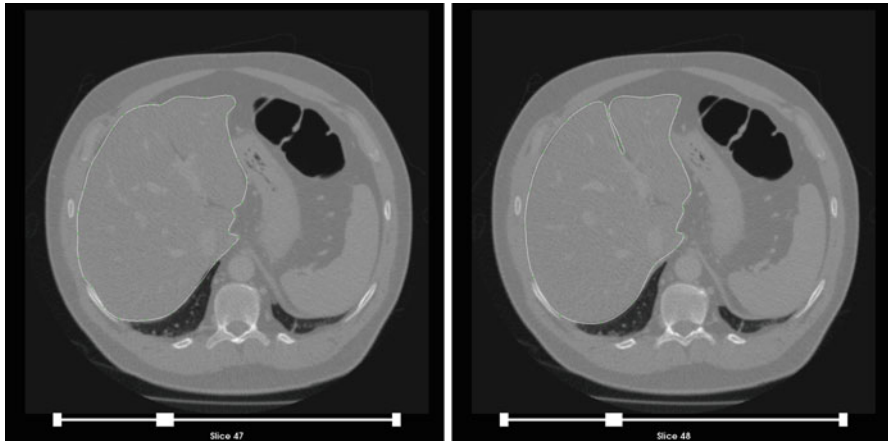


**Fig. 9.5** Drastic polygon shape difference between corresponding polygons on adjacent data slices

between two adjacent data slices, a vessel or anatomical structure can end and a new one begin. Establishing or correcting the sheer number of correspondences present in vascular networks can be a daunting task. In Sect. 9.3 an alternative solution to the correspondence problem is provided.

### 9.1.2.2 Geometric Problems

The spacing between data slices does not capture how the same corresponding shape entity varies from one slice to the next, creating problems in the triangle tiling process. Specifically connecting two very different contours (Fig. 9.5) can create self-intersections in a model. Whilst this problem can be alleviated with intermediate contour interpolation, the problem can be exacerbated if the organ branches. Christiansen and Sederberg's [47] tiling algorithm is reviewed in Sect. 9.4, including their elegant solution to tiling branches. VTK-snap (ITK [48]) is a tool that allows to build organs and vascular networks by stacking individual extruded volume blocks without polygon correspondences; however, the extra internal geometry created between adjacent blocks creates excessive visual clutter if one were to try to inspect internal objects at the same time.

An alternative solution to tiling branching organs which is presented in Sect. 9.4.2 draws from an analogy with Metaballs [49] where instead of a composition of spheres to approximate an object's organic like shape, we use a composition of surfaces.



## 9.2 Modelling from CT Contours

In this section, we describe the fundamental modelling steps (Fig. 9.6) that are required to transform a 2D polygon contour into 3D geometry constructs that can be used as building blocks of a variety of reconstruction strategies.

In our examples, we use VTK's [50] DICOM reading and viewing capabilities (`vtkDICOMImageReader` and `vtkImageViewer2` respectively) and the `vtkContourWidget` spline editor to keep track of the polygon contour geometry, whilst the target 3D world is IGSTK's image-guided surgery viewer [51]. The work in this chapter draws from the development of two medical imaging applications: `CAS_Annotate` (contour editing and reconstruction algorithms) and `CAS_Navigate` (visualization) [52]. We point out that the modelling issues addressed are common to any framework dealing with geometry extracted from a planar polygon contour representation.

We first describe the transformations in the following subsection, and some relevant practical problems are addressed, next, we review David Eberly's ear clipping algorithm for triangulating 2D polygon contours [53], and present resilient

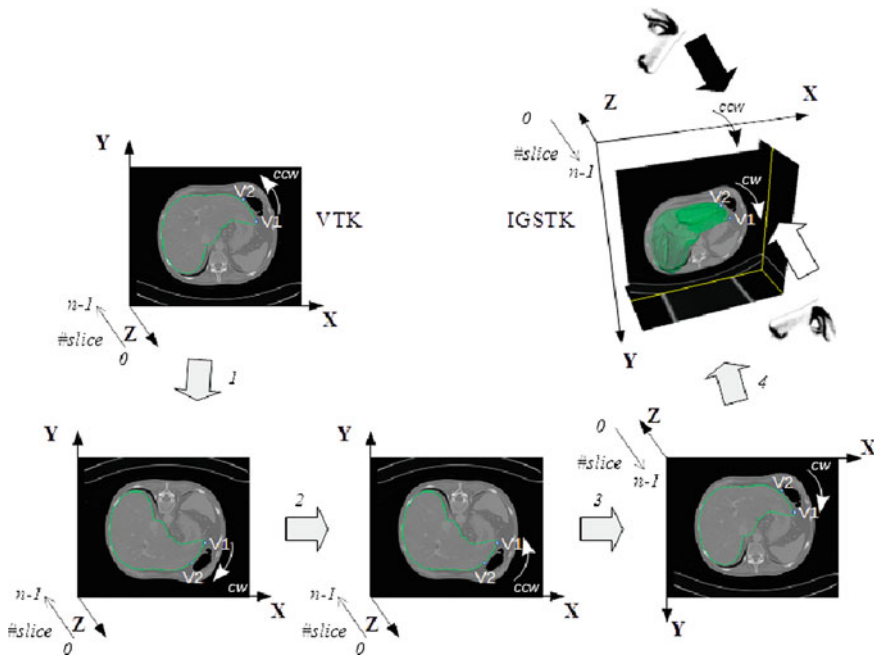


**Fig. 9.6** Four step transformation pipeline from VTK to IGSTK coordinates. Vertex ordering of the polygons changes with the transformations. Initially, vertex ordering is arbitrarily counterclockwise (*ccw*) or clockwise (*cw*) before step 1, and is forced to be consistently *ccw* in step 2 enabling later the creation of 3D models whose normals are also consistently oriented and pointing outwards



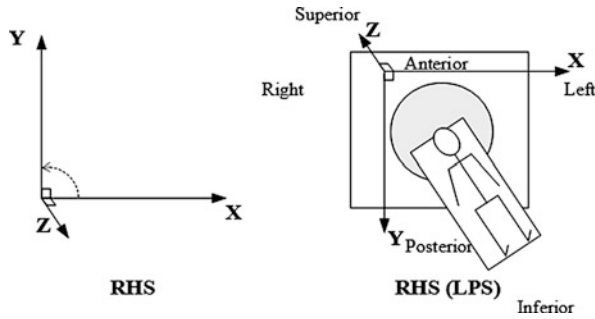


**Fig. 9.7** Source and target coordinate systems. The source coordinate system on the left is a right-hand system (VTK); whilst the target coordinate system is a right-hand system oriented with the patient-centred coordinate system (*x* increases to *Left*, *y* increases to the *Posterior*, *z* increases to *Superior*), (IGSTK)

solutions that we found for key steps of this algorithm. We conclude this section presenting our polygon contour file format which supports branching.

### 9.2.1 Transformation Pipeline (from VTK to IGSTK)

The first important observation one can make from Fig. 9.6 before any transformation, is that the source coordinate system (VTK) and the target coordinate system (IGSTK) are both right-hand systems (Fig. 9.7).

A second observation is that simply rotating the source coordinate system on the *X* axis to align *Z* with the target coordinate system *Z*, results in the image to be vertically flipped. VTK stores the lower left pixel as the first pixel in the image, whereas DICOM stores the upper left as the first pixel.

For any *x*, *y* value in a polygon contour, the first step in the transformation pipeline is to flip VTK’s *y* values; this can be done by retrieving the *y**max* constant with VTK’s `GetDisplayBounds` function and subtracting *y*:

```
double*bound s = imageView->GetImageActor()->GetDisplayBounds ()
ymax = bounds [1]
y = ymax-y
```

(9.1)

A direct result from this transformation is that any polygon contour that was defined in counterclockwise order has now clockwise order. This aspect is important for modelling, as a rendering speed-up known as *back-face culling* which is often exploited in many visualization engines is achieved by not rendering polygons whose normal points away from the camera/viewer. A clockwise vertex order can

result in the polygon not being drawn in some viewing conditions and the inside of the model being rendered instead. The  $z$  value of a point is calculated by:

$$zvalue = ((totalnumberofslices-1) - selected\ slice\ number) * zspacing \quad (9.2)$$

where  $zspacing$  can be retrieved by querying `vtkDICOMImageReader` reader object through the `GetPixelSpacing()` function.

The second step in the transformation pipeline is to ensure that all polygon contours are specified in counterclockwise order. We point out that the user initially is likely to define contours with arbitrary vertex ordering. In Sect. 9.2.3 we present an algorithm to ensure counterclockwise vertex ordering in all polygons that has proved to work 100% in all our datasets.

The third step is conceptual. One can observe that the counterclockwise vertex order polygons, when viewed from above the data slice (LPS Superior) remain counterclockwise, but are invisible or seen as clockwise when viewed from below (LPS Inferior). This means that whilst the polygons can all be stored in the counterclockwise convention, when we wish to triangulate or close the bottom polygons, we need to reverse the triangle order.

The fourth and final transformation step is to apply the DICOM data position and orientation transformation (Eq. 9.3) to the result of step 2 to finally align the images with LPS.

The DICOM standard [54, 55], contains tags that provide information regarding the image position and orientation. The *Image Position* is reflected in the translation component  $T$  in Eq. (9.3), the *Image orientation* specifies the direction cosines of the transformation required to ensure that the images are aligned with the LPS convention (the  $d$  parameters in Eq. (9.3) are used to create the cross-product  $N$ , which together define the rotation component). In addition, a third tag called the *Patient position*, allows one to record the patient position with respect to the scanner.

$$\begin{pmatrix} x' \\ y' \\ z' \\ 1 \end{pmatrix} = \begin{pmatrix} d[0] & d[3] & N_x & T_x \\ d[1] & d[4] & N_y & T_y \\ d[2] & d[5] & N_z & T_z \\ 0 & 0 & 0 & 1 \end{pmatrix} \begin{pmatrix} x \\ y \\ z \\ 1 \end{pmatrix} \quad (9.3)$$

The  $d$  and  $T$  parameters can be retrieved with `reader->GetImageOrientationPatient()`, and `reader->GetImagePositionPatient()` respectively.

We point out that there are several benefits in leaving this matrix transformation to last as several modelling algorithms can be solved in 2D with simpler implementations. The following subsections describe some of the tools that are required to triangulate a polygon contour. This triangulation technique is then used in volume-based reconstruction (vascular structures in Sect. 9.3) and surface-based reconstruction (organs in Sect. 9.4).

### 9.2.2 Duplicate Vertices

Duplicate vertices can create problems in several algorithms; one way to remove them is to create a VTK filter object (`vtkCleanPolyData`). However, this can unnecessarily add seconds of computation. A faster approach is to either tackle the root of the problem or to observe whether a pattern of duplicate vertex occurrences exists that can be exploited. The former reveals that duplicates when they occur, occur only once and they appear in consecutive order in the polygon. Hence simply creating a temporary vector between the vertex to be inserted and the last vertex that was added, measuring its length and discarding vertices whose vector length is below a tolerance of for example 0.0001 works much faster as only the last added vertex is checked.

### 9.2.3 2D Polygon Vertex Order Consistency Problem

Tiling algorithms that triangulate polygon vertices from adjacent slices often rely on the assumption that all polygons have the same vertex order. One method to determine if a given vertex sequence is counterclockwise or clockwise is to use the *surveyor's area formula* [56] also known as the shoelace formula:

$$A = \frac{1}{2} \left| \sum_{i=1}^n \det \begin{pmatrix} x_i & x_{i+1} \\ y_i & y_{i+1} \end{pmatrix} \right| \quad (9.4)$$

where  $x_{n+1} = x_1$  and  $y_{n+1} = y_1$ ,

if the points are labelled sequentially in the counterclockwise order direction, then the sum of the above determinants is positive and the absolute value sign can be omitted. If the sum is negative then the order was clockwise. This formula assumes a Cartesian coordinate system where  $+Y$  is up and  $+X$  is to the right. This formula is applied during step 2 of the transformation pipeline (Fig. 9.6). We found this method to work 100% correctly with all our datasets.

### 9.2.4 Triangulation by Ear Clipping [53]

Whilst high mesh quality 2D triangulation algorithms exist, such as the Delaunay Triangulation, in this subsection we review an approach that is easier to implement and has provided good results in practice. The 2D triangulation algorithm is an important building block in the different reconstruction approaches described in Sects. 9.3 and 9.4. Before describing the main steps of the algorithm, we introduce the following concepts:

A polygon is defined by a sequence of vertices ( $V$ ) in a doubly linked list,  $V_{n+1}$  is  $V_1$ , and the previous vertex of  $V_1$  is  $V_n$ . The polygon provided is *simple*, no vertex is connected by more than two vertices. An *ear* of a polygon is a triangle formed by three consecutive vertices ( $V_{i-1}$ ,  $V_i$ ,  $V_{i+1}$ ), where the internal angle at  $V_i$  is less than  $\pi$  radians (convex vertex) and there are no other vertices of the polygon inside this triangle. A Reflex vertex is one where the interior angle made by its two connecting edges is larger than  $\pi$  radians.

The first step of the algorithm is to calculate the internal angle at each vertex ( $V_{i-1}$ ,  $V_i$ ,  $V_{i+1}$ ) of the list. If the internal angle is larger than  $\pi$  radians, then the vertex is flagged as being reflex (a solution to calculating the internal angle of irregular polygons is provided in Sect. 9.2.5). The second step is to access each vertex of the list and if a vertex was not flagged as reflex, a point in polygon inclusion test is performed with all vertices of the polygon contour and the triangle defined by ( $V_{i-1}$ ,  $V_i$ ,  $V_{i+1}$ ). Here it is important that there are no duplicate vertices (see Sect. 9.2.2), as a duplicate vertex would wrongly signal a point inside the proposed triangle. If there are no vertices inside in the triangle, then the vertex id is added to an ear list. A solution for the point in polygon test is provided in Sect. 9.2.6. In the top row, second column from the left in Fig. 9.8, one can observe the result of these two steps, in practice an ear list is created, and the vertices are simply flagged whether they are reflex ( $r$ ), the ( $e$ ) is illustrative only as the ears are kept in a separate list.

The third step is to access the first ear in the earlist ( $V_2$ , top row, second column from left), and create a triangle **1** for the first ear, remove the vertex from the earlist and from the vertex list thus shrinking the polygon contour that needs triangulation. The internal angle at the previous and next vertex of the removed vertex is recalculated with the new geometrical configuration only if they were flagged as reflex before (top row, third column from left). If the internal angle became convex, a point-in-polygon test is carried out with all the original vertices to see whether a new ear can be added to the end of the earlist. In this example, the previous and next vertex remained reflex after the first vertex was removed. The next ear in the earlist is vertex 5, note that vertex 4 which was reflex becomes an ear added to the end of the earlist, once triangle **2** is created. The same happens to vertex 7 once the ear defined by ( $V_4$ ,  $V_6$ ,  $V_7$ ) is triangulated. We note that this algorithm is not starting point invariant, even inserting new ears at the head of the earlist instead of the back will generate different triangle configurations. We leave the optimization of the triangle aspect ratio as an exercise to the reader. Gueziec [57] provides a triangle fairness function for a triangle's aspect ratio:

$$c = \frac{4\sqrt{3}a}{l_0^2 + l_1^2 + l_2^2} \quad (9.5)$$

where  $c$  varies from 0 (thin) to 1 (equilateral),  $a$  is the triangle area, and  $l_0^2$ ,  $l_1^2$ ,  $l_2^2$  the squared length of the three edges of the triangle. Finally, an additional mesh quality test is to test for edge intersection when proposing an ear triangle. Care needs to be taken to ensure that the system does not become overconstrained, in

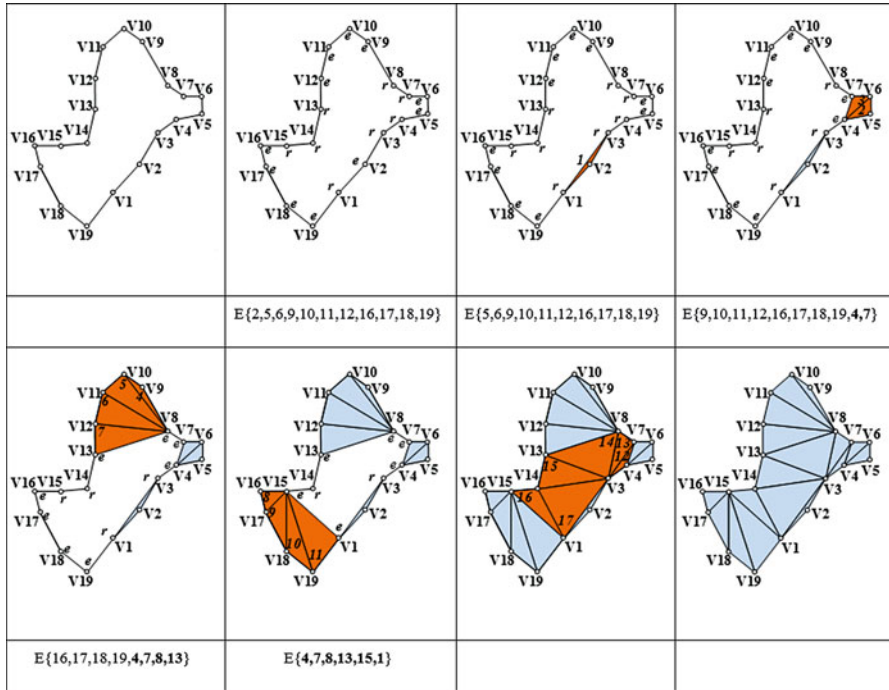


**Fig. 9.8** Triangulation by Ear Clipping. From the top-left to top-right and bottom-left to bottom-right. The inner angle of each vertex is first computed to determine if they are reflex (*r*) or potential ear vertices (*e*) that can be used for triangulating three consecutive polygon vertices, an earlist *E* is created from *e* vertices that do not contain other vertices in their ear triangle; ear vertices are iteratively removed from the front of *E*, shortening/clipping the polygon and creating triangles in orange (e.g. {*V*1, *V*2, *V*3}). New ear vertices are added to the end of *E* after each triangulation when previous reflex vertices become non-reflex and their associated ear triangle does not contain other vertices inside (e.g. *V*4, *V*7)

practice we did not implement this step, but a visual inspection of the models did not find any degenerate triangulation. An integral part of this triangulation algorithm is the calculation of the internal angle at vertices of irregular polygons. In the next subsection, a reliable solution is presented.

### 9.2.5 Internal Angle Calculation of Irregular Polygons

Given three consecutive counterclockwise vertices (*V*<sub>1</sub>, *V*<sub>2</sub>, *V*<sub>3</sub>), what is the internal angle formed between the edge (*V*<sub>1</sub>, *V*<sub>2</sub>) and the edge (*V*<sub>2</sub>, *V*<sub>3</sub>)? The answer to this question can be found by answering another question instead:

*What is the clockwise angle transformation required to make the first edge (*V*<sub>1</sub>, *V*<sub>2</sub>), align with the second edge (*V*<sub>2</sub>, *V*<sub>3</sub>)?*

This, in turn, can be determined with six steps:

1. Normalizing the vectors defined by  $(V_1 - V_2)$  and  $(V_3 - V_2)$  to unit length
2. Calculate respectively the angles  $\alpha$  and  $\beta$  of each normalized vector with the  $X$  axis using the *acos* function (in C/C++ *acos* returns a positive or zero value between  $[0, \pi]$  radians)
3. Consult Fig. 9.9 to localize in which of the four quadrants the previous vertex  $V_1$  is in, this can be done by analyzing the resulting signs of  $V1.X() - V2.X()$ , and the  $V1.Y() - V2.Y()$
4. Consult Fig. 9.9 to localize in which of the four quadrants the next vertex  $V_3$  is in, analyzing the resulting signs of  $V3.X() - V2.X()$ , and  $V3.Y() - V2.Y()$
5. If vertex  $V_1$  and vertex  $V_3$  are in the same quadrant, determine the relation of angle magnitude between  $\alpha$  and  $\beta$
6. Use Fig. 9.9 with steps (3, 4, 5) to look up and apply the correct formula that answers the above question.

If the total angle is larger or equal to  $\pi$  radians, then the angle is reflex and cannot be considered as a possible ear for triangulation. Only convex vertices can be considered, otherwise, the resulting triangle would be outside the actual boundaries of the original polygon. In the next subsection, the last requisite to establish whether a convex vertex can be marked as an ear for triangulation is given. No vertices can be found inside the ear.

### 9.2.6 Point in Polygon Test for Convex Polygons

An important step in the triangulation algorithm described in Sect. 9.2.4, is given three counterclockwise vertices  $(V_1, V_2, V_3)$ , determine if there is a vertex  $P$  from the original contour polygon vertex list that is not  $V_1, V_2$  or  $V_3$  that is inside the proposed triangle configuration. Only if there are no vertices inside, can the vertex with the edges forming the proposed triangle be considered an ear. This amounts to a point-in-polygon test, several solutions exist for convex and concave polygons [58], fortunately, the polygon being tested is always a triangle, which is convex and yields a very simple six-step solution (Fig. 9.10):

1. Create vectors  $V_2 - V_1, V_3 - V_2$  and  $V_1 - V_3$ .
2. Create respective perpendicular vectors  $\vec{N1}(-(V_{2y} - V_{1y}), V_{2x} - V_{1x}), \vec{N2}(-(V_{3y} - V_{2y}), V_{3x} - V_{2x}), \vec{N3}(-(V_{1y} - V_{3y}), V_{1x} - V_{3x})$ .
3. Create vectors  $P - V_1, P - V_2, P - V_3$ .
4. Calculate the inner product between  $\vec{N1}$  and the vector  $P - V_1$ , if the result is negative, the vertex  $P$  is outside the triangle, if it is positive proceed to step 5.
5. Calculate the inner product between  $\vec{N2}$  and the vector  $P - V_2$ , if the result is negative, the vertex  $P$  is outside the triangle, otherwise proceed to step 6.

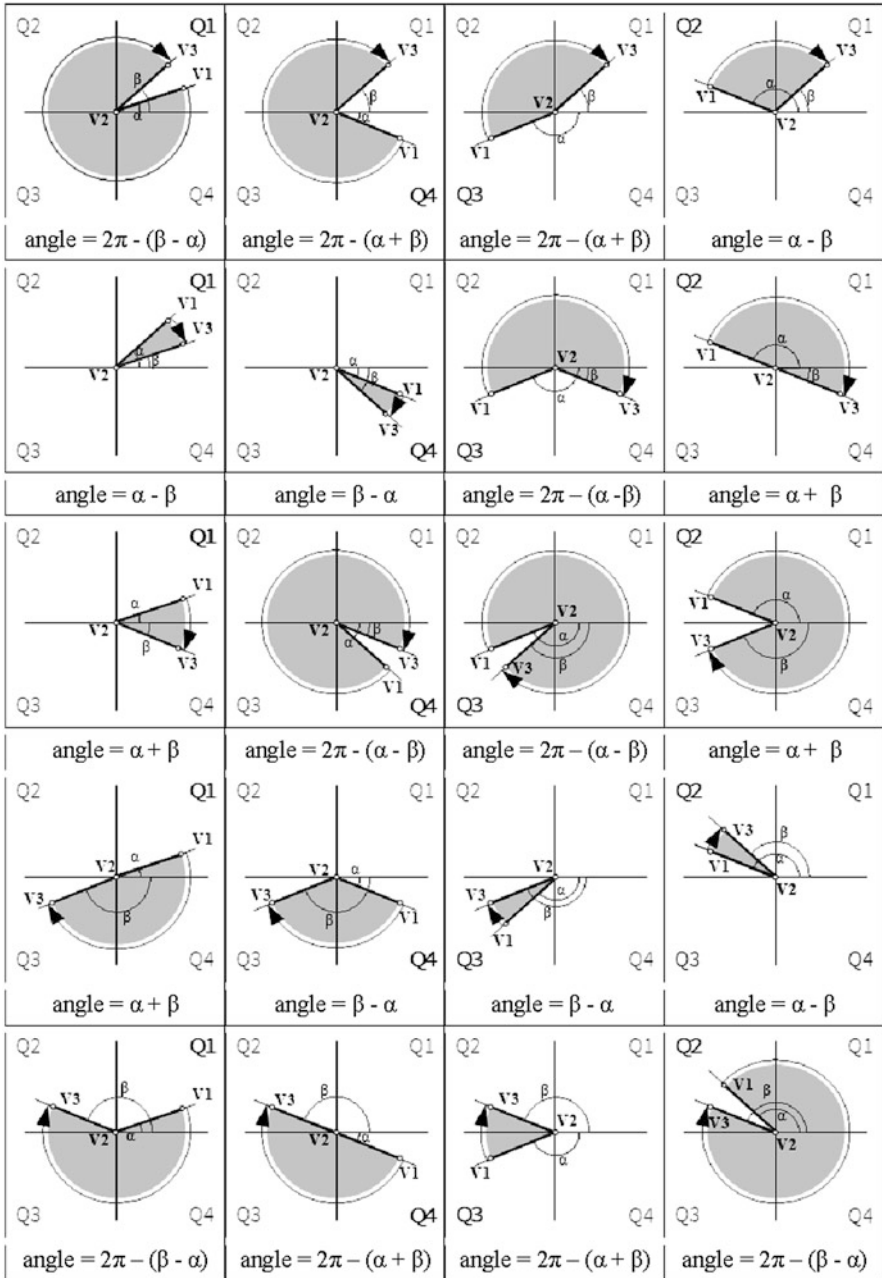


**Fig. 9.9** Internal angle calculation for irregular counterclockwise polygons ( . . . , V1, V2, V3, . . . ). The area in grey represents the inside of the polygon in different edge configurations. The circular arrow represents the internal angle

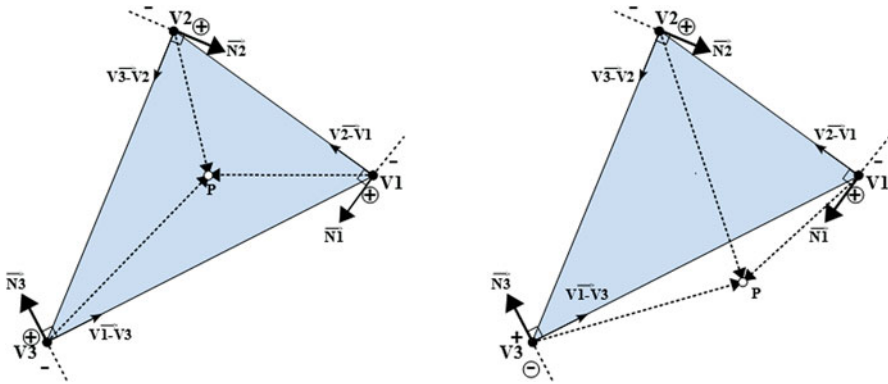


**Fig. 9.10** Point in polygon test for triangles. (Left) ALL inner products  $(P - V1$  with  $\vec{N1}$ ),  $(P - V2$  with  $\vec{N2}$ ) and  $(P - V3$  with  $\vec{N3}$ ) yielded a positive value, the vertex  $P$  is inside; (right) ONE OF the inner products, the one between  $P - V3$  and  $\vec{N3}$  is negative, the vertex  $P$  is outside

6. Calculate the inner product between  $\vec{N3}$  and the vector  $P - V3$ , if the result is negative, the vertex  $P$  is outside the triangle (Fig. 9.10, right), otherwise the vertex  $P$  is inside, as all three tests yielded positive (Fig. 9.10, left).

### 9.2.7 Polygon Contour File Format

Table 9.1 illustrates our polygon contour file format. The first line indicates that there are 155 data slices with or without polygon contours. The second line indicates the number of polygon contours in the first slice, in this case, there are no polygon contours, the same happens with the second and third slice. Line 5 indicates that the fourth slice has 1 polygon contour, line 6 indicates that there are 4 vertices in the polygon contour, and the polygon has no polygon correspondence links with previous slices, there is however, one polygon correspondence with a polygon in the next slices. Lines 7–10 provide the coordinates of the four vertices of the polygon. Line 11 provides the polygon contour id of the only correspondence, in this case [4 0] refers to the first polygon (0) in slice id 4 (the fifth slice). If there were links with previous slices, the polygon contour ids of those links would be listed first, one in each line. If there were no polygon correspondence links, then line 6 would be 4 0 0, and line 11 would be deleted. Line 12, indicates that slice 5 has one polygon, line 13 indicates that the polygon has three vertices and a polygon correspondence link with a previous slice, as well as two polygon correspondence links with the next slice (a branch). Line 17 has the contour id of the link with the previous slice, lines 18 and 19 have the contour ids of the link with the branches.



**Table 9.1** Example polygon contour file text file with polygon correspondences

Line numbers for illustration	Actual file data
1	155
2	0
3	0
4	0
5	1
6	4 0 1
7	91.705582 180.143860 4.800018
8	105.783516 178.699982 4.800018
9	106.866432 163.178162 4.800018
10	94.232391 167.870804 4.800018
11	4 0
12	1
13	3 1 2
14	96.037254 160.651352 6.400024
15	106.144485 157.763565 6.400024
16	114.446854 161.373291 6.400024
17	3 0
18	5 0
19	5 1

### 9.3 Modelling Vascular Structures

Establishing or correcting the sheer number of correspondences between polygon contours in vascular networks can be a daunting task. If the purpose of the application in mind is to have a spatial representation of the vascular network which can be used for resection planning for example, then a volume contour extrusion approach can provide such information without requiring any correspondences to be established. In this section, we apply the algorithms described in Sect. 9.2 to present one possible volume-based solution (Fig. 9.11).

The main idea is to extract the vertices from each polygon contour and apply the first three steps of the modelling pipeline described in Fig. 9.6. The  $Y$  values of the vertices are inverted, duplicate vertices are removed (Sect. 9.2.2), counterclockwise ordering is forced on all polygon contours (Sect. 9.2.3) and the polygon is triangulated by ear clipping (Sects. 9.2.4, 9.2.5 and 9.2.6) from above with its counterclockwise order. The polygon contour is then duplicated and the  $Z$  values are set to belong to the next lower slice. Since there is a 1–1 correspondence with the copied polygon, triangle tiling is a matter of simply connecting the extruded vertices with the original vertices as shown in the left of Fig. 9.12 (triangle  $V1, V1', V2$ , triangle  $V2, V1', V2'$ , etc.). The extruded contour is then triangulated from below, keeping the vertices in counterclockwise order, but reversing the order of the solution triangle ears. Finally, transformation step 4 (Eq. 9.3) of the modelling pipeline (Fig. 9.6) is applied to all vertices. Table 9.2 shows the model complexity



**Fig. 9.11** Modelling vascular structures. (Left) liver1; (centre) liver2; (right) kidney

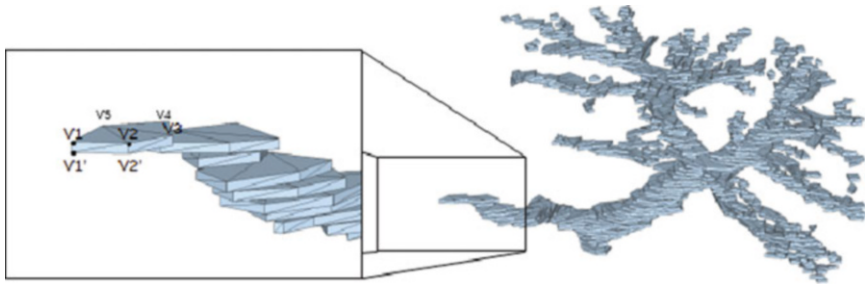


**Fig. 9.12** Volume-based reconstruction of a vascular network (liver1)

**Table 9.2** Vascular structures model complexity<sup>a</sup>

Model	#Slices	#Contours	#Control vertices	#Triangles	#Vertices
liver1_veins_low	155	590	3710	10,452	6406
liver1_veins_high	''	''	''	274,178	139,304
liver2_veins_low	74	300	2194	6680	3940
liver2_veins_high	''	''	''	147,752	75,228
kidney_veins_low	390	734	4152	12,584	7760
kidney_veins_high	''	''	''	341,142	172,782

<sup>a</sup>Please note that the model complexity shown in this chapter may be different from previously published model complexity for the same models, as a result of refinements of the new presented implementations

associated with the respective low-resolution versions shown in Fig. 9.11 and includes the high-resolution versions, where the polygon contour widgets were set to extract more vertices. All models were generated in less than 1 s using a Sony Vaio laptop with an Intel i7 2.80 Ghz processor, 6 GB RAM and an AMD Radeon 6630M graphics acceleration card. All reconstruction software was written in C++, OpenGL visualization is accelerated by the graphics card. It should be noted that manually annotating the contours for liver1's vascular network took approximately 2 h, for liver2's vascular network it took 2.5 h, and for the kidney's vascular network it took also approximately 2.5 h. In the next section, we present solutions for reconstructing organs.

## 9.4 Modelling Organs

Organs are topologically much simpler to model than vascular structures. The rightmost organ (kidney) in Fig. 9.13 is the result of a surface-based reconstruction which did not require any correspondences to be labelled between any of the contour polygons and is comprised of just one surface. However, the two organs (liver1 and liver2) on the left of Fig. 9.13 branch once towards the organs' lower right.

In this section, we apply the algorithms described in Sect. 9.2 to present three surface-based reconstruction solutions: One for organs that do not have branches (Sect. 9.4.1). Another solution which creates multiple composite surfaces to support branching without polygon correspondences is described in Sect. 9.4.2. A third surface-based reconstruction approach which requires polygon correspondences and creates a single surface that supports basic branching is detailed in Sect. 9.4.3. Finally, details on the resulting model complexity of the three approaches are provided in Sect. 9.4.4.

### 9.4.1 *Surface-Based Reconstruction for Organs with Simple Topology*

As mentioned earlier, some organs such as the kidney do not have branches, hence no polygon correspondence information is required as the correspondence is implicit. The first step of the surface-based reconstruction is to extract the vertices from each polygon contour and apply the first three steps of the modelling pipeline described in Fig. 9.6. The  $Y$  values of the vertices are inverted, duplicate vertices are removed (Sect. 9.2.2), counterclockwise ordering is forced on all polygon contours (Sect. 9.2.3) and the topmost polygon is triangulated by ear clipping (Sects. 9.2.4, 9.2.5 and 9.2.6) from above with its counterclockwise order. We then apply Christiansen and Sederberg's [47] triangle tiling algorithm to connect polygons from adjacent slices. We chose this algorithm because it allows for polygons to be

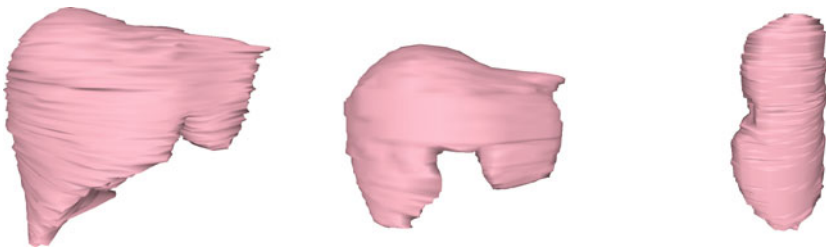


**Fig. 9.13** Modelling organs. (Left) liver1; (centre) liver2; (right) kidney

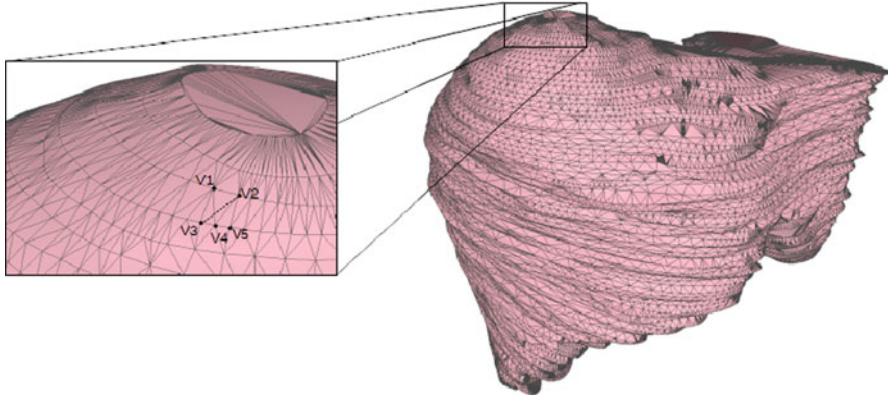


**Fig. 9.14** Surface-based reconstruction of an organ (*liver1\_high*)

tiled which have a different number of vertices between them, the achieved quality and their elegant single surface solution for branching which is described further ahead in Sect. 9.4.3.

The tiling algorithm starts by finding two vertices, one on each slice that have the smallest distance to each other. A bridge edge is created ( $V1$  and  $V3$ , Fig. 9.14 left), then two diagonal distances are calculated using the bridge vertices and the corresponding next vertices of the contours in the adjacent contour (distance  $V1 - V4$  and distance  $V3 - V2$  which is illustrated with a dashed line in Fig. 9.14). The shortest distance  $V1 - V4$  is chosen to create the triangle ( $V1, V3, V4$ ) instead of the triangle ( $V1, V3, V2$ ). The bridge vertex from the bottom contour then moves forward, and the same process is performed with bridge vertices  $V1$  and  $V4$ . The distance from bridge vertex  $V4$  to  $V2$  is smaller than the distance of bridge vertex  $V1$  to  $V5$ , and the triangle ( $V1, V4, V2$ ) is created. This process continues until all vertices have been visited, and all contours visited. The last contour, the bottommost contour is then triangulated from below, keeping the vertices in counterclockwise order, but reversing the order of the solution triangle ears. Finally, transformation step 4 (Eq. 9.3) of the modelling pipeline (Fig. 9.6) is applied to all vertices.

### 9.4.2 Composite Surfaces for Branching

If a data slice has more than one polygon contour, for example where an organ branches, then polygon contour information is required to guide the tiling process. Alternatively, one can decompose the contours of the organ into two separate contour files, and apply the surface-based reconstruction described in Sect. 9.4.1 to each file. Specifically, a contour file for the branch subpart can be created where the topmost polygon copies several control vertices of a larger overlapping polygon that exists in the contour file of the main organ part (Fig. 9.13, left and centre).

### 9.4.3 Single Surface with Branching

For branching contours, Christiansen and Sederberg [47] propose the following tilling algorithm:

1. find the closest vertex pair between the branched polygons
2. create a new vertex  $V_{mid}$ , which is positioned half-way between the vertex pair found in (1) and is halfway in-depth between the slice with branches and the slice immediately before the branch
3. the branched contour polygons are inserted into one ordered polygon that goes through  $V_{mid}$ . The new polygon definition goes through the closest pairs and midpoint ( $V_{mid}$ ) twice as it bridges the adjacent polygon and returns (Fig. 9.15 bottom).

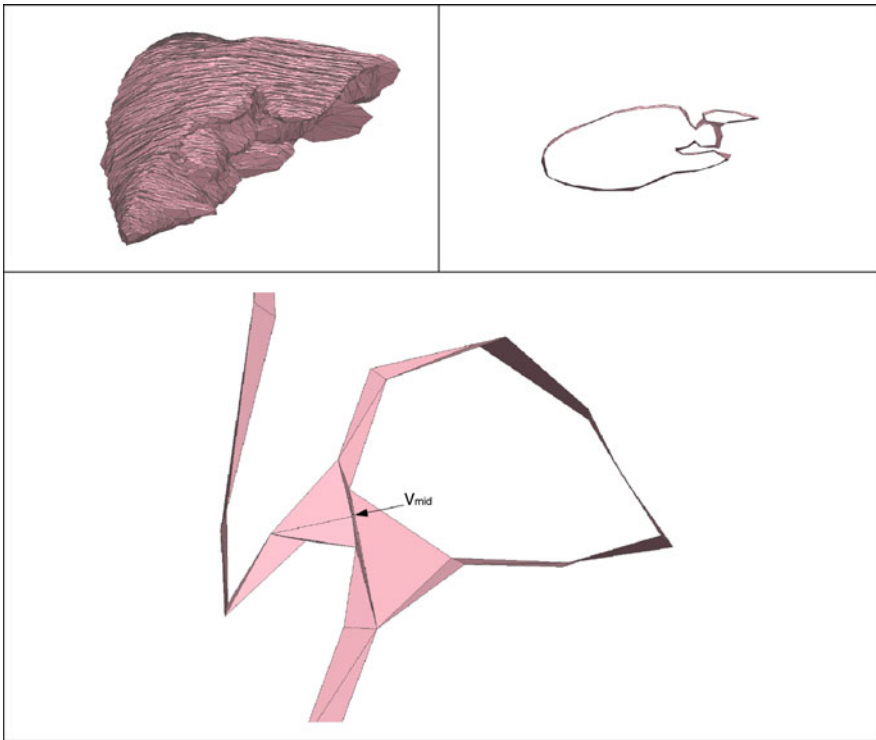


**Fig. 9.15** Single surface branching support. Top left: overall view of the reconstructed liver1 model with branching support (*liver1\_with\_branch\_low*); top right: two tiled polygons from the model in top left, the top larger polygon is tiled with the bottom two smaller polygons using new vertex  $V_{mid}$ ; bottom: close-up of top right

This new polygon creates a 1–1 relation with the polygon before the branch, and the next branch polygons below, each tile 1–1 with the old branch polygon definitions by ignoring the new vertex.

### 9.4.4 Model Complexity

Table 9.3 shows the model complexity associated with the respective models shown in Fig. 9.13, including the high-resolution versions, where the polygon contour widgets were set to extract more vertices. The high-resolution versions of the reconstructions help to “inflate” the models in some areas as more vertices become available to represent the underlying curves. This effect is particularly noticeable when examining the top edge of reconstructed rib bones [59]. As with the models in the previous section all models were generated in less than 1 second using a Sony Vaio laptop with an Intel i7 2.80 Ghz processor, 6 GB RAM and an AMD Radeon 6630M graphics acceleration card. All reconstruction software was written in C++, OpenGL visualization is accelerated by the graphics card. It should be noted that manually annotating the contours for liver1 took approximately 1 h 20 min, for liver2 it took around 1 h 30 min, and for the kidney it took 1 h 37 min. For the subparts (liver1\_b and liver2\_b) and the tumour object, it took around 10–15 min to annotate each.

**Table 9.3** Organ model complexity

Model	#Slices	#Contours	#Control vertices	#Triangles	#Vertices
liver1_low	155	113	2492	4974	2489
liver1_high	”	”	”	61,946	30,975
liver1b_low	”	6	40	76	40
liver1b_high	”	”	”	717	1430
liver1_with_branch_low	”	118	2527	5046	2525
liver1_with_branch_high	”	”	”	63,232	31,618
tumour_low	”	7	28	52	28
tumour_high	”	”	”	1574	789
liver2_low	74	59	1626	3248	1626
liver2_high	”	”	”	32,954	16,479
liver2b_low	”	19	277	550	277
liver2b_high	”	”	”	6947	3489
kidney_low	390	262	4245	8486	4245
kidney_high	”	”	”	87,566	43,785

## 9.5 Visualization, Putting the Models Together

We point out that all the reconstructed models are made of triangles; during development we stored the different models in Stanford University's PLY format [60]. A basic OpenGL viewer with alpha blending (Figs. 9.1, 9.11 and 9.13) was also implemented. However, our target application for the reconstructed models was to provide intraoperative spatial reasoning support to the surgeon. The IGSTK distribution contains an example application for image-guided surgery which contains several features in a stable state machine software environment. For instance, it allows to interact with several types of surgical trackers, read and display DICOM images, read and render 3D objects in the .msh format (Fig. 9.16) over the DICOM images. We build on this functionality to create the CAS\_Navigate tool, by adding an option to set different transparency settings for different objects, and an option to retain a colour for a model or generate a new pseudo-random one. These options allowed us to determine that the composite surfaces (Fig. 9.2, top row) both with a transparency setting of 0.4 could be a viable solution for branching organs, as the

**Fig. 9.16** Example .msh file with two triangles and four vertices

```

ObjectType = Scene
NDims = 3
NObjects = 1
ObjectType = Mesh
NDims = 3
ID = 0
BinaryData = False
TransformMatrix = 1 0 0 0 1 0 0 0 1
Offset = 0 0 0
CenterOfRotation = 0 0 0
ElementSpacing = 1 1 1
Color = 1 0 0 1
PointType = MET_FLOAT
PointDataType = MET_FLOAT
CellDataType = MET_FLOAT
NCellTypes = 1
PointDim = ID x y ...
NPoints = 4
Points =
0 84.8448 201.757 150.401
1 88.7002 211.396 150.401
2 78.4191 209.468 150.401
3 79.7042 215.894 150.401
CellType = TRI
NCells = 2
Cells =
0 0 1 2
1 1 3 2

```

two parts look as one. In turn, the volume-based reconstructed models are rendered completely opaque. The results of the reconstructions were shown to two surgeons. Both surgeons consider that the representation of organ and vascular structure is realistic and useful for surgical planning and navigation [52].

## 9.6 Conclusion

We have shown how volume-based reconstruction and composite surface-based reconstruction can be used to overcome time-consuming polygon correspondence annotation when modelling vascular networks and organs respectively. Creating a semi-transparent surface skin for the outer objects, and opaque volume blocks for the internal vascular structures allows one to hide the additional geometry created between volume blocks. In contrast, a completely volume-based block reconstruction for organs and vascular structures would create too much visual clutter to be able to easily see the vascular structures from outside an organ.

This approach has also recently been applied to bone tissue modelling. Figure 9.17 compares volume-based reconstruction of the rib cage and spine of a pig (right) with surface-based reconstruction (left). The latter took an additional 50 min to create the polygon correspondences required for the 19 surfaces (17 ribs, and 2 surface objects to represent the front and back of the spine). Here the inner geometry of volume blocks of the bone do not obstruct completely the organ and veins, as one can navigate around inside the rib cage. Visually either approach appear viable, the highest triangle count version (high-resolution volume-based reconstruction of the bones + low-resolution versions for the liver and vascular network) is comprised of just over half a million triangles and rendered smoothly at interactive rates with a Sony Vaio laptop with an Intel i7 2.80 GHz processor, 6 GB RAM, and an AMD Radeon 6630M graphics acceleration card. We found that

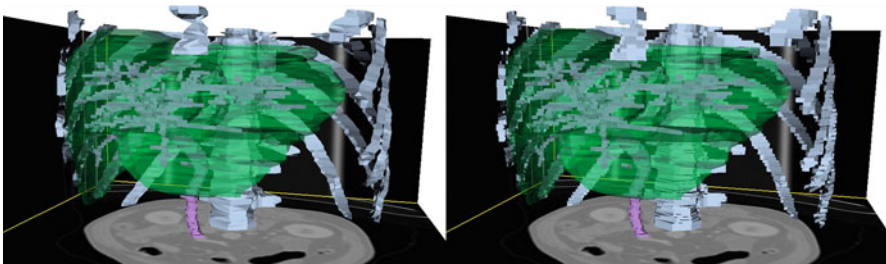


**Fig. 9.17** Bone tissue modelling and visualization in CAS\_Navigate. (Left) Surface-based reconstructed models (liver2 + liver2b + bone) and volume-based reconstruction (veins2); (right) volume-based reconstructed models (veins2 + bone) and surface-based reconstruction (liver2 + liver2b)



the low version of the models actually provided enough shape detail for our target application.

Our implementation of Christiansen and Sederberg's [47] tilling algorithm produced surface models without geometric errors for the kidney and liver2. But can still encounter difficulty [1, 61] when drastic changes of polygon shape occur between slices as a result from the inherent limitation in scanner resolution. Bak and Mill applied Christiansen and Sederberg's tilling algorithm when modelling complex geological structures, and report that additional problems can arise when the polygons in adjacent slices are not mutually centred, nor are they similar in size. They suggest a mapping that translates and scales the polygons onto an arbitrary unit square. After that, they centre the polygons and reduce them to a similar size before tilling. They also suggest manual editing of the polygons to make them more similar (e.g. for organs this could be to make a polygon contour step over a small local fold that only exists in one of the adjacent polygons) or to insert intermediate polygons between the two planes. The latter is a promising solution which we leave for the readers to implement as an exercise.

The good news is that the slice by slice reconstruction is resilient to the problem, always generating a global model and the alpha blending actually makes it difficult to notice any artefact (Fig. 9.2 liver1 has a tilling artefact in one slice).

Today many surgeries rely on the ability of the surgeon to create [62] and memorize a 3D image in their mind often by just looking at a series of 2D images previous to the operation. This map which is used in resection planning, allows weighting several risks, for example, the likelihood of inadvertently severing a blood vessel in the presence of more or less underlying blood vessel ramifications. On the other hand, the limitation of resolution between CT slices makes it impossible to model without error when particular structures begin, join or stop exactly. However, since resection planning relies on the general presence of more or less blood vessel ramifications, rather than high detail shape information, perhaps the resilience of a reconstruction method should be preferred over shape aesthetics. As such, the authors hope that the techniques presented here complement the segmentation and modelling research of others in the future, and would further shorten the time necessary to bring these 3D roads maps into the regular operation room.

**Acknowledgements** This work was partially funded by Programa de Cooperación Transfronteriza España Portugal (POCTEP) and Fondo Europeo de Desarrollo Regional (FEDER) Reference code: 0401\_RITECA\_II\_4\_E.

## References

1. D. Meyers, Reconstruction of Surfaces from Planar Contours, Ph.D. Thesis, University of Washington, 1994
2. J.C. Nebel, in *Deformable Avatars. IFIP—The International Federation for Information Processing*, ed. by N. Magnenat-Thalmann, D. Thalmann. Soft Tissue Modelling from 3D Scanned Data, vol 68 (Springer, Boston, MA, 2001). [https://doi.org/10.1007/978-0-306-47002-8\\_8](https://doi.org/10.1007/978-0-306-47002-8_8)

3. J.F. Oliveira, D. Zhang, B. Spanlang, B. Buxton, Animating scanned human models. *J. WSCG* **11**(2), 362–369 (2003). ISSN: 1213-6972
4. R.C. Gonzalez, R.E. Woods, *Digital Image Processing*, 3rd edn. (Addison-Wesley Publishing Company, Boston, MA, 1992)
5. N. Otsu, A threshold selection method from gray-level histograms. *IEEE Trans. Syst. Man Cybern.* **9**(1), 62–66 (1979). <https://doi.org/10.1109/TSMC.1979.4310076>
6. V. Leonardi, V. Vidal, J.-L. Mari, M. Daniel, in *3D Reconstruction from CT-Scan Volume Dataset Application to Kidney Modeling*. Proceedings of the 27th Spring Conference on Computer Graphics (SCCG '11) (2011), pp. 111–120. doi:<https://doi.org/10.1145/2461217.2461239>
7. S. Luo, X. Li, J. Li, Review on the methods of automatic liver segmentation from abdominal images. *J. Comput. Commun.* **2**(2), 1–7 (2014). <https://doi.org/10.4236/jcc.2014.22001>
8. A. Gotra, L. Sivakumaran, G. Chartrand, K.N. Vu, F. Vandenbroucke-Menu, C. Kauffmann, S. Kadoury, B. Gallix, J.A. de Guise, A. Tang, Liver segmentation: indications, techniques and future directions. *Insights Imaging* **8**(4), 377–392 (2017). <https://doi.org/10.1007/s13244-017-0558-1>
9. G. Tsechpenakis, in *Multi Modality State-of-the-Art Medical Image Segmentation and Registration Methodologies*, ed. by A. S. El-Baz, U. R. Acharya, M. Mirmehdi, J. S. Suri. Deformable Model-Based Medical Image Segmentation, vol 1 (Springer-Verlag, New York, 2011), pp. 33–67. <https://doi.org/10.1007/978-1-4419-8195-0>
10. M. Kass, A. Witkin, D. Terzopoulos, Snakes: active contour models. *Int. J. Comput. Vis.* **1**(4), 321–331 (1988)
11. X. Xie, M. Mirmehdi, MAC: magnetostatic active contour model. *IEEE TPAMI* **30**(4), 632–646 (2008). <https://doi.org/10.1109/TPAMI.2007.70737>
12. T.F. Cootes, C.J. Taylor, D.H. Cooper, J. Graham, Active shape models—their training and application. *Comput. Vis. Image Underst.* **61**(1), 38–59 (1995). <https://doi.org/10.1006/cviu.1995.1004>
13. T.F. Cootes, C.J. Taylor, *Statistical Models of Appearance for Computer Vision* (Imaging Science and Biomedical Engineering, University of Manchester, Manchester, UK, 2004). Tech Report
14. S. Osher, J.A. Sethian, Fronts propagating with curvature-dependent speed: algorithms based on Hamilton-Jacobi formulations. *J. Comput. Phys.* **79**(1), 12–49 (1988). [https://doi.org/10.1016/0021-9991\(88\)90002-2](https://doi.org/10.1016/0021-9991(88)90002-2)
15. Z. Ma, J.M.R.S. Tavares, R.N. Jorge, T. Mascarenhas, A review of algorithms for medical image segmentation and their applications to the female pelvic cavity. *Comput. Methods Biomech. Biomed. Eng.* **13**(2), 235–246 (2010). <https://doi.org/10.1080/10255840903131878>
16. S. Ghose, A. Oliver, R. Martí, X. Lladó, J. Vilanova, J. Freixenet, J. Mitra, D. Sidibé, F. Meriaudeau, A survey of prostate segmentation methodologies in ultrasound, magnetic resonance and computed tomography images. *Comput. Methods Programs Biomed.* **108**(1), 262–287 (2012). <https://doi.org/10.1016/j.cmpb.2012.04.006>
17. P.P.R. Filho, P.C. Cortez, A.C. da Silva Barros, V.H.C. Albuquerque, J.M.R.S. Tavares, Novel and powerful 3D adaptive crisp active contour method applied in the segmentation of CT lung images. *Med. Image Anal.* **35**, 503–516 (2017). <https://doi.org/10.1016/j.media.2016.09.002>
18. D.A.B. Oliveira, R.Q. Feitosa, M.M. Correia, Segmentation of liver, its vessels and lesions from CT images for surgical planning. *Biomed. Eng. Online* (2011). <https://doi.org/10.1186/1475-925X-10-30>
19. M. Archana, S. Ramakrishnan, Segmentation of CT liver images using phase based level set method. *Biomed. Sci. Instrum.* **49**, 7–12 (2013)
20. A. Zidan, N.I. Ghali, A.e. Hassamen, H. Hefny, in *Level Set-Based CT Liver Image Segmentation with Watershed and Artificial Neural Networks*. 12th International Conference on Hybrid Intelligent Systems (HIS) (2012), pp. 96–102. <https://doi.org/10.1109/HIS.2012.6421316>
21. X. Wang, J. Yang, D. Ai, Y. Zheng, S. Tang, Y. Wang, Adaptive Mesh Expansion Model (AMEM) for liver segmentation from CT image. *PLoS One* (2015). <https://doi.org/10.1371/journal.pone.0118064>

22. T. Heimann, H.P. Meinzer, Statistical shape models for 3D medical image segmentation: a review. *Med. Image Anal.* **13**(4), 543–563 (2009). <https://doi.org/10.1016/j.media.2009.05.004>
23. B. Tsagaan, A. Shimizu, H. Kobatake, K. Miyakawa, in *Medical Image Computing and Computer-Assisted Intervention*, ed. by D. Takeyoshi, R. Kikinis. An Automated Segmentation Method of Kidney Using Statistical Information (Springer, Berlin, Heidelberg, 2002), pp. 556–563
24. A. Skalski, J. Jakubowski, T. Drewniak, in *Kidney Tumor Segmentation and Detection on Computed Tomography Data*. IEEE International Conference on Imaging Systems and Techniques (IST) (2016). <https://doi.org/10.1109/IST.2016.7738230>
25. K.H. Zou, S.K. Warfield, A. Bharatha, C.M.C. Tempny, M.R. Kaus, S.J. Haker, W.M. Wells III, F.A. Jolesz, R. Kikinis, Statistical validation of image segmentation quality based on a spatial overlap index. *Acad. Radiol.* **11**(2), 178–189 (2004). [https://doi.org/10.1016/S1076-6332\(03\)00671-8](https://doi.org/10.1016/S1076-6332(03)00671-8)
26. G.C. Lin, W.J. Wang, C.M. Wang, S.Y. Sun, Automated classification of multispectral MR images using Linear Discriminant Analysis. *Comput. Med. Imaging Graph.* **34**(4), 251–268 (2010). <https://doi.org/10.1016/j.compmedimag.2009.11.001>
27. W. Bieniecki, S. Grabowski, in *Nearest Neighbor Classifiers for Color Image Segmentation*. Proceedings of the International Conference Modern Problems of Radio Engineering, Telecommunications and Computer Science (2004), pp. 209–212
28. C. Cortes, V. Vapnik, Support vector networks. *Mach. Learn.* **20**(3), 273–297 (1995)
29. D.S. Jodas, A.S. Pereira, J.M.R.S. Tavares, A review of computational methods applied for identification and quantification of atherosclerotic plaques in images. *Expert Syst. Appl.* **46**, 1–14 (2016). <https://doi.org/10.1016/j.eswa.2015.10.016>
30. İ. Dağ, B. Saka, D. Irk, Galerkin method for the numerical solution of the RLW equation using quintic B-splines. *J. Comput. Appl. Math.* **190**(1–2), 532–547 (2006). <https://doi.org/10.1016/j.cam.2005.04.026>
31. F. Khalifa, M. Abou El-Ghar, B. Abdollahi, H.B. Frieboes, T. El-Diasty, A. El-Baz, A comprehensive non-invasive framework for automated evaluation of acute renal transplant rejection using DCE-MRI. *NMR Biomed.* **26**(11), 1460–1470 (2013). <https://doi.org/10.1002/nbm.2977>
32. J.-W. Xu, K. Suzuki, in *Computer-Aided Detection of Hepatocellular Carcinoma in Hepatic CT: False Positive Reduction with Feature Selection*. 2011 IEEE International Symposium on Biomedical Imaging: From Nano to Macro (2011), pp. 1097–1100. <https://doi.org/10.1109/ISBI.2011.5872592>
33. Q. Dou, H. Chen, Y. Jin, L. Yu, J. Qin, P.-A. Heng, in *Medical Image Computing and Computer-Assisted Intervention – MICCAI 2016*, Lecture Notes in Computer Science, ed. by S. Ourselin, L. Joskowicz, M. Sabuncu, G. Unal, W. Wells. 3D Deeply Supervised Network for Automatic Liver Segmentation from CT Volumes, vol 9901 (Springer, Cham, 2016), pp. 149–157. [https://doi.org/10.1007/978-3-319-46723-8\\_18](https://doi.org/10.1007/978-3-319-46723-8_18)
34. H. Madero Orozco, O.O. Vergara Villegas, V.G. Cruz Sánchez, H. J. Ochoa Domínguez, M. J. Nandayapa Alfaro, Automated system for lung nodules classification based on wavelet feature descriptor and support vector machine. *Biomed. Eng. Online* **14**, 9 (2015). <https://doi.org/10.1186/s12938-015-0003-y>
35. Y. Wang, G. Morrell, M.E. Heibrun, A. Payne, D.L. Parker, 3D multi-parametric breast MRI Segmentation using hierarchical support vector machine with coil sensitivity correction. *Acad. Radiol.* **20**(2), 137–147 (2013). <https://doi.org/10.1016/j.acra.2012.08.016>
36. Y.-C. Lin, J.-L. Wu, I.-C. Lee, C.-H. Wu, A. Kumar, K.-C.J. Liu, Y.-Y. Wang, CT image segmentation with supervised clustering using hierarchical support vector machines. *Int. J. Comput. Consum. Control* **5**(2), 41–49 (2016)
37. Z. Ma, J.M.R.S. Tavares, R. M. Natal Jorge, in *A Review on the Current Segmentation Algorithms for Medical Images*. International Conference on Computer Imaging Theory and Applications (2009), pp. 135–140
38. A. Rosebrock, Deep Learning for Computer Vision with Python. Pyimagesearch (2017)

39. N.R. Pal, S.K. Pal, A review on image segmentation techniques. *Pattern Recogn.* **26**(9), 1277–1294 (1993). [https://doi.org/10.1016/0031-3203\(93\)90135-J](https://doi.org/10.1016/0031-3203(93)90135-J)
40. A. Das, S.K. Sabut, Kernelized fuzzy C-means clustering with adaptive thresholding for segmenting liver tumors. *Procedia Comput. Sci.* **92**, 389–395 (2016). <https://doi.org/10.1016/j.procs.2016.07.395>
41. H. Song, W. Kang, Q. Zhang, S. Wang, Kidney segmentation in CT sequences using SKFCM and improved GrowCut algorithm. *BMC Syst. Biol.* **9**(Suppl 5), S5 (2015). <https://doi.org/10.1186/1752-0509-9-S5-S5>
42. D. Shen, G. Wu, H.-I. Suk, Deep learning in medical image analysis. *Annu. Rev. Biomed. Eng.* **19**, 221–248 (2017). <https://doi.org/10.1146/annurev-bioeng-071516-044442>
43. Y. Liu, K. Gadepalli, M. Norouzi, G.E. Dahl, T. Kohlberger, A. Boyko, S. Venugopalan, A. Timofeev, P.Q. Nelson, G.S. Corrado, J.D. Hipp, Detecting Cancer Metastases on Gigapixel Pathology Images. arXiv preprint arXiv:1703.02442 (2017)
44. T. Heimann, B. van Ginneken, M.A. Styner, Y. Arzhaeva, V. Aurich, C. Bauer, A. Beck, C. Becker, R. Beichel, G. Bekes, F. Bello, G. Binnig, H. Bischof, A. Bornik, P.M. Cashman, Y. Chi, A. Cordova, B.M. Dawant, M. Fidirich, J.D. Furst, D. Furukawa, L. Grenacher, J. Hornegger, D. Kainmüller, R.I. Kitney, H. Kobatake, H. Lamecker, T. Lange, J. Lee, B. Lennon, R. Li, S. Li, H.P. Meinzer, G. Nemeth, D.S. Raicu, A.M. Rau, E.M. van Rikxoort, M. Rousson, L. Rusko, K.A. Saddi, G. Schmidt, D. Seghers, A. Shimizu, P. Slagmolen, E. Sorantin, G. Soza, R. Susomboon, J.M. Waite, A. Wimmer, I. Wolf, Comparison and evaluation of methods for liver segmentation from CT datasets. *IEEE Trans. Med. Imaging* **28**(8), 1251–1265 (2009). <https://doi.org/10.1109/TMI.2009.2013851>
45. Sliver, Sliver (2018). <http://www.sliver07.org>
46. C.L. Bajaj, E.J. Coyle, K.-N. Lin, Arbitrary topology shape reconstruction from planar cross sections. *Graph. Models Image Process.* **58**(6), 524–543 (1996). <https://doi.org/10.1006/gmip.1996.0044>
47. H.N. Christiansen, T.W. Sederberg, in *Conversion of Complex Contour Line Definitions into Polygonal Element Mosaics*. SIGGRAPH '78 (1978), pp. 187–192. <https://doi.org/10.1145/965139.807388>
48. ITK, ITK-SNAP (2018). <http://www.itksnap.org>
49. J. Shen, D. Thalmann, in *Interactive Shape Design Using Metaballs and Splines*. Proc. Eurographics Workshop on Implicit Surfaces '95 (1995), pp. 187–196
50. W. Schroeder, K. Martin, B. Lorensen, *The Visualization Toolkit*, 4th edn. (Kitware, New York, 2006)
51. IGSTK, The Image Guided Surgery Toolkit (2018). <http://www.igstk.org>
52. J.F. Oliveira, J.L. Moyano-Cuevas, J.B. Pagador, H. Capote, F.M. Sánchez-Margallo, Preoperative and intraoperative spatial reasoning support with 3D organ and vascular models: derived from CT data using VTK and IGSTK. *Int. J. Creat. Interfaces Comput. Graph.* **6**(2), 56–82 (2015). ISSN: 1947-3117
53. D. Eberly, Triangulation by Ear Clipping (2008). <http://www.geometrictools.com>
54. O.S. Pinykh, *Digital Imaging and Communications in Medicine (DICOM) A Practical Introduction and Survival Guide*, 2nd edn. (Springer, Heidelberg, 2012). ISBN: 978-3-642-10849-5
55. IGSTK, DICOM Data Orientation (2018). [https://public.kitware.com/IGSTKWIKI/index.php/DICOM\\_data\\_orientation](https://public.kitware.com/IGSTKWIKI/index.php/DICOM_data_orientation)
56. B. Braden, The surveyor's area formula. *Coll. Math. J.* **17**(4), 326–337 (1986)
57. A. Gueziec, Surface simplification inside a tolerance volume. Technical Report, Yorktown Heights, NY 10598, March 1996. IBM Research Report RC 20440 (1996)
58. J.F. Oliveira, M. Ziebart, J. Iliffe, J. Turner, S. Robson, Trixel Buffer Logic for I/O bound point in N-polygon inclusion tests of massive bathymetric data. *J. WSCG* **21**(1), 79–88 (2013). ISSN: 1213-6972
59. J.F. Oliveira, Surface vs volume based reconstruction of bone tissue using CAS\_Annotate and CAS\_Navigate. *J. Biomed. Eng. Med. Imaging.*, ISSN: 2055-1266 **4**(5), 19–26 (2017). <https://doi.org/10.14738/jbemi.45.3771>

60. Stanford University, The Stanford 3D Scanning Repository (2018). <http://graphics.stanford.edu/data/3Dscanrep/>. Last accessed 20 Jan 2018
61. P.R.G. Bak, A.J.B. Mill, in *Three Dimensional Applications in Geographical Information Systems*, ed. by J. Raper. Three Dimensional Representation in a Geoscientific Resource Management System for the Minerals Industry (Taylor & Francis, Inc., Bristol, PA, 1989), p. 162
62. C.T. Yeo, A. MacDonald, T. Ungi, A. Lasso, D. Jalink, B. Zevin, G. Fichtinger, S. Nanji, Utility of 3D reconstruction of 2D liver computed tomography/magnetic resonance images as a surgical planning tool for residents in liver resection surgery. *J. Surg. Educ.* (2017). <https://doi.org/10.1016/j.jsurg.2017.07.031>

# Index

## A

- Abdominal Aortic Aneurysms (AAA)
  - ANSYS Workbench 16.1, 92, 93
  - Asian population, incidence, 87
  - cause of, 85–86
  - computational method-based analysis, 88
  - CVD, 84
  - first principal stress, 94, 95
  - FSI analysis, 93
  - inlet and outlet boundary conditions, 92, 93
  - limitations, 98
  - mesh generation, 92
  - Navier–Stokes equations, 91
  - PC-MRI, 91
  - rupture in, 86–87
  - structural deformation, 96
  - three-dimensional model
    - CT scan, 89
    - geometry reconstruction, 88, 89
    - image segmentation, 90
    - mesh model file conversion, 90
    - mesh model refinement, 90
  - types, 85–86
  - validation, 93, 94
  - velocity and pressure, 97–98
  - WSS, 92, 94, 96–97
- Allergen sensitization, 52
- Allergic skin reactions quantification by PPGI
  - antihistaminic therapy, 59
  - automatic threshold technique, 59–61
  - computer-based imaging technique, 51
  - data acquisition and signal analysis, 53–54
  - functional prick and intradermal test, 54, 55
  - heartbeat synchronal perfusion, 54
  - histamine-induced skin reaction, 56

- IDT, 52, 53
  - pulse amplitude, 57
  - SPT, 52, 53
  - study population characteristics, 52
  - vascular response, 55–59
- Alternative forced choice (AFC), 182
- Aluminum (Al), 170
- Angular dispersive X-ray diffraction (ADXRD), 148, 150
- Anisotropy skull conductivity, 114–115
- ANSYS workbench, 91
- Application specific integrated circuit (ASIC), 151
- Arbitrary Eulerian Lagrangian (ALE) method, 88, 91, 96
- Artifact spread function (ASF), 174–175
- Artificial neural networks (ANN), 222
- Automatic Exposure Control (AEC)
  - performance, 169–170

## B

- Back-face culling, 227
- Beer–Lambert equation, 35
- Binary space-partitioning (BSP) tree, 193
- Bio-heat transfer equation (BHTE), 113
- Blackbody radiation, IRT, 3–5
- Block matching method, 44–45
- Bragg equation, 150
- Bragg peak, 140
- Brain Extraction Tool (BET), 109
- Breast abnormalities detection, IRT, 8, 10
- Breast cancer
  - breast tissue vs. 2D histopathology, 151–152

- Breast cancer (*cont.*)
  - diffraction profiles, 152–154
  - diffractometer design and pixelated diffraction, 148–150
  - medical and security areas, 154–155
  - pixelated and non-pixelated diffraction, 150–151
  - XRD, 147–148
- Breast conserving surgery (BCS), 147
- Breast thermography, 10
- Breath-hold cine (bTFE sequence) and LGE (TFE), 72
  
- C**
- Camera-based PPG (cbPPG), 32
- Cardiac pulse, IRT
  - carotid vessel complex, 20
  - superficial temporal vessel complex, 20
  - thermal facial region and vascular maps, forehead, 21
- Cardiac resynchronization therapy (CRT)
  - planning
    - global workflow, 69–70
    - landmark-based registration, 69
  - LGE-MRI to CT registration
    - cine-MRI, 73–74
    - generated model for patients, 76, 79, 80
    - NCC curve, 74
    - patient-specific model results, 75
    - results, 75, 78
  - multimodal image processing
    - characteristics, 70
    - LGE-MRI, 72
    - LV and veins, CT images, 70–71, 75–76
    - mechanical description, STE, 71–72, 75, 77
  - registration, 72
  - 17-segment bulls-eye representation, 69
  - STE to CT registration
    - DTW, 73
    - patient-specific model results, 75
    - surgical gestures, 73
    - 2D dynamic contour, 73–74
- Cardiac SENSE coils, 72
- Cardiovascular diseases (CVDs), 84
- Carrico index, 23
- Cerebral aneurysm, 84–85
- Cerebrospinal fluid (CSF), 109, 112, 113, 117, 119, 120, 127
- Charge coupled devices (CCDs), 169
- Cheyne–Stokes respiration, 15
- Chronic heart failure (HF), 68
- Chronic wounds, IRT, 13–14
  
- Cold stimulation, 10
- Complementary metal-oxide-semiconductor (CMOS) active pixel sensor (APS), 169
- Compton cameras, 137, 142–143
- Compton scattering, 136
  - Compton camera principle, 142–143
  - design criteria, 144
  - image reconstruction principle, 145–146
  - in vivo proton range verification, 138–140
  - prompt gamma emission, 140–142
  - SOE, 137, 146–147
- Computed tomography (CT)
  - geometric problems, 225
  - image segmentation
    - classifier methods, 222–223
    - deformable models, 221–222
    - diagnostic and treatment algorithms, 219
    - liver and kidney, 220
    - manual segmentation, 219
    - thresholding and region growing, 220–221
  - inherent spatial resolution limitation, 223
- LGE-MRI
  - cine-MRI, 73–74
  - generated model for patients, 76, 79, 80
  - NCC curve, 74
  - patient-specific model results, 75
  - results, 75, 78
- LV and veins segmentation, 70–71
- modelling and visualization, 218
- organs modelling
  - composite surfaces, 238
  - model complexity, 237, 240
  - single surface with branching, 239–240
  - surface-based reconstruction, 226, 237–238, 242
- problems of reconstruction, 223
- STE
  - DTW, 73
  - patient-specific model results, 75
  - surgical gestures, 73
  - 2D dynamic contour, 73–74
- topological problems, 224–225
- vascular structures, 235–236
- visualization, 241–242
- volume-based reconstruction, 242–243
- VTK to IGSTK
  - CAS\_Annotate and CAS\_Navigate, 226
  - convex and concave polygons, point-in-polygon test, 232, 234
  - duplicate vertices, 229

- irregular polygons, internal angle
    - calculation, 231–233
  - polygon contour file format, 234–235
  - transformation pipeline, 226–228
  - triangulation by ear clipping, 229–231
  - 2D polygon vertex order consistency
    - problem, 226, 229
  - Computer-based imaging technique, 51
  - Continuous waveform analysis, 21
  - Continuous wavelet transform (CWT), 18
  - Contrast Detail phantom for MAMmography (CDMAM), 172–173
  - Contrast-to-noise ratio (CNR), 167
  - Convolutional neural network (CNN)
    - architecture, 223
  - Coupled momentum method (CMM), 88
  - CSF, *see* Cerebrospinal fluid
- D**
- Deep brain stimulation (DBS), 104
  - Detective quantum efficiency (DOE), 167
  - Detector air kerma (DAK), 170
  - DICOM standard, 228
  - Digital breast tomosynthesis (DBT)
    - algebraic methods, 164
    - breast detection
      - AEC performance, 169–170
      - a-Se TFT, 168
      - CCDs, 169
      - CMOS APS, 169
      - CNR, 167
      - detector element failure, 171
      - detector response, 170
      - DQE, 167
      - electronic noise, 170–171
      - MTF, 171–172
      - noise analysis, 170
      - PPS, 168
      - QC methods, 169
      - quantum noise, 170–171
      - SNR, 167–168
      - structure noise, 170
      - TFTs, 167–168
      - uncorrected defective elements, 171
    - definition, 160
    - digitized video cameras, 162
    - dose levels, 164, 167
    - geometric tomography, 160–161
    - geometries, 163–164
    - image intensifiers, 162
    - image quality measurements
      - background trends and artifacts, 176
      - CDMAM, 172–173
      - European QC Protocol, 174–175
      - geometric distortion, 176
      - missed tissue, 175–176
      - MTF, 175
      - structure noise, 176
      - 3D structured phantoms, 172
      - TOR MAM, 172–173
      - z-resolution, 165–166, 173–175
    - medical imaging applications, 162
    - MGD, 164, 167
    - performance evaluation
      - breast software phantoms, 178–179
      - clinical trials, 177
      - image acquisition and reconstruction, 177
      - microcalcifications, 177
      - simulated lesions, 178–180
      - 2D mammography, 176, 178
      - X-ray spectrum, 177
      - X-ray tracing, 180–182
    - quasi 3D X-ray imaging technique, 163
    - reconstruction algorithm, 164–166
    - shift-and-add concept, 161–162
    - TFT technology, 162
    - 2D digital mammography, 163
  - Digital image processing, 42
  - Dirichlet BC, 114
  - DistancePPG, 32
  - Dry eye syndrome, 12–13
  - Ductal carcinoma, 10, 11
  - Dynamic time warping (DTW), 73
- E**
- Electrical skull anisotropy, 120–122, 128–129
  - Electroconvulsive therapy (ECT), *see* Human head model
  - Electronic noise, 167, 170–171
  - Endovascular Aneurysm Repair (EVAR), 86
  - Energy dispersive X-ray diffraction (EDXRD), 148, 150, 151
  - Entrance surface air kerma (ESAK), 167
- F**
- Fast Fourier transform (FFT), 20
  - Feature space, 106–107
  - Filtered back projection (FBP), 164
  - Finite element analysis (FEA) methods, 88
  - Finite element methods (FEM), 105
  - Flat-field correction, 170
  - Flat-panel detectors, 167
  - Fluid–structure interaction (FSI), 83, 88, 93–96



FMRIB's Software Library (FSL), 106, 108, 109  
 Frames per second (FPS) rate, 204–205, 211  
 Full field digital mammography (FFDM), 163  
 Full width at half maximum (FWHM), 174–175  
 Fuzzy c-means, 223  
 Fuzzy volume rendering, 194

## G

Gamma-ray energies, 139–140  
 Geant4 simulation toolkit, 140  
 GetPixelSpacing() function, 228  
 Graphics processing unit (GPU), 195  
 Graves' orbitopathy, 13  
 Greybody radiation, IRT, 5  
 Greymatter (GM), 109, 112, 113, 117, 119, 120

## H

Heat dissipation, 127  
 Herzman's photoplethysmographic device, 32, 33  
 Human head model
 

- anisotropy skull conductivity, 114–115
- blood perfusion and metabolic heat, 124–127
- electrode and skin interface, 116
- electrode modelling, 110–111
- fat layer, 126–127
- isotropic and anisotropic versions, 111, 112
- measurement analysis, 116–117
- mesh generation, 111, 112

 MRI
 

- flowchart, 106, 107
- registration, 106–108
- tissue segmentation, 108
- types, 105–106

 pharmacotherapy, 104  
 RHM development, 108–110  
 temperature behavior
 

- electrical skull anisotropy, 120–122, 128–129
- input currents, threshold of, 123–124, 129
- isotropic cases, 117–118, 127–128
- thermal skull anisotropy, 119–122, 128–129

 temperature distribution, 129–130  
 tES, 104  
 types, tissues, 112

volume conductor model, 112–114  
 waveforms, 104  
 Hybrid-camera approach, 61–62

## I

Image noise, 167  
 Image-order method, 194  
 Image orientation, 228  
 Image position, 228  
 ImageVis3D, 205, 211  
 Imaging PPG (iPPG), 32  
 In-focus/focal plane, 160–161  
 Infrared thermography (IRT) imaging, 33
 

- advancement, 25–26
- mass fever screening, 2
- medical (*see also* Medical applications, IRT)
  - non-invasive measurement technique, 2
  - non-radiating measurement technique, 2
  - physical principles, 3–7
  - proactive and preventive approach, 2
  - 3D representations, 25–26

 Intradermal test (IDT), 52, 53  
 Intraluminal thrombus (ILT), 92  
 Inversion recovery (IR), 72  
 Isotropic model, 117–118, 127–128  
 Iterative algorithm, 146–147

## K

Kanade–Lucas–Tomasi (KLT) feature tracker, 46–47  
 Kernel-based Fuzzy c-means algorithm (KFCM), 223  
 Kirchhoff's law, 5  
 Klein–Nishina formula, 144  
 k-nearest neighbour (kNN) classifiers, 222

## L

Laser Doppler fluxmetry (LDF), 47  
 Laser Doppler perfusion imaging (LDPI), 47  
 Late gadolinium enhancement (LGE)
 

- cine-MRI, 73–74
- fibrosis characterization, 72
- generated model for patients, 76, 79, 80
- NCC curve, 74
- patient-specific model results, 75
- results, 75, 78

 Left ventricle (LV), 70–71  
 Lempel–Ziv–Markov chain algorithm (LZMA), 196  
 Linear discriminant analysis (LDA), 222

**M**

- Magnetic resonance images (MRI)
    - flowchart, 106, 107
    - LGE
      - cine-MRI, 73–74
      - fibrosis characterization, 72
      - generated model for patients, 76, 79, 80
      - NCC curve, 74
      - patient-specific model results, 75
      - results, 75, 78
    - registration, 106–108
    - tissue segmentation, 108
    - types, 105–106
  - Markov Chain Monte Carlo method, 146
  - Maximum likelihood expectation maximization (MLME), 146, 164
  - Maximum principal stress theory, 94–95
  - Maximum shear stress theory, 94–95
  - Maxwell's equation, 112
  - Mean arterial pressure (MAP), 23
  - Mean glandular dose (MGD), 164, 167
  - Medical applications, IRT, 9
    - diagnostic monitoring
      - breast abnormalities detection, 8, 10
      - dry eye syndrome, 12–13
      - ocular disease, 12–13
      - rheumatic diseases, 10–12
      - wound assessment, 13–14
    - monitoring, signs
      - cardiac pulse, 19–22
      - Pearson product-moment correlation, 24, 25
      - perfusion, 22–25
      - respiratory rate, 14–19
    - research studies, 8
  - MeshLab, 89, 90, 92
  - MIALite, 90
  - Modulation transfer function (MTF), 171–172, 175
  - Monte Carlo-based conversion factors, 167
  - Movement artifact detection and compensation, PPGI plethysmogram
    - motion tracking and compensation algorithms, 44–47
    - movement events assessment, 43–44
- N**
- National Health Service Breast Screening Programme (NHSBSP) reports, 181
  - Navier–Stokes equations, 91
  - Nikon XT H 225 System, 153

- Noise power spectrum (NPS), 181
  - Noncontact PPG (ncPPG), 32
  - Normalized cross-correlation (NCC) curves, 74
  - Normalized mutual information (NMI), 74
- O**
- Object-order method, 194
  - Ocular disease, 12–13
  - Optical flow method, 45–46
  - Optical hybrid imaging, 61–62
  - Out-of-core rendering
    - GPU, 195
    - level of detail/multi-resolution techniques
      - blocking schemes, 194
      - Bone B data set, 200, 202, 207
      - FPS rate, 204–205, 211
      - ImageVis3D, 205, 211
      - Manix data set, 200, 202, 210
      - Material A data set, 200, 202, 208
      - Material B data set, 200, 202, 209
      - Melanix data set, 200, 202, 206, 211
      - observer's distance, 200, 205
      - PSNR value, 202–204, 212
    - memory-mapped file, 193, 196
    - spatial data structures
      - BSP tree, 193
      - Haar wavelet transform, 196
      - kd-tree, 193
      - LZMA, 196
      - octrees, 193
      - preprocessing step, 196, 199, 201, 202
      - proposed architecture, 195–196
      - shell, 193
      - stored blocks, 196
      - user interaction, 199–200, 203
    - volume rendering
      - composition step, 197
      - compression results, 200, 204
      - computational time, 198, 201
      - high-resolution model, 197
      - image-order, 194, 197
      - level-of-detail technique, 197
      - Linux Ubuntu 10.13 64-bit version, 197–198
      - Manix files, 198–200
      - matrix, 197
      - Melanix files, 198–200
      - object-order, 194, 197
      - proposed architecture, 195–196
      - transfer function, 194

**P**

- Passive pixel sensor (PPS) technology, 168
- Patient position, 228
- Peak signal-to-noise ratio (PSNR), 196, 202–204, 212
- Phase contrast magnetic resonance imaging (PC-MRI), 91
- Phase-sensitive IR (PSIR) techniques, 72
- Photon scattering
  - definition, 136–137
  - elastic/Rayleigh scattering, breast cancer
    - breast tissue vs. 2D histopathology, 151–152
  - diffraction profiles, 152–154
  - diffractometer design and pixelated diffraction, 148–150
  - medical and security areas, 154–155
  - pixelated and non-pixelated diffraction, 150–151
  - XRD, 147–148
- inelastic/Compton scattering, 136
  - Compton camera principle, 142–143
  - design criteria, 144
  - image reconstruction principle, 145–146
  - in vivo proton range verification, 138–140
  - prompt gamma emission, 140–142
  - SOE, 137, 146–147
- XRD, 136
- Photoplethysmography imaging (PPGI) system
  - applications
    - clinical trial, 51–61
    - skin perfusion, 47–51
  - history, 32, 33
  - movement artifacts, detection and compensation, 43–47
  - optical hybrid imaging, 61–62
  - in reflective mode, 63
  - remote measurement and signal
    - composition, 32–38
    - signal analysis, 38–42
- Physical principles, IRT
  - blackbody radiation, 3–5
  - greybody radiation, 5
  - temperature measurement, 5–7
  - thermal cameras, 7
  - thermal radiation, 3
- Pixellated X-ray diffraction (PixD), 148–150
- PMMA, 170, 171, 173, 175, 176
- Point spread function (PSF), 174
- Polygon, 230
- PPGI system, *see* Photoplethysmography imaging system

- Principal component analysis (PCA), 153
- Prompt gamma rays, *see* Photon scattering
- Proton beam therapy (PBT)
  - Compton camera principle, 142–143
  - design criteria, 144
  - image reconstruction principle, 145–146
  - in vivo proton range verification, 138–140
  - prompt gamma emission, 140–142
  - SOE, 146–147

**Q**

- Quality Control (QC) methods, 169

**R**

- Rayleigh scattering
  - breast tissue vs. 2D histopathology, 151–152
  - diffraction profiles, 152–154
  - diffractometer design and pixelated diffraction, 148–150
  - medical and security areas, 154–155
  - pixelated and non-pixelated diffraction, 150–151
  - XRD, 147–148
- Realistic human head model (RHM), *see* Human head model
- Region of interest (ROI), 16–17, 71, 170
- Relative error (RE), 116–117, 121
- Remote PPGI measurement and signal composition
  - detected light intensity, 36
  - direct skin surface reflections, 36
  - evidence-based medical diagnostics, 34
  - first-and second-generation, 36–37
  - history, 32, 33
  - low-cost cameras (webcams and smartphone cameras), 37–38
  - reflection mode, 35
  - regions of interest, 35
  - signal waveform genesis, 34–36
- Respiratory rate (RR) monitoring, IRT
  - algorithms and experimental settings, 16
  - bradypnea, 15
  - capnography (exhaled carbon dioxide measurement), 15
  - fusion algorithms, 17
  - image preprocessing and enhancement, 16
  - impedance pneumography (respiration-modulated thoracic impedance), 15
  - inspiration and expiration, 14

- piezoplethysmography (thoracic/abdominal effort measurement), 15
  - respiration waveform extraction, 16, 18–19
  - ROI selection, 16–17
  - root mean squared error, 19
  - spirometry (flow measurement), 15
  - tachypnea, 15
  - thermistors (respiration-modulated temperature differences), 15
  - Response function, 170
  - Rheumatic diseases, 10–12
  - Right unilateral (RUL), 110, 114, 119, 120
  - ROI, *see* Region of interest
- S**
- Scanto3D plugin, 90
  - Search space, 107
  - Search strategy, 107
  - Shear-warp, 194
  - Shock index (SI), 23
  - Shoelace formula, 229
  - Shoulder immobility, 12
  - Signal analysis, PPGI system
    - automatic multidimensional signal
      - post-processing, 42
    - fast Fourier transform, 40
    - heart rate, 38
    - perfusion index, 38
    - respiratory rate, 38
    - respiratory rate variability, 38
    - skin perfusion visualization, 41–42
    - space-resolved mapping, 41–42
    - time–frequency domain, 40
    - time series analysis, 38
    - transient perfusion signals, 40, 41
    - visual analysis, 39
    - zero-crossings, 39
  - Signal-difference-to-noise ratio (SDNR), 170
  - Signal-to-noise ratio (SNR), 167–168
  - Signal transfer property (STP), 170
  - Similarity metric, 107, 108
  - SIMPLE method, 91
  - Simultaneous algebraic reconstruction technique (SART), 164
  - Skin allergy test, 51
  - Skin perfusion
    - bilateral heartbeat-related amplitude, 49–50
    - changes after mechanical irritation, 47
    - distribution, melanoma, 47–49
    - multiwavelength illumination PPGI study, 50–51
    - remote SpO<sub>2</sub>, 50–51
  - Skin prick test (SPT), 52, 53
  - Slice sensitivity profile (SSP), 174
  - SOE, *see* Stochastic Origin Ensemble
  - Source coordinate system (VTK)
    - CAS\_Annotate and CAS\_Navigate, 226
    - convex and concave polygons, point-in-polygon test, 232, 234
    - duplicate vertices, 229
    - irregular polygons, internal angle calculation, 231–233
    - polygon contour file format, 234–235
    - transformation pipeline, 226–228
    - triangulation by ear clipping, 229–231
    - 2D polygon vertex order consistency problem, 226, 229
  - Space-resolved mapping, 41–42
  - Spatial resolution, 73
  - Speckle tracking echography (STE)
    - DTW, 73
    - echographic image, 75, 77
    - mechanical description, 71–72
    - patient-specific model results, 75
    - surgical gestures, 73
    - 2D dynamic contour, 73–74
  - Splatting, 194
  - Stefan-Boltzmann law, 4, 5
  - Stochastic Origin Ensemble (SOE), 137, 146–147
  - Supervised classifiers, 222
  - Support vector machines (SVM), 222
  - Surveyor’s area formula, 229
- T**
- Target coordinate system (IGSTK)
    - CAS\_Annotate and CAS\_Navigate, 226
    - convex and concave polygons, point-in-polygon test, 232, 234
    - duplicate vertices, 229
    - irregular polygons, internal angle calculation, 231–233
    - polygon contour file format, 234–235
    - transformation pipeline, 226–228
    - triangulation by ear clipping, 229–231
    - 2D polygon vertex order consistency problem, 226, 229
  - Texture slicing, 194
  - Thermal cameras, IRT, 7
  - Thermal capacitance, 127
  - Thermal imaging, *see* Infrared thermography (IRT)
  - Thermal radiation, IRT, 3

Thermal skull anisotropy, 119–122,  
128–129  
Thermographic index, 11  
Thin film transistor (TFT), 162, 167–168  
Thoracic aneurysm, 85  
3D infrared thermography, *see* Infrared  
thermography (IRT)  
Threshold-based segmentation method, 90  
Tissue thermal diffusion, 20  
TOR MAM, 172–173  
Transcranial direct current stimulation (tDCS),  
104  
Transcranial electrical stimulation (tES), 104  
Transthoracic echocardiography, 72  
2D dynamic contour, 73

**U**

Unsupervised classifiers, 222  
User-defined function (UDF), 91

**V**

Volume conductor model, 112–114  
Volume ray casting, 194

**W**

Wall shear stress (WSS), 87, 92, 94, 96–97  
White matter (WM), 109, 112, 113, 117, 119,  
120  
Wide local excision (WLE), 151, 152  
Wilks' lambda method (HCC), 222  
Wound assessment, IRT, 13–14

**X**

X-ray diffraction (XRD), 136, 147–148

**Z**

Zero padding, 18